

AD A103567

ARO 15284.2-MS

(5)

RAPID CYCLE CASTING OF STEEL

FINAL REPORT

LEVEL III
AUG 1981

D. APELIAN, G. LANGFORD

Contractor: Drexel University, Philadelphia, PA 19104

Reporting Period: July 1, 1977 - August 31, 1980

Effective date of Contract: July 1, 1977

Contract expiration date: August 31, 1980

Sponsored by

Defense Advanced Research Projects Agency (DoD)

ARPA order No. 3397

Monitored by Dr. Phillip Parrish under Contract No. DAAG29-77-C-0028

The views and conclusions contained in this document are those of the authors and should not be interpreted as necessarily representing the official policies, either expressed or implied, of the Defense Advanced Research Projects Agency or the U. S. Government.

DTIC FILE COPY

Approved for public release.

Distribution Unlimited.

819

01038

DTIC
ELECTED
S SEP 1 1981 D

D

2

THE VIEW, OPINIONS, AND/OR FINDINGS CONTAINED IN THIS REPORT ARE THOSE OF THE
AUTHOR(S) AND SHOULD NOT BE CONSTRUED AS AN OFFICIAL DEPARTMENT OF THE ARMY
POSITION, POLICY, OR DECISION, UNLESS SO DESIGNATED BY OTHER DOCUMENTATION.

UNCLASSIFIED

SECURITY CLASSIFICATION OF THIS PAGE (When Data Entered)

REPORT DOCUMENTATION PAGE		READ INSTRUCTIONS BEFORE COMPLETING FORM
1. REPORT NUMBER	2. GOVT ACCESSION NO.	3. RECIPIENT'S CATALOG NUMBER
	AD-A103 567	
4. TITLE (and Subtitle)	5. TYPE OF REPORT & PERIOD COVERED Final, July 1, 1977 to December, 1980	
(6) Rapid Cycle Casting of Steel		
7. AUTHOR(s)	6. PERFORMING ORG. REPORT NUMBER	
Dixen George Apelian, Langford	(15) DAAG29-77-C-0028, ARPA Order-3397	
8. PERFORMING ORGANIZATION NAME AND ADDRESS Department of Materials Engineering Drexel University, 32nd & Chestnut Streets Philadelphia, Pa. 19104	10. PROGRAM ELEMENT, PROJECT, TASK AREA & WORK UNIT NUMBERS (12) 527	
11. CONTROLLING OFFICE NAME AND ADDRESS U. S. Army Research Office Post Office Box 12211 Research Triangle Park, NC 27709	11. REPORT DATE July 1981	
12. MONITORING AGENCY NAME & ADDRESS (if different from Controlling Office) (9) Final rept. 1 Jul 77 31 Aug 80	13. NUMBER OF PAGES	
	14. SECURITY CLASS. (of this report) Unclassified	
	15a. DECLASSIFICATION/DOWNGRADING SCHEDULE	
16. DISTRIBUTION STATEMENT (of this Report) Approved for public release; distribution unlimited.	17. DISTRIBUTION STATEMENT (of the abstract entered in Block 20, if different from Report) NA	
18. SUPPLEMENTARY NOTES The view, opinions, and/or findings contained in this report are those of the author(s) and should not be construed as an official Department of the Army position, policy, or decision, unless so designated by other documentation.		
19. KEY WORDS (Continue on reverse side if necessary and identify by block number) Rapid solidification, diffusion, mass transport, infiltration, segregation, ternary segregation, particle valve, heating methods, atomization, deoxidation, decarburization, powder resistivity, carbon steels, malleable high carbon steels, high speed steel, stainless steel, tin bronzes, iron-silicon, iron-phosphorous, joining, mold logic.		
20. ABSTRACT (Continue on reverse side if necessary and identify by block number) A rapid-cycle casting process for steel via diffusion solidification (SD) has been developed. Solidification takes place by carbon redistribution between iron-saturated high-carbon liquid iron and low carbon pre-existing solid iron in a refractory mold. Since no heat need be rejected to the surroundings during this process, the solidification time is shorter and the economic scaling law is less dependent on the size of the casting than in conventional casting processes. The metallurgical and processing aspects of SD casting were addressed and the necessary parameters have been developed to design a rapid		

20. ABSTRACT CONTINUED

cycle casting machine. These process parameters in addition to the metallurgical quality variables have been included in an economic feasibility analysis of the SD process. Pages (i) - (iv) summarize these developments.

Accession For	
NTIS GRA&I	<input checked="" type="checkbox"/>
DTIC TAB	<input type="checkbox"/>
Unannounced	<input type="checkbox"/>
Justification	
By _____	
Distribution/ _____	
Availability Codes	
Dist	Avail and/or Special
A	

DTIC
SELECTED
S D
SEP 1 1981
D

RAPID CYCLE STEEL CASTING, PROGRESS REPORT

SUMMARY

We are developing a rapid-cycle casting process for steel. Solidification takes place by carbon redistribution between iron-saturated high-carbon liquid iron and low carbon pre-existing solid iron in a refractory mold. That is, a mold is first filled with steel shot, heated, and then quickly infiltrated with molten cast iron at its liquidus temperature. Since no heat need be rejected to the surroundings during this diffusion solidification (SD) process, the solidification time is shorter and the economic scaling law is less dependent on the size of the casting than in conventional casting processes; i.e. $t_{SD} \propto L^{6/5}$ instead of L^2 . Furthermore, no riser is necessary because of the large fraction (60% or more) of pre-existing solid, and shrinkage porosity can be controlled by lowering the total oxygen content of the casting components. There is little or no thermal shock to the mold because the process is essentially isothermal and the casting temperature is reduced by 150 to 200°C. Hence, it may be possible to achieve production rates for steel casting analogous to die casting but without the material problems normally associated with the high melting point of steel.

The original DARPA proposal listed a series of twelve objectives to be completed so as to "develop the design of a rapid cycle casting machine", i.e., to enable a realistic analysis of the economic basis of diffusion-solidification casting as a processing principle.

These objectives and our progress in achieving them are listed below:

1. Measure the attainable rate of heating of low-carbon steel shot in a refractory mold.

This objective has been attained. Two direct methods and one indirect method have been proven feasible and their economic parameters established.

2. Establishment of the operating characteristics and reliability of the quick-acting valve for controlling liquid metal flow into the shot-filled mold.

This objective has been attained. A complete analysis of the particle valve has been made, together with fundamental experimental measurements of break-through pressures. The particle valve is in everyday use for infiltration measurements, inert gas atomization runs, and also for filtration of the melt.

3. Development of a method of controlling mold permeability to waste gases, pressurizing gas, and liquid metal.

This objective has been attained qualitatively. Investment molds have been proven feasible.

4. Measurement of the tensile properties of partially frozen diffusion-solidified castings.

The "hot tensile test" method has been proven; we have obtained finite strength of diffusion-solidified steel castings at the casting temperature within five minutes of infiltration.

5. Demonstration of avoidance of hot-metal channeling in the shot during infiltration.

This objective has been attained by proving with decanting experiments that channelling does not occur when the liquid cast iron is at its liquidus temperature (i.e. saturated with respect to solid austenitic iron).

6. Check the validity of the theoretical expression for infiltration pressure.

The infiltration process has been experimentally evaluated. Operable combinations of shot size, casting depth, and infiltration pressure can be predicted theoretically.

7. Work out the detailed techniques for making suitable non-permanent molds.

We have made our own investment molds successfully and made diffusion-solidified steel castings with them. Excellent surface finish and density have been obtained.

8. Establish the specifications and manufacture of permanent molds.

Several recent and process-simplifying revelations regarding the casting logic render this objective relatively unimportant; existing molding techniques such as the Shaw process, phosphate bonded alumina or other refractories bonded with colloidal silica could probably be easily adapted.

9. Cast selected engineering parts by the diffusion-solidification process.

There was insufficient response within the contract period from mission agencies to justify production of a specific part. This objective is therefore deferred to later projects; two agencies have made interesting suggestions: (1) Navy - gunmetal valve body castings free of interconnected shrinkage porosity*; (2) American Dental Association - Ti-Cu dental inlay, cast at substantial lower temperature.†

10. Development of the atomization technique and economic parameters.

We have demonstrated the range of utility of the Drexel inert gas atomization apparatus; the particle valve works routinely, about 30 runs have been made, 0.003% oxygen in the shot has been attained, and an adequate supply of high quality shot has been made.

11. Ductility-controlling variables

Decarburization of high-carbon commercial shot has been demonstrated with control of carbon activity in CO/CO₂ mixtures. This enables ductile castings to be obtained with \$0.20/lb. shot. The relationship between oxygen content and ductility of heat treated castings has been established. The mechanisms of formation and control of shrinkage cavitation have been identified.

* Mr. Charles A. Zanis made this suggestion

† Dr. Richard Waterstrat made this suggestion.

12. Failure Analysis

Scanning electron microscopy has been used to confirm the efficacy of solid-state vacuum-carbon deoxidation of the shot during heating to the casting temperature - such castings do not fail at the shot-melt interface.

Several supplementary experiments conducted by senior thesis students are highly pertinent to this project; the following tasks are in progress:

- Heat treatment. One student used unfunded two-dimensional diffusion-solidified welds in steel to study the heat-treat sensitivity of the last metal to freeze.
- Impact transition temperature. Another student is making massive (100 by 500 by 1 mm thick) welds from which U notch Charpy impact specimens can be made to study the impact behavior of the infiltrant, diffusion-enriched, and base metal zones in diffusion-solidified castings.
- Adiabatic solidification. A third student has precompacted loose shot to higher packing densities to increase the fraction solidified adiabatically from 75% to 100%. No difficulty in infiltration was encountered in spite of large decreases in as-compacted porosity.

We have described the current art of casting and joining by diffusion solidification. Much of the economic and process parameters (especially the attainable heating rates and cycle times) have been worked out, but a great deal of processing/structure/properties research remains to be done. We have shown that diffusion solidification is applicable to a long and growing list of ferrous and nonferrous alloys. The process requires no new or exotic materials or technologies in order to be practiced; its success in the market place will probably depend on finding specific applications with improved properties and ease of achieving those properties.

TABLE OF CONTENTS

	<u>Page</u>
1. Diffusion Solidification - An Overview	1
2. Diffusion Solidification Casting Manufacture	20
3. Performance Evaluation of the Particle Valve	160
4. Manufacture of Low Carbon Steel Shot of Controlled Purity	206
5. Kinetics of Interactive Liquid Metal Infiltration and Diffusion Solidification	229
6. Microsegregation of Ternary Alloying Elements in Steels Cast by Diffusion Solidification	374
7. Structure and Properties of Steels Cast by Diffusion Solidification	432
8. Economic Model for a Rapid Cycle Steel Casting Process Using Diffusion Solidification	467
9. Conclusions	514
10. Publications, Presentations and Personnel	519

1. DIFFUSION SOLIDIFICATION - AN OVERVIEW

G. Langford

D. Apelian

TABLE OF CONTENTS: Section 1. Diffusion Solidification - An Overview

	<u>Page</u>
1.1 Introduction.	3
1.2 The SD Process.	4
1.3 Process Advantages.	9
1.4 Metallurgy of Diffusion Solidification.	10
1.5 Specific Applications of Diffusion Solidification	13
1.6 Joining by SD	17
References.	19

1. DIFFUSION SOLIDIFICATION - AN OVERVIEW

1.1 INTRODUCTION

A better mousetrap ... ? We're always hoping to find unique and innovative processes which will have operating advantages over existing processes or will create novel metallurgical microstructures, not to mention a whole new industry. Diffusion Solidification (SD) may be such a process.

There are strong incentives to reduce costs and increase productivity by mechanizing existing and new molding and casting processes. Die casting of steel, for example, has been of great interest for decades; however, it has not become an economic reality because of high casting temperatures and thermal shock to the die. The new process, SD, offers lower casting temperatures, less shrinkage, and faster solidification rates than conventional casting processes, and will permit the rapid cycle casting of steel.

Conventional thermal solidification casting entails many labor-intensive steps. Castings made with minimum labor often have a poor surface finish; casting defects such as macrosegregation, hot tears, and blowholes are also difficult to control. Rheocasting⁽¹⁾, on the other hand, is a recent development which involves casting of semi-solid alloys that have been vigorously stirred. The resulting slurry of solid spheroids suspended in a liquid flows with moderate viscosity. Advantages of the rheocasting process are:

- Reduced attack of die or mold because of the reduced temperature (by 100°C for steel) and higher viscosity of the slurry.
- Reduced porosity and smaller riser made possible by reduced fraction liquid and improved interdendritic fluid flow.

1.2 THE SD PROCESS

Many metals, including steel, can be cast at still lower temperatures than rheocasting by diffusion solidification⁽²⁾. Liquid iron having a high carbon content is brought into contact with a low carbon solid iron isothermally, and the liquid solidifies by rejecting carbon to the surrounding solid iron. The mold is first filled with uniform-sized low carbon steel shot, then heated and subsequently infiltrated with liquid cast iron (2 to 4% C) under moderate pressure; Figure 1⁽²⁾ explains the mechanism of SD.

Historically, diffusion solidification has been used where high temperatures were either undesirable or unattainable. The ancient cement steels were made by hammering together wrought iron strips and carbonaceous material near the eutectic temperature because existing heating technology could not melt low carbon steels (but see ref. (3)). Dental amalgams were invented for repair of dental cavities because a hard, wear resistant, and easily formable filler material was needed, no mineral cement or polymer was suitable, and no metal alloys were available which could be poured into a live tooth.

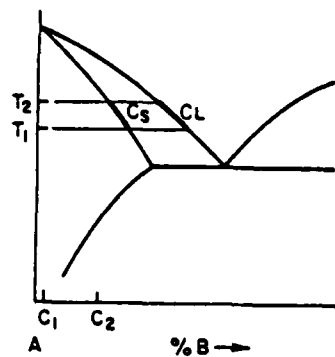
Consider the liquid and solid region of the phase diagram shown in Figure 2, which compares conventional casting, Rheocasting and SD casting. In the Rheocasting process solidification occurs by manipulation of temperature on an isocomposition line, whereas the diffusion solidification process is carried out isothermally by manipulation of composition, i.e., by solute rejection from the liquid phase. Both processes exploit the phase diagram rather than suffer its consequences. In steels then, carbon diffuses into the preheated spherical low carbon steel particles out of the high carbon liquid under essentially isothermal conditions. The

b) MECHANISM: SOLID AND LIQUID MIXED INSTANTANEOUSLY IN A REFRactory VESSEL



START AT TEMPERATURE T_1 ,
NO DIFFUSION HAS TAKEN PLACE

a) PHASE DIAGRAM



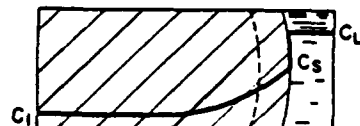
C_1 = COMPOSITION OF PREEXISTING SOLID

C_2 = AVERAGE COMPOSITION OF THE
MIXTURE OF SOLID AND LIQUID

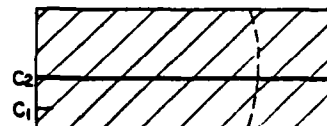
C_s = SOLUTE CONCENTRATION AT
SOLID/LIQUID INTERFACE

C_L = COMPOSITION OF LIQUID

$T_2 - T_1$ = TEMPERATURE RISE DUE TO THE
HEAT OF SOLIDIFICATION



PARTIALLY SOLIDIFIED; HEAT IS
EVOLVED AT THE SOLID/LIQUID
INTERFACE AS B DIFFUSES INTO
THE SOLID; C_L DECREASES



COMPLETELY SOLIDIFIED; ENTIRE PRODUCT
HAS BEEN HEATED TO T_2 . IF HELD
SUFFICIENTLY LONG, HEAT WILL BE
DISSIPATED AND THE PRODUCT WILL
RETURN TO TEMPERATURE T_1 ; SOLID IS
HOMOGENEOUS WITH RESPECT TO B

Figure 1. General mechanism of diffusion solidification.²

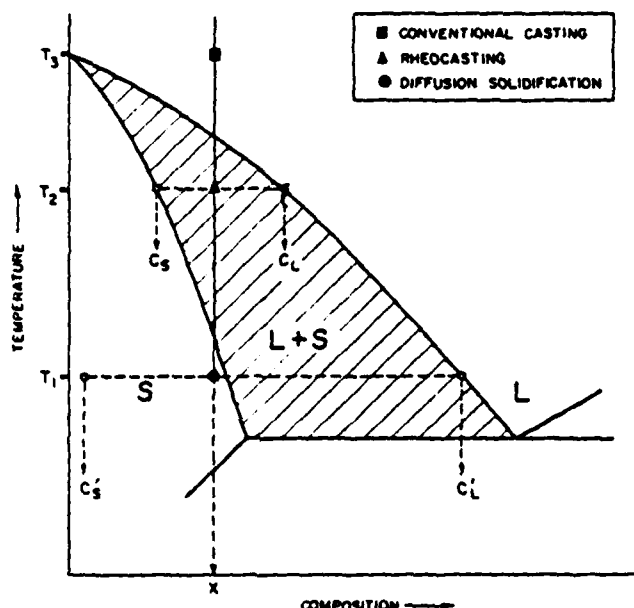


Figure 2. Phase diagram illustrating three processes for casting alloy X.

- Conventional casting at temperature T_3 .
- ▲ Rheocasting: alloy X is cooled to T_2 , and isothermally agitated. The solid-liquid nondendritic mixture consists of liquid phase of composition C_L of an amount f_L , and solid phase of composition C_S of an amount f_S , such that $f_S C_S + f_L C_L = X$.
- Diffusion solidification: f_S amount of solid particles of composition C'_S , and at temperature T_1 , are infiltrated by f_L amount of liquid of composition C'_L , such that $f'_S C'_S + f'_L C'_L = X$.

average carbon content of the mixture is within the all-austenite portion of the iron carbon phase diagram so complete solidification can take place. The process has practical utility because the large solubility of carbon in face-centered cubic austenite permits the solid particles to absorb the excess carbon from a large amount of liquid.

The general process steps for diffusion solidification of steel are:

- The liquid is initially held at its liquidus temperature - the process temperature.
- The solid particles are heated and held also at this process temperature.
- The liquid is rapidly infiltrated into the solid particles, filling the mold before significant SD takes place to block further infiltration.
- Since the liquidus temperature rises with decreasing carbon content of the liquid, diffusional loss of the carbon to the solid low carbon austenitic shot forces the liquid to freeze as a smooth layer on the surface of the shot.

In practice a refractory mold is filled with low-solute shot, a barrier of coarse refractory particles is placed on the top, and then the melt charge is added as shown in Figure 3. The particle valve^(2,4) between shot and melt prevents premature infiltration between the two until sufficient pressure is exerted above the melt to break the liquid's surface tension; the particle valve and shot are then infiltrated and SD proceeds. The necessary sequence of operations for the entire process (using a wax pattern/investment mold logic) is:

- make the core.
- place the core in an injection molding machine and form the wax pattern around it.
- invest the pattern and core with a refractory slurry to make the mold.
- dewax and bond the mold.

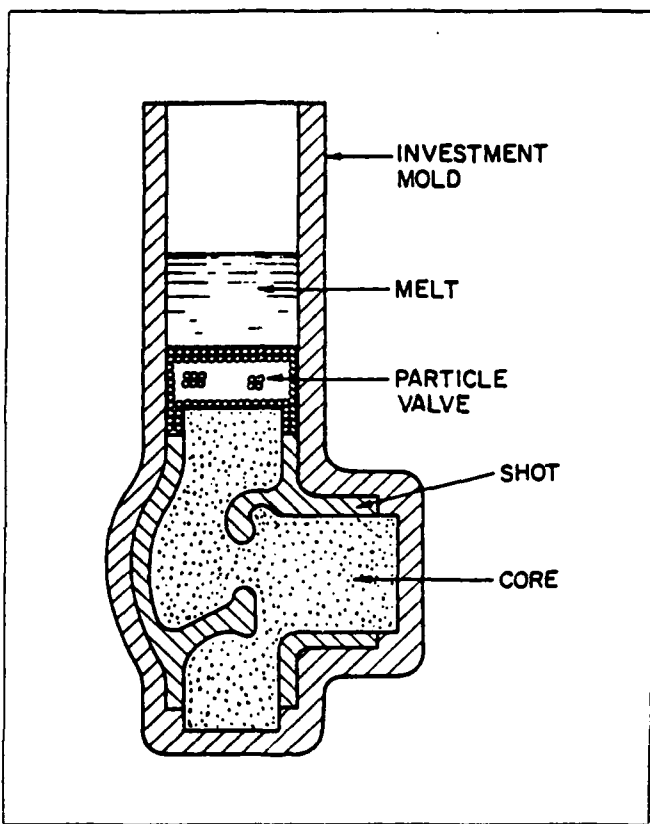


Figure 3. Sectional drawing of assembled mold for SD casting.

- emplace the shot, particle valve, and melt charge.
- heat to casting temperature in vacuum*.
- pressurize the casting vessel to infiltrate the casting.
- homogenize.
- cool to room temperature and remove mold, core and particle valve

1.3 PROCESS ADVANTAGES

In conventional casting solidification occurs via heat transport over a temperature range and the final structure is dendritic; in SD castings solidification occurs via mass transport, the process is isothermal and the liquid-solid front is planar.

Other advantages of the SD process are that casting takes place at a lower temperature - reduced by 150-200°C - and that the process can be carried out isothermally to cause 100% solidification and to obtain complete homogenization of the resulting casting, all without rejecting any heat to the mold.

Solidification time in conventional casting processes is dependent on casting dimensions and mold characteristics. In SD castings, the solidification time is essentially independent of casting dimensions and is controlled by the infiltrable shot size. Furthermore, the mold characteristics do not control the solidification time in SD castings. In brief, solidification time and mold filling time in the SD process are shorter when compared to conventional castings.

- In conventional casting, t_s , time for solidification, is proportional to ℓ^2 , where ℓ is the dimensional term, length (Chorinov's Rule (4)).

*This step is the key to obtaining a true rapid-cycle process.

- In SD casting, on the other hand, t_{sd} , time for solidification, is proportional to $\frac{l^{6/5}}{(P^{2/5})}$; where P is the infiltration pressure available.⁽²⁾

The weaker dependence of solidification time on workpiece dimension can be advantageous when considering the SD process for automation. Cycle times comparable to die casting ought to be achievable with the SD process. There is much less of a problem of thermal shock to the "die" (mold), and the microstructure of the resultant casting is homogeneous with respect to carbon because of its rapid diffusion over these short distances.

In SD, the preheated solid particles occupy approximately 5/8 of the final volume of the casting prior to infiltration of the liquid phase; therefore, solidification shrinkage and heat of solidification to be accommodated are at least proportionately reduced. Although in conventional castings a riser is needed and the solidification shrinkage is concentrated in the last liquid to freeze, no riser is needed in diffusively solidified castings and the solidification shrinkage is isolated, uniformly distributed and smaller in amount. If the workpiece will subsequently be worked or hot isostatically pressed⁽⁶⁾, or if it must be free of connected porosity, this better control of the shape and distribution of casting porosity is an advantage.

1.4 METALLURGY OF DIFFUSION SOLIDIFICATION

Diffusion solidification as a casting technique produces unique properties and microstructures without resort to extreme pressures, and it may therefore compete favorably with hot isostatic pressing as a way of consolidating atomized metal powder (shot). The atomized shot has the benefits of rapid solidification (because of the small size of individual

particles) and of the controlled melting and solidification environments, and the infiltrating liquid has the benefits of vacuum melting and of filtration by the particle valve. The distribution and magnitude of shrinkage cavitation are controlled by the particle size distribution of the shot and by the content of inclusions (such as aluminum oxide or silicates in steel). Steel castings have been made by SD with more than 99% of theoretical density, for example⁽²⁾.

Since solidification proceeds simultaneously throughout the casting during SD, hot tearing and macrosegregation of impurities and alloying elements are decreased. The microstructure of diffusion-solidified steels is more like that of wrought steel than of cast steels - there is no columnar zone. The grain size and grain orientation of the diffusionally solidified casting is instead controlled by the grains in the initially solid portion of the charge.

It is possible to produce completely homogeneous microstructures free of microsegregation by SD since the particle size is chosen to minimize the freezing time by minimizing the diffusion distance consistent with successful forced infiltration under a reasonable external pressure. Most alloy systems to which SD can be applied are nearly completely homogenized soon after the completion of freezing. Figure 4 shows a typical design monogram which combines the theoretical kinetics of forced liquid infiltration and SD. It has recently been discovered that it may even be possible to achieve relatively good homogenization with respect to third alloying elements (i.e. those not taking part in the basic SD mechanism, such as silicon and manganese in a plain Fe-C-Mn-Si steel).^{*} Manganese,

*Detailed discussion in Chapter 6.

for example, can have positive microsegregation (more Mn in the last metal to freeze), and negative or even neutral microsegregation depending on whether the shot has low, high, or the same manganese concentration as the liquid. Apparently, the sharp carbon differential at the solid-liquid interface⁽²⁾ and elastic interaction due to the difference in size of Fe and X atoms act to defeat the mechanism usually leading to microsegregation (slow diffusion in the solid, rapid mixing in the liquid). This is not necessarily a general phenomenon in SD, it is only a possibility. Presumably, the liquid-state and solid-state concentrations of the third alloying elements can be made to be nearly identical at the solid-liquid interface, thus defeating the usual ternary distribution coefficient given by the ratio of the solid and liquid solubilities of that element in the alloy system. Bear in mind that SD occurs isothermally and is a transient phenomenon between initially out-of-equilibrium components: the original solid and the infiltrant liquid.

There are other advantages for SD castings. Pieces with small surface to volume ratios or those with drastic changes in cross-section can easily be produced because the casting solidifies without rejecting heat to the surroundings. Also, the casting will be free of laps and cold shuts because the mold is heated prior to infiltration.

Excellent ductility of SD steel castings can be obtained if they are adequately infiltrated and if metallurgical bonding is achieved at the original solid-liquid interface. Surface and subsurface scales such as silicates are especially harmful and lead to dotted-line fractures along the particles outlining the original shot surface. All that is necessary

to correct this fault is to leave sufficient carbon in the original shot to reduce the silicates during heating to the process temperature⁽²⁾. It is even possible to reduce the shrinkage cavitation below the theoretical amount if the total number of remaining inclusions is substantially less than the number of inter-shot interstices⁽²⁾.

1.5 SPECIFIC APPLICATIONS OF DIFFUSION SOLIDIFICATION

We do not attempt to list all possible SD alloy systems; instead we will discuss only those systems to which the SD technique has actually been applied. We hope the reader will invent some applications of his own.

The iron-carbon system is the ideal one for SD because of the large interstitial solubility of carbon in face-centered cubic austenite. Therefore, the particle size of the low carbon shot and the low process temperature relative to the melting point of the shot combine to eliminate any chance of sintering shrinkage by bulk diffusion of the iron from the shot-shot grain boundaries to the free surfaces of the shot. Diffusion solidification casting and welding have been applied to plain carbon steels from 0.1 to over 1% C⁽²⁾, see Figure 5a, and current research at Drexel University continues to emphasize this system. Incidentally, steels below 0.1% are best made by partial thermal SD rather than by carbon SD; this is done simply by heating the shot to a slightly lower (say, 25 to 100°C) temperature than liquis of the same composition⁽²⁾. Langford and Cunningham have reported mechanical properties up to 185 ksi (1300 MPa) tensile strength coupled with 15% reduction of area in a W1-type tool steel made by SD⁽²⁾. Carbon SD casting offers a way of making homogeneous ultrahigh carbon tool steels up to the maximum solubility of carbon in austenite

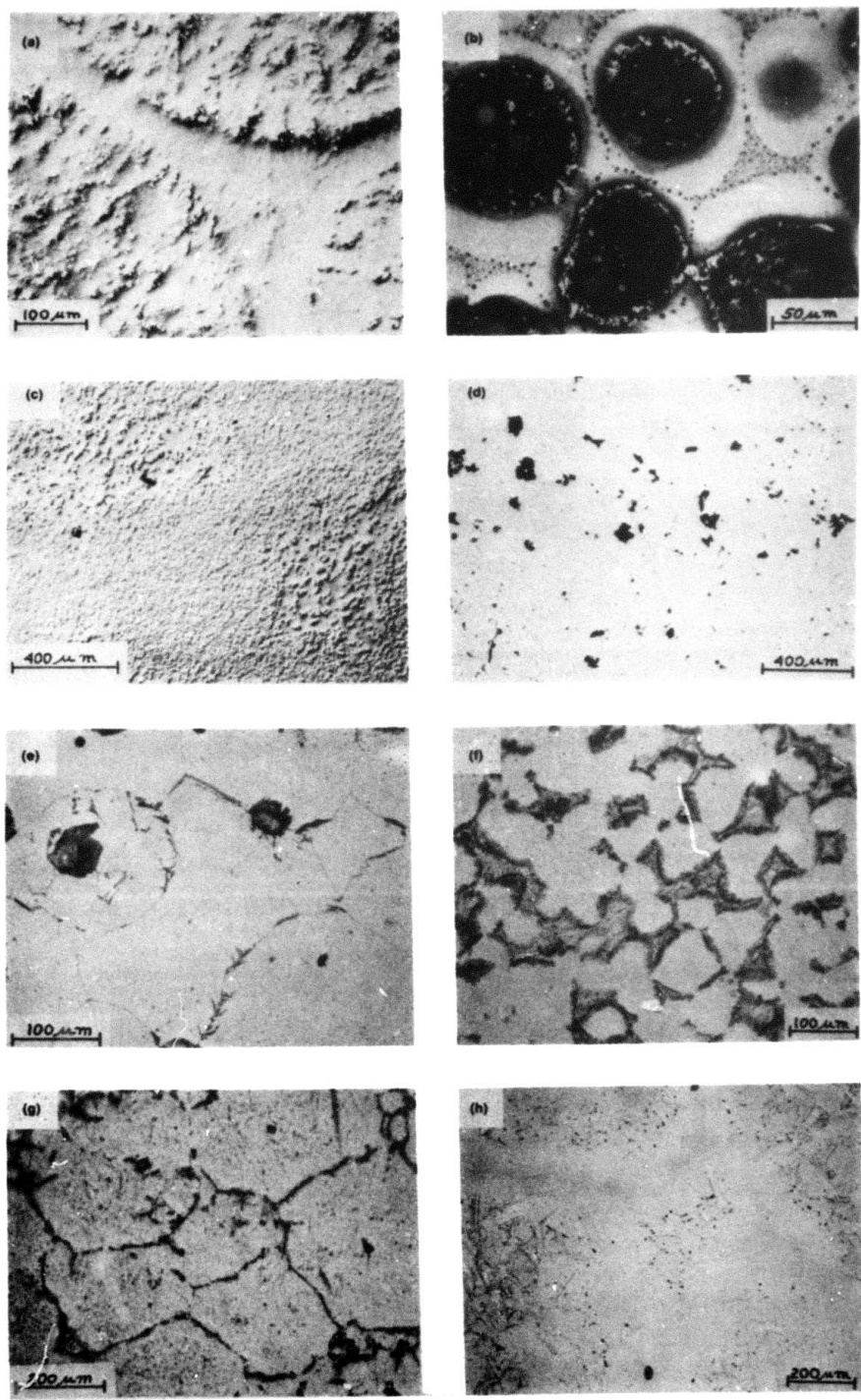


Figure 5. Microstructures of SD castings. (a) Fe-1% C (Nomarski interference contrast, unetched); (b) Stainless steel made from Fe-0.2% C shot and Fe-8% Ni-18% Cr-3% C melt (Fry's reagent); (c) High-speed steel made from type M2 wire and Fe-2.3% Si-4% Cr-2% V-3.5% C melt (Nomarski interference contrast, unetched); (d) Malleabilized steel made from Fe-1% Si-0.2% C shot and Fe-0.2% Si-4.0% C melt (unetched); (e) Fe-3% Si (1% nital); (f) Fe-4% P (1% nital); (g) Al-5% Li (0.5% HF); (h) Cu-10% Sn made from coarse Cu shot and Cu-25% Sn melt (H_2O/NH_4OH).

(2.2%), which is quite difficult to do conventionally without obtaining a graphitic or white cast iron microstructure.

The current fundamental research of Fe-C-X SD welds indicates that hardenable steels with up to several per cent of various alloying elements can be made by SD without harmful microsegregation; as a result, many new alloy steels may become necessary/possible.

Stainless steels have been made at Drexel University by SD casting; the solidification can be made to occur either by carbon diffusion (martensitic types) or by chromium or nickel (or both) diffusion; we are not yet sure which will give the best results. Figure 5b shows the microstructure of one such stainless steel casting.

High speed steel cutting tools have been made by SD or simply by liquid infiltration⁽⁷⁾; Figure 5c shows a typical microstructure. No attempt is made to obtain a homogeneous microstructure. Instead, the shot and infiltrant are treated as metallurgically separate entities; for example, silicon was used in Ref.⁽⁷⁾ to counteract the tendency of heavy alloying elements (e.g. molybdenum) to concentrate in the last metal to freeze.

Malleable castings with 1.5 to 2% C have been made at Drexel University by SD infiltrating Fe-0.1% C-ca.2% Si shot with Fe-3.5% C-2% Si liquid to make a homogeneous austenite, and then graphitizing the casting; see Figure 5d. The high silicon speeds graphitization, and there are no graphite flakes in the original SD casting to cause internal stress risers. The process temperatures (both for casting and for heat treating) are similar to those used for conventional malleable iron. The SD process offers a way of making larger nodular graphite castings than can be done

conventionally by casting white iron, and the uniform and stable composition of the shot and liquid make SD casting a more reliable method than inoculation to obtain nodular graphite.

The magnetically useful iron-silicon and iron-phosphorus systems are also tractable for SD casting. Figure 5e shows an Fe-6% Si casting made by SD, and Figure 5f shows an Fe-3% P casting made (partially) by SD. The iron-phosphorus system has too low a distribution ratio of solute between solid and liquid to permit complete homogenization with respect to phosphorus, so some high-phosphorus liquid will always remain at the casting temperature unless the percentage solid is raised by compaction of the shot before infiltration. These castings demonstrate the microstructure and morphology of SD much better than the iron-carbon system because there are no phase transformations upon cooling to room temperature.

Among nonferrous systems, we have obtained the aluminum-lithium microstructure by SD shown in Figure 5g. Here, lithium raises both the specific volume and the modulus of elasticity of aluminum. It is difficult with conventional casting technology to retain lithium in the liquid and to obtain adequate fluidity. In SD casting, we have shown that a uniform lithium distribution is possible and we are developing an infiltration technique to overcome the high reactivity of lithium in liquid aluminum.

The copper-tin system is promising (Figure 5h) the advantage to be gained here by SD casting is to obtain a uniform distribution of shrinkage porosity as compared to conventional casting in shapes for which directional solidification is difficult to obtain.

Many more systems are probably compatible with SD casting; one should

look for the following metallurgical features:

- a distribution ratio (C_S/C_L) above 0.4 and preferably close to 1, so that solidification can occur isothermally or even adiabatically.
- a steep solidus line, so the shot does not have to be heated too closely to its melting point.
- rapid diffusion of the SD alloying element in the solid compared to the self-diffusion of the principal element, so the shot will not sinter excessively.

1.6 JOINING BY SD

Transient liquid phase bonding was recently invented^(8,9) to utilize brazing technology in situations where it was advantageous for the joining material to "go away" once its objective of effecting a sound joint was achieved. A sheet of metal which forms a low-melting eutectic with the base metal is placed between the pieces to be joined; upon heating above the eutectic temperature but below the melting point of either base metal or filler, a layer of eutectic liquid is formed by diffusion between base and filler. This involves a substantial amount of melting of the base metal, which serves to widen the original gap between the pieces. Side-ways fluid flow then permits the (perhaps) ill-fitting pieces to nestle closer together. Subsequent solidification occurs when diffusion of the filler metal into the substance causes the eutectic liquid to disappear. Careful choice of the elemental composition of the filler metal can permit the resultant bond and the diffusion zone to have the same properties and microstructure as the base metal.

This technique avoids overheating the pieces to be joined compared to conventional thermal welding and need not leave a residue with inferior properties (because of the relatively low melting points of conventional

brazing metal or hard solder).

In transient liquid phase bonding, no method exists to ensure controlled directional feeding of liquid as solidification of the joint proceeds and so shrinkage cavitation can occur. An alternative technique called SD welding⁽²⁾ avoids this difficulty and speeds up the solidification/homogenization process by minimizing the amount of liquid filler metal to be frozen. A tapered gap between the preheated workpieces is filled rapidly by forced infiltration with solid-saturated liquid which causes no remelting of the substrate at all. The width of the gap and the angle of taper are chosen so that the available infiltration pressure is just able to fill the gap before freezing shuts the entrance portal and so that feeding of liquid can prevent shrinkage porosity. These conditions are essential not just to permit prompt isothermal freezing but also to allow the weld to homogenize in a reasonable time. In the Fe-C system, for example, a 1mm gap freezes in about ten minutes at 1350°C but takes 100 times as long before the local C "bulge" becomes comparable to the statistical variation in C content of the steel substrate. Steels can be welded by carbon diffusion at temperatures as low as the eutectic, but higher temperatures are usually necessary to allow the carbon potential of the substrate to reduce any undesirable oxides at the original solid/liquid interface.

References

1. R. D. French and F. S. Hodi, eds.: Rheocasting: Proceedings of the Work Shop on Rheocasting held at Army Materials and Mechanics Research Center, February 3-4, 1977. MCIC-78-35, Metals and Ceramics Information Center, Columbus, Ohio. p. 145.
2. G. Langford and R. E. Cunningham: Steel Casting by Diffusion Solidification, Met. Trans. vol. 9B, 1978, pp. 5-19.
3. D. H. Avery and P. Schmidt: A Metallurgical Study of the Iron Bloomery, Particularly as Practiced in Buhaya, J. Metals, vol. 31 (No. 10), 1979, pp. 14-20.
4. M. Paliwal, D. Apelian and G. Langford: Performance of a Porous Refractory Valve for Liquid Metals, Met. Trans., vol 11B, 1980, pp. 39-50.
5. N. Chorinov: Theory of Solidification of Castings, Giesserei, vol. 27, 1940, pp. 177-186, 201-208 and 222-225.
6. H. D. Hanes, D. A. Seifert and C. R. Watts eds.: Hot Isostatic Processing, MCIC-77-34, Metals and Ceramics Information Center, Columbus, Ohio, November, 1977, p.99.
7. G. Langford: High Speed Steel Made by Liquid Infiltration, Mat. Sci. and Eng., vol. 28, 1977, pp. 275-284.
8. D. S. Duvall, W. A. Owczarski and D. F. Paulonis: TLP Bonding - a New Method for Joining Heat Resistant Alloys. Welding Journal, vol. 53 (No. 4), 1974, pp. 203-214.
9. G. S. Hoppin, III and T.F. Berry: Activated Diffusion Bonding, Welding Journal, vol. 49 (No.11), 1970, research supplement pp. 505-S-509-S.

2. DIFFUSION SOLIDIFICATION CASTING MANUFACTURE

H. Sreshta

G. Langford

D. Apelian

SUMMARY

Various heating methods for manufacturing SD castings are described: electrical heating (direct and indirect), direct gas heating and radiative heating. The advantages and limitations of the heating methods are discussed. The economic SD variables (heating time and efficiency) are estimated for direct electrical induction heating and radiative heating of shot. One kg of unbonded shot can be heated to SD process temperatures (1400°C) in 100 to 200 seconds at heating efficiencies of 10 to 15 percent by direct induction heating. The electrical resistivity of unbonded steel spheroids is an important parameter which influences the economic variables for direct induction heating. The electrical resistivity is extremely high up to 200°C , causing the "incubation period" previously observed but above 200°C the resistivity is controlled by the surface oxides on the particles permitting electrical conduction in the bed at temperatures of about 400°C . The incubation period can be circumvented by preheating the powders. One kg of unbonded shot can be heated to process temperatures in 2000 seconds at heating efficiencies of 5 percent by the radiative heating method. The heating time is controlled by the heat transport rate in the bed which again appears to be controlled by electronic conductivity. Theoretical estimates of the SD economic variables are made for gas heating of shot. A process efficiency of 50 percent is expected and one kg of shot can be heated to process temperatures in 100 seconds using a 1 kW compressor to pump the gas. The heating rates and efficiencies could be greatly increased if the shot could be electrically bonded (by a pre-sintering or mechanical treatment, for example) before the start of the casting cycle. Direct induction heating and radiative heating methods are applicable to SD casting manufacture using a batch process. A semi-continuous process is required for manufacturing SD castings using the direct gas heating method.

TABLE OF CONTENTS: Section 2. Diffusion Solidification Casting Manufacture

	<u>Page</u>
2.1 Introduction.	24
2.2 SD Heating Economics.	25
2.3 Direct Induction Heating for SD Casting Manufacture . . .	26
i. Frequency of Induction Heating.	28
ii. Resistivity of Packed Beds.	31
iii. Incubation Period	33
iv. Effect of Magnetic Transformation	34
v. Induction Coils	35
vi. Mold Geometry	36
vii. Power Input to Packed Bed	36
viii. Simultaneous Heating of Melt Charge and Shot. . . .	36
2.3.1 Problems of Direct Induction Heating for Manufacturing SD Castings	37
i. Cracking of Packed Bed During Heating	37
ii. Preferential Coupling	38
iii. Heating of the Particle Valve	38
iv. Mold Limitations.	39
2.3.2 Advantages and Disadvantages of Induction Heating	39
2.4 Gas Heating	40
2.4.1 Economics of Gas Heating.	41
2.4.2 Advantages and Disadvantages of Gas Heating	45
2.5 Radiative Heating	45
2.5.1 Molds for Radiative Heating	50
2.5.2 Advantages and Disadvantages of Radiative Heating	51

	<u>Page</u>
2.6 Casting Machines.	51
i. Casting Machine via Induction Heating	52
ii. Casting Machine via Gas Heating	52
iii. Casting Machine via Radiative Heating	55
2.7 Conclusions	58
References.	60
Appendices.	61
Appendix 2A: Induction Heating Experimental Results.	62
Appendix 2B: Room Temperature Resistivity of Powders	92
Appendix 2C: Electrical Resistivity of Shot as a Function of Temperature	101
Appendix 2D: Cracking Phenomena in Induction-Heated Packed Bed .	116
Appendix 2E: Direct Heating of Shot by Gas	121
Appendix 2F: Radiative Heating Experimental Results.	137
Appendix 2G: Thermal Diffusivity of Shot	142
Appendix 2H: Investment Molds for Manufacturing SD Castings. . .	148

2. DIFFUSION SOLIDIFICATION CASTING MANUFACTURE

2.1 Introduction

Casting manufacture in the SD process can be accomplished in several ways, and involves the following basic steps: (1) heating the SD components to process temperature, (2) melt transfer at process temperature, (3) solidification of melt and (4) casting homogenization. The last three steps are common to SD casting methods and are essentially controlled by kinetic equations. The first step is important for two reasons: (1) it dictates the casting machine design, and (2) the process economics are strongly influenced by the heating time and efficiency. The magnitude of the heating time is important as it dictates the feasibility of using the SD process for rapid cycle casting of steels. If the heating time is less than the conventional casting solidification time, then the SD process has economic gains over the conventional process in terms of production rate. On the other hand, if the heating and conventional solidification times are comparable, then the SD process can be competitive with the conventional process only if it gives superior casting quality. Hence rapid cycle steel casting via the SD process becomes a reality only when the cycle time for casting manufacture is not controlled by the heating time or the heating time is comparable to the SD solidification and homogenization time. The SD solidification and homogenization times are

proportional to the square of the shot size and are very much less than the conventional solidification time which is proportional to the square of the casting's volume to surface ratio. The weaker dependence of solidification time on casting size in the SD process can be advantageous only if the heating time is not excessive. The time criterion for rapid cycle steel casting is based on the magnitude of the heating time.

The heating routes considered are grouped into two main categories : direct and indirect. Direct heating methods dissipate energy throughout the mass of the casting components and include: induction heating of metallic components and heating of shot by hot gas. The indirect methods refer to heat transfer from an external source to the outside surface of individual (or grouped) casting components followed by conductive and radiative heat transfer within the bulk.

SD casting manufacture in permanent molds has been successfully demonstrated using permanent molds.⁽¹⁾ The objective of this research work was to evaluate the economics of heating the SD components to process temperatures and to design feasible casting machines for the heating routes.

2.2 . SD Heating Economics

SD casting manufacture must satisfy the following

economic objectives:

- Minimization of heating time
- Uniform heating of the SD components
- Maximization of heating efficiency

The heating time can be considered as an economic variable in terms of production rate, the production rate increasing with decreasing heating time. Uniform heating of the SD components is essential as the SD process requires that the shot and melt be brought into contact under isothermal conditions. The melt must be saturated with solvent and shot at the melt temperature. Casting quality is the economic variable associated with uniform heating of the two major SD components: shot and melt. It has been shown in chapter 5 that deviations from ideal thermal conditions may be beneficial or adverse to the casting quality. Since a criterion has not yet been established to evaluate casting quality for different possible thermal conditions of melt and shot, it is assumed that ideal thermal conditions are essential for high quality SD castings. Heating efficiency gives an estimate of the power requirements for the SD process and it is desirable to operate the SD process at a high heating efficiency to minimize energy costs.

2.3 Direct Induction Heating for SD Casting Manufacture

Induction Heating (IH) is one of the two methods of using direct dissipation of electrical energy to heat the work material. It provides a means of precise heating of

electrically conductive objects. IH is locally clean, fast, repeatable and lends itself to automatic cycling. Some of the general advantages of IH are: (1) no contact is required between the work load and heat source, (2) very high temperatures can be attained, (3) rapid heating of the work-piece is easily achieved, (4) higher efficiency than that offered by many furnace methods can be realized, (5) heating depth can be controlled by changing the frequency of the alternating field, (6) working conditions are cooler and cleaner, and (7) vacuum or controlled atmosphere may be used to protect the workpiece.

The use of direct IH for manufacturing SD castings depends on the impedance of the individual components. Cast iron (melt charge) in the form of lumps can be easily melted by IH and much literature is available outlining procedures for induction melting of alloys. The particle valve (PV), which necessarily consists of refractory particles, will remain inert to the induction flux because of its high resistivity, ($\rho > 10^{12} \Omega \cdot m$). This implies that PV must be heated by the cast iron and shot during IH. The IH of loosely packed shot in a bed is a new area which has not yet been reported in literature. However, the results of IH of unsintered low alloy steel compacts⁽²⁾ does offer a guideline to predict the IH characteristics of powders. The key to making SD castings by IH revolves within the

task of inducing substantial electrical currents in a packed bed of low carbon steel powders.

The economic objectives for IH are interrelated, and so it may not be possible to satisfy all three criteria simultaneously. The economic variables for IH of shot are influenced by the process parameters listed below:

- . frequency of IH
- . resistivity of packed bed (shot)
- . incubation period
- . effect of magnetic transformation
- . induction coil design
- . mold geometry
- . power input

The above parameters will be discussed with emphasis on the economic variables. The experimental procedure and results are given in Appendix 2A.

i. Frequency of IH

The frequency of IH is an important heating parameter as it controls the reference depth (the dimensions of the zone where power is dissipated in the charge). The depth of penetration, δ , is defined as the depth at which the induced current has reached 37 percent of its value at the surface of the charge. It is governed by the relationship⁽²⁾:

$$\delta = 0.018 \left(\frac{\rho}{\mu f} \right)^{1/2} \quad (1)$$

where:

δ - depth of penetration, m

ρ - resistivity of charge, $\Omega \cdot \text{m}$

μ - magnetic permeability, $\text{T} \cdot \text{m} \cdot \text{A}^{-1}$

f - frequency, kHz

The reference depth is inversely proportional to the square root of frequency. At low frequencies, the depth of penetration is large, whereas at high frequencies, the depth of penetration is small, i.e., skin heating is observed.

For high efficiency heating, δ must be less than equal to a quarter of the packed bed diameter, d_{PB} (2)

$$\delta \leq d_{PB}/4 \quad (2)$$

Substituting for δ from Eq. (2) in Eq. (1) gives the criterion for efficient IH:

$$d_{PB} \geq 0.072 \left(\frac{\rho}{\mu f} \right)^{1/2} \quad (3)$$

The energy input to the charge under efficient power transfer conditions is localized in a volume annulus bounded by $r = (d_{PB} - 2\delta)/2$ and $r = d_{PB}/2$; where r is the radius of the charge. The interior of the charge in this case is heated by conduction and radiation from the hot zone (volume annulus where input energy is dissipated). This means that uniform heating under efficient power transfer conditions is possible only if the power input to the hot zone is equal to the energy transferred to the interior of the charge. The power input to the charge is essentially controlled by the power rating of the IH equipment. Experimental results indicate that radial heat transport in the packed bed is a slow process and so will control the heating time as in an indirect heating method. Hence it is only possible to attain uniform temperature distribution in the packed bed with minimal heating time if δ is large enough to permit the entire packed bed to be heated simultaneously at the expense of the heating efficiency. This is in agreement with our experimental results*. S100 ($d_p = 0.216\text{mm}$) shot could be heated uniformly at low frequencies from room temperature to process temperatures of 1400°C in about 300 seconds at efficiencies of 10 to 15 percent.

*The results of the induction heating runs are given in Appendix 2A.

ii. Resistivity Of Packed Beds

The depth of penetration is proportional to the square root of the resistivity of the packed bed. No data was available in the literature giving the resistivity of a packed bed of low carbon steel shot. Room temperature resistivity was measured for the different powders used for IH runs. The experimental procedure and results are given in Appendix 2B.

The room temperature resistivity of steel shot as determined in Appendix 2B follows the relationship given by:

$$\rho = \rho_0 h_{PB}^n \quad (4)$$

where ρ_0 and n are constants, and h_{PB} is the height of packed bed. The resistivity is not a constant but a function of the bed height probably because the number of high (series) resistance contacts increase with bed height. The resistivity is strongly influenced by the surface morphology of the powders. Conta⁽²⁾ attributed the high resistivity of particles in a bed to adsorbed gases on the particle surface at room temperature. This postulation agrees with our experimental results. The adsorption phenomenon is controlled by the surface area of the particles. S200 powder had a lot of surface perturbations whereas S211 powder had a

relatively smooth surface. The large difference in the resistivity of particles with the same size but with different surface morphologies confirms that the resistivity is controlled by the gases adsorbed on the particles at room temperature.

The resistivity as a function of temperature was measured for different size shot. The experimental procedure and results are given in Appendix 2C.

The resistivity of S100 powder in an argon atmosphere dropped from $7 \Omega \cdot m$ at $37^\circ C$ to $0.0015 \Omega \cdot m$ at $400^\circ C$. The resistivity was approximately constant with a value of $0.00145 \Omega \cdot m$ in the temperature range of $400^\circ C$ to $950^\circ C$. The strong temperature dependence of resistivity upto $400^\circ C$ prevents efficient heating of the powder using a single induction frequency. Once the packed bed resistivity approaches a constant value, the particles can be efficiently heated.

Most of the IH runs were done at 4.2 kHz. At this frequency and with a resistivity of the packed bed equal to $0.00145 \Omega \cdot m$ the depth of penetration was 50 mm below the Curie temperature and 250 mm above the Curie temperature. The large depth of penetration accounted for the uniform heating in the radial direction. However, the efficiency was low ($\eta < 15$ percent).

The resistivity of shot in vacuum is two orders of magnitude lower than the resistivity of shot measured in argon. The large difference may be due to oxidation of the shot during heating in an argon atmosphere or to an adsorbed layer of argon gas on the shot surface which will control the shot resistivity.

Since no induction heating runs were done in vacuum, it is difficult to estimate the heating times and efficiencies of IH of shot in vacuum. However, the magnitude of the saturation value of the resistivity does indicate that higher heating efficiencies and lower heating times may be realized for induction heating of shot in vacuum.

iii. Incubation Period

An incubation period is observed during IH of unbonded shot. The cause is attributed to the high resistivity of the packed bed⁽²⁾, resulting in poor load coupling to the induction flux. The heating during this period is slow and inefficient.

The incubation period is a function of the power input to the charge and the particle size. The power input controls the duration of the incubation period. At lower power inputs it was difficult to study the incubation phenomenon; the rapid change in the resistivity with temperature required adjustments

of the capacitance in the resonant circuit, and so it was difficult to maintain a steady input to the charge.

The incubation period had an inverse relationship to shot size. The S212 ($d_p = 1.85$ mm) shot showed no signs of an incubation period, the reason being that the incubation heating efficiency and the heating efficiency of this powder were comparable and very low (6 percent). The S100 powder showed a characteristic incubation period.

The incubation period is characterized by a low heating efficiency (6 to 7 percent). During this period, the particles are heated by magnetic hysteresis losses. An incubation period of 1200 to 1800 seconds will control the heating time. The incubation period can be circumvented by preheating the particles to an adequate coupling temperature that ensures load coupling to the induction flux. The coupling temperature for S100 powder was found to be in range of 375°C to 425°C .

iv. Effect Of Magnetic Transformation

The Curie temperature for low carbon steel shot is 771°C . Below this temperature the powders are magnetic and above it the powders are non-magnetic. At the Curie temperature there is a sudden change in the magnetic permeability as given by:

below 771°C , $\mu = 3.1 \times 10^{-5}$ Tesla/(Ampere/Meter) (5)

above 771°C , $\mu = 1.25 \times 10^{-5}$ Tesla/(Ampere/Meter) (6)

The depth of penetration is inversely proportional to the square root of the magnetic permeability. The sudden decrease in the permeability at the Curie temperature will result in an increase of the depth of penetration. Such an increase may violate the inequality given by Eq. (3). leading to poor load coupling. With audio frequency heating, this has not been much of a problem. The charge impedance changes at the magnetic transformation but this can be offset by adding sufficient capacitance to the heating coil circuit.

v. Induction Coils

The induction coils influence the longitudinal temperature distribution in the packed bed. Experimental results indicate that at least three turns should be placed above and below the charge to heat the packed bed uniformly in the axial direction. If this is not done, then longitudinal gradients are predominant in the packed bed and it takes a long time to equilibrate the temperature gradients. Oddly shaped work pieces may require impractical, inefficient or multiple coil geometries. It is desirable to space the coil turns as close as possible and reduce the gap between the coils and the charge for efficient heating. The diameter of the coil tubing does influence the economic variables in terms of power losses in the coils.

vi. Mold Geometry

Particles contained in cylindrical molds can be rapidly and uniformly heated using audio frequency induction. No experimental work has been done on irregularly shaped packed beds. The IH characteristics of audio frequency heating for irregularly shaped molds containing particles can be extrapolated from the experimental results. The considerable depth of penetration at 4.2 kHz for low carbon steel particles will permit uniform heating of packed beds with varying cross sections. However, localized hot spots may result near the surface of the larger cross sections due to greater power dissipation in these areas combined with earlier sintering there.

vii. Power Input To Packed Bed

The power input to the packed bed has little influence on the efficiency of heating. However, it does affect heating time. At high power inputs ($> 20\text{kw}$) the packed bed could be raised to process temperatures in 180 seconds. The time for heating could be further cut down by the use of self-coupling IH units, where there is no idle time to compensate for changes in load impedance.

viii. Simultaneous Heating Of Melt Charge And Shot

Although the melt charge and shot had the same size

and shape, and approximately the same oxygen content, the shot coupled preferentially to the induction flux resulting in meltdown of the shot region. The preferential coupling is obviously due to the fact that the melt charge had higher resistivity than the shot. This problem could be avoided by using separate coils for heating the melt charge and shot using appropriate induction heating frequencies to ensure good coupling to the shot and melt charge regions. Alternatively, the shot could be heated to process temperature using IH and the melt heated elsewhere could then be transferred into the heated packed bed.

2.3.1 Problems Of Direct Induction Heating For Manufacturing SD Castings

1. Cracking of Packed Bed during Heating

The cracking phenomenon observed during IH of particles in a mold is discussed in Appendix 2D. Cracks in the packed bed of low carbon steel particles will affect the casting quality by changing the local packing density. The cracks can be avoided if at sintering temperatures (1000° to 1200°C) the power input to the bed is shut off for a short time to allow the particles to sinter together. This idle period during heating need last only 100 to 200 seconds for shot diameters of 0.216 mm to 1.85 mm.

ii. Preferential Coupling

The high resistivity of a packed bed of low carbon steel shot accounts for the preferential heating of bulk metallic components in the vicinity of the bed. SD casting manufacture by IH using a single coil will therefore require that the cast iron charge above the shot have the same electrical properties as the shot itself so that both components can be simultaneously heated to process temperature.

iii. Heating Of The Particle Valve

The material used for the particle valve must not be wetted by the cast iron liquid or interact with the cast iron and low carbon steel particles at process temperatures. This dictates the use of non-conducting ceramics like silica, alumina, mullite etc., which cannot be heated by induction. The particle valve must be heated indirectly by the cast iron charge above and low carbon particles below it. The cast iron and shot can be raised to process temperatures in about 200 seconds by IH. In the same time the temperature of the particle valve will be raised by a few hundred degrees. To avoid this problem it may be necessary to preheat the alumina particles elsewhere to about 1000°C . At these temperatures the alumina particles do not sinter together. Alternatively, the particle valve could be reduced in thickness - perhaps to a few particle diameters - if ways could be

found to make it so thin reliably.⁽³⁾

iv. Mold Limitations

For audio frequency IH heating rates of 3° to 5°C/s in the packed bed have been attained. The mold material is non-conducting and so is not heated by induction. The inside of the mold quickly attains the temperature of the particles, but the outside remains relatively cold resulting in large temperature gradients across the mold wall. The mold material must be able to withstand these temperature gradients or it may be necessary to preheat the mold to avoid thermal shock problems. Heating the particles to 3° to 5°C/s in a fully dense alumina crucible resulted in cracking of the crucible. No experiments were done using the type of molds cited in Reference (4) which lie at two extremes: unbonded vacuum molds and strongly dense permanent molds.

2.3.2 Advantages And Disadvantages of IH.

1. Advantages:

- . It lends itself to automatic cycling.
- . The low carbon steel particles can be rapidly heated to SD casting temeratures.
- . The method could be used for manufacturing SD castings by batch process.

ii. Disadvantages:

- The IH of steel particles is a complex phenomenon. The operating conditions will vary depending on the particles used and the geometry of the casting. The thermal power history to attain a uniform casting temperature in the SD components must be known prior to manufacturing the casting.
- An idle time for 100 to 200 seconds to avoid cracks in the packed bed may have to be included in the heating schedule.
- Preheating of some types of molds may be necessary to avoid thermal shock at the heating rates attained during direct IH.

2.4 Gas Heating

Gas heating could be used as a direct heating method by passing the hot gas through the shot contained in an impermeable mold. The method cannot be used by itself to manufacture SD castings, as at casting temperature the gas path will be obstructed by the melt. Gas heating is therefore limited to heating the shot and PV to process temperature. The theoretical and experimental analysis of heating shot by gas is given in Appendix 2E.

2.4.1 Economics of Gas Heating

The heating time and heating efficiency of shot depend on the value of Y^* (dimensionless distance) which is given by (5):

$$Y^* = \frac{h_v L}{c_g G} \quad (7)$$

where:

Y^* - dimensionless distance

h_v - volumetric heat transfer coefficient

L - casting length (height of packed bed)

c_g - specific heat of gas

G - Gas mass velocity

The heating efficiency expressed as a function of Y^* is given by:

$$\eta = -97 + 120 Y^{*0.1} - 6.6 Y^{*0.3} + .005 Y^{-1} \quad (8)$$

The above equation is valid for $Y^* < 50,000$. For $Y^* > 50,000$, the efficiency is assumed to be 100 percent. The heating time is given by:

$$t_H = \frac{Z^* \rho_s c_s (1 - \epsilon)}{h_v} + \frac{\rho_g L \epsilon}{G} \quad (9)$$

where:

z^* - dimensionless time

ρ_s - density of shot

c_s - specific heat of shot

ϵ - void fraction

ρ_g - density of gas

z^* , dimensionless time, is a function of y^* and is given by:

$$z^* = 9.8 + 1.2 y^* + 8.8 \times 10^{-0} (y^*)^2 - 2.5 \times 10^{-10} (y^*)^3 \quad (10)$$

The volumetric heat transfer coefficient, h_v , can be obtained using Furnas' emperical equaliton (6) given in Appendix 2E.

The heating efficiency and time can be calculated using Eqs. (8) and (9) respectively. For example, a calculation for heating time and efficiency for process conditions given in Table I. gives $t_H=95$ seconds and $\eta=54$ percent.

The experimental efficiency is lower than the theoretical efficiency calculated using Eq. (8) because of heat loss from the packed bed walls. Comparison of the experimental and theoretical efficiencies shown in Fig. E.3 leads to an approximate relationship given by:

$$\eta_E = \eta_T - 25 \quad (11)$$

Table I. Process conditions used for estimating
gas heating time and efficiency.

Gas medium - Helium
Gas mass velocity - 1.0 kg/m².s
Casting temperature - 1400°C
Casting length - 100 mm
Shot size - 1.0 mm
Void fraction - 0.38

where η_E is the experimental heating efficiency and η_T is theoretical heating efficiency. The expected heating efficiency must have a value in between η_E , the upper bound efficiency and η_E , the lower bound efficiency for gas heating of shot. The experimental heating time is for a packed bed with heat losses to the surroundings and so is greater than the theoretical heating time. Comparison of experimental and theoretical heating times shown in Fig. E.4 leads to an approximate relationship given by:

$$(t_H)_E = 1.5 (t_H)_T \quad (12)$$

where $(t_H)_E$ is the experimental heating time and $(t_H)_T$ is the theoretical heating time. The expected heating time must have a value in between $(t_H)_E$, the upper bound heating time, and $(t_H)_T$, the lower bound heating time for gas heating of shot.

The upper bound efficiency and lower bound heating time can be estimated using Eqs. (8) and (9). The lower bound efficiency and upper bound heating times can be estimated using Eqs. (11) and (12). The upper bound and lower bound efficiencies and heating times can be used to obtain reasonable estimates for the economic variables.

2.4.2 Advantages And Disadvantages Of Gas Heating

i. Advantages

- . A rapid cycle casting process is possible as heating times less than the SD solidification time are attainable in this heating route. For the process conditions given in Table I, the heating time (lower bound) is 95 seconds and the SD solidification time is 293 seconds.
- . The heating efficiency is high and could be increased by recuperating the sensible heat of gas leaving the mold. For the process conditions given in Table I, the heating efficiency (upper bound) is 54 percent.

ii. Disadvantages

- . The casting machine is complex, requiring a high capital investment.
- . The mold technology must be developed.
- . The pilot plant casting machine must be developed to evaluate the feasibility of manufacturing castings using this heating route.

2.5 Radiative Heating

Radiative heating is an indirect method for heating SD components to process temperatures. The charge is contained in a mold which is surrounded by a hot source maintained at high temperatures. At high temperatures,

(1200° to 1500°C) radiation is the predominant mode of heat transfer. A hot source can be provided in several ways, for example by a high temperature silicon carbide resistance winding. A graphite susceptor couples efficiently to the induction flux and can be rapidly heated to SD casting temperatures.

The susceptor could be maintained at SD casting temperatures with power inputs of about 10 kw for manufacturing SD castings of diameter 50 to 70 mm and height of 100 mm. Fig. 1 illustrates a typical radial temperature distribution in a cylindrical mold containing shot when placed in a heated susceptor at a temperature T_H . The temperature distribution is at an arbitrary time during the heating process. The heating of shot is an unsteady process. The rate of heat transport from the susceptor to the mold is given by:

$$Q_1 = \alpha_1 (T_H^4 - T_m^4) \quad (13)$$

Across the mold wall, the rate of heat transport is given by:

$$Q_2 = \frac{\alpha_2 k_m (T_m - T_s)}{t_m} \quad (14)$$

The heat transport rate in the packed bed is given by:

$$Q_3 = \frac{\alpha_3 k_{PB} (T_s - T_{cl})}{d_{PB}} \quad (15)$$

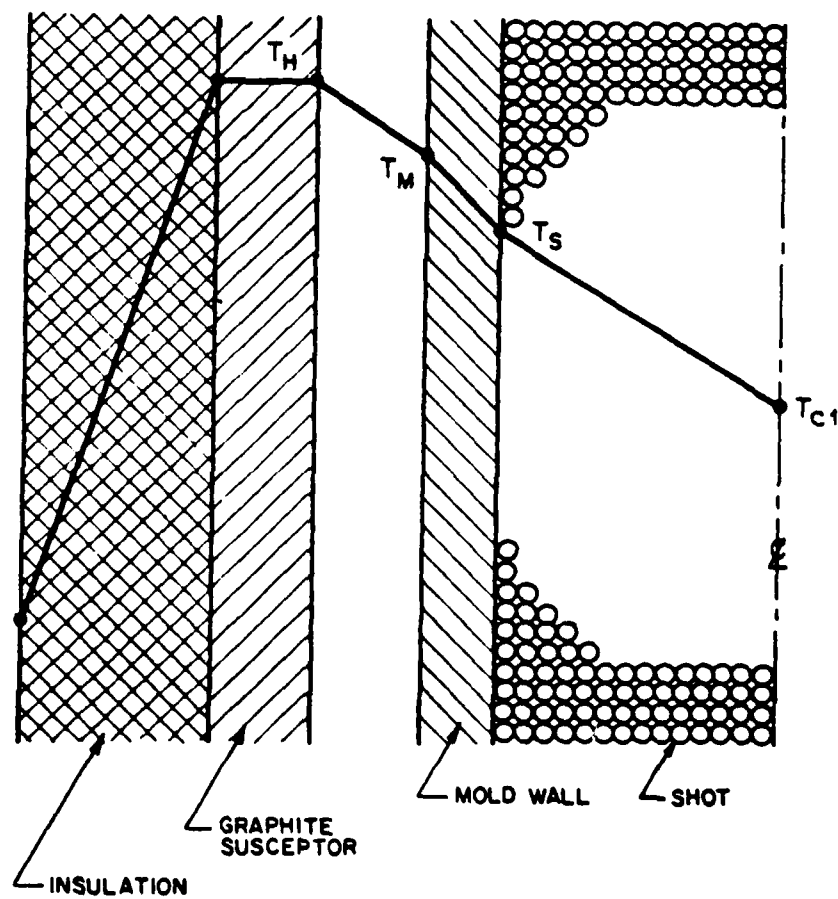


Figure 1. Radial temperature distribution during radiative heating.

where:

- Q_1 - rate of heat transfer between hot source and mold
 Q_2 - rate of heat transfer across mold wall
 Q_3 - rate of heat transfer in packed bed of shot
 T_H - susceptor (hot source) temperature
 T_m - mold wall temperature
 T_s - mold wall - packed bed interface temperature
 T_{cl} - temperature at the center of the packed bed
 k_m - thermal conductivity of the mold
 k_{PB} - thermal conductivity of the packed bed
 ϵ_m - emmisivity of the mold surface
 $\alpha_1, \alpha_2, \alpha_3$ - geometric factors

The slowest rate of heat transport given by Equations

(13) (14) and (15) will control the heating time.

For example, if $Q_2 > Q_3$, then the heating time is controlled by heat transport in the packed bed of shot.

Appendix 2F gives the experimental results for heating S100 shot in a cylindrical alumina mold. From the results it is evident that the packed bed heats at a very slow rate during the early stages of heating. The surface of the packed bed attained casting temperature in about 1200 seconds while the interior temperature increased by 100°C during the same period. The large driving force for heat flow is offset by low thermal conductivity of the bed during this period. After

1200 seconds, the packed bed interior temperature increased from 400°C to 1350°C in 1000 seconds. This period is characterized by enhanced thermal conductivity of the packed bed resulting from bonding between the particles.

A packed bed containing 1.2 kg. of shot was heated from 350°C to 1350°C in 2200 seconds. The heating time can be reduced by increasing the susceptor temperature which would raise the packed bed surface temperature to casting temperature more rapidly promoting sintering at the packed bed surface and accelerating the radial heat flow into the bed. The heating efficiency was estimated to be only 4.2 percent. The efficiency can be increased by using a susceptor and by shielding the opening at the top of the susceptor to reduce radiation losses.

The heating time for indirect heating can be estimated if the thermal diffusivity of shot is known as a function of temperature. The thermal diffusivity of shot calculated from resistivity data is given in Appendix 2G.. The data is in agreement with the experimental results. Below 400°C , The thermal diffusivity has a low value and is temperature sensitive. Above 400°C , the thermal diffusivity attains an asymptotic value approximately 0.2 times that of solid iron. The rapid increase in the temperature at the

center of the packed bed above 400°C , as shown in Fig. F.2, confirms the validity of thermal diffusivity values calculated from resistivity data. The thermal diffusivity of investment molds is of the order of $10^{-7} \text{ m}^2/\text{s}$.

Below 400°C , the packed bed thermal resistance controls the heat transfer rate and above 400°C , the heat transfer rate is controlled by the mold wall thermal resistance. The controlling resistance to heat transfer could be used to estimate an approximate heating time for a given casting shape by using the Gurney-Lurie charts for transient heat transfer.⁽⁷⁾

2.5.1 Molds For Radiative Heating

The molds used for indirect heating must have thin walls such that the mold wall resistance to heat transfer does not control the heating time. Investment molds become the ideal choice for manufacture irregularly shaped castings in the thin walled molds. Appendix 2H outlines the feasibility of using investment molds for manufacturing SD castings. The investment shells must have at least six coats to withstand an external pressure of 750 kPa and can be made impermeable to the pressurization gas by coating the molds with a glaze having a softening point 100° to 300°C below the casting temperature.

2.5.2 Advantages and Disadvantages of Radiative Heating.

i. Advantages

- . The heating time could be considerably reduced by preheating the SD components to about 400°C before placing them in a hot furnace at casting temperature.
- . The heating efficiencies could be increased by adequate insulation of the furnace from the surroundings.
- . The capital cost is lower than other heating routes as castings could be made by heating the components in a furnace located in a pressure vessel.
- . The mold technology is available.

ii. Disadvantages

- . For irregularly shaped castings, the time of heating is controlled by the largest cross-section.
- . The thermal properties of the mold may dictate the heating rate to avoid thermal cracking in the mold.
- . Radiative heating cannot be used for permanent and vacuum molds.

2.6 Casting Machines

Casting machine design is based on the heating method used to heat SD components to process temperature. The Three casting machines that have been designed are:

- i. Casting Machine via Induction Heating
- ii. Casting Machine via Gas Heating
- iii. Casting Machine via Radiant Heating

i. Casting Machine via Induction Heating

Casting Machine using induction heating is shown in Fig. 2. The mold consists of a thin ceramic shell backed up with coarse refractory particles. A layer of fine refractory particles is placed at the top of the mold to make the mold region impermeable to the pressurization gas.

A single induction coil could be used to heat the melt charge and shot to process temperature provided the melt charge and shot have the same resistivity. Separate coils could be used to heat the melt charge and shot if they have different electrical properties.

The process feasibility of this machine has not yet been confirmed as no castings have been manufactured. This casting machine could be used as a batch process or semicontinuous process depending on how the SD components are heated to process temperature.

ii. Casting Machine via Gas Heating:

The flow sheet for the casting machine is shown in Fig. 3. In this machine the shot and melt charge have to be heated separately. The slowest step in the process will control the cycle time.

LEGEND

1. Fine refractory particles
2. Induction coil
3. Container
4. Coarse refractory particles
5. Melt charge
6. Particle valve
7. Shot
8. Thin walled mold

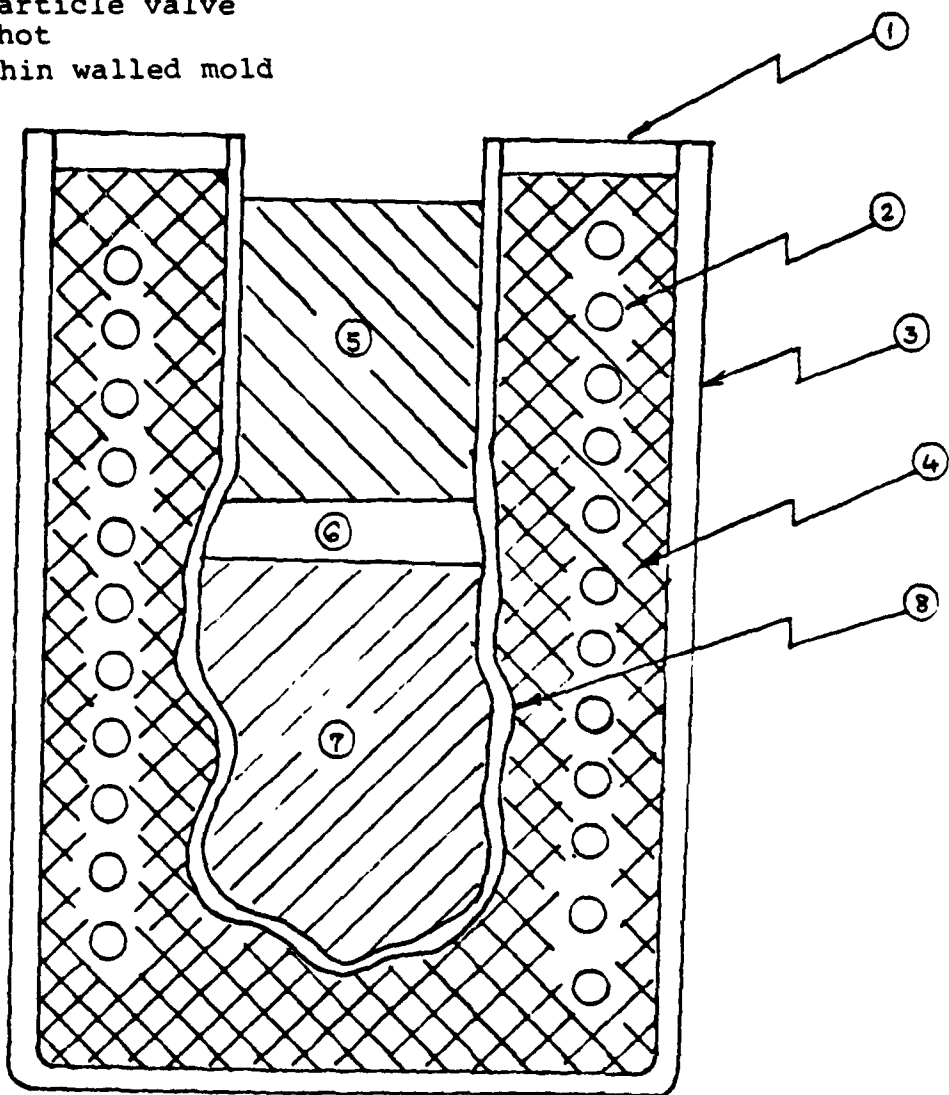


Figure 2. SD casting machine using induction heating.

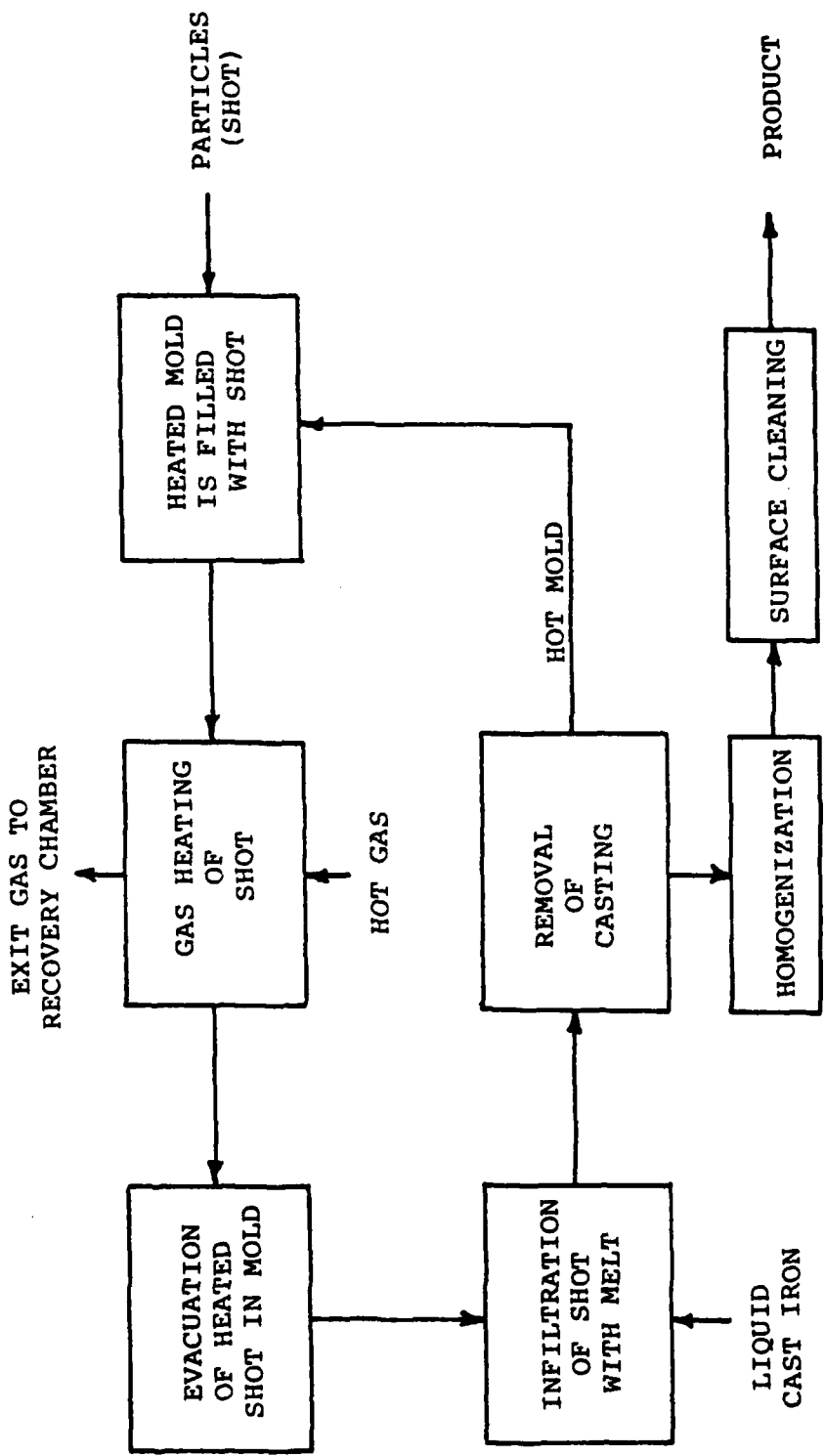


Figure 3. Flow sheet for manufacturing SD castings in permanent molds by gas heating.

No castings have been manufactured using this machine. The technology of impermeable permanent molds for this casting machine has yet to be developed. This machine has a high process efficiency and production rate. However, these economic gains are offset by the high capital costs for the machine components.

iii. Casting Machine via Radiant Heating:

The basic components of the casting machine are shown in Fig. 4. The furnace is enclosed in a pressure vessel permitting the furnace to be evacuated or pressurized. Investment molds are used for this casting machine.

This casting machine uses a batch process. The casting manufacture involves: Heating components to casting temperature, melt transfer, solidification and homogenization and finally allowing the furnace to cool to room temperature. The batch process could be modified to a semi-continuous one as shown in Fig. 5. In this casting machine, the cycle time is controlled by the slowest process step. The high capital investment costs are offset by the increased heating efficiency and low cycle time.

LEGEND

1. induction coils
2. graphite susceptor
3. insulation
4. mold
5. radiation shields
6. cast iron
7. particle valve
8. shot
9. graphite disc

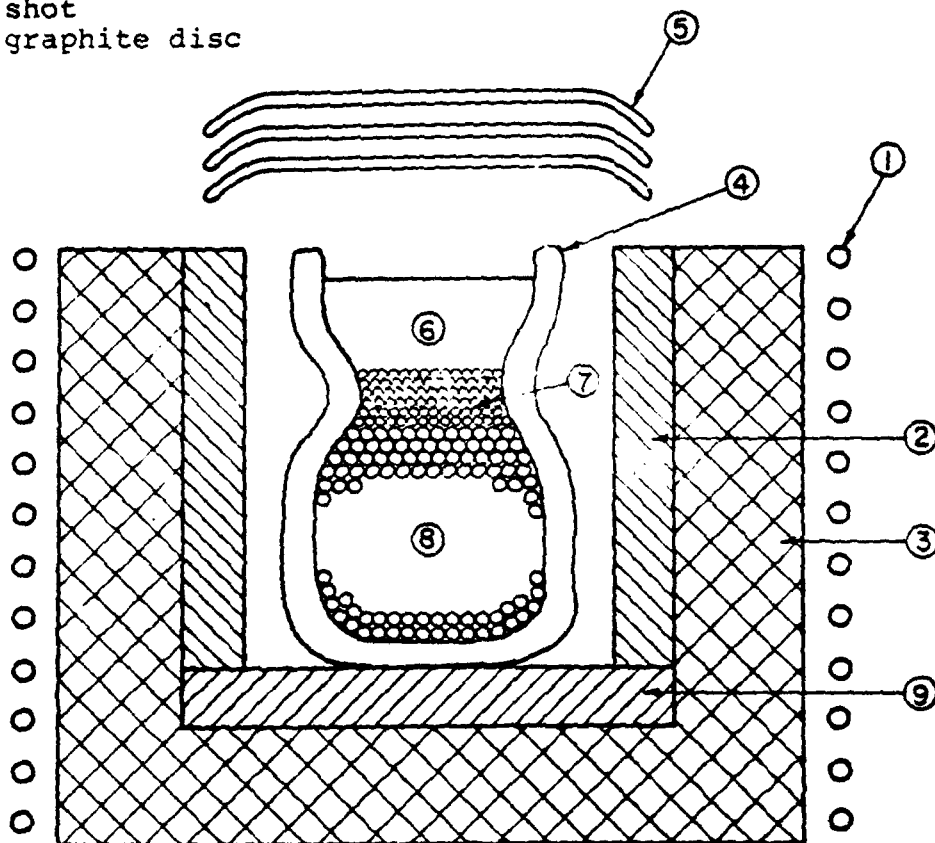


Figure 4. Radiative heating setup for manufacturing SD castings.

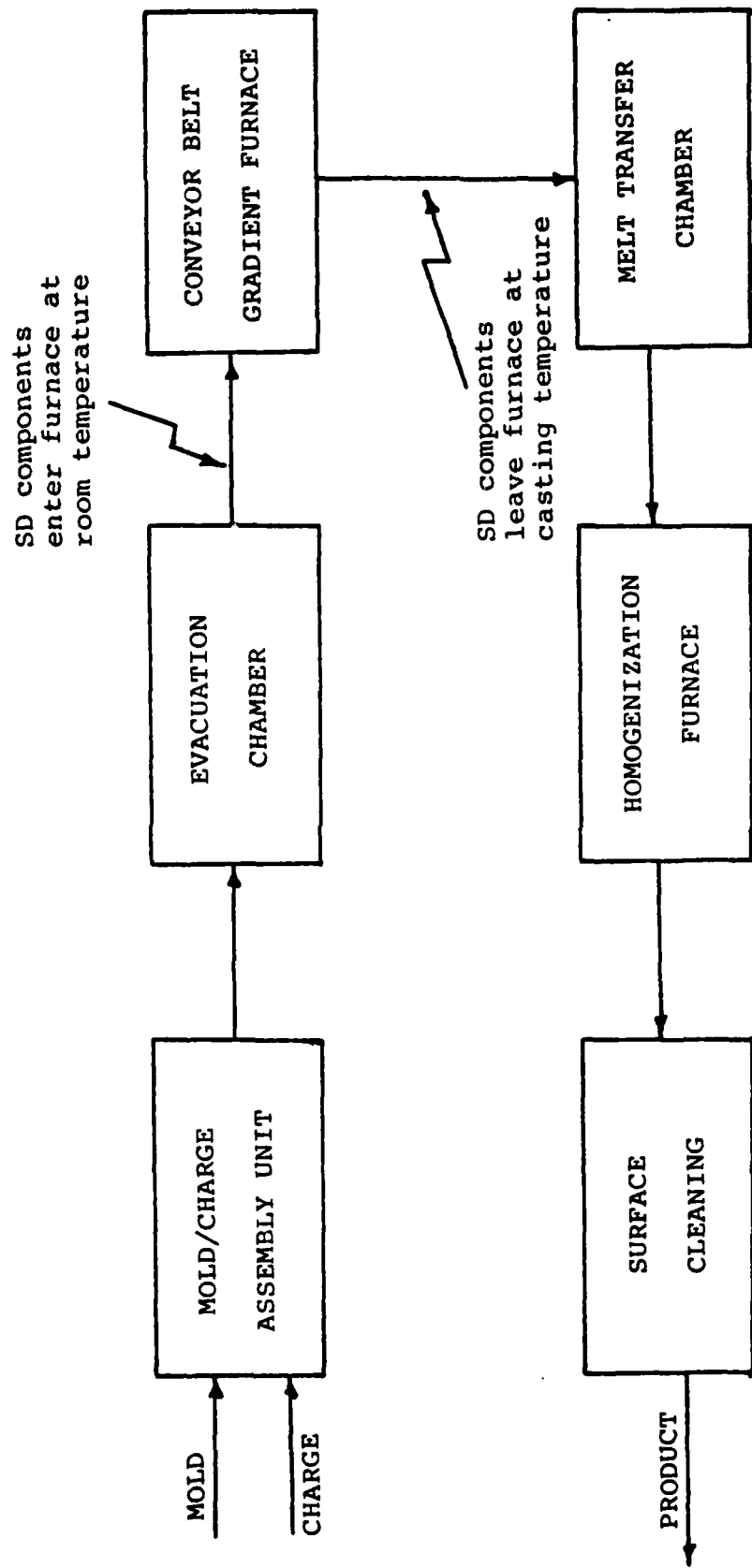


Figure 5. Flow sheet for a semi-continuous SD casting machine using the radiative heating route.

2.7 Conclusion

SD castings have been successfully made using the radiative heating route. The casting machine uses a batch process for manufacturing castings, and has a low process efficiency and a high cycle time for casting manufacture. The production rate is essentially dictated by the volume of the furnace. Since a rapid cycle steel casting process is not attainable by using a radiative heating batch process casting machine, SD castings must rely on their superior quality in order to compete with conventional castings. However, if the radiative heating route can be converted to a semi-continuous process, then SD castings may have an economic edge over conventional castings in terms of low cycle time and superior casting quality.

Casting machines via gas heating and induction heating routes have yet to be developed. The induction heating route promises low cycle times at the expense of low heating efficiencies. The prime advantage of induction heating routes is that the bulk of the mold materials used for casting manufacture could be re-cycled. The short heating times make it possible to attain a rapid cycle steel casting process. Gas heating, on the other hand, would make rapid cycle castings of steel a reality. This can be attributed

to the low heating times attainable in the gas heating. The casting machine is complex because it involves two steps:

1. Heating the shot by hot gas
2. Transferring the melt into the heated packed bed of shot.

The economic gains resulting from low cycle times and high heating efficiencies are partly offset by the high capital investment for gas and melt handling equipment.

As of today, SD castings can be manufactured via the radiant heating route using a batch process. The direct heating routes, induction heating and gas heating have not yet been established as feasible routes for SD casting manufacture. The key to rapid cycle steel casting manufacture depends on the process development of the casting machines via the direct heating routes.

REFERENCES

1. G. Langford and R. E. Cunningham: Met. Trans. B, 1978, Volume 9B, pp. 5-19.
2. R. L. Conta: IEEE Trans. on industrial applications, Vol. IA-13, No. 4, pp 330-334.
3. Chapter 3, This Report.
4. D. Apelian and G. Langford: Rapid Cycle Steel Casting. Proposal for research written for the Defense Advanced Research Program Agency, 1977.
5. Schumann, T. E. W.; J. Franklin Inst., 1929, 208, pp 405-416.
6. Furnas C. C., Trans. Amer. Inst. Chem. Engrs. 1930, Vol. 24, pp 28-39.
7. C. O. Bennett and J. E. Meyers: Momentum, Heat, and Mass Transfer, McGraw-Hill Book Company, 1974, pp 280-284.
8. Lof G.O.G. et al: Industrl. Engg. Chem. 1948, 40.
9. Ford, H. and Saunders, O. A., J. Iron and Steel Inst., 1940, 141.
10. Gamson, B. W., and Hougen, O. A., Trans. Amer. Inst. Chem. Engrs. 1934, 141.
11. Denton, AERE, H.P.C., 1949, 35.
12. Coppage, J.E., and London, A. L., Chem. Engg. Progress, 1956, Vol. 52 (2), pp 52F-63F.
13. Kunii, D., and Smith, J. M., AICHE Journal, Vol. 6, 97, (1960).
14. "Ceramic Shell Investment Casting with DuPont Ludox", E. I. DuPont de Nemours & Co., Wilmington, DE.

APPENDICES

APPENDIX 2A

INDUCTION HEATING EXPERIMENTAL RESULTS

This appendix summarizes the experimental results of induction heating of steel powders. The relationships and notations used for evaluating the data are given at the end of the appendix.

1. Experimental Procedure

The particles were placed in a crucible insulated with fiberfrax*, a light weight thermal insulation made from aluminasilica fibers. An alumina tube, 6.35 mm (0.25 in.) in diameter was placed in the center of the packed bed to maintain an inert atmosphere to minimize the oxidation of the particles during the heating period. Power was supplied to the particles through an induction coil closely surrounding the crucible. Thermocouples were placed at different locations in the packed bed. Temperatures were recorded using a multipoint Honeywell temperature recorder. Figures A.1, A.2, A.3 and A.4 show the different setups used for the evaluating the induction heating characteristics of steel powders. The setup shown in Fig. A.4 was used to study the simultaneous induction heating of melt and shot. The setup shown in

*Registered Trade mark and Product of the Carborundum Co.

LEGEND

1. induction coils
2. crucible
3. fiberfrax
4. alumina tube
5. shot

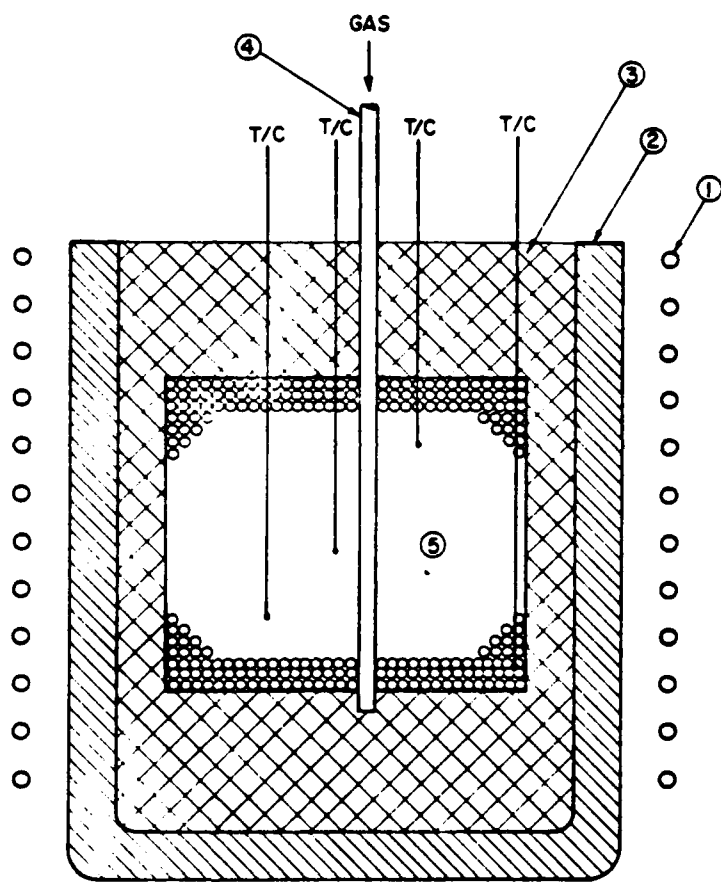


Figure A.1. Induction heating setup with vertical insertion of thermocouples.

LEGEND

1. alumina tube
2. fiberfrax
3. induction coil
4. alumina crucible
5. thermocouple
6. shot

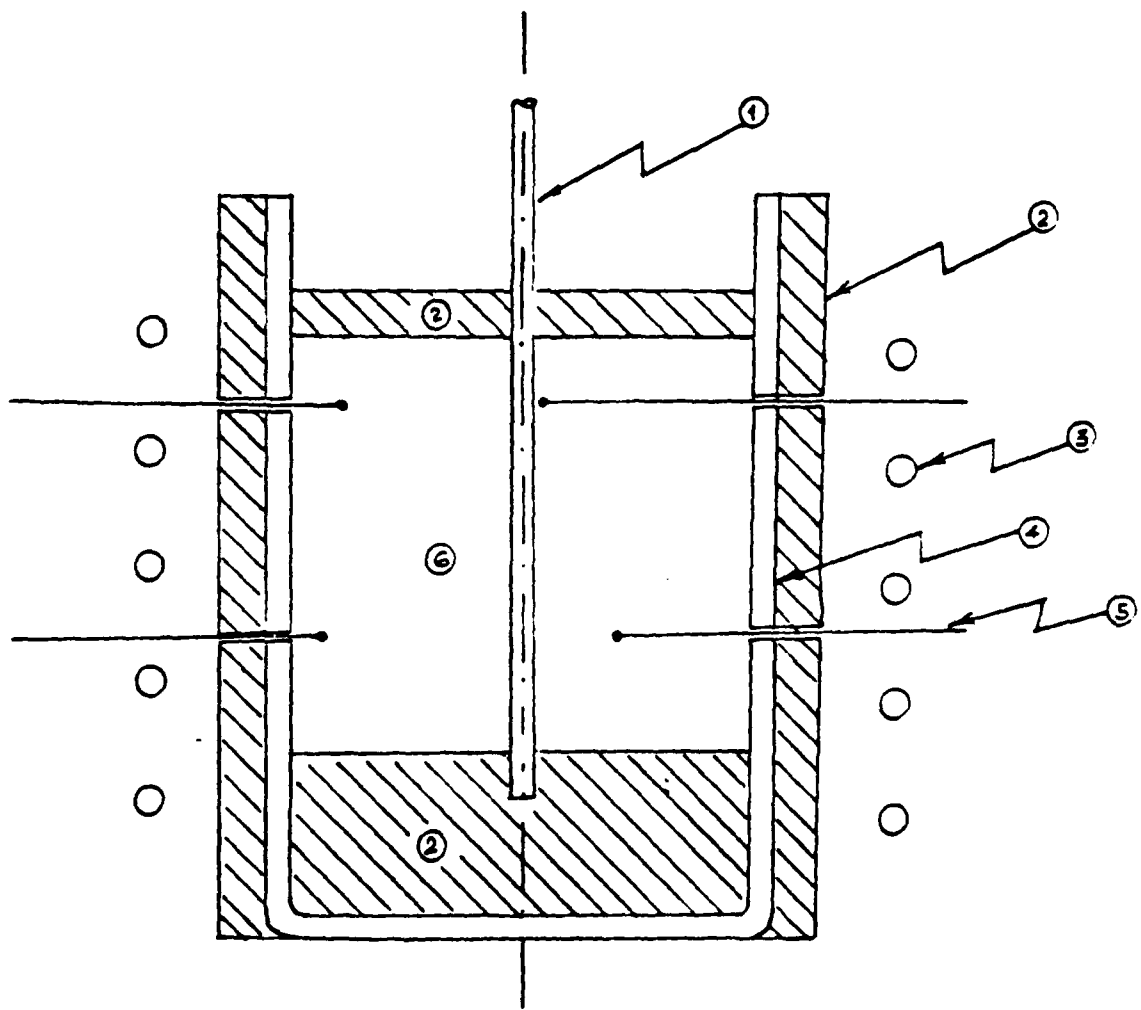


Figure A.2. Induction heating setup with radial insertion of thermocouples.

LEGEND

1. induction coils
2. silica crucible
3. fiberfrax
4. nichrome wire
5. variable resistor
6. ammeter
7. shot

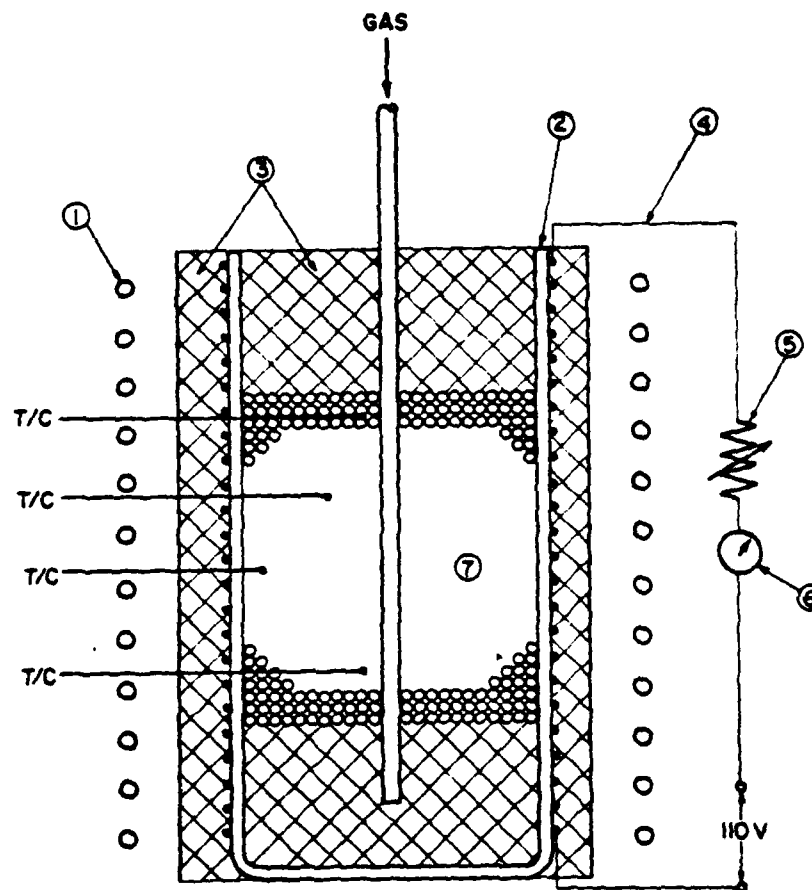


Figure A.3. Induction heating setup for heating powders preheated by resistance heating.

LEGEND

1. alumina tube
2. fiberfrax
3. crucible
4. induction coils
5. alumina particles ($<250\mu\text{m}$)
6. mullite crucible
7. melt charge
8. particle valve
9. shot

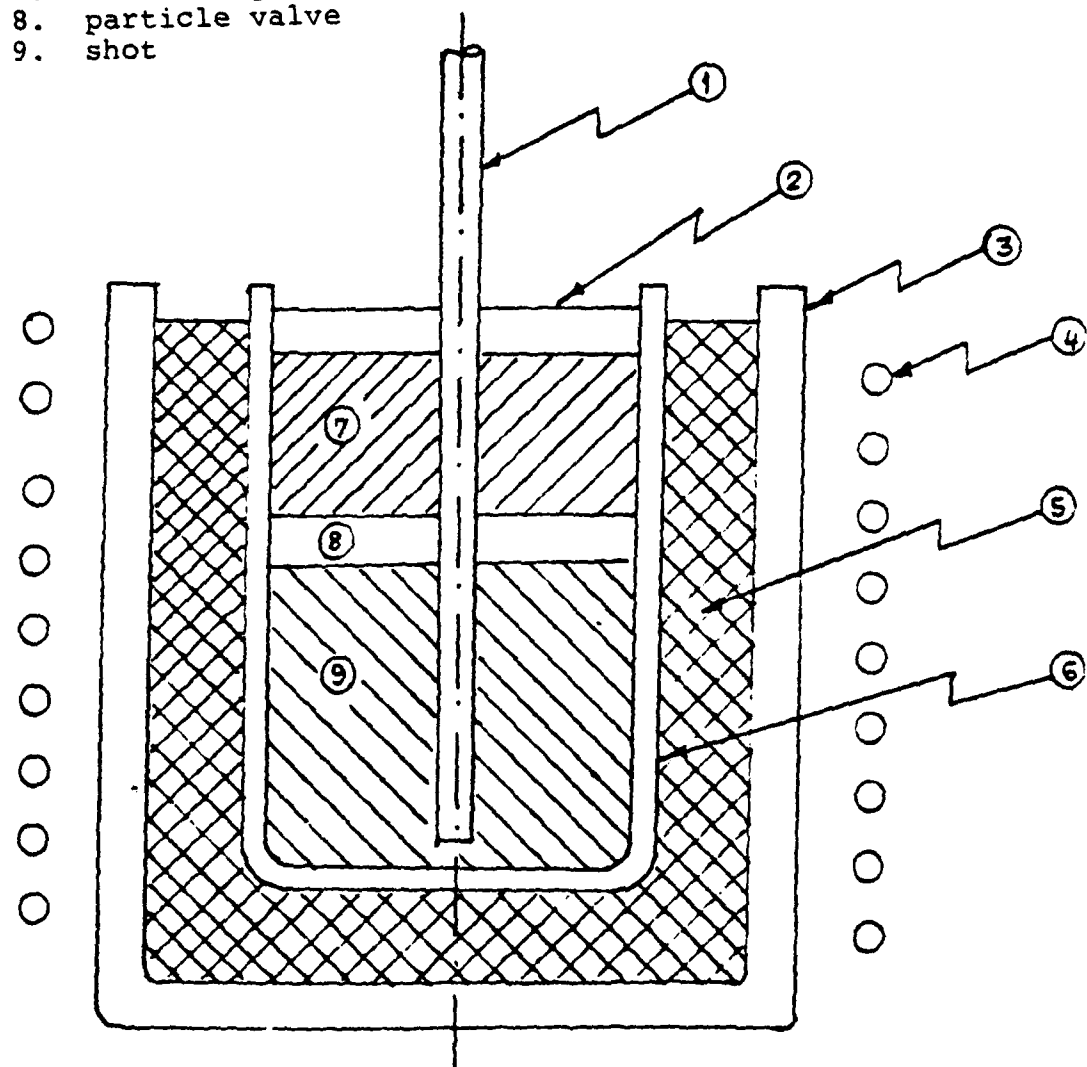


Figure A.4. Simultaneous heating of melt charge and shot by induction.

Fig. A.3 was used to study the induction heating characteristics of preheated powders. These particles were preheated by indirect resistance heating.

2. Experimental Parameters

The important experimental parameters for direct induction heating of steel particles are listed below:

- Shot
- Setup
- Packed bed
- Atmosphere

The values for the experimental parameters for IH of shot are given in Tables A-II. Tables A-III and A-IV give the experimental parameters for simultaneous IH of melt charge and shot. Appendix 5G gives the characteristics of powders listed in Table A-1. A cylindrical packed bed geometry was used in all the induction heating runs. The crucible containing the particles was insulated from the surroundings with fiberfrax. A Taylor Winfield 450 kHz 10 KW radio frequency generator* was used to heat the particles in run #9. In the other runs, the particles were heated using an Inductotherm, 4.2 kHz, 30 KW audio frequency generator.

*The author is indebted to the staff of the Laboratory for the Research of the Structure of Matter, University of Pennsylvania, for allowing him to use this equipment.

TABLE A.1 - Shot, set-up and atmosphere used for IH runs

Run#	Shot**	d _p mm	Set up Figure	Heating Atmosphere
1	I300	0.780	A.1	Air
2	S200	0.780	A.1	Air
3	S211	0.216	A.1	Nitrogen
4	S100	0.216	A.1	Nitrogen
5	S100	0.216	A.1	Argon
6	S100	0.216	A.2	Argon
7*	S100	0.216	A.2	Argon
8	S100	0.216	A.2	Air
9	S100	0.216	A.2	Air
10*	S100	0.216	A.2	Argon
11	S200	1.850	A.2	Argon
12	S100	0.216	A.3	Argon
13	S100	0.216	A.3	Argon
14	S100	0.216	A.3	Nitrogen
15	S100	0.216	A.2	Nitrogen
16	S100	0.216	A.2	Nitrogen
17	S212	1.85	A.2	Nitrogen
18	S212	1.85	A.2	Nitrogen

* Runs 7 and 10 were used to measure the resistivity of the packed bed of shot using a four point technique. The results are given in Appendix 2C.

** See Appendix 5G (Chapter 5) for explanation of the symbols used to characterize the shot.

Table A-II - Packed bed and coil parameters for IH of shot.

Run#	d_{PB} mm	l_{PB} mm	W kg	d_C mm	d_S mm	l_S mm	S mm	g mm	N 9
1	68	188	3.50	6.35	130	150	15	31	9
2	77	100	2.00	6.35	130	155	17	27	9
3	77	90	1.80	6.35	130	110	10	27	9
4	77	83	1.70	6.35	130	125	10	27	9
5	63	130	1.60	6.35	130	150	16	34	9
6	55	130	1.50	6.35	130	150	15	38	9
7	55	120	1.40	6.35	130	205	35	38	13
8	58	80	1.00	6.35	100	120	8	21	13
9	57	80	1.00	6.35	100	120	8	21	13
10	58	80	0.92	6.35	100	120	8	21	13
11	60	80	0.75	6.35	100	120	8	40	9
12	50	80	0.70	6.35	130	220	25	25	10
13	58	80	1.00	9.50	110	165	16	25	10
14	60	80	1.00	9.50	110	165	16	25	10
15	60	75	0.95	9.50	110	165	16	25	10
16	60	85	1.20	9.50	110	165	16	25	10
17	60	80	0.90	9.50	110	165	16	25	10
18	60	85	1.10	9.50	110	165	16	25	10

Table A III - SD components for simultaneous induction heating of melt charge
and shot

Run#	shot	Melt Charge	PV	$d_p(s)$ mm	$d_p(mc)$ mm	$d_p(PV)$ mm	w_{CI} kg	w_s kg	w_{PV} kg
19	S213	M31	PVI	1.1	1.1	1.6	.500	.500	.05
20	S213	M31	PVI	1.1	1.1	1.6	.500	.500	.05

Table A-IV - Coil parameters for simultaneous heating of melt charge and shot

Run#	d_{PB} mm	d_c mm	d_s mm	l_s mm	S	g	N
19	60	9.5	110	165	16	25	10
20	60	9.5	110	165	16	25	10

Results.

The induction heating of low carbon spheroidal powders (shot) will be discussed with emphasis to the following factors:

- . temperature distribution in packed bed
 - . incubation-period phenomena
 - . maximum packed bed temperature
 - . heating time
 - . heating efficiency
 - . reheating of packed bed
 - . packed bed after heating
 - . preferential coupling
 - . suppression of induction flux
 - . simultaneous heating of the melt charge and shot.
- i. Temperature Distribution in Packed Bed

The temperature distribution in the packed bed was evaluated by recording the temperature at different locations as a function of time. The maximum longitudinal and radial temperature gradients observed for the heating runs are listed in Table A-V.

In audio frequency (4.2 kHz) induction heating, the radial temperature gradients were small in magnitude. Figure A.5 shows the temperature distribution in Run #6. The packed bed heats uniformly in the radial direction.*

* In contrast to audio frequency heating, radio frequency induction heating (450 kHz) resulted in large temperature gradients (Run #9, Fig. A.6).

Table A-V - Temperature gradients and maximum
temperature attained during IH of shot

Run #	Temperature Gradients		Maximum Temperature
	T _L °C	T _R °C	T _{MAX} °C
1	160	60	890
2	180	70	771
3	330	60	1115
4	426	200	1000
5	-	120	1350
6	650	100	1400
7	700	30	1440
8	300	-	1320
9	-	520	940
10	200	-	1450
11	30	-	771
12	400	100	1200
13	220	-	1400
14	740	-	1400
15	1100	-	>1540
16	300	-	780
17	580	-	1420
18	280	-	1540

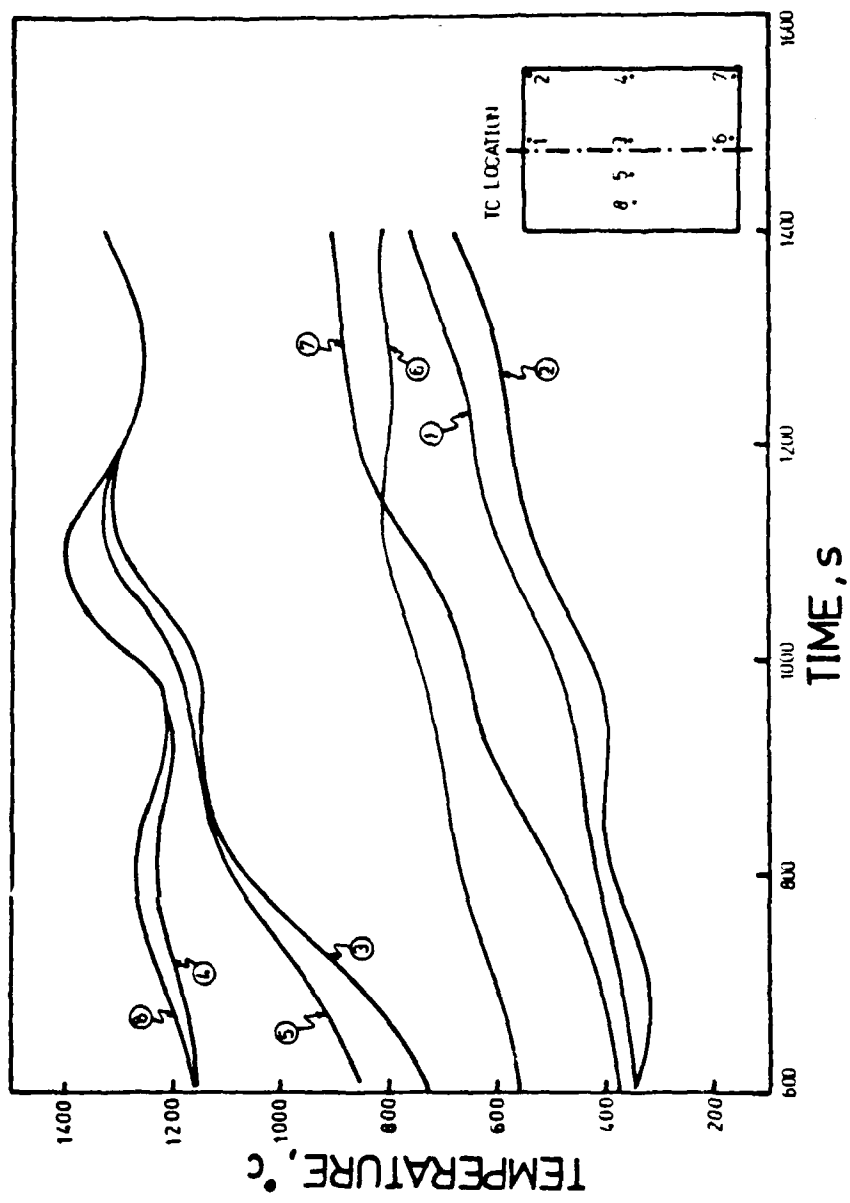


Figure A.5. Thermal history for run #6 showing longitudinal and radial temperature gradients in the packed bed.

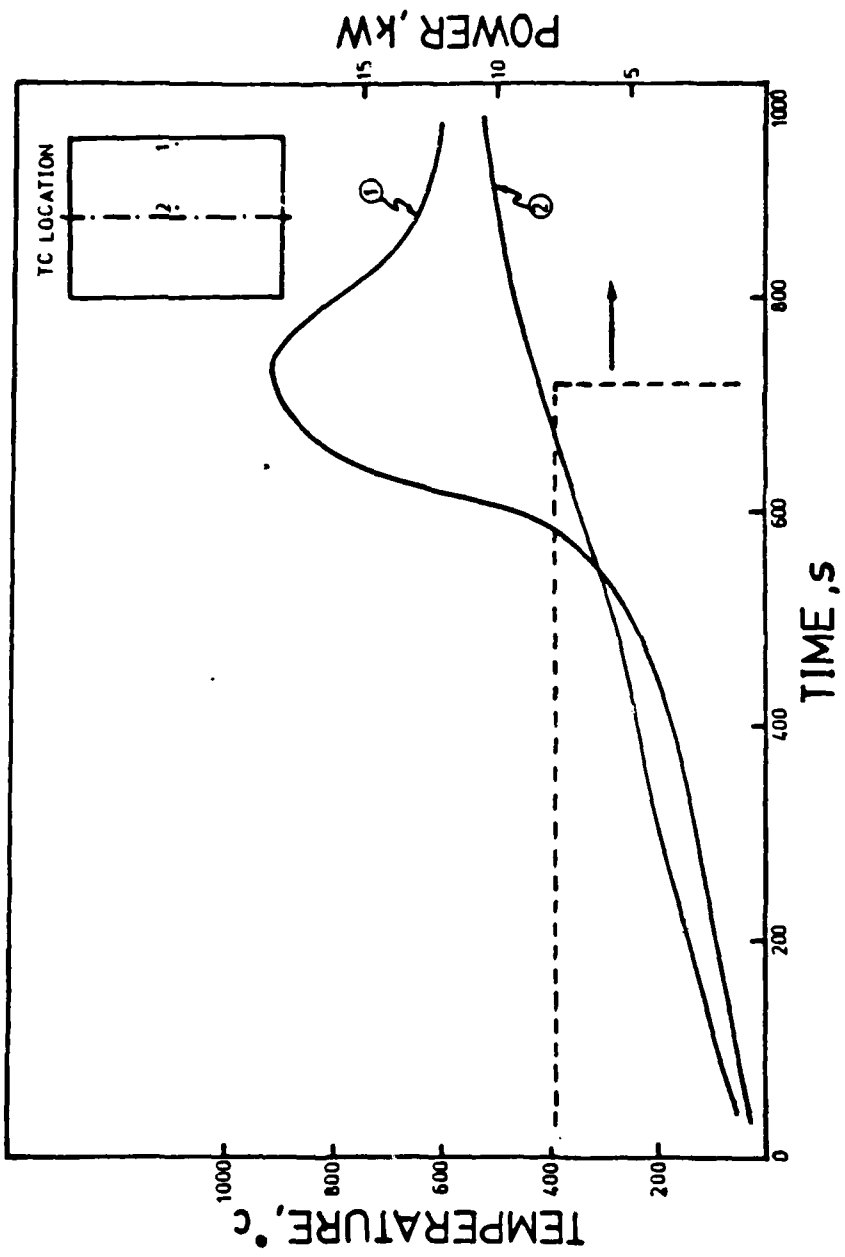


Figure A.6 Radial temperature gradients during radio frequency heating

For audio frequencies large longitudinal gradients were observed during induction heating. The temperature at the middle part of the packed bed always exceeded the temperature at the top and bottom of the bed. The temperature-time data for Run #5 shown in Fig. A.5 is an example of the longitudinal temperature gradients observed in the packed bed during induction heating. The longitudinal temperature gradients could be minimized by appropriate variations of the local coil spacing along the packed bed. This was done in Run #7, and the results are shown in Fig. A-7. The temperature at the top of the bed was considerably lower than the rest of the bed. The low concentration of coil turns at the top of the bed accounted for this temperature difference. Experimental results indicated that longitudinal temperature gradients could be minimized if three to four coil turns were concentrated at the top and bottom of the packed bed.

ii. Incubation Period Phenomena

An incubation period was observed during the heating of low carbon spheroidal steel particles. The incubation period was characterized by a low packed bed heating rate. The duration of the incubation period depends on the power input to the charge, the packed bed temperature and the particles in the bed. The incubation period was short

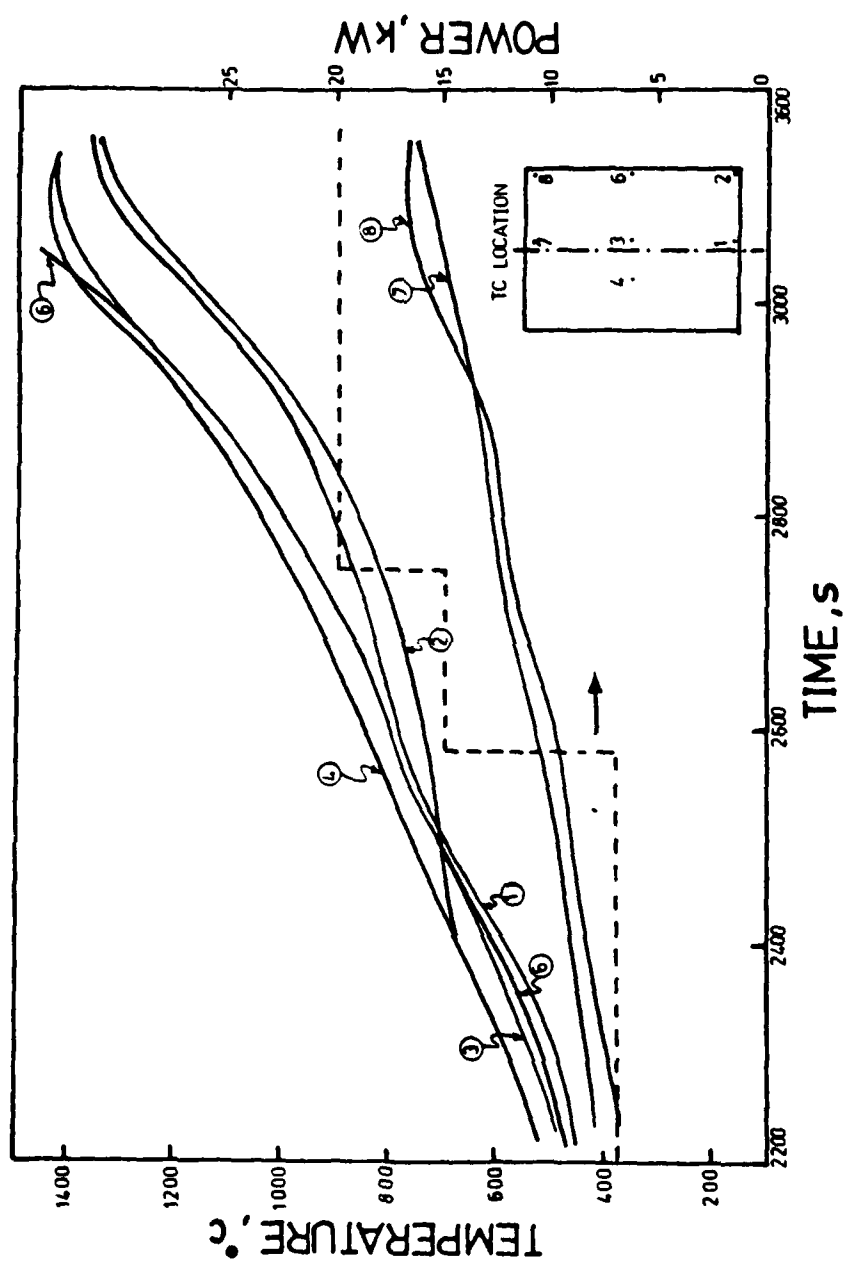


Figure A.7. Temperature equilibration between the middle and bottom parts of the bed by increasing the concentration of coil turns at the bottom of the bed.

lived at high power inputs. The influence of high power inputs on the incubation periods could not be studied due to the rapid change in load coupling characteristics of the packed bed with temperature.

The coupling temperature represents the temperature at which there is a sudden increase in the heating rate.* This temperature is influenced by the particles and the frequency of induction heating. If the coupling temperature exceeded the Curie temperature for iron (771°C) then the packed bed could not be heated above the Curie temperature regardless of the power input density to the charge. The incubation period results are given in Table A-VI.

iii. Maximum Packed Bed Temperature

Once the packed bed couples to the induction flux, then SD casting temperature could be easily attained. On the other hand, heavily oxidized particles did not couple to the induction flux. For these particles the maximum attainable temperature was 771°C as shown in Fig. A.9 for S200 ($d_p = 1.85 \text{ mm}$) powder. The maximum temperatures attained in the packed bed for the induction heating runs are given in Table A-V.

iv. Heating Time

The heating time is defined as the time to raise the packed bed to SD casting temperature after the packed bed

*The long incubation period can be circumvented by preheating the packed bed to the coupling temperature (Run #14, Fig. A.8).

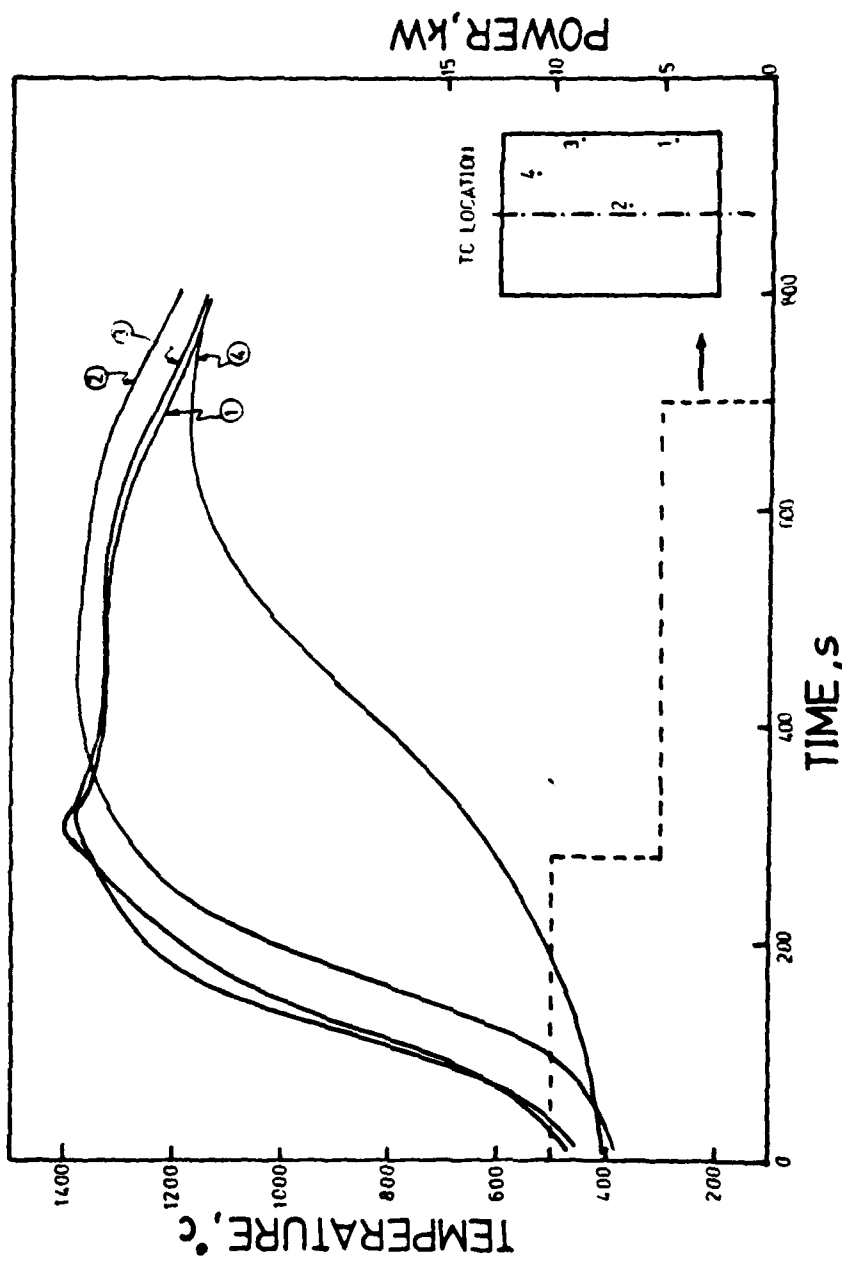


Figure A.8. Thermal-power history of S100 powder preheated to coupling temperature.

Table A-VI - Incubation period results for IH of shot

Run#	P _I kW	t _{IP} s	T _{CT} °C	r _{IP} %
1	5	1300	340	11.2
2	-	-	771	9.4
3	5	-	771	7.4
4	5	1250	426	7.2
5	7.5	1280	426	6.0
6	-	-	-	-
7	-	-	450	9.2
8	5.0	900	490	7.1
9	6.8	540	300	4.6
10	-	-	-	-
11	-	-	771	-
12	-	-	-	-
13	-	250	420	-
14	-	-	-	-
15	-	-	-	-
16	-	-	777	-
17	-	-	-	-
18	-	-	-	-

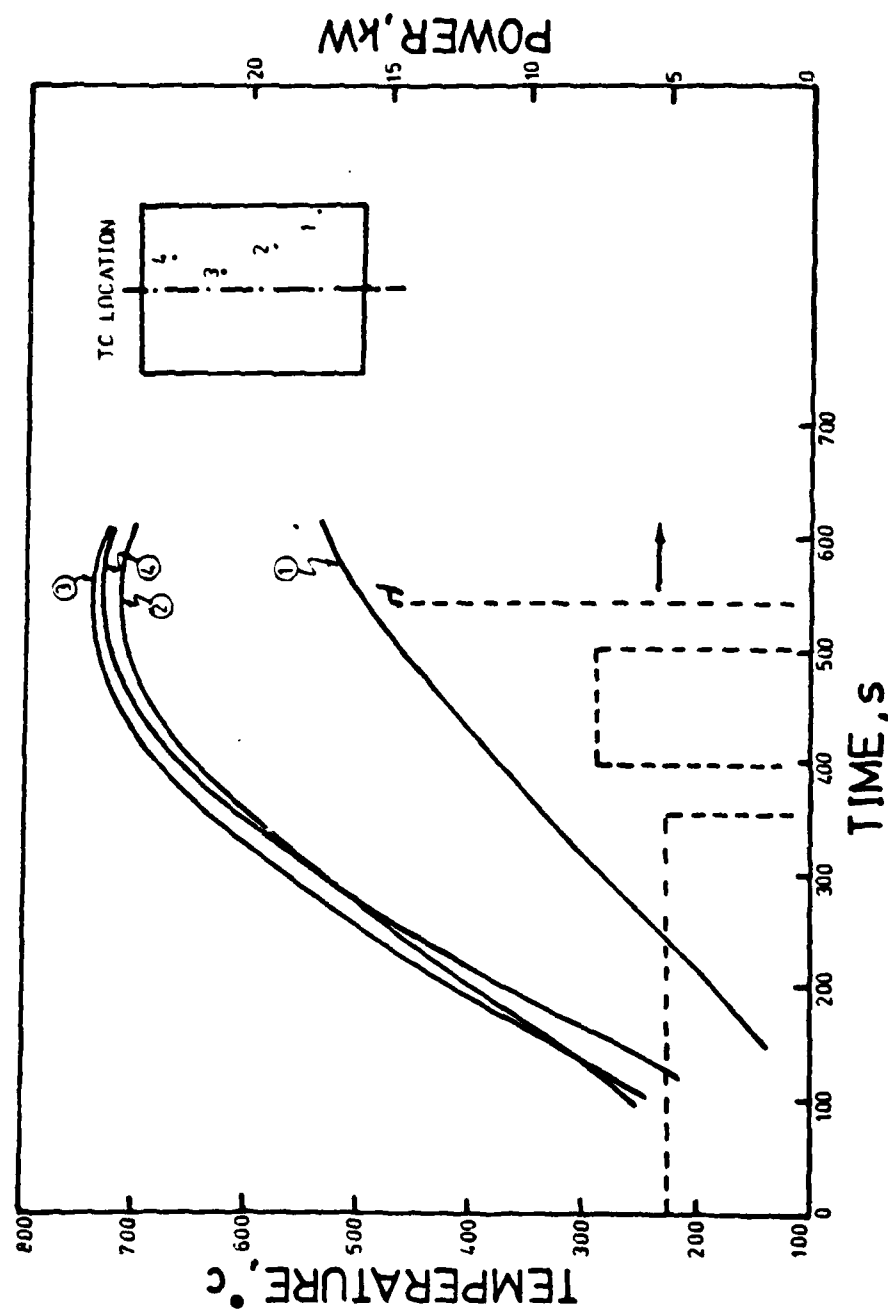


Figure A.9. Thermal-power history for heavily oxidized S200 powder.

couples to the induction flux. At high power levels, using a manual induction unit, heating times of 300 seconds were observed. The heating times for the different runs are given in Table A.VII.

v. Heating Efficiency

The heating efficiency for the experimental runs is given in Table A.VII. Small size particles S100 ($d_p = .216$ mm) could be heated from the coupling temperature to process temperatures at efficiencies of 10 to 15 percent. Larger size particles, S212 ($d_p = 1.85$ mm) could be heated from room temperature to process temperature at efficiencies of 6 to 7 percent.

vi. Reheating of the Packed Bed

After heating the packed bed to process temperature and then cooling it to room temperature, it could be reheated to SD casting temperatures in about 300 seconds. In this case, no incubation period was observed. Figure A.10 shows the temperature-time history for packed bed reheating in Run #5.

vii. Packed Bed After Heating

The particles in the packed bed had sintered together when SD casting temperatures were attained. The packed bed had oxidized in certain areas. In most runs, longitudinal

Table A.VII- Economic variables for IH runs

Run#	t_H s	r_H %
1	-	20.4
2	-	-
3	-	5.2
4	-	19.6
5	300	7.8
6	-	-
7	800	6.5
8	1000	13.9
9	-	-
10	-	-
11	-	-
12	-	-
13	750	13.2
14	300	16.2
15	-	-
16	-	-
17	1400	6.0
18	1100	7.2

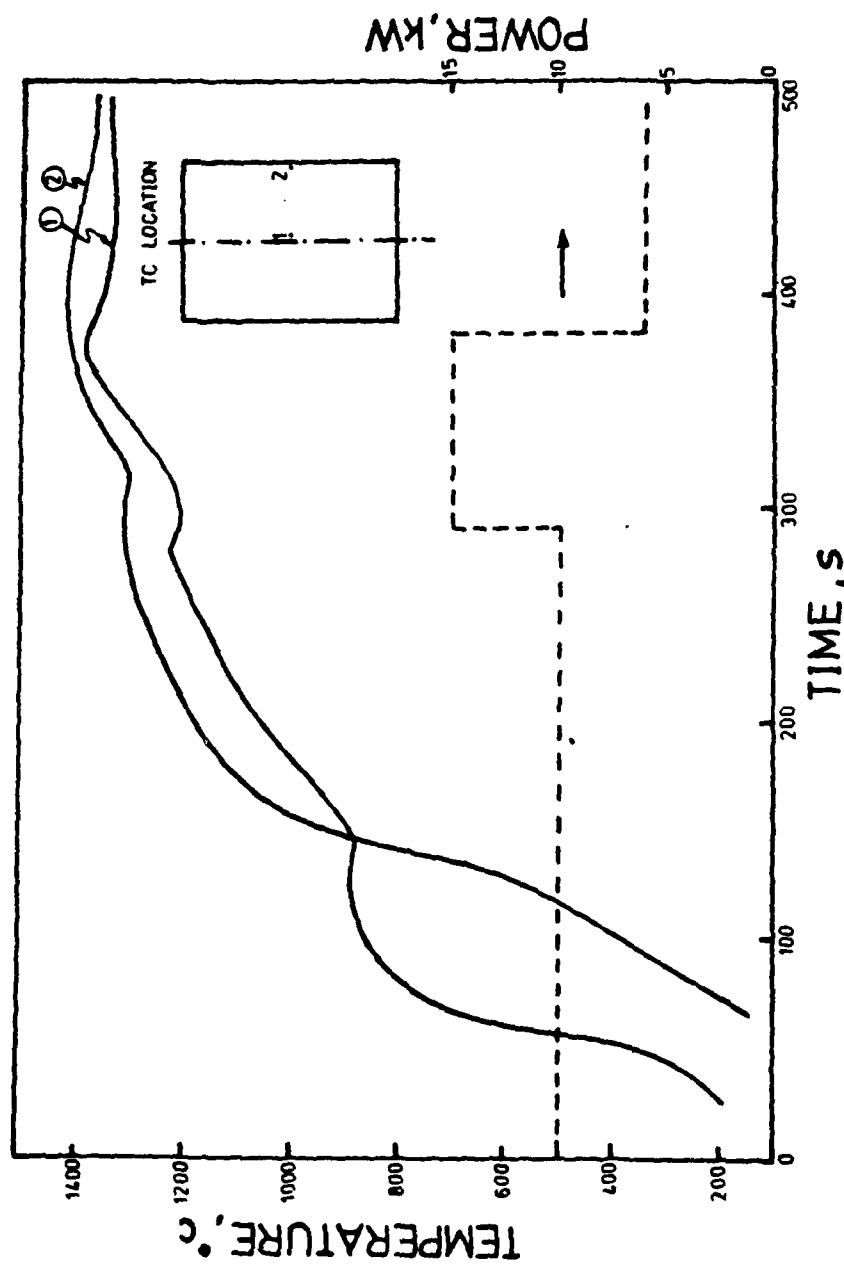


Figure A.10. Thermal-power history for S100 powder reheated after attaining SD casting temperatures.

cracks propagating radially and radial shrinkage at the center of the packed bed was observed. Figure A.11 shows the packed bed after heating for Run #10. At high power inputs, the cracking phenomena could be avoided. Figure A.12 shows the packed bed after heating for Run #5. In this case, no cracks were observed. The cracking mechanism during induction heating of particles in a bed is discussed in Appendix 2D.

viii. Preferential Coupling

The aim of Run #15 was to determine if the cracks observed could be avoided by placing a weight on top of the packed bed. The weight was in the form of a thin carbon steel disc above which ceramic blocks were placed. A number of slots were cut in the disc to reduce its tendency to couple to the induction flux.

It was found that nearly all the power supplied was dissipated in the steel disc, resulting in melting of the disc and top portion of the packed bed. The packed bed remained relatively inert to the induction flux, even above the coupling temperature. The packed bed was heated by transport of heat from the disc. Figure A.13 shows the temperature-time history for Run #15.

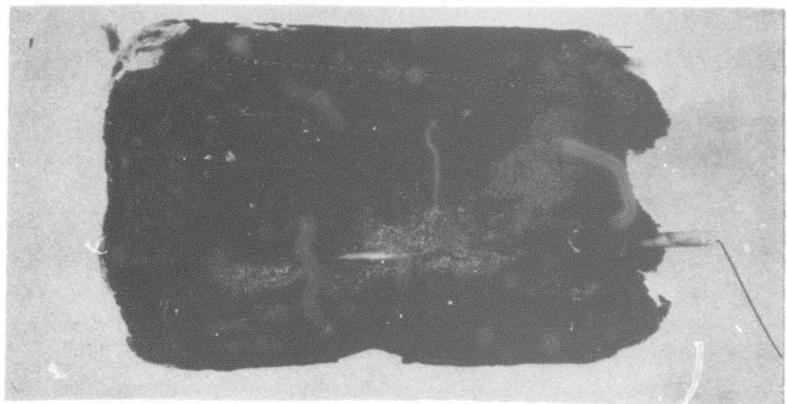


Figure A.11. Packed bed after heating for run# 10.



Figure A.12. Packed bed after heating for run# 5.

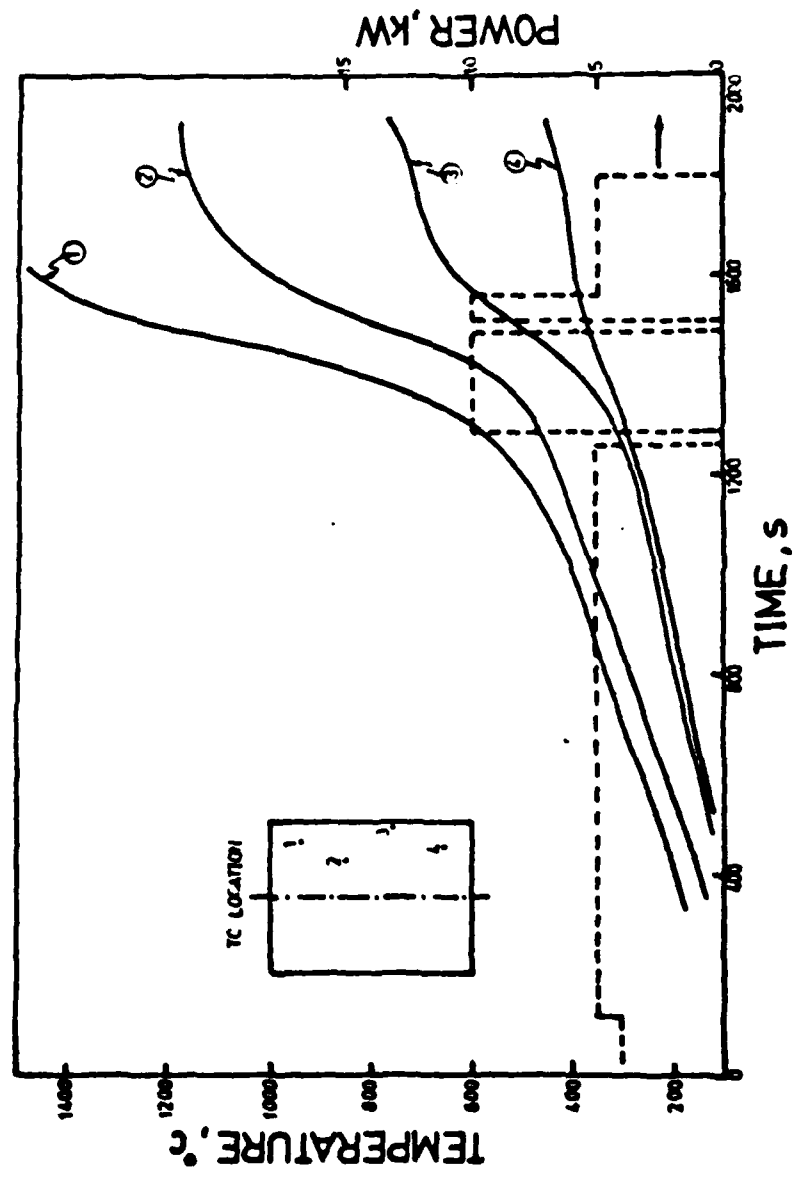


Figure A.13. Thermal-power history for run #15 showing the effect of a metallic conductor placed on top of the bed.

ix. Suppression of Induction Flux

In run #16, a weight inert to the induction flux was placed on top of the bed. The weight considerably retarded the induction heating characteristics of the packed bed. Even at power inputs of 10 kW, the maximum temperature attained in the packed bed was only 780°C . On removal of a part of the weight the packed bed temperature could be raised to 1200°C . Figure A.14 gives the temperature-time results from Run #16.

x. Simultaneous Heating of Melt Charge and Shot

Setup shown in Fig. A.4 was used for simultaneous heating of melt charge and shot. In Run #19, the coil concentration was higher around the shot region. The result was that the shot melted before the melt charge attained the desired melt temperature. In Run #20, the coil concentration was decreased around the shot region. However, the result of IH indicated that the flux preferentially coupled to the shot region, melting the shot.

4. Discussion

During IH (Induction Heating) of low carbon steel particles the heat is generated in the bed by electrical resistance and magnetic hysteresis losses. The resistance losses result from the induced currents in the load. The hysteresis losses result from the influence of an alternating magnetic field on the load. Above the Curie

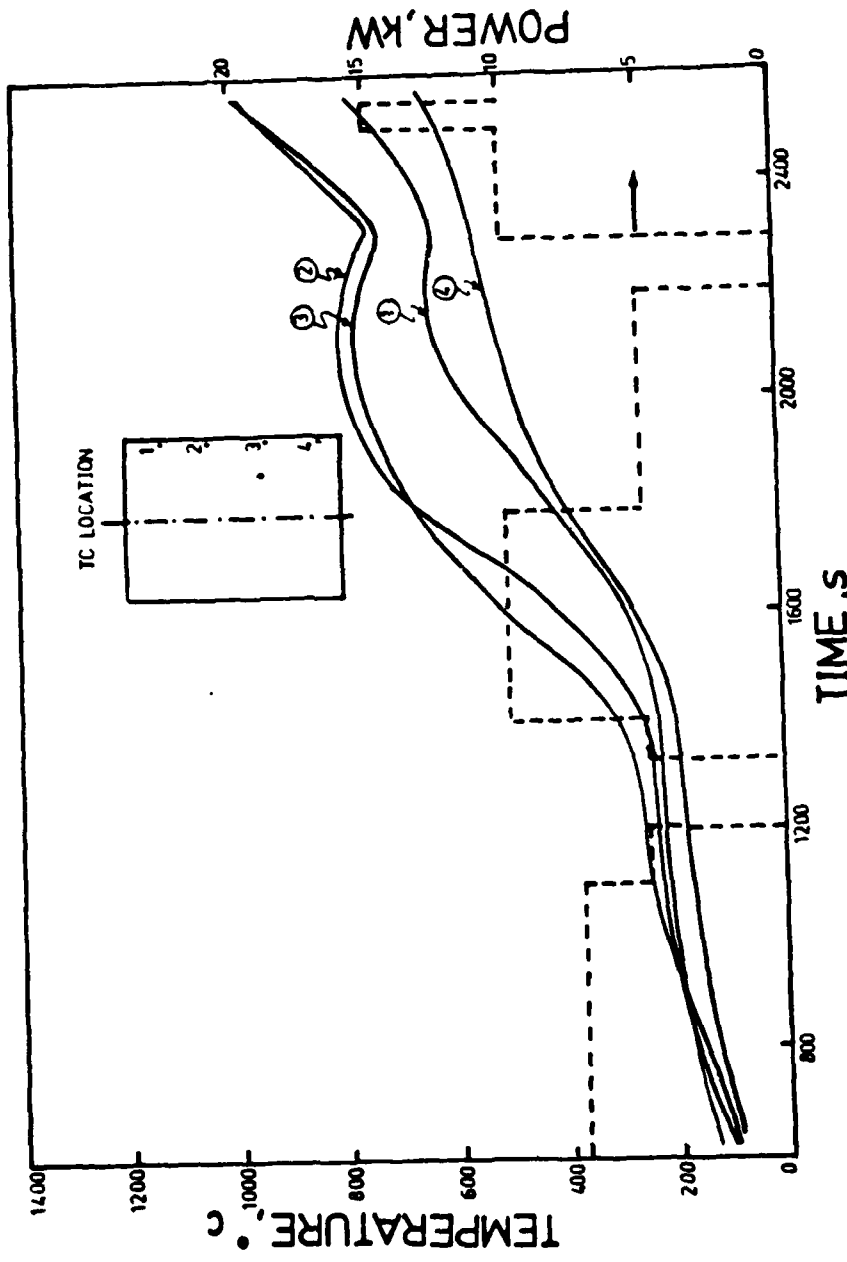


Figure A.14. Thermal-power history for run #16 showing the effect of an inert weight placed on top of the bed.

temperature (771°C for iron) the hysteresis phenomenon within individual particles is absent and the packed bed can be heated only by resistance losses between particles.

The incubation period encountered during the IH of particles is attributed to the high packed bed resistivity. The adsorbed gases on the particles account for the non conducting nature of the packed bed at low temperatures. A non conducting charge can be heated only by hysteresis losses since they involve motion of magnetic domains within the isolated particles. Once the gases were desorbed, the resistivity is controlled by the oxide surface layer on the particles. If the oxide surface layer is small as in the case of S100 shot, the packed bed begins to conduct electricity at about 400°C . Heavily oxidized powder, S200, ($d_p = 1.85 \text{ mm}$) causes the packed bed to remain non conducting even at the Curie temperature. During the incubation period the packed bed is non conducting and can be heated only by hysteresis losses within each individual particle. The incubation period can be prolonged by placing an inert (ceramic) weight on top of the bed. The weight restrains electrical contact of the particles in the direction of the electrical field permitting heat generation in bed only by hysteresis losses upto the Curie temperature. A metallic conductor whose size is large compared to the individual particles is preferentially coupled by the induction flux. The lower resistivity of the conductor permits large I^2R resistance losses in it compared to the packed bed.

At audio frequency IH, the high packed bed resistivity, (0.001 ohm .m), accounts for the depth of penetration being greater than the radius of the charge, resulting in uniform heating of the packed bed in the radial direction. At radio frequencies, the depth of penetration is less than the radius of the bed. The interior of the packed bed is heated by conduction and radiation from the zone where heat is generated by resistance losses.

Simultaneous heating of melt charge and shot of the same size and shape resulted in preferential coupling of the shot.

LIST OF NOTATIONS

- d_c - coil diameter (tubing)
 d_s - coil diameter (solenoid)
 d_{PB} - diameter of packed bed
 g - distance between coil and charge
 l_{PB} - height of packed bed
 l_s - length of coil
 N - number of coil turns
 P_t - total power input from induction unit
 P_w - power utilized in heating charge
 S - spacing between coil turns
 t_{IP} - incubation period
 t_H - heating time
 T_{CT} - coupling temperature
 T_{MAX} - maximum temperature attained in the packed bed
 T_L - maximum longitudinal temperature gradients in bed
 T_R - maximum radial temperature gradients
 η_{IP} - IH efficiency during incubation period
 η_H - IH efficiency after packed bed couples to the
induction flux
 η - efficiency = $(P_w/P_t) \times 100$

APPENDIX 2B

ROOM TEMPERATURE RESISTIVITY OF POWDER

1. Apparatus

The set up for measuring room-temperature resistivity is shown in Fig. B.1. The particles are contained in a glass tube. Electrical contact is made with the packed bed using a brass plate and copper rod. The contacts are connected to a solid-state, Keithley Electrometer.

Resistance in the range of 0 to 10^{18} ohms can be accurately measured using this electrometer.

2. Experimental Procedure

The particles were poured into the glass tube. The tube was tapped a few times to maximize the packing of the particles in the bed. A copper rod was inserted into the tube and allowed to make electrical contact with the particles at the top of the bed. The resistance between the electrical contacts was recorded from the electrometer and the packed bed height was measured. The experiment was repeated for different packed bed heights.

3. Theoretical Considerations of Packed Bed Resistivity

The packed bed refers to the packing of spherical particles in a container. A single size of spherical

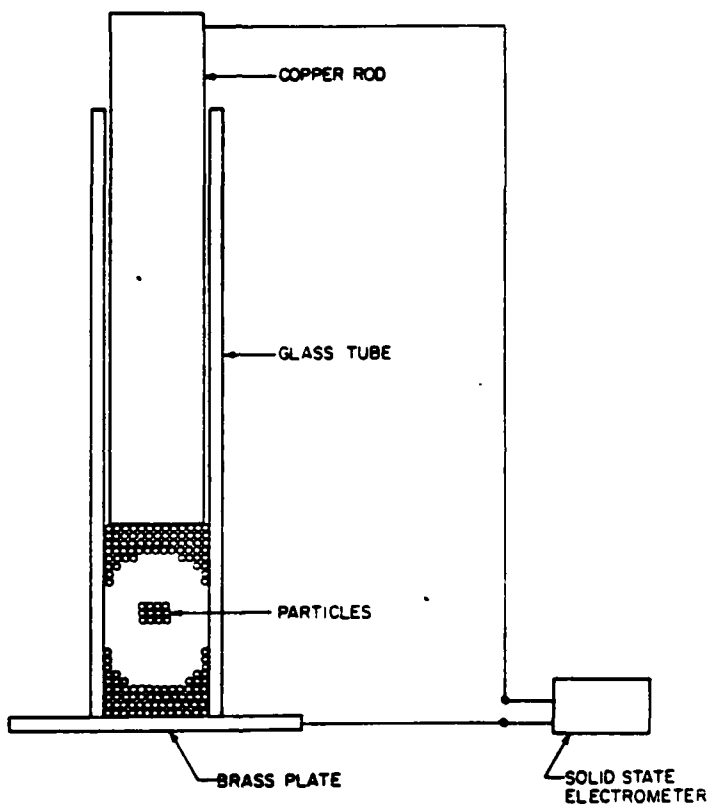


Figure B.1. Room temperature resistivity apparatus.

particles can be assumed to have an orthohombic packing in such a bed.

Consider a packed bed of diameter, d_{PB} , and height, h_{PB} . The resistance of the bed can be assumed to be the sum of parallel resistances. Each parallel resistance is a function of the number of particles (of diameter d_p) that can be contained in a length equivalent to h_{PB} , and the particle resistance, r_p .

The particle resistance at room temperature is given by:

$$r_p = r_m + 2(r_o + r_G) \quad (B.1)$$

where:

r_m - metallic resistance

r_o - oxide layer resistance

r_G - adsorbed gas layer resistance

A single parallel resistance is the sum of individual particle resistance in the packed bed height and is given by:

$$R_p = n_p r_p = 2 \frac{h_{PB}}{d_p} (r_o + r_G) \quad (B.2)$$

where n_p is equal to the number of particles in a height, h_{PB} .

The number of parallel resistances (n) is given by the

product of packed bed area and the surface density of the packing. It can be calculated using Eq. (B.3)

$$n = 0.453 \frac{d_{PB}}{d_p}^2 \quad (B.3)$$

The packed bed resistance, R_T , is the parallel sum of resistance of value R_p and is given by:

$$R_T = 4.4 \frac{h_{PB} d_p (r_o + r_g)}{d_{PB}^2} \quad (B.4)$$

The resistivity of the packed bed is given by:

$$\rho_{PB} = 3.4 d_p (r_o + r_g) \quad (B.5)$$

Equation B.5 predicts that the packed bed resistivity is a constant. The experimental results do not agree with this simple theoretical approach. The theory assumes that the particles do not contact each other in the radial direction. The resistance of the packed bed is not just the sum of parallel resistances but an interwoven complex of series and parallel resistances. The theory also assumes that the packing is orthohombic along the entire height of the packed bed. Packing irregularities do exist.

Experimental results indicate that the resistivity of the packed bed is a strong function of the packed bed height and can be expressed by the relationship given by:

$$\rho_{PB} = \rho_o h_{PB}^n \quad (B.6)$$

where ρ_o and n are constants.

Neglecting the contact resistance of the electrodes the measured resistance can be expressed in terms of h_{PB} using Eq. (B.6).

$$R_T = R_{PB} = \frac{\rho_o}{A_{PB}} h_{PB}^{n+1} \quad (B.7)$$

where, A_{PB} is the area of the packed bed. The constants ρ_o and n can be evaluated from the intercept and slopes of log-log plots of R_T vs. h_{PB} .

4. Contact Resistance

The contact resistance was estimated by placing a 20 mm long copper rod between the electrical contacts. The resistance was in the range of 1 to 2 ohms and could be considered negligible compared to the resistance of the packed bed.

5. Contact Pressure

The contact pressure is the pressure exerted by the

electrical contacts while measuring the resistance of the bed. The contact pressure for all the experimental runs was 66,200 Pa.

6. Results

The data R_T vs. h_{PB} are plotted in Fig. B.2 and Fig B.3 for the different powders. The constants ρ_0 and n for different shot are given in Table (B.1)

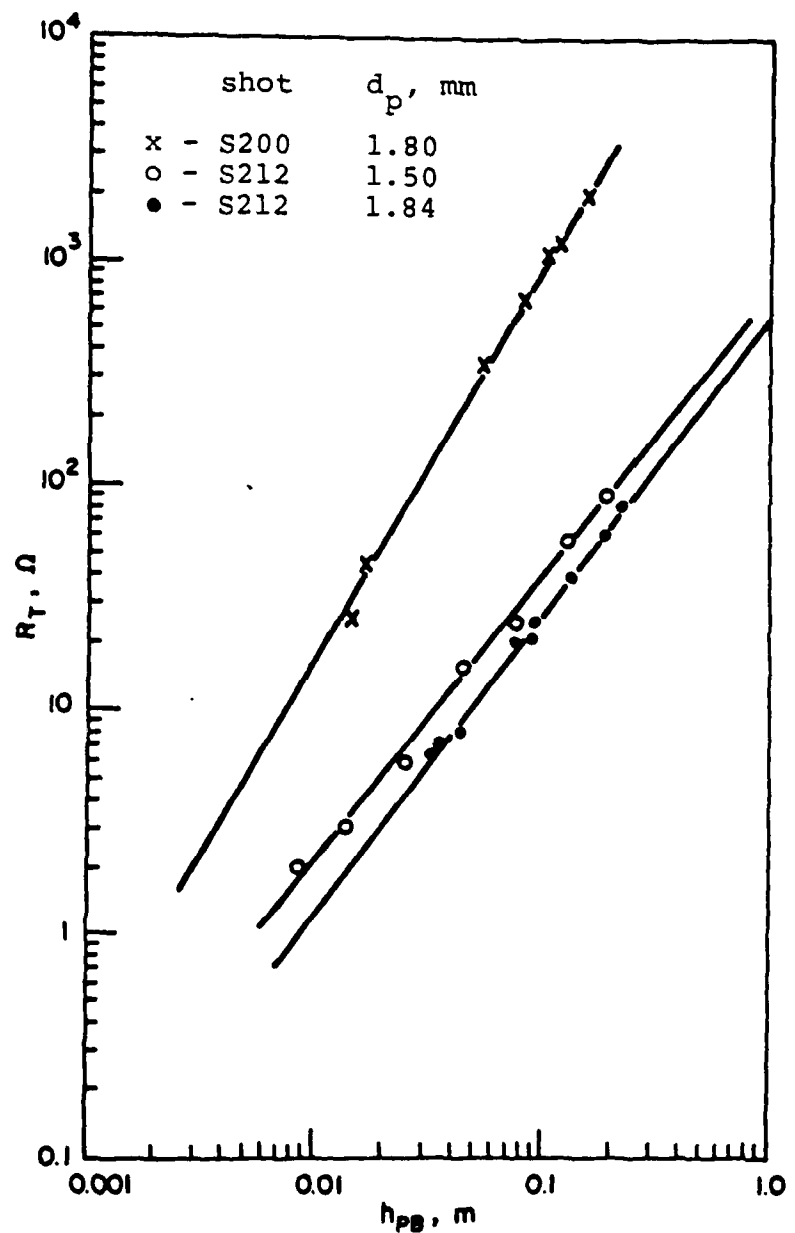


Figure B.2. Resistance of S200 ($d_p = 1.8$ mm), S212 ($d_p = 1.5$ mm) and S212 ($d_p = 1.84$ mm) as a function of packed bed height.

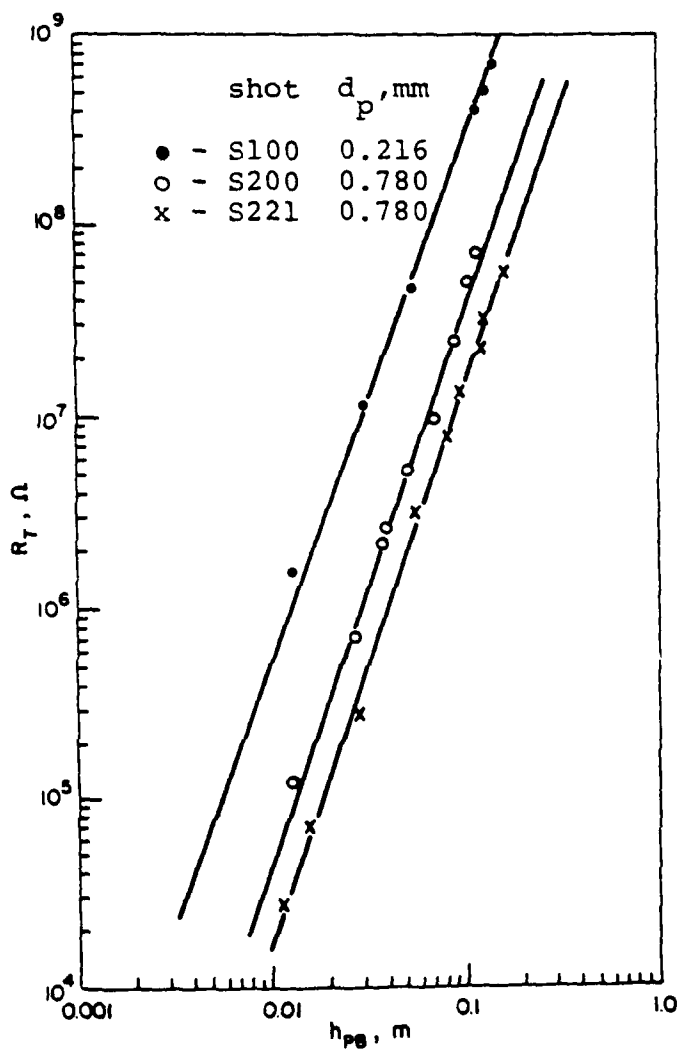


Figure B.3. Resistance of S100, S200 and S221 powder as a function of bed height.

Table B.1. Room temperature resistivity constants for different shot.

Shot	d_p mm	ρ_o^*	n
S100	0.216	3.9×10^6	1.90
S200	0.780	2.3×10^6	2.00
S212	1.85	9.5	0.80
S200	1.85	1.5×10^{-7}	1.67
S212	1.50	9.7×10^{-2}	0.25
S212	1.85	6.7×10^{-2}	0.30

* The values of constants give the resistivity in $\Omega \cdot m$ for the packed bed height in meters (Refer Eq. (B.6)).

APPENDIX 26

ELECTRICAL RESISTIVITY OF SHOT AS A FUNCTION OF TEMPERATURE

1. Apparatus

The set up for measuring resistivity of shot as a function of temperature in an argon atmosphere is shown in Fig. C.1. The set up used for measuring resistivity of shot as a function of temperature in vacuum is shown in Fig. F.9, Appendix 5F (Chapter 5).

2. Experimental Procedure

The resistivity of shot in a packed bed was measured using a four point technique. The electrical analog of the resistivity set up is shown in Fig. C.2. The current through the circuit is given by:

$$I = V_{RB}/R_{RB} \quad (C.1)$$

where V_{PB} is the voltage drop across the external resistance, R_{PB} is the external resistance and I is the current through the packed bed.

The resistivity of the packed bed is given by:

$$\rho_{PB} = \frac{V_{PB} A_{PB}}{I L_{PB}} \quad (C.2)$$

LEGEND

1. induction coils
2. alumina crucible
3. fiberfrax
4. graphoil gasket
5. current leads
6. voltage leads
7. shot
8. alumina tube

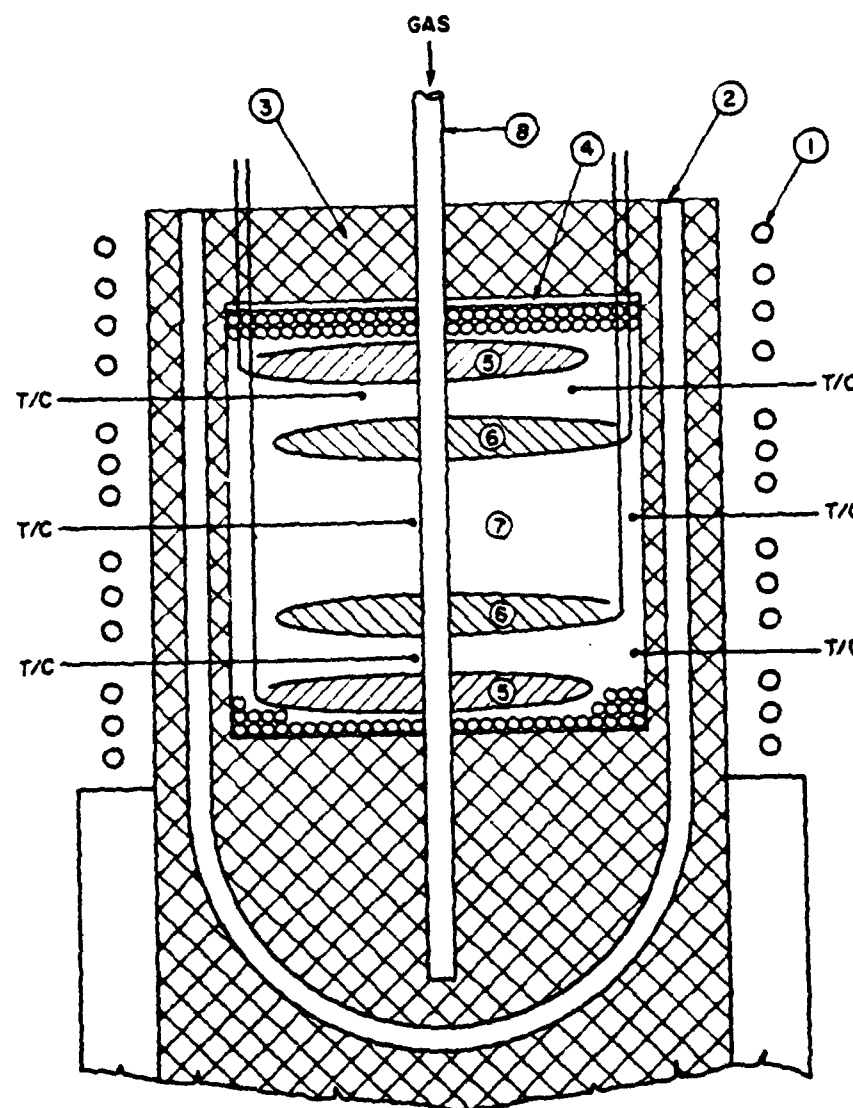


Figure C.1. Induction heating and resistivity measurement setup with radial insertion of thermocouples.

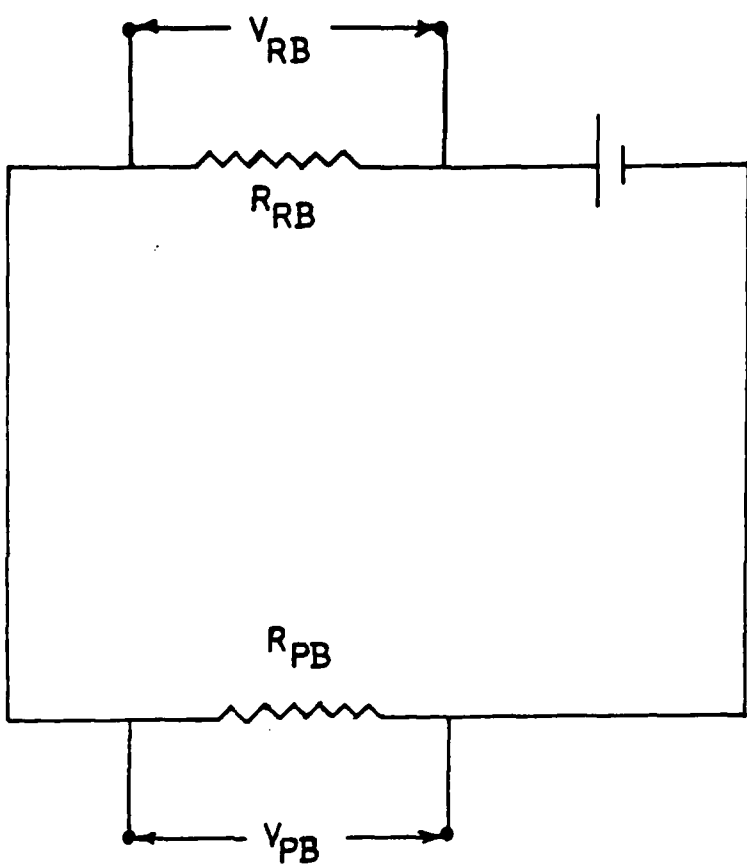


Figure C.2. Electrical analog used for measuring resistivity.

where ρ_{PB} is the packed bed resistivity, V_{PB} is the voltage drop across the packed bed, A_{PB} is the cross-sectional area of the packed bed and L_{PB} is the height of packed bed.

For the experiments where the resistivity was measured in vacuum, the packed bed diameter was 6.35 mm., and the height was 100 mm. The resistivity of unbonded particles was measured upto 1400°C . The packed bed was then allowed to cool to room temperature in the furnace. The resistivity of the sintered or bonded shot was then measured as a function of temperature.

3. Results

The resistivity for unbonded shot in argon was measured in IH runs# 7 and #10, Appendix 2A. The results are summarized in Table C-I and plotted in Fig. C.3. The resistivity data for unbonded shot in vacuum is given in Tables C-II, C-III and C-IV and plotted in Fig. C.4*. The resistivity data for bonded shot in vacuum is given in Tables C-V , C-VI and C-VII and plotted in Fig. C.5*.

4. Discussion.

The resistivity of unbonded shot is very strongly

* Values of resistivity from 100°C to 1300°C at 100°C intervals were interpolated. The value of resistivity at 1400°C was extrapolated.

Table C-I. - Resistivity data as a function of temperature
in argon for unbonded S100 shot ($d_p = .216$ mm)

T °C	$\rho \times 10^2$ Ω·m
36	739.000
48	660.000
48	79.300
72	44.900
106	6.060
118	4.020
122	3.330
130	2.910
136	2.430
144	2.130
146	1.900
152	1.740
163	1.440
163	.133
167	.123
172	.112
197	.782
206	.667
220	.560
239	.502
263	.423
269	.396
279	.357
284	.330
303	.291
324	.254
337	.211
349	.185
367	.158
390	.132
426	.125
554	.135
706	.179
775	.134
809	.142
885	.146
982	.143
1076	.116
1159	.108
1432	.081

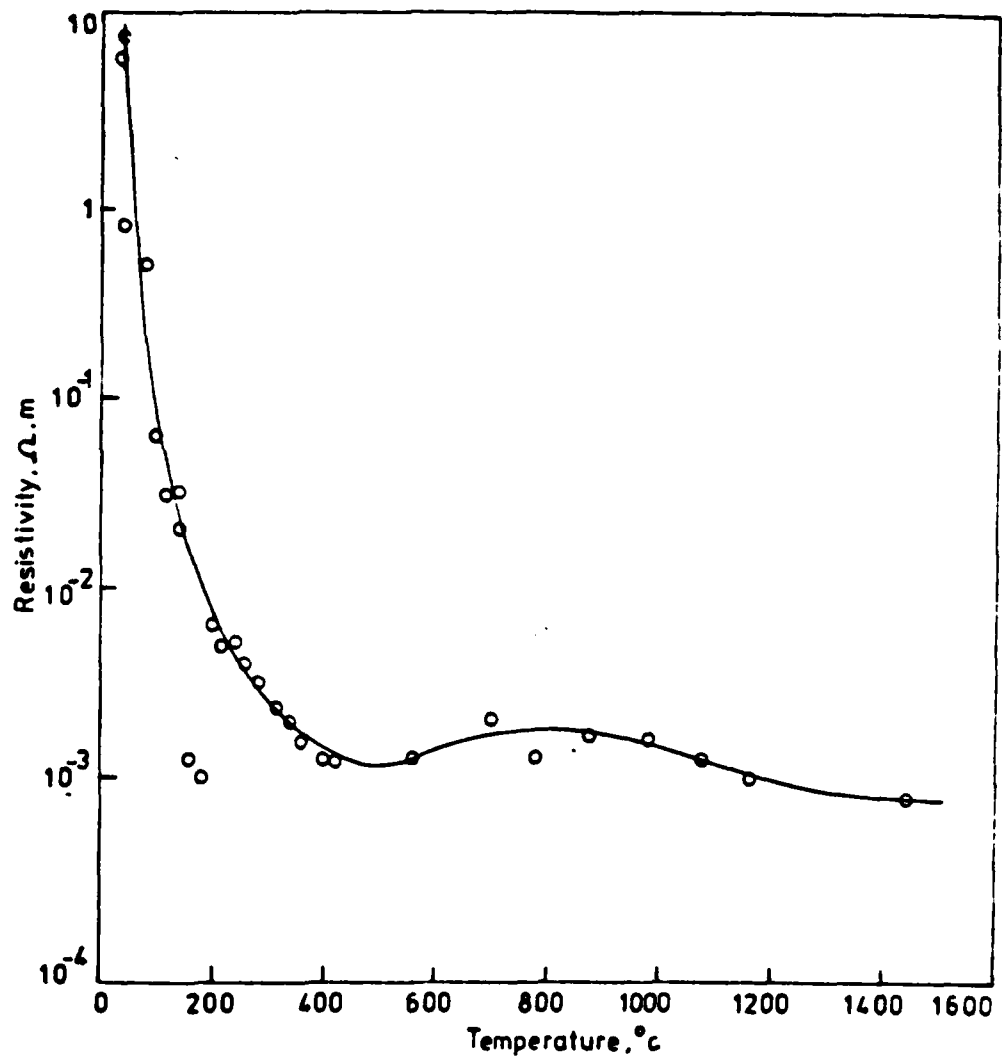


Figure C.3. Resistivity as a function of temperature for unbonded S100 shot; $d_p = 0.216$ mm, atmosphere - argon.

Table G-II - Resistivity data as a function of temperature in vacuum for unbonded
S100 shot; $d_p = 0.275$ mm.

T °C	R _{PB}	V _{PB} mV	V _{PB} mV	ρ $\Omega \cdot m$
25	150	.20	1960.00	475.099856250
80	150	3.30	3880.00	55.860225523
140	150	126.00	3620.00	1.364969428
190	150	2000.00	816.00	.019384074
230	150	2476.00	160.00	.003070112
310	150	2512.00	8.24	.000155845
420	150	2512.00	2.24	.000042366
520	150	3560.00	1.96	.000026157
610	150	3560.00	.86	.000011424
680	150	3560.00	.68	.000009075
740	50	2680.00	1.56	.000009218
790	50	2680.00	1.72	.000010164
840	50	2680.00	1.88	.000011109
890	50	2680.00	2.00	.000011818
930	50	2680.00	1.90	.000011227
975	50	2680.00	1.74	.000010282
1020	50	2680.00	1.76	.000010400
1150	50	2680.00	1.63	.000009644
1285	30	2432.00	2.10	.000008205
1380	30	2560.00	1.90	.000007045
1385	30	2560.00	1.84	.000006830

Table G-III - Resistivity data as a function of temperature in vacuum for unbonded
S221 shot; $d_p = .78$ mm.

$T_{^{\circ}C}$	R _{RB}	V _{RB} mv	V _{PB} mv	ρ $\Omega \cdot m$
45	10000	4080.00	2200.00	1.707875300
80	10000	6020.00	156.00	.082077052
170	10000	6220.00	19.00	.009675131
225	10000	5432.00	4.32	.002518939
350	1000	3840.00	.80	.000065986
440	100	3700.00	3.76	.000032187
545	100	3720.00	2.50	.000021286
625	10	1760.00	8.00	.000014397
675	10	1840.00	7.20	.000012394
735	10	1800.00	6.80	.000011965
780	10	1840.00	7.40	.000012738
825	10	1840.00	7.84	.000013496
870	10	1772.00	7.72	.000013799
915	10	1772.00	7.72	.000013799
930	10	1800.00	8.00	.000014077
1010	10	1720.00	7.20	.000013259
1075	10	1800.00	7.08	.000012458
1135	10	1726.00	6.00	.000011049
1195	10	1720.00	5.88	.000010828
1240	10	1700.00	5.68	.000010583
1284	10	1720.00	5.44	.000010018
1320	10	1660.00	5.20	.000009922

Table C-IV - Resistivity data as a function of temperature in vacuum for unbonded

S226 shot; $d_p = 1.85$ mm.

T	R_{PB}	V_{RB}	V_{PB}	ρ
$^{\circ}C$		mV	mV	$\Omega \cdot m$
60	10000	5728.00	428.00	.236665198
135	10000	6108.00	52.20	.026550003
330	100	3940.00	48.00	.000385868
545	100	3900.00	5.48	.00044505
685	100	3600.00	2.06	.000018124
795	10	2600.00	12.20	.000014862
895	10	2320.00	11.81	.000016123
975	10	2080.00	11.52	.000017542
1050	10	2200.00	11.36	.000016355
1115	10	2120.00	9.60	.000014343
1170	10	2000.00	8.48	.000013429
1220	10	1840.00	7.08	.000012187
1270	10	1900.00	6.72	.000011202
1315	10	1760.00	6.20	.000011158
1345	10	1880.00	6.28	.000010580

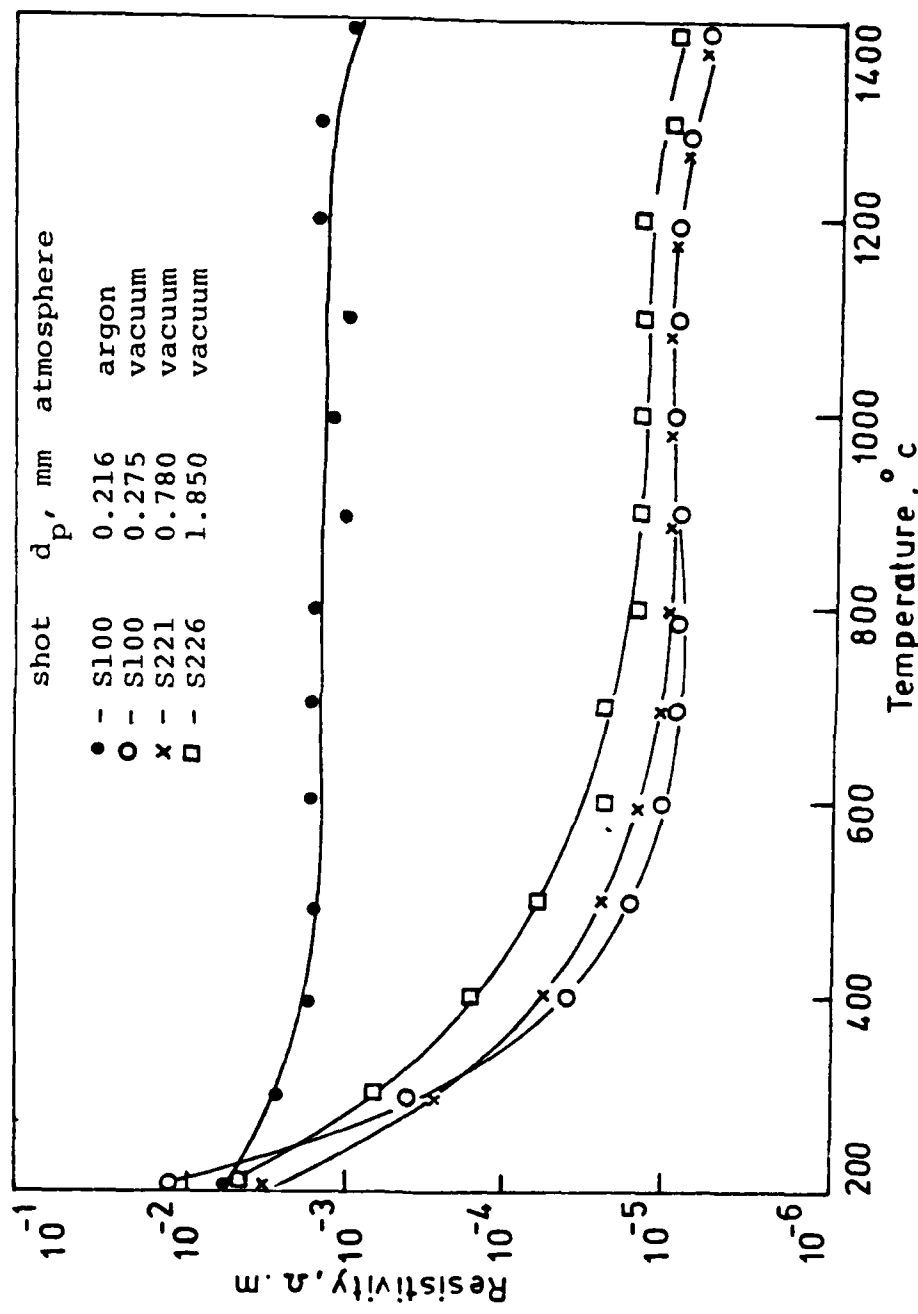


Figure C.4. Resistivity of unbonded shot as a function of temperature

Table C-V - Resistivity data as a function of temperature in vacuum for bonded
S100 shot; $d_p = .175$ mm.

T_{oc}	R_{RB}	V_{RB} mV	V_{PB} mV	ρ $\Omega \cdot m$
20	1	432.00	1.36	.000000997
83	1	432.00	2.54	.000001862
170	1	432.00	3.25	.000002383
265	1	432.00	3.73	.000002735
435	1	420.00	4.92	.000003710
775	1	408.00	7.24	.000005620
1035	1	400.00	7.80	.000006176
1195	1	380.00	7.68	.000006401
1320	1	380.00	7.20	.000006001

Table C-VI - Resistivity data as a function of temperature in vacuum for bonded
S221 shot; $d_p = 0.78$ mm.

T	σ_c	R _{RB}	V _{RB} mV	V _{PB} mV	ρ $\Omega \cdot m$
20		1	440.00	1.76	.000001267
100		1	440.00	2.28	.000001641
250		1	440.00	3.60	.000002591
335		1	424.00	4.84	.000003616
400		1	440.00	5.20	.000003743
435		1	440.00	5.68	.000004089
580		1	412.00	6.68	.000005235
720		1	412.00	8.20	.000006304
830		1	392.00	9.12	.000007369
930		1	385.00	9.20	.000007569
1030		1	376.00	9.20	.000007750
1105		1	380.00	9.40	.000007835
1170		1	360.00	9.00	.000007918
1220		1	328.00	8.21	.000007928
1270		1	320.00	8.08	.000007998
1320		1	388.00	9.76	.000007967

Table C-VII - Resistivity data as a function of temperature in vacuum for bonded

S226 shot; $d_p = 1.85$ mm.

T $^{\circ}\text{C}$	R_{RB}	V_{RB} mV	V_{PB} mV	ρ $\Omega \cdot \text{m}$
20	10	1800.00	1.60	.000002815
80	10	1816.00	2.32	.00004046
300	10	1776.00	2.92	.00005208
545	10	1736.00	3.88	.00007079
700	10	1704.00	4.92	.00009145
810	10	1680.00	5.92	.00011161
910	10	1632.00	6.16	.00011955
980	10	1624.00	6.24	.00012170
1070	10	1648.00	6.40	.00012300
1135	10	1656.00	6.60	.00012623
1195	10	1656.00	6.64	.00012700
1245	10	1650.00	6.64	.00012746
1295	10	1664.00	6.72	.00012791
1330	10	1648.00	6.60	.00012685

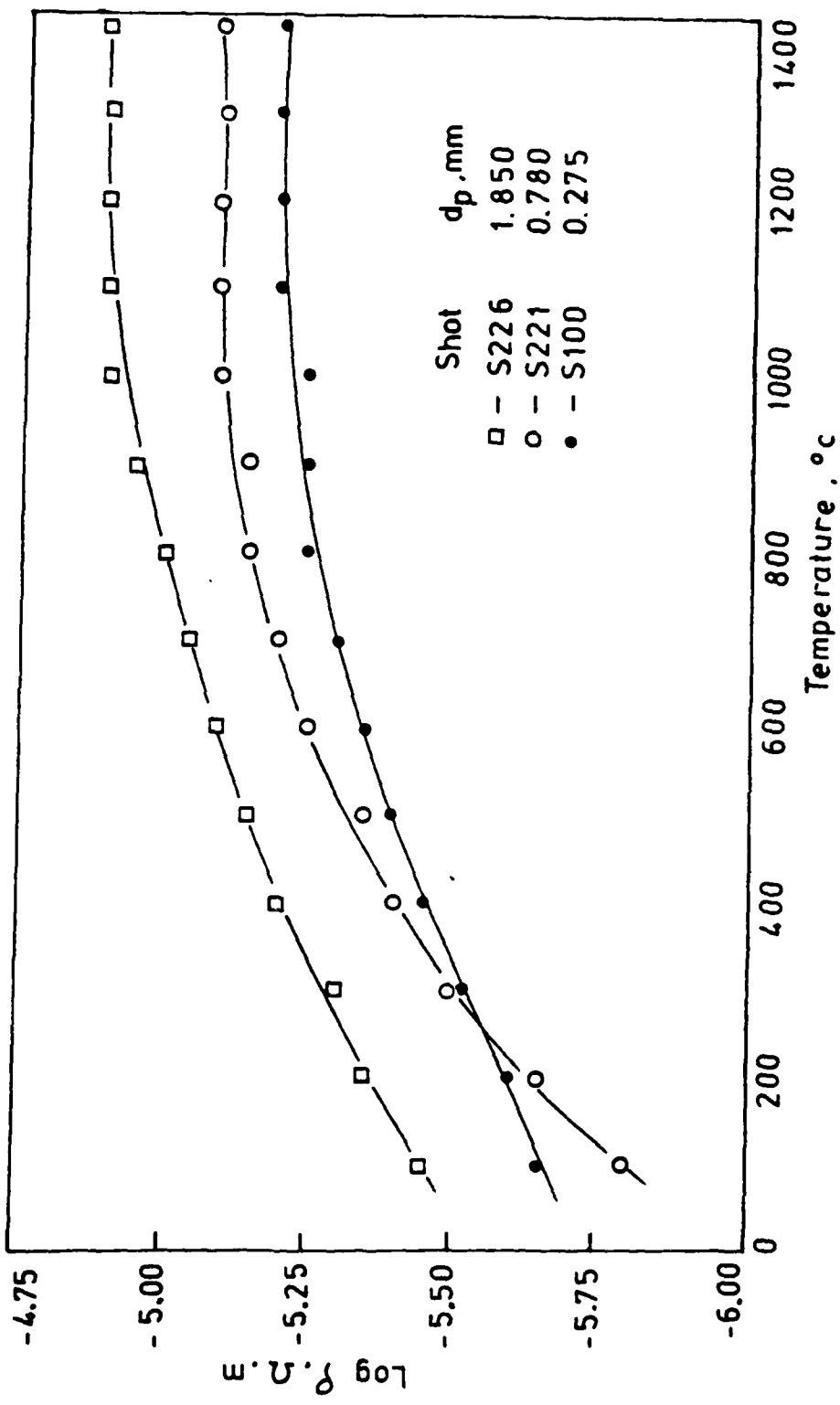


Figure C.5. Resistivity of bonded shot as a function of temperature.

dependent on temperature up to 300°C . Above 400°C , the resistivity saturates as shown in Fig. C.4. At higher temperatures, (above 1200°C .), there is a gradual drop in resistivity. The resistivity of unbonded shot measured in argon and vacuum differed by two orders of magnitude. The difference may be due either to oxidation of the particles during heating, or an adsorbed gas layer on the surface of the particles.

Once the particles are bonded, they behave just like metals and the resistivity increases with temperature as shown in Fig. C.5. However, for temperatures above 1000°C , the resistivity reaches a saturated value.

APPENDIX 2D

CRACKING PHENOMENA IN INDUCTION-HEATED PACKED BED

The cracks observed on heating the packed bed of low carbon steel shot to process temperatures of 1400°C have longitudinal orientation and penetrate in the radial direction. In most cases, the cracks were restricted to the central part of the packed bed where radial shrinkage was observed. However, in some cases, the longitudinal cracks extended beyond the shrinkage zone and were connected by tangential cracks.

Electro-magnetic forces act on the individual particles in the bed during induction heating. The force is in the axial direction and its magnitude is directly proportional to the induced current in the charge. The current density is maximum at the surface of the charge, and so the force acting on the particles is maximum along the outer circumference of the bed. Below sintering temperatures, the packed bed contains particles that are not bonded together, so the force resulting from the induced current raises the particles above the packed bed. The particles should slide back to the original packed bed geometry on removing the input power to the charge. However, while heating the particles to process temperatures the particles begin to sinter together at temperatures greater than 1000°C .

The sintering of particles results in their occupying the same position they did in the force field. This is responsible for the formation of ridges observed at the top of the bed. Ridge formation was also observed at the bottom of the packed bed, but the effect was very small as the particles at the bottom were in contact with a rigid mold surface (compressed fiberfrax).

The ridge formation resulted in poorer packing in the original packed bed geometry. To accomodate for this depletion the original packed bed geometry must change. The change is brought about by a shrinkage in the midsection of the packed bed.

If the ridge formation is severe, i.e., more particles have been raised above the packed bed, then the shrinkage is much more at the midsection of the packed bed to accomodate the depletion of the particles in the bed. There is a limit to the amount of cylindrical shrinkage permissible at the midsection of the bed, as the maximum shrinkage depth is at the point where the gravitational force balances the induction force. In such cases the depletion of particles due to ridge formation is accomodated in the packed bed by the formation of cracks oriented in the direction of the external induction force.

In two of the heating runs, numbers 5 and 18 (Appendix 2A), no cracks or shrinkage were observed. In these runs, the particles were heated rapidly using high

power inputs. It was difficult to maintain high power levels to a charge whose load coupling characteristics are very sensitive to temperature. The induction unit had manual controls and so the power to the charge had to be frequently shut off to balance the load by adjusting the voltage and capacitor controls.

Consider two situations during the heating of the particles in the bed at high power inputs. The packed bed temperature is below the sintering temperature and the power to the charge is shut off. In this case the particles will fall back and regain their original mold geometry. However, if the particles are rapidly heated to sintering temperatures and the power to the charge is shut off, then the particles should slide back to the original mold geometry. At this stage, if sufficient time is given for the particles to sinter together before reapplying power, then the particles are no longer loosely held. On reapplying power the induction force acts on the bed rather than the individual particles. In such cases no ridge formation, cracks or shrinkage are observed in the packed bed. The results of runs number 5 and 18 (Appendix 2A) substantiate the above explanation.

An alternative mechanism for the cracking phenomena can be attributed to non-uniform sintering of particles in the bed. Longitudinal temperature gradients were observed

in the packed bed during heating. The top and bottom parts of the bed were at a lower temperature than the middle part of the bed. At high temperatures this non-uniform temperature distribution in the bed results in the particles sintering at a faster rate in the middle part of the bed. The enhanced sintering rate at the center could be responsible for crack nucleation due to shrinkage resulting from sintering of the particles.

Once the cracks are formed then there is a much higher resistance across the cracks than at the crack tips. This reduces the amount of heat dissipated at the sides of the cracks and so the particles located in this zone are heated much less than the particles located at the tips of the crack. The particles at the crack tips sinter to a greater extent and the shrinkage resulting from sintering leads to the propagation of the crack.

One method of preventing cracks is to stop heating after rapidly attaining temperatures of 1000°C to 1200°C to permit the particles to sinter together for about 100 seconds. The sintered bed can then be raised to process temperatures.

Another suggested method was to place a weight on top of the packed bed as was done in run numbers 15 and 16 (Appendix 2A). However, the weight reduces the induced current density in the charge by inhibiting electrical

continuity between the particles in the circumferential direction (the direction of maximum electrical field in the packed bed). The net effect of the weight is that the packed bed remains inert to the induction flux and can be heated only by magnetic hysteresis.

APPENDIX 2E

DIRECT HEATING OF SHOT BY GAS

1. Introduction

A feasible heating route to SD casting manufacture is to heat particles contained in an impermeable mold with hot gas followed by infiltration of the hot porous solid with melt at casting temperature. The heating time (t_H) and heating efficiency (η) is estimated for steel particles of different sizes to attain uniform packed bed temperatures of 400°C to 900°C . The results are compared to values obtained by using Furnas' emperical equation for heat transfer coefficient⁽⁶⁾ and Schumann's Solution for transient heat transfer from a gas stream to a bed of solids.⁽⁵⁾

2. Theory

The transient heat transfer between a gas stream and bed of particles was analysed by Schumann⁽⁵⁾. The analysis was subject to the following assumptions:

- a. the bed is initially at uniform temperature
- b. the heating fluid enters the bed at constant rate and temperature
- c. the heat transfer coefficient between fluid and solid is constant throughout the bed

- d. the thermal diffusivity of the solid is so large that the temperature gradient in the particle is negligible
- e. the packed bed has adiabatic walls.

The above assumptions are valid for gas heating of shot (spherical iron particles in the size range of 0.254 to 1.27 mm) and so Schumann's Solution can be used to estimate the heating efficiency and heating time if the heat transfer coefficient is known.

The heat transfer coefficient can be obtained by using relationships obtained by Furnas,⁽⁶⁾ Lof and Hawley,⁽⁸⁾ Ford and Saunders,⁽⁹⁾ Gamson and Hougen,⁽¹⁰⁾ Denton⁽¹¹⁾ and Coppage and London⁽¹²⁾. Furnas obtained an emperical relationship for heat transfer between air and iron balls at temperatures upto 750°C. Other investigators used different solid materials and lower temperatures for estimating the heat transfer coefficient. The SD process temperature ranges from 1200°C to 1400°C., and so the Furnas' relationship is the best for estimating the heat transfer coefficient for shot heating in the SD process. Furnas' relationship for heat transfer coefficient is given by:⁽⁶⁾

$$h_v = (0.0187(G/\rho_o)^{0.7} T^{0.3} \ln VF)/d_p^{0.9}$$

$$\ln VF = (1.68 - 3.56c^2) \quad (E-1)^*$$

* A list of notations is given at the end of the appendix.

where:

h_v - coefficient of heat transfer in kcal per second per cubic meter of bed volume per degree difference between gas and solid.

G - gas melt velocity, $\text{Kg}/\text{m}^2\text{s}$

ρ_0 - density of gas at 0°C

T - average absolute temperature of bed, K

d_p - diameter of particles, m

ϵ - void fraction

For comparison purposes the volumetric heat transfer coefficient has also been calculated using Coppage et al equation for volumetric heat transfer coefficient⁽¹²⁾.

$$h_v = (6.77 (1-\epsilon) G c_g \text{Re}^{-0.3}) / (\text{Pr } d_p \epsilon) \quad (\text{E-2})$$

The heat transfer coefficient calculated from Coppage et al equation and Furnas' equation for Nitrogen gas has been compared in Fig. E.1. The results calculated from Coppage et al equation are much higher than those calculated from Furnas' equation, especially for very small shot diameters. The estimation of heating time and efficiency using Schumann's analysis will be based on the heat transfer coefficient calculated from the Furnas equation.

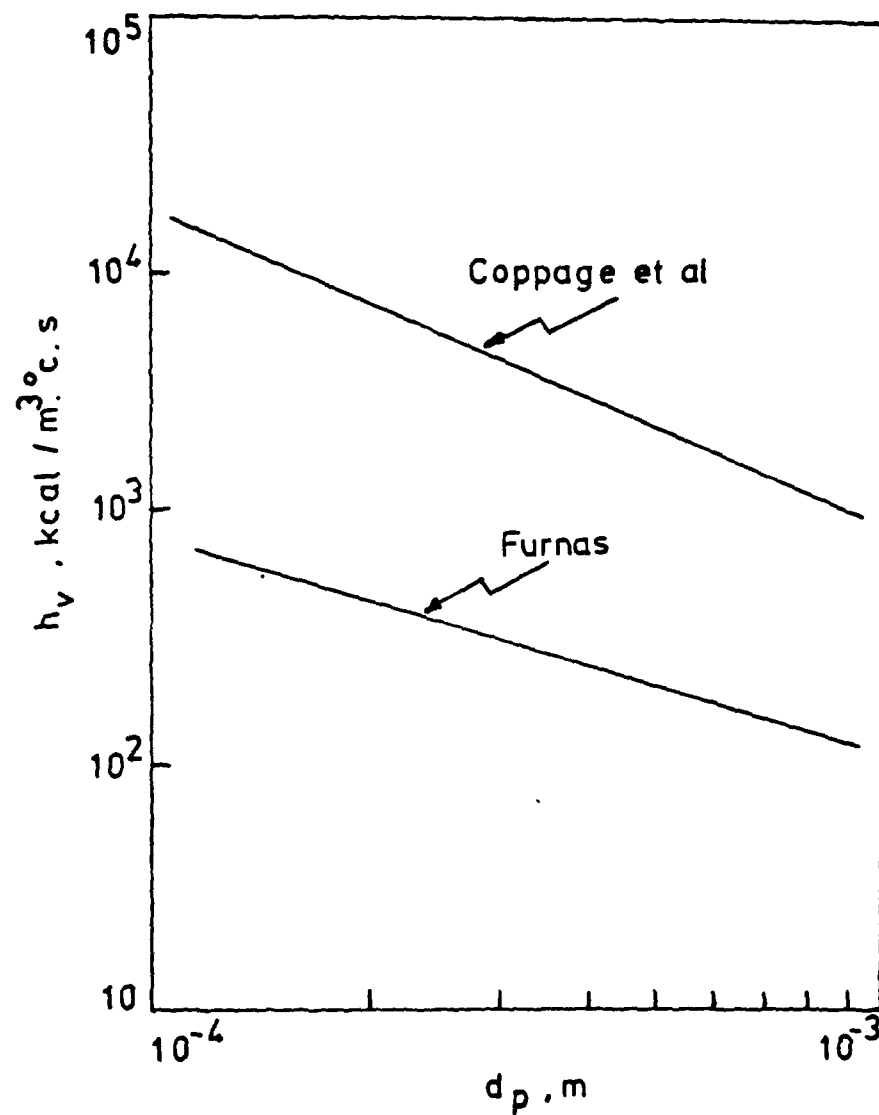


Figure E.1. Volumetric heat transfer coefficient as a function of shot size; heating gas- nitrogen, casting temperature = 1400°C , gas mass velocity = $1.0 \text{ kg/m}^2\text{s}$

3. Heating efficiency

The efficiency of gas heating can be approximately estimated from the temperature-time profile of the gas outlet temperature using Eq. E-3.

$$\eta = 1 - \int_0^{t_H} (T_O/T_I) dt \quad (E-3)$$

A series of temperature-time profiles in terms of dimensionless quantities for transient heating of packed beds was given by Schumann⁽⁵⁾ and are called Schumann's Curves. The value of Y (dimensionless distance) is given by⁽⁵⁾:

$$Y = (h_v x) / (c_g G)$$

$$Y^* = Y(x = L)$$

$$= (h_v L) / (c_g G) \quad (E-4)$$

The value of Z (dimensionless time) is given by:⁽⁵⁾

$$Z = \frac{h_v}{\rho_s C_s (1 - \epsilon)} \left(t - \frac{\rho_g x \epsilon}{G} \right)$$

$$Z^* = Z (T_O/T_I = 1, x = L) \quad (E-5)$$

The efficiency of heating is the function of the dimensionless distance, Y , and is given approximately by:

$$\eta = 1 - \int_0^{Z^*} Y^* dz \quad (E-6)$$

4. Heating time

The heating time can be calculated from the dimensionless quantity Z^* and can be expressed by:

$$t_h = \frac{Z^* \rho_s c_s (1-\epsilon)}{h_v} + \frac{\rho L \epsilon}{G} \quad (E-7)$$

5. Relationship between Y^* , Z^* and η

The Schumann Curves have been extended by Furnas⁽⁶⁾ to values of $Y^* = 500$. For values of $Y^* > 500$, the Y^* and Z^* values have been extrapolated. Table E-I gives the relationship between Y^* , Z^* and η for Y values ranging from 1 to 50,000. For $Y^* > 50,000$, the efficiency is assumed to be 100 percent. Hence, once the value of Y^* is known, the heating time and efficiency can be estimated from the corresponding values of Z^* and for the given Y^* value.

Expressions for η and Z^* as a function of Y^* were obtained by curve fitting the data in Table E-I using the least squares method. An expression for η as a

Table E-I. Relationship between Y*, Z* and efficiency

Y*	Z*	T _I , %
1	8	15.3
5	20	26.2
10	24	42.2
15	35	43.9
20	45	44.9
30	55	54.5
40	70	56.8
50	83	61.2
60	93	64.6
70	108	66.0
80	120	66.5
90	130	69.4
100	140	71.4
150	210	74.3
200	250	76.8
250	300	80.3
350	416	84.9
400	470	85.6
450	520	86.7
500	570	87.9
600	710	88.6
700	820	90.5
800	930	91.1
900	1080	91.6
1000	1200	94.5
2000	2350	96.0
3000	3600	96.5
4000	4800	97.0
5000	6000	97.4
7000	8500	98.0
8000	10000	98.3
9000	11000	98.5
10000	12500	98.6
20000	25000	99.5
50000	63000	100.0

function of Y^* obtained by curve fitting is given by:

$$\eta = -97 + 120(Y^*)^{0.1} - 6.6(Y^*)^{0.3} + (.005/Y^*) \quad (E-8)$$

Z^* as a function of Y^* obtained by curve fitting is given by:

$$Z^* = 98 + 1.25Y^* + 8.8 \times 10^{-6} Y^{*2} - 2.5 \times 10^{-10} Y^{*3} \quad (E-9)$$

6. Experimental Procedure

The experimental setup for gas heating of shot is shown in Fig. E.2. Inert gas (N_2 , Ar or He) is heated in a heat exchanger. The hot gas is then brought into contact with the shot in the packed bed chamber. A flow meter is used to measure gas flow rate. The heat exchanger, consisting of a 3" mild steel pipe is connected to the heat exchanger by a 3/4" mild steel pipe. A layer of steel wool was used at the gas inlet port to reduce entrance effects. The shot is poured into the chamber only after a steady state temperature is attained in the chamber. The gas inlet temperature was measured prior to adding the shot. After adding the particles gas outlet temperature was measured as a function to time.

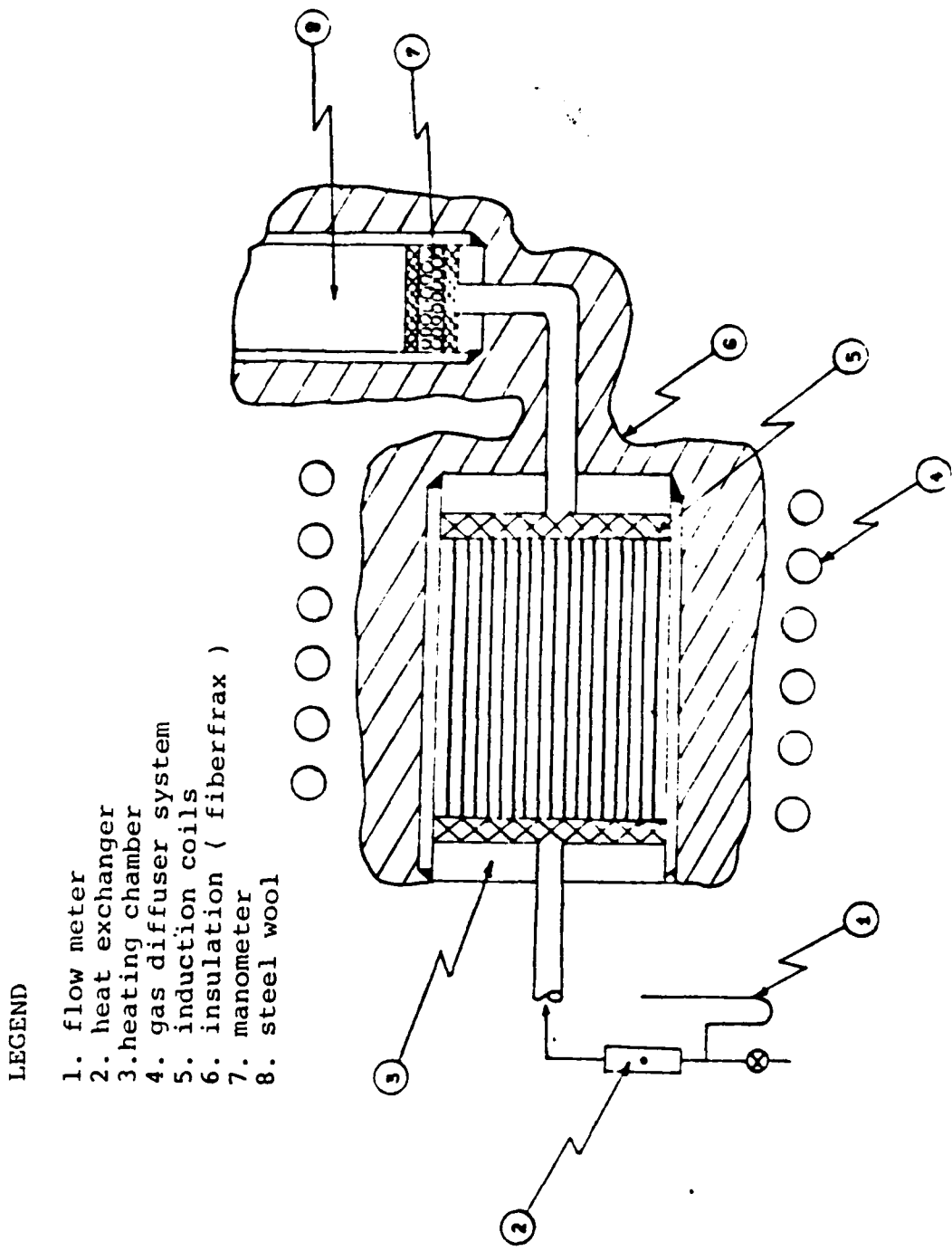


Figure E.2. Experimental setup for gas heating of shot.

The experimental variables for the gas heating runs are given in Table E-II.

7. Results

The efficiency calculated using Eq. E-1 and the corresponding heating times for the experimental runs is given in Table E-III. The heating efficiency and heating time calculated using Schumann's Solution and heat transfer coefficient obtained from Furnas' equation are also given in Table E-III.

8. Discussion

The heating efficiency determined in the experimental runs was for a packed bed with heat losses to the surroundings. The major sources of heat losses to the surroundings are the steel walls of the packed bed chamber and radiation losses from the top of the bed. In the SD process the shot will be contained in molds at process temperature and heat losses to the surroundings can be considered to be negligible. For the case of no heat losses to the surroundings, the efficiency and time of heating are more accurately determined using the Furnas equation and Schumann's Solution. A comparison between the experimental and theoretical efficiency and time is shown in Figs. E.3 and E.4.

Table E-II. Process Variables For Gas Heating Runs

Run No.	Heating Gas	T* °C	Q ₃ 10 ⁴ m ³ /s	W kg	d _p mm	d _{pb} mm	L mm
7	Nitrogen	440	6.37	1.0	1.49	53	94
8	"	460	6.37	1.0	0.97	53	94
9	"	465	6.37	1.0	0.69	53	94
11	"	465	6.37	1.0	1.83	53	94
12	"	455	6.37	1.0	1.09	53	94
13	"	590	7.43	1.0	1.54	53	95
15	"	825	8.55	1.0	1.11	53	99
16	"	790	8.55	1.0	1.11	53	99
17	"	730	8.55	1.0	1.54	53	99
18	"	535	3.27	1.0	1.84	53	96
19	"	545	3.27	1.0	1.10	53	96
20	"	570	3.27	1.0	1.54	53	147
21	"	635	5.68	1.0	1.54	53	97
22	"	660	5.68	1.0	1.11	53	100
23	"	645	7.78	1.0	1.84	53	98
24	"	820	7.78	1.5	1.84	53	147
25	"	810	8.55	1.0	3.67	53	105
26	"	820	8.55	1.0	3.01	53	106
27	"	815	8.55	1.0	2.60	53	99
28	Argon	845	7.20	1.0	3.67	53	98
29	"	850	7.20	1.0	1.84	53	98
30	Nitrogen	890	8.55	1.0	11.10	53	110
31	"	865	8.55	1.0	6.35	53	105
32	"	865	8.55	1.0	1.84	53	105

* T - Gas inlet temeprature

Q - Gas flow rate

W - Mass of shot

d_p - diameter of shotd_{pb} - diameter of packed bedL_{pb} - height of packed bed

Table E-III. Heating Times And efficiency For Gas Heating of Shot

<u>Run No.</u>	<u>Experimental Results</u>		<u>Theoretical Results</u>	
	<u>t_H, s</u>	<u>$\eta, \%$</u>	<u>t_H, s</u>	<u>$\eta, \%$</u>
7	2400	40	1235	57
8	1400	42	1115	64
9	1700	35	1065	68
11	3200	28	1270	54
12	2200	36	1160	62
13	2700	24	1080	60
15	1800	28	1135	58
16	1300	37	1000	65
17	3400	27	1055	60
18	3400	31	2490	59
19	3000	34	2215	66
20	4000	32	3260	68
21	1600	38	1470	60
22	1400	34	1400	66
23	1500	38	1170	57
24	3000	30	1660	65
25	1800	26	1400	49
26	1600	30	1330	52
27	1400	34	1215	53
28	3200	24	2045	55
29	2600	25	1655	63
30	1800	22	1890	34
31	2000	19	1690	43
32	1400	42	1015	68

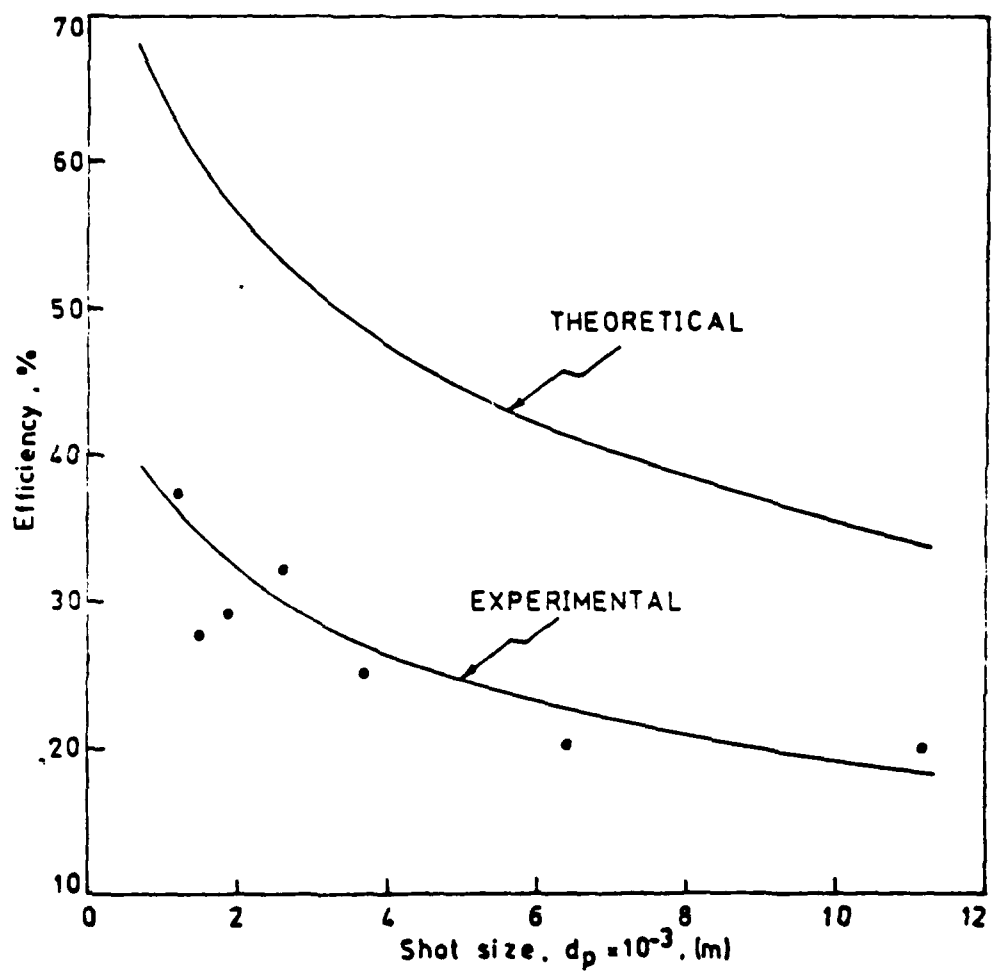


Figure E.3. Comparision of theoretical and experimental heating efficiencies as a function of shot size; heating gas - nitrogen, $G = 0.444 \text{ kg/m}^2 \cdot \text{s}$, $T_c = 850^\circ\text{C}$, $L = 0.095 \text{ m}$

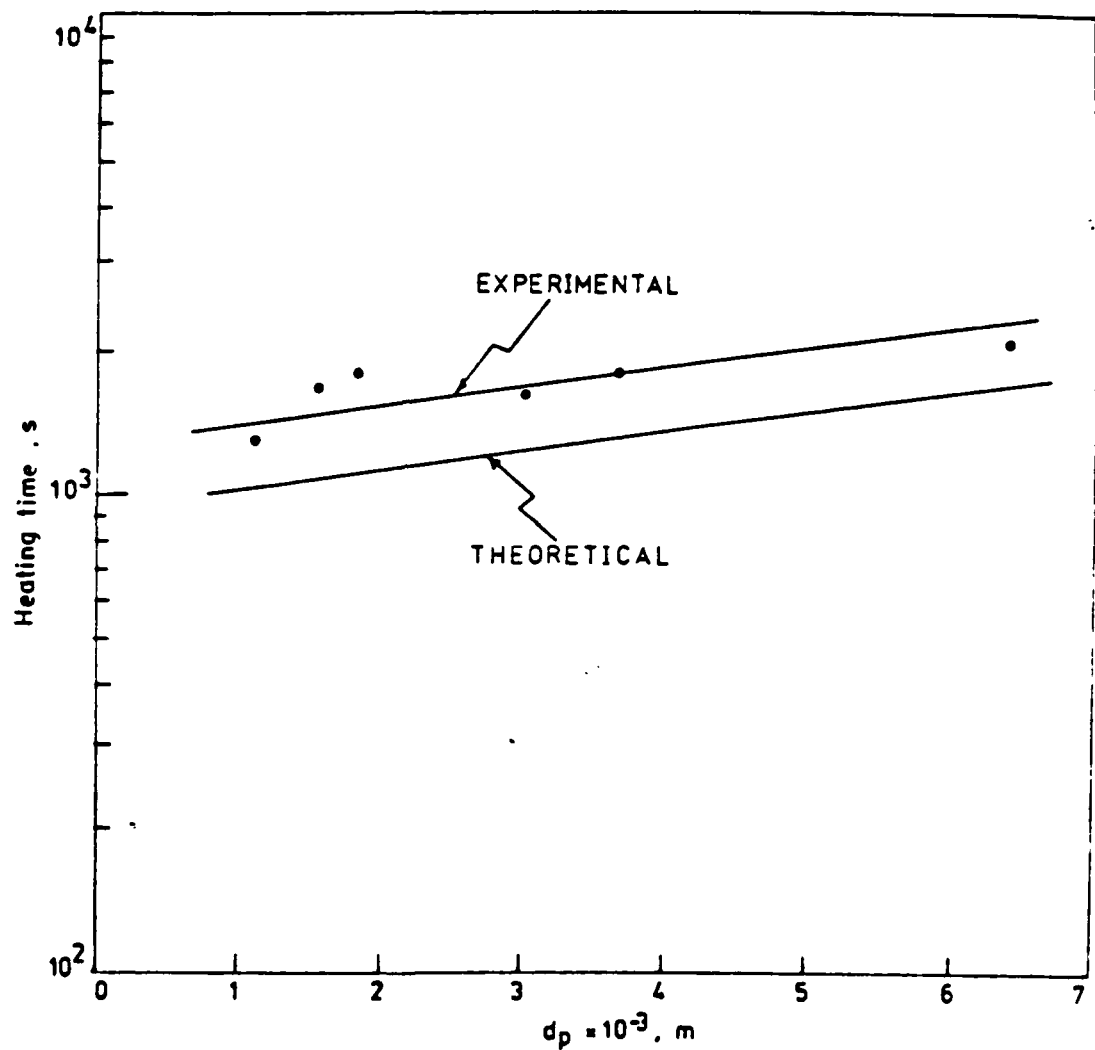


Figure E.4. Comparision of theoretical and experimental heating times as a function of shot size;
heating gas - nitrogen, $G = 0.444 \text{ kg/m}^2 \cdot \text{s}$,
 $T_c = 850^\circ\text{C}$, $L = 0.095 \text{ m}$

9. Conclusions.

The heating time and efficiency for gas heating of shot can be estimated using Schumann's Solution for a given set of process variables. The experimental results could be used to estimate a lower bound for gas heating efficiency and an upper bound for the heating time.

LIST OF NOTATIONS

- c_g - Specific heat of gas
 c_g - Specific heat of shot
 d_p - shot size
 G - Superficial gas mass velocity
 h_v - Volumetric heat transfer coefficient
 L - Casting length (height of packed bed)
 Pr - Prandtl's number ($c_p/\mu k$)
 Re - Reynolds number ($Gd_p/(1-\epsilon)$)
 T - Temperature
 T_c - Casting temperature
 T_I - Gas inlet temperature
 T_o - Gas outlet temperature
 t - Time
 t_H - Heating time
 x - Distance from gas inlet port
 Y - Dimensionless distance
 Y^* - Y ($x = L$)
 Z - Dimensionless time
 Z^* - $Z(x=L, T_o/T_I=1)$
 η - heating efficiency
 ρ_o - Gas density at $0^\circ C$
 ρ_g - Gas density
 ρ_s - Shot density
 ϵ - Void fraction
 μ - Gas viscosity

APPENDIX 2F

RADIATIVE HEATING EXPERIMENTAL RESULTS

1. Experimental Procedure

The experimental set up for radiative heating is shown in Fig. F.1. The shot was placed between layers of alumina particles in an alumina crucible. Thermocouples (W-Re) were placed at different locations in the packed bed as shown in Fig. F.1. The temperature was recorded using a multipoint Honeywell temperature recorder. The graphite susceptor was heated using a 10kHz, 25kW induction unit. The crucible was preheated to about 500°C to prevent it from cracking due to thermal shock. This was done by operating the unit at a power input of 1 to 3 kW. After preheating the crucible the power input was increased to 12 kW.

2. Experimental Parameters

a. Packed Bed

Powder - S100 ($d_p = .216$ mm.)

$d_{PB} = 67$ mm., $l_{PB} = 80$ mm., $W = 1.27$ kg.

b. Susceptor (Graphite)

ID = 83 mm., OD = 103 mm., $l = 305$ mm.

c. Insulation

The insulation around the susceptor consisted of

LEGEND

1. induction coils
2. fiberfrax
3. graphite felt
4. graphite susceptor
5. alumina crucible
6. graphite disc
7. pyrolytic graphite
8. alumina particles
9. shot

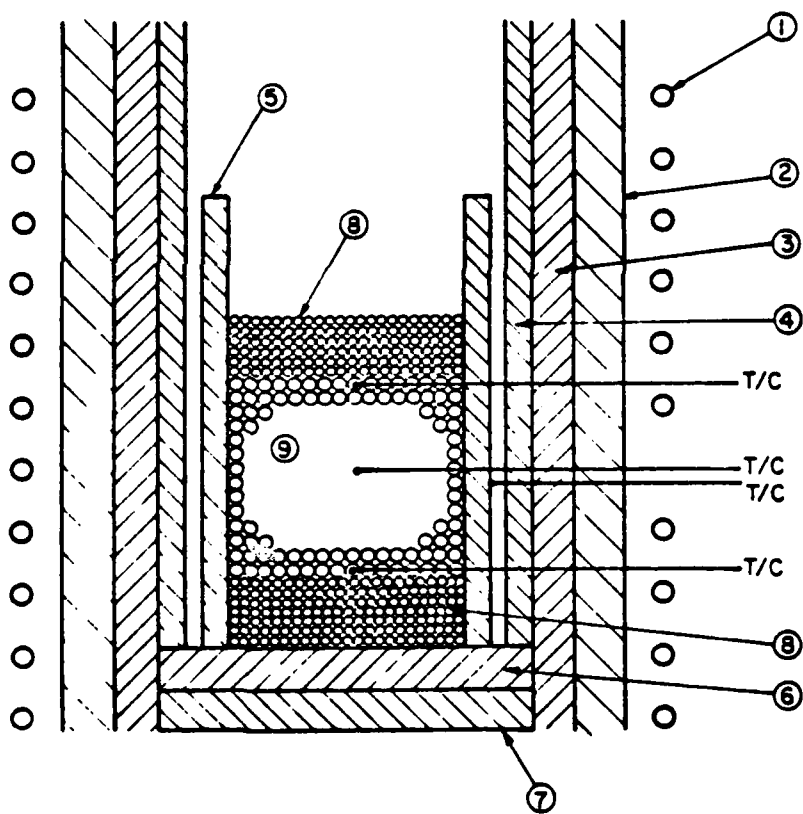


Figure F.1. Radiative heating setup

12.5 mm of fiberfrax. The packed bed was insulated at the top by a 50 mm layer of alumina particles and at the bottom by a 100 mm layer of alumina particles.

d. Crucible (Alumina)

ID = 67 mm , OD = 77 mm, l = 188 mm

e. Coils

$d_C = 9.5 \text{ mm}$, $d_S = 165 \text{ mm}$, $l_S = 300 \text{ mm}$, $N = 11 \text{ turns}$.

3. Results

Figure F.2 shows the temperature distribution in the packed bed as a function of time. The packed bed heats uniformly in the longitudinal direction. Large radial temperature gradients (600°C to 900°C) were observed for a period of 1500 seconds. During this period the interior temperature increased by 200°C . After 1500 seconds the interior temperature rapidly increased. A heating time of about 2200 seconds was required to attain a uniform packed bed temperature of 1350°C . The heating efficiency was 4.2 percent.

The crucible showed no signs of cracks. The particles in the bed had sintered together. The packed bed surface was uniform and showed no signs of cracks.

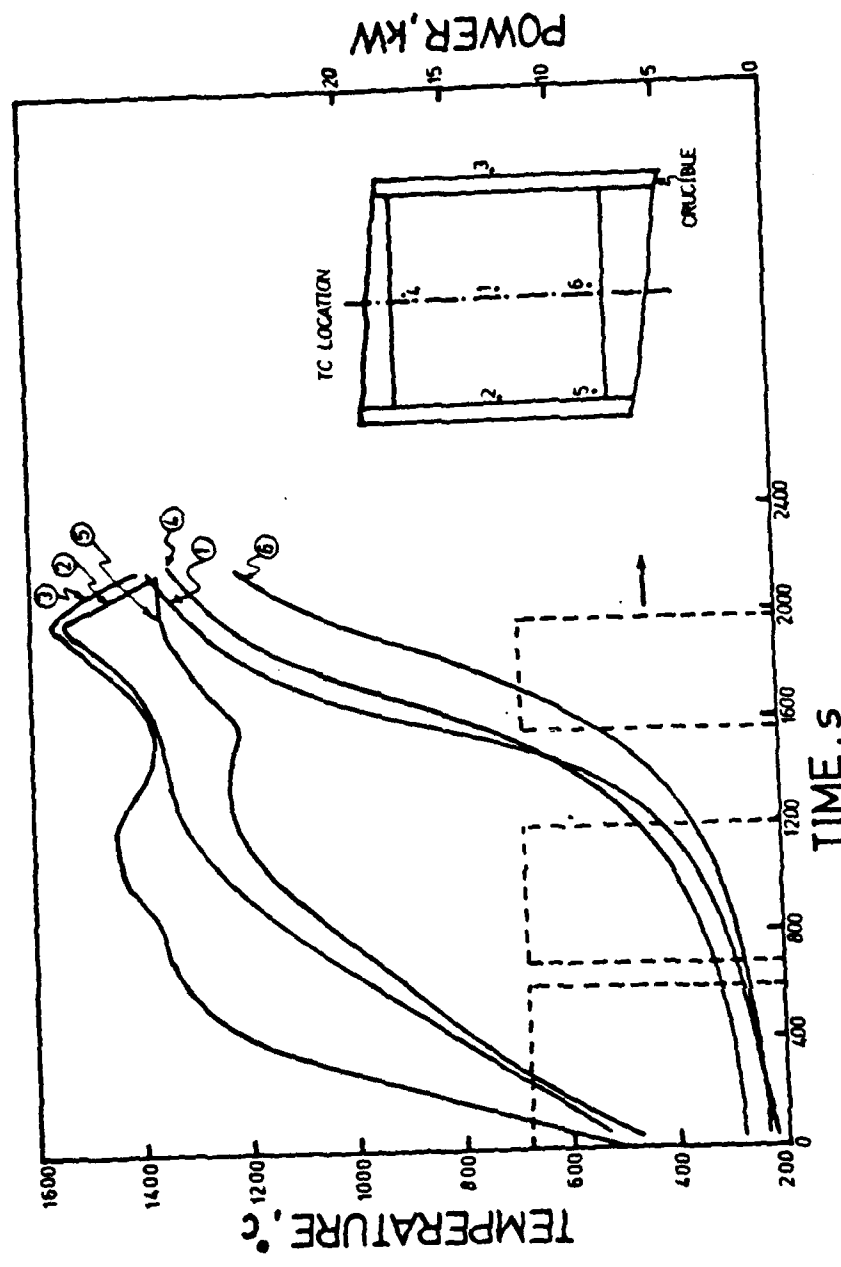


Figure F.2. Temperature distribution in the packed bed during radiative heating.

LIST OF NOTATIONS

- h_{rs} - heat transfer coefficient of thermal radiation, solid surface to solid surface.
- h_{rv} - heat transfer coefficient of thermal radiation, void space to void space.
- k - thermal conductivity
- ρ - emmisivity of solid surface
- d_p - shot size
- T - temperature
- β - (effective length between centers of two neighbouring solids in the direction of heat flow)/(average diameter of solid).
- γ - (effective thickness of solid)/ d_p
- ϕ - effective thickness of fluid film
- ϵ - void fraction
- α - thermal diffusivity
- \mathcal{L} - Lorentz Number
- ρ - density
- Subscripts
- PB - packed bed
- s - solid
- g - gas

APPENDIX 2G

THERMAL DIFFUSIVITY OF SHOT

The thermal diffusivity of shot is an important parameter which controls the heating time for SD casting manufacture via the indirect heating route. The thermal diffusivity of shot as a function of temperature in a gas atmosphere can be estimated by calculating the thermal conductivity of shot using Kunii et al equation.⁽¹³⁾

$$\frac{k_{PB}}{k_g} = \epsilon \left(1 + \frac{\beta h_{rv} d_p}{k_g} \right) + \frac{\beta (1-\epsilon)}{\frac{1}{1/\phi + h_{rs} d_p/k_g} + \gamma \frac{k_g}{k_s}} \quad (G-1)$$

where:

$$h_{rs} = 5.42 \times 10^{-5} \left(\frac{P}{p-2} \right) \left(\frac{T+273}{100} \right)^3 \quad (G-2)$$

$$h_{rv} = \left(\frac{(1-p)}{1 + \frac{\epsilon(1-p)}{2(1-\epsilon)p}} \right) \left(\frac{T+273}{100} \right)^3 \quad (G-3)$$

$$\beta = 1, \phi = 2/3, p = 0.27 \text{ (for iron)} \quad \phi = f(k_s/k_g, \epsilon)$$

In vacuum the thermal conductivity can be obtained

* A list of notations is given at the end of this Appendix

from Eq. (G-1) by taking the limit $k_g \rightarrow 0$.

$$\frac{k_{PB}}{k_s} = \frac{h_{rv} d_p}{k_s} + \frac{(1 - \epsilon)}{(k_s/h_{rs} d_p) + 2/3} \quad (G-4)$$

The thermal diffusivity of the packed bed in a gas atmosphere is given by:

$$\alpha_{PB} = k_{PB} / ((C_p \rho)_s (1 - \epsilon) + (C_p \rho)_g) \quad (G-5)$$

In vacuum the thermal diffusivity is given by:

$$\alpha_{PB} = k_{PB} \alpha_s / k_s (1 - \epsilon) \quad (G-6)$$

The thermal diffusivity of a packed bed can also be calculated from resistivity-temperature data. The thermal conductivity and resistivity of a material can be related to each other using the Lorentz Number, ($\alpha^L = 5.9 \times 10^{-12}$ kcal. ohm/sec°K for iron):

$$k_{PB} = \frac{\alpha^L (T+273)}{\rho_{PB}} \quad (G-7)$$

The thermal diffusivity of a packed bed of shot can be calculated from resistivity-temperature data using Eq. (G-8).

$$\alpha_{PB} = \frac{\alpha^L (T+273) \alpha_s}{(1-\epsilon) \rho_{PB} k_s} \quad (G-8)$$

The resistivity-temperature data for different shot sizes is given in Appendix 2C. The thermal diffusivity of a packed bed in vacuum as a function of temperature calculated using the resistivity data and Eq. (G-8) is shown in Fig. G.1.

A comparison of normalized thermal diffusivity, the ratio of thermal diffusivity of packed bed to thermal diffusivity of solid calculated from Kunii et al equation and resistivity data is given in Fig. G.2 for a shot size of 0.275 mm.

A comparison of thermal diffusivity of a packed bed of shot, ($d_p = .216$ mm.), in argon calculated from Kunii et al equation and resistivity data is given in Fig. G.3.

The thermal diffusivity values calculated using Kunii et al equation and resistivity data differ from each other by two orders of magnitude. Kunii et al analysis is valid for unbonded particles and so does not account for the enhancement in thermal diffusivity resulting from bonding at the contact points between the particles.

The thermal diffusivity of S100($d_p = 0.216$ mm.) in argon calculated from resistivity data differs from the thermal diffusivity calculated using Kunii's equations, (for the same conditions), by a factor of 3 as shown in Fig. G.3. The difference could be attributed to oxidation of the particles during the heating period.

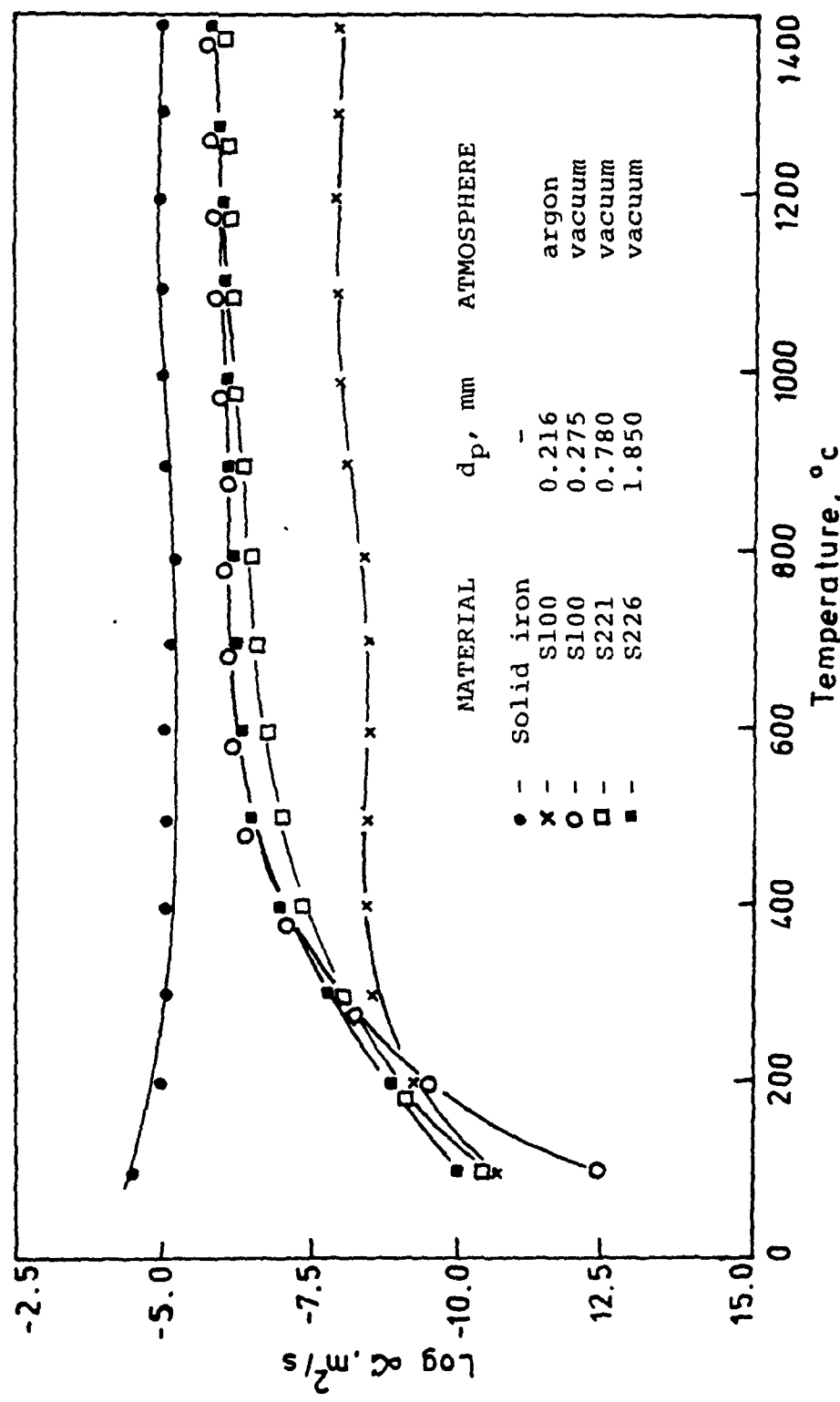


Figure G.1. Thermal diffusivity of unbonded shot as a function of temperature calculated from resistivity - temperature data.

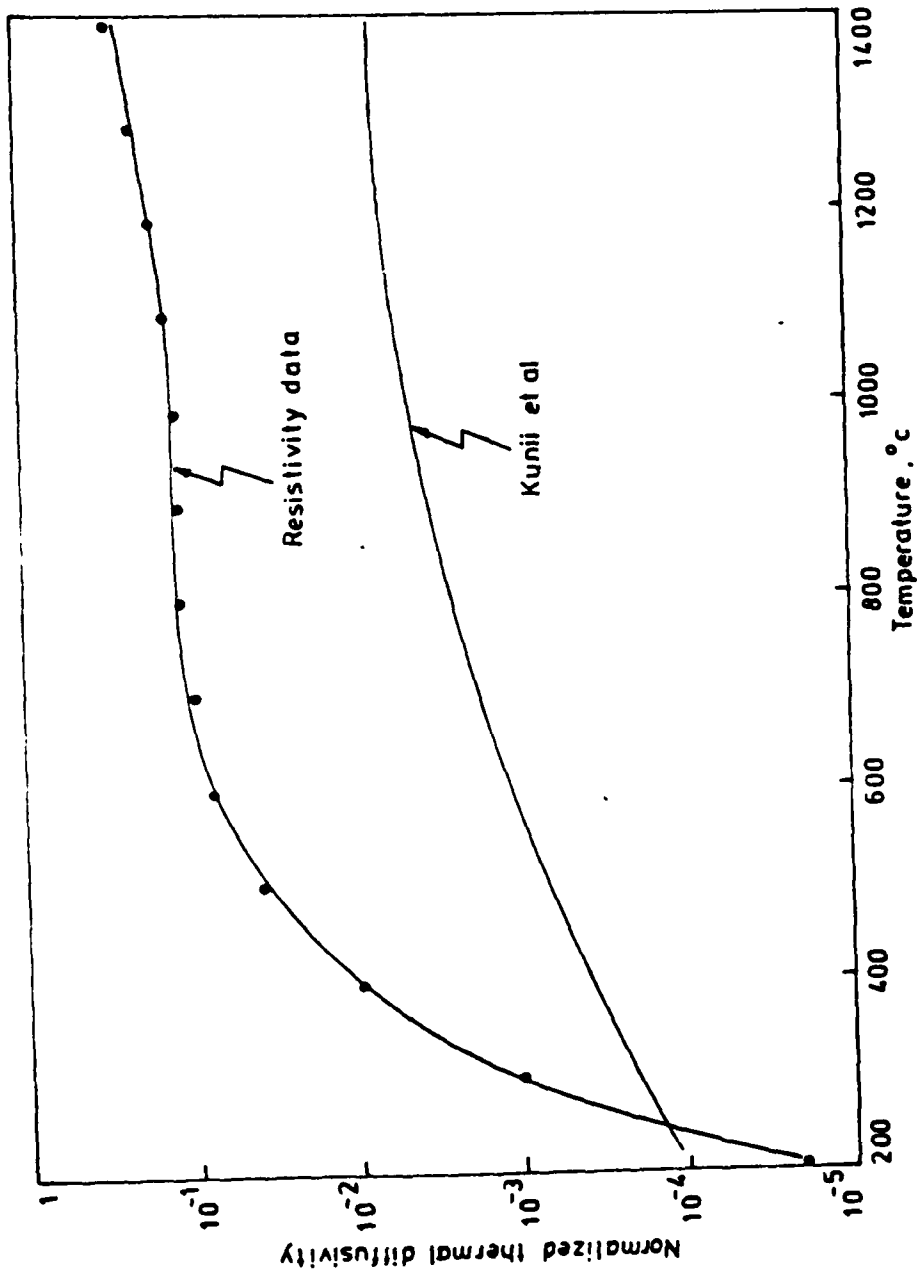


Figure G.2. Comparision of normalized thermal diffusivity as a function of temperature calculated from Kunii et al equation and resistivity - temperature data; atmosphere - vacuum, shot size = .275mm

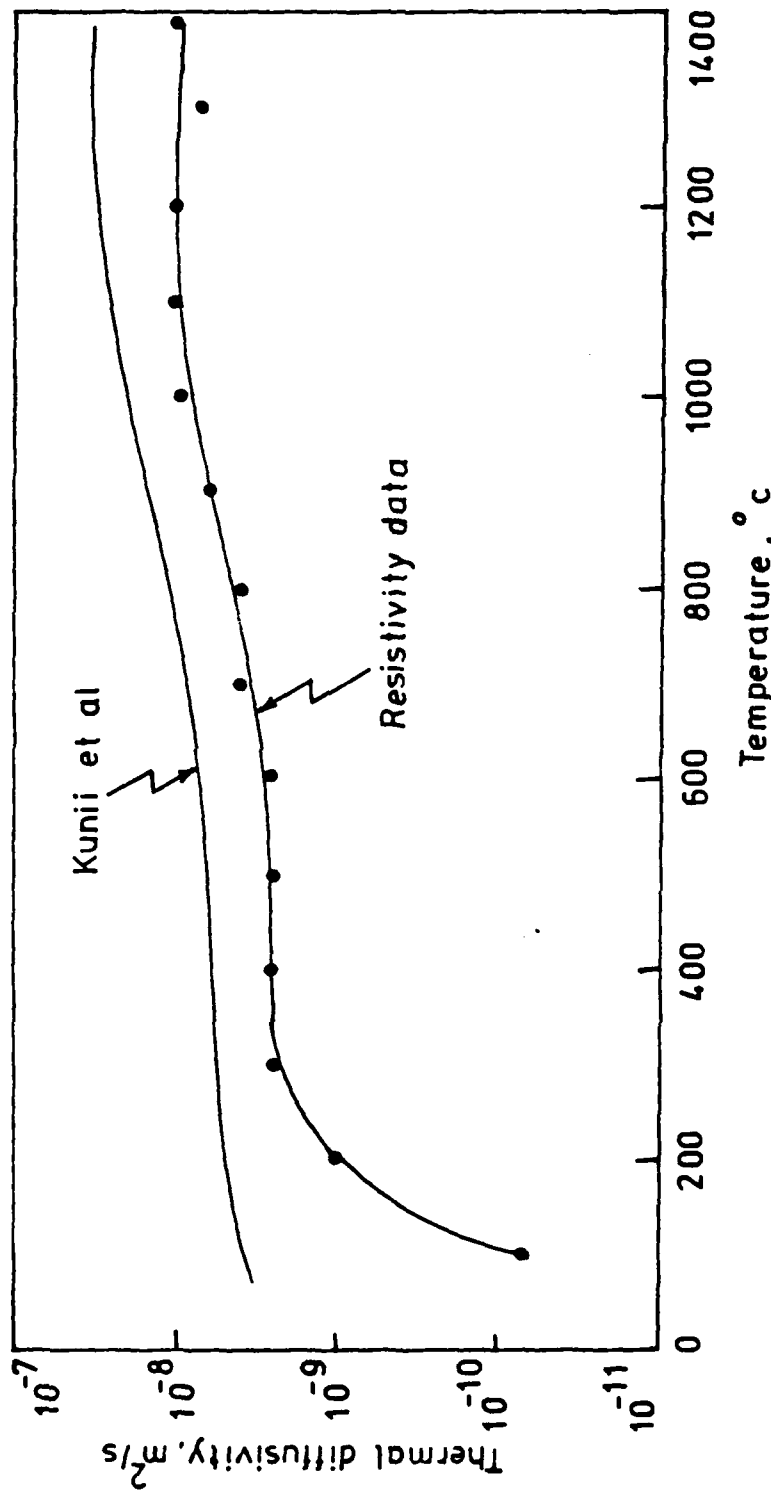


Figure G.3. Comparision of thermal diffusivity as a function of temperature calculated from Kunii et al equation and resistivity-temperature data for S100 ($d_p = .216$ mm) in an argon atmosphere.

APPENDIX 2H

INVESTMENT MOLDS FOR MANUFACTURING SD CASTINGS

Apelian and Langford⁽⁴⁾ have discussed the feasibility of using investment molds (lost wax pattern) for manufacturing SD castings. Investment molds fall under the category of permeable molds. To use the investment mold for SD casting manufacture it is essential to infiltrate the melt into the shot region before the pressurization gas enters the shot region through the permeable mold wall. Alternatively, the investment molds can be made impermeable to the pressurization gas by coating them with glaze suspensions. At casting temperatures the glaze forms a viscous fluid layer on the mold wall which prevents the pressurization gas from entering the shot region through the mold wall. Since SD castings have not yet been manufactured in conventional investment molds, it is essential to know whether the investment molds can be adapted to the SD process.

1. Casting Manufacture

a) Materials

A number of investment shells have been made using the standard procedure⁽¹⁴⁾. The prime coat and back-up

coat slurries have compositions similar to those used for fused silica shells (Table III in reference 14). The prime stucco coat was 75 μm . zircon (zirconium silicate) sand. The back-up stucco coat was 850 μm to 300 μm alumina-silicate sand. The coating schedule for different shells made is listed in Table H-I.

All shells, except 1 and 3, were able to withstand an external pressure of 790 kPa during the de-waxing operations. Since only five coats were given to shells 1 and 3, these molds did not have sufficient strength to withstand external pressure during the de-waxing operation. The molds were not fired in the conventional process as firing takes place while heating the SD components to casting temperature.

Some of the molds were coated with glaze suspension using the immersion technique. Two glazes G1 and G2 were used and their properties are listed in Table H-II. In some of the runs, closed-one-end mullite tubes were used as molds for comparing castings made in permanent molds, to those made in investment molds. The shot and melt used for manufacturing the different castings are given in Table H-III. Irregular alumina particles having an average size of .65 mm. were used to separate the shot from the melt.

b) Heating and Casting Procedure

The mold and its contents were heated in a cylindrical

Table H-I. - Coating Schedule for Investment Shells

Shell Number	Coating Schedule
1, 3	C1S1, C1S1, C1S1, C2S2, C2
4, 5, 6	C1S1, C1S1, C1S1, C2S2, C2S2, C1
7, 8, 9	C1S1, C1S1, C1S1, C2S2, C1S2, C1S2, C1
10, 11, 12	C1S1, C1S1, C1S1, C2S2, C1S1, C1
13, 15	C1S1, C1S1, C2S2, C1S2, C1S2, C1S2, C1
16, 17, 18	C1S1, C1S1, C2S2, C2S2, C1S1, C1S2, C1
19, 20, 21	C1S1, C1S1, C1S1, C2S2, C1S1, C1S2, C1S2, C1
22, 24	C1S1, C1S1, C1S2, C1S2, C1S2, C2S2, C2S2, C1
25	C1S1, C1S1, C2S2, C1S1, C1S1, C2S2, C1S2, C1
26, 27, 28	C1S1, C1S1, C2S2, C2S2, C2S2, C2
29, 30, 31	C1S1, C1S1, C1S1, C2S2, C2S2, C2S2, C2
32, 33, 34	C1S1, C1S1, C2S2, C1S1, C2S2, C1S1, C2S2, C2

Notations Used in Coating Schedule

- C1. Primary slurry coat
- C2. Backup slurry coat
- S1. Stucco coat with 75 μm zircon sand
- S2. Stucco coat with 80 μm to 300 μm alumina-silicate sand

Table H-II. - Properties of Glazes

Glaze	Softening Point °C	Thermal Expansion
		/°C
G1*	1000 °C	4.7×10^{-6}
G2**	1120 °C	8.0×10^{-6}

* Manufactured by SCM, Code P-1401-P

** Manufactured by The O Hommel Co., Code 2GF-184-C

Table H-III.- SD components for castings

Run#	Casting	type	Shot d_p ,mm	Melt w/o carbon	# fine coats	Mold # coarse coats	glaze
1C1	C1	S221	0.776	2.3	4	2	-
1C1	C2	S223	0.776	2.3	5	2	G1
1C2	C3	S223	0.776	2.3	5	2	-
1C6	C4	S221	0.776	4.0	7	1	-
1C9	C5	S221	0.650	2.3	7	1	G2

graphite cored 10 kHz induction furnace. The temperature in the furnace was measured using W-5pct Re/W-26pct Re thermocouples. The furnace was enclosed within a vessel which could be evacuated or pressurized for melt transfer.

The furnace chamber was evacuated during the heating period. Melt was transferred to the solid region at casting temperature by instantaneous gas pressurization of the furnace chamber.

2. Results

Five successful castings designated as C1 to C5 were made by the SD process using investment molds. The surface of the SD castings C1, C2, C4 and C5 are shown in Figs. H.1 to H.4. The process variables for casting manufacture are given in Table H-IV.

The density as a function of casting length for C1 and that of a casting made in a permanent mold (PC1), for the same conditions as C1 is given in Table H-V. A comparison of density as a function of length for castings C2, C3 and a casting made in a permanent mold (PC2) is given in Table H-VI.

3. Discussion

The densities of casting C1 and PC1 as a function of length are approximately the same, indicating that no pressurization gas entered the shot region during melt

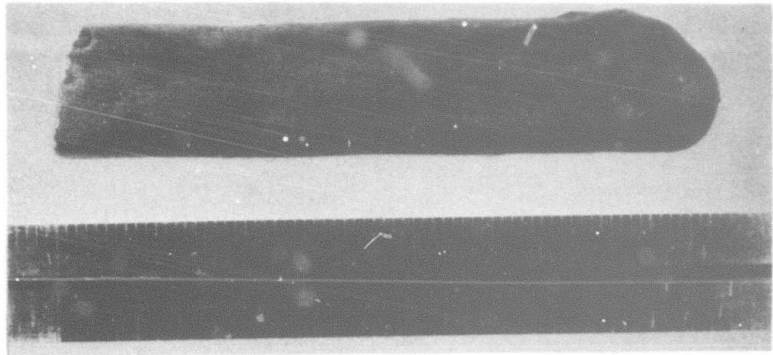


Figure H.1. Investment casting C1 (IC1 #4)

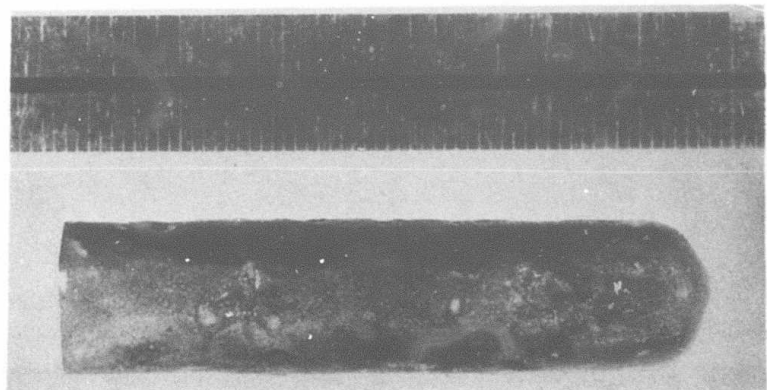


Figure H.2. Investment casting C2 (IC2 #9)

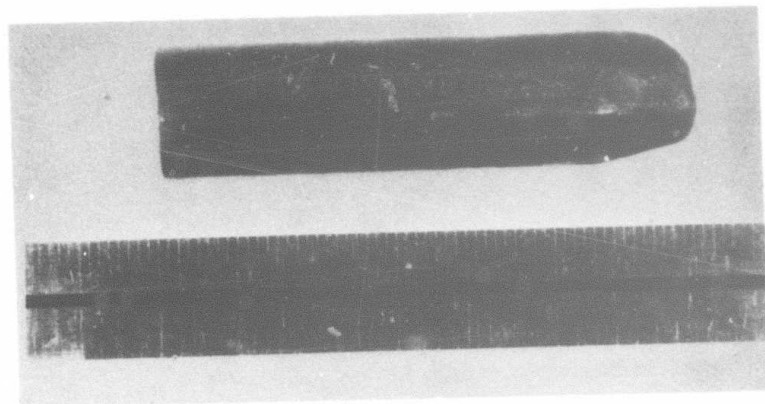


Figure H.3. Investment casting C4 (IC6 #19)

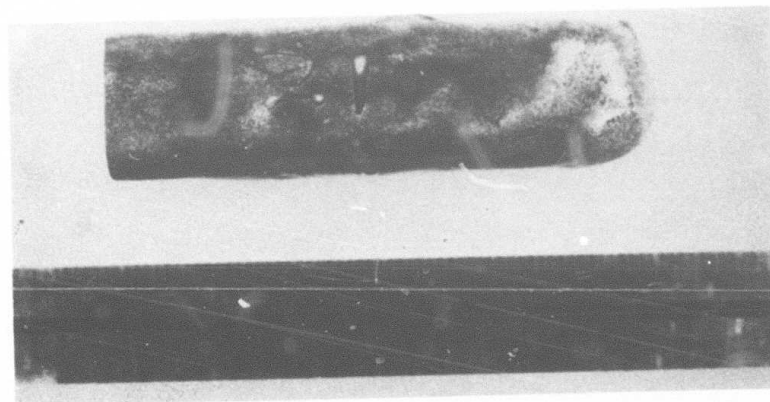


Figure H.4. Investment casting C5 (IC9 #21)

Table H-IV - SD variables for castings

Run#	Casting	Casting Temperature °C	Melt Transfer Pressure kPa
IC1	C1	1360	308
IC2	C2	1360	446
IC2	C3	1360	446
IC6	C4	1200	400
IC9	C5	1360	500

Table H-V. - Density vs casting lengths for castings Cl
and PCl

Length mm	Density, kg/m ³ × 10 ⁻³	
	Cl	PCl
5	7.75	7.74
15	7.74	7.73
25	7.74	7.73
35	7.74	7.74
45	7.74	7.74
55	7.74	7.74
65	7.75	7.74
75	7.75	7.75
85	7.74	7.75

Table H-VI. - Density vs. casting lengths for castings
C2, C3 and PC2

Length mm	Density, kg/m ³ × 10 ⁻³		
	C3	C2	PC2
5	7.65	7.67	7.67
15	7.63	7.67	7.66
25	7.54	7.66	7.60
35	7.51	7.65	7.52
45	7.48	7.57	7.52
55	7.48	7.50	7.58
65	7.48	7.48	7.57
75	7.49	7.51	7.37*
85	-	7.51	-

* Partially infiltrated region

transfer. Significant density variation is observed for castings C2, C3 and PC2. The castings C2 and PC2 have comparable densities, indicating that the glazed investment mold acts as an impermeable mold at casting temperature. C3, however, has a lower density especially at the bottom of the casting. The difference between C2 and C3 was that C2 was made in a mold coated with a glaze. The lower density of C3 in comparison with C2, could have resulted only from the pressurization gas entering the mold during melt transfer.

4. Conclusion

Conventional investment molds can be used for manufacturing SD castings provided the molds have at least six coats. The investment molds can be made impermeable to the pressurization gas by coating them with a glaze which has a softening point of about 100 to 300°C below the casting temperature.

3. PERFORMANCE EVALUATION OF THE PARTICLE VALVE.

M. Paliwal

D. Apelian

G. Langford

SUMMARY

A particle valve for liquid metals consisting of an aggregate of non-wetting refractory particles can have metallurgical applications ranging from atomization to filtration to a quick-acting valve for rapid cycle casting of steel by diffusion solidification. The performance of such a particle valve is evaluated experimentally and theoretically. The supportable head over the particle valve is derived as a function of particle size and liquid surface tension. The experimentally determined breakthrough pressures in the Sn/Al₂O₃ and Hg/Al₂O₃ systems agree with and confirm the derived expression

$$P_{BR} = -10 \cdot 928 \left(\frac{\gamma_{LV}}{d} \right) \cdot \cos \theta_A'$$

where γ_{LV} is the liquid-vapor surface tension, d is the particle diameter, and θ_A' is the apparent advancing contact angle between the liquid and solid. Several mechanisms are identified which may cause failure of the particle valve by disruption or premature breakthrough. Failure can be initiated by buoyancy or turbulent forces acting on the individual particles causing flotation; the breakthrough pressure can be exceeded momentarily by forces caused by various impacts such as droplets falling into the liquid metal. The critical operating limits are given. It is shown that a particle valve can be relied upon when utilized within these limits.

TABLE OF CONTENTS: Section 3. Performance Evaluation of the Particle Valve

	<u>Page</u>
3.1 Introduction.	163
3.2 Derivation of Breakthrough Pressure - Theoretical Considerations.	165
3.3 Experimental Procedure.	173
• Sn/Al ₂ O ₃ System.	173
• Hg/Al ₂ O ₃ System.	175
3.4 Results and Discussions	176
• Particle Valve Performance	176
Required Breakthrough Pressures.	176
Reliability of the Particle Valve.	180
Spherical vs. Irregular Particles.	182
Particle Valve Height.	182
• Disruption Mechanism of the Particle Valve.	183
Failure Due to Direct Impingement of Liquid Droplets on the Particle Valve (Splash Mechanism). . . .	183
Failure by Augmented Hydrostatic Pressure Caused by an Impinging Liquid Droplet	187
Failure Due to Buoyancy Forces Acting on Individual Particles ~ Flotation	193
• Effect of Impurity Contents in the Liquid	194
3.5 Conclusions	197
References	198
Appendix 3A: Particle Size Requirement to Avoid Failure of the Particle Valve by Buoyancy Forces.	199

3. PERFORMANCE EVALUATION OF THE PARTICLE VALVE

3.1 INTRODUCTION

In the SD process of casting steels a melt of high carbon content is pressure infiltrated into a bed of preheated low carbon shot. The melt is isolated from the shot by the particle valve, PV (an aggregate or bed of coarse, non-wetting refractory (Al_2O_3) beads (1,2,3)).

Figure 1 illustrates the general arrangement of the SD casting process. Because of the non-wetting nature of the liquid cast iron on Al_2O_3 , the surface tension forces can prevent the liquid cast iron from penetrating the PV. When melt transfer is required, a gas pressure is applied in excess of that pressure which can be supported by the PV, causing infiltration first of the particle valve bed and subsequently of the steel shot bed.

For a PV to be effective, the breakthrough pressure required to initiate metal flow through the PV should be greater than the pressure exerted by the metallostatic head of the melt above it. It should be pointed out here that it is undesirable either to under-design or to over-design the PV. A PV which is under-designed will cause slow seepage of the melt through the PV before infiltration pressure is applied causing blockage of the top of the shot bed due to premature freezing. On the other hand, an over-designed PV will unnecessarily require higher infiltration pressures.

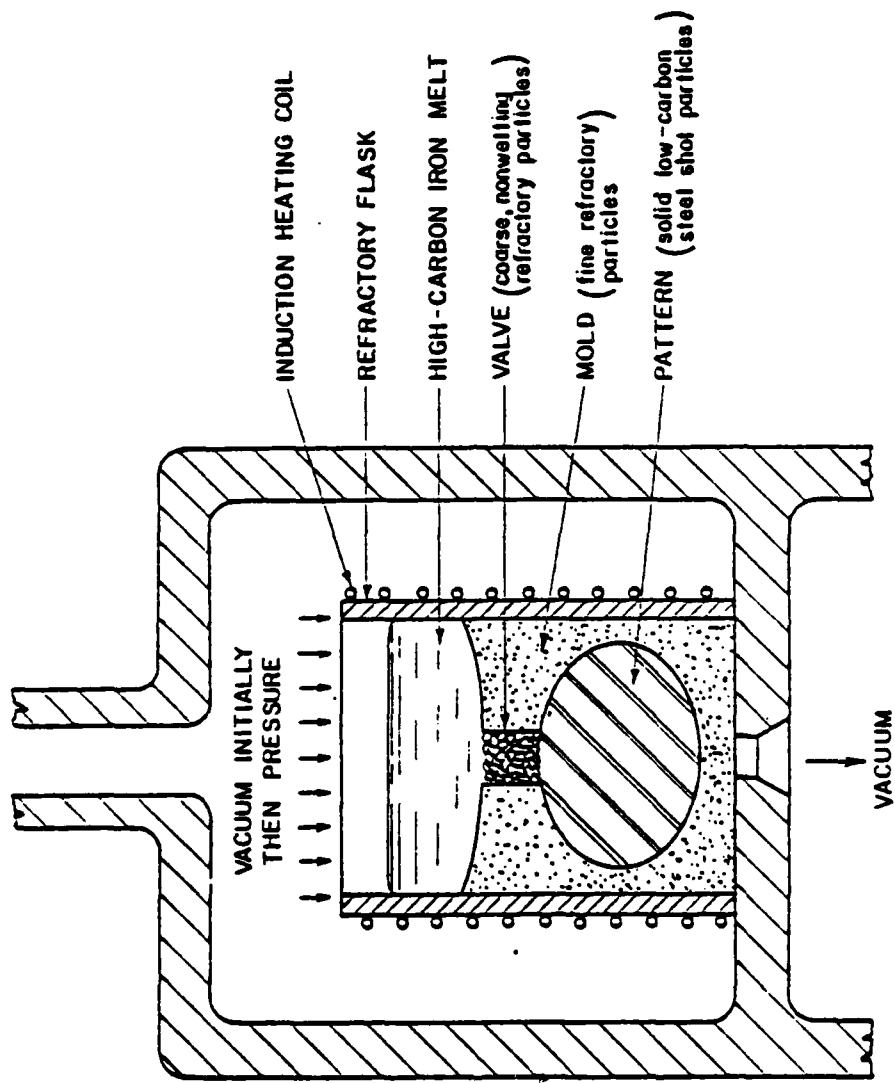


Figure 1. General arrangement for steel casting by diffusion solidification. The PV separates the melt from the steel shot during melting and heating to process temperature. Subsequent pressurization of the chamber causes melt transfer by exceeding the breakthrough pressure of the PV.

The objectives of this part of the study are:

- (i) To derive and measure the required breakthrough pressure to initiate liquid metal flow through the PV.
- (ii) To evaluate the range of variation of the breakthrough pressure of a PV for a given particle size as a function of particle shape, PV height and packing efficiency.
- (iii) To investigate the relative importance of various failure mechanisms which can cause the PV to permit premature initiation of liquid metal flow.

3.2 DERIVATION OF BREAKTHROUGH PRESSURE - THEORETICAL CONSIDERATIONS

Wetting characteristics of the liquid solid system is an important parameter when considering the flow of a liquid phase through a porous medium. Two distinct cases exist: (i) the liquid wets the medium, or (ii) the liquid is non-wetting.

For the case of wetting liquid, the surface tension forces do not act as the major barrier for flow, such as in the case of water flow through soils. Various investigators, D'Arcy (4), Poiseuille (5), and Kozeny and Carman (6) have attacked the problem and offer governing equations relating the pressure needed for a given flow rate as a function of the bed length and permeability and viscosity of the liquid. In these investigations the permeability factor was considered as an overall parameter taking into account the bed porosity, tortuosity of the existing channels, surface area of the porous medium, etc.

For non-wetting liquids, which is the case of interest here, surface tension forces must be overcome for flow to be initiated. The pressure required to force the liquid through a constriction is given by Laplace's equation (7):

$$P_{BR} = \gamma_{LV} \left(\frac{1}{r_1} + \frac{1}{r_2} \right) \quad (1)$$

where r_1 and r_2 are the principal radii of curvature* of the liquid-vapor interface at any point on its surface.

The principal radii of curvature of the liquid surface in contact with a solid are a function of the geometry of the orifice and the contact angle, θ , between the solid and the liquid. Thus one can define

$$P_{BR} = \gamma_{LV} \left(\frac{1}{R_1} + \frac{1}{R_2} \right) \cos \theta \quad (2)$$

where R_1 and R_2 are the radii as defined by the orifice geometry. When the magnitude of $\cos \theta$ is equal to 1, the liquid is tangential to the solid surface and R_1 and R_2 become the principal radii of curvature.

When the liquid is not stationary but rather moving down the capillary, the contact angle is taken as the advancing contact angle, θ_A (8). In the dynamic situation, taking into account the advancing contact angle and the characteristic surface roughness of the particles

* Radii of curvature have the same sign if their centers of rotation lie on the same side of the interface. If the centers of rotation are on opposite sides of the interface, the radii of curvature have opposing signs (positive and negative). To be consistent with our definition of P_{BR} , a radius of curvature is assigned a negative sign when its center of rotation lies on the side of the interface occupied by the liquid.

gives rise to an apparent advancing contact angle, θ'_A (8,9,10). For a capillary of circular cross-section, R_1 and R_2 are equal to the capillary radius, $-r_c$. Eq. (2) is then modified to:

$$P_{BR} = - \frac{2\gamma_{LV}}{r_c} \cos \theta'_A \quad (3)$$

For penetration of a liquid into a capillary of non-circular cross-section, when radii of curvature are not well defined, an alternative approach (11) is to define an effective radius or hydraulic radius, m , as the ratio of the area of the orifice to the perimeter of the orifice, or as the ratio of the volume to the surface area of the pore.

$$m = \frac{A}{L} = \frac{\text{area of orifice}}{\text{perimeter of orifice}} \quad (4)$$

or alternatively

$$m' = \frac{V}{A} = \frac{\text{volume of pore}}{\text{surface area of pore}} \quad (5)$$

The breakthrough pressure can then be defined in terms of the hydraulic radius, m :

$$P_{BR} = - \frac{\gamma_{LV} \cos \theta'_A}{m} \quad (6)$$

For a capillary of circular cross-section, $m = \frac{r_c}{2}$, and the use of the hydraulic radius concept yields a breakthrough pressure which is identical to the one obtained by the use of the radii of curvature approach, Eq. (3).

The usual packing of spheres into a mold can be approximated by an orthorhombic arrangement giving a porosity of about 40% (12).

Irrespective of the packing arrangement and total porosity of the bed, the smallest pore will be the interstitial site formed by three touching spheres on a given cross-sectional plane. The latter interstitial site can also be thought of as a triangular orifice, as illustrated in Fig. 2a. It can be safely assumed that a differential fluid element will have to penetrate through such a minimum constriction site during flow through the maze-like medium. Thus, the PV will yield or become operable at the "maximum" breakthrough pressure corresponding to the "minimum" constriction site.

Taking into consideration two distinctly different liquid phase geometries within the triangular orifice and the corresponding hydraulic radii gives rise to two different breakthrough pressures. For the case shown in Fig. 2a, $m = 0.0257d$ and

$$P_{BR} = -38.9 \left[\frac{\gamma_{LV}}{d} \right] \cos \theta_A' \quad (7)$$

whereas for the case shown in Fig. 2b, $m = 0.0387d$ and

$$P_{BR} = -25.84 \left[\frac{\gamma_{LV}}{d} \right] \cos \theta_A' \quad (8)$$

where d is the diameter of the beads in the particle bed. Previously, Langford and Cunningham (1) have used an approximate breakthrough pressure for non-wetting liquids:

$$P_{BR} = \left[\frac{20\gamma_{LV}}{d} \right] \quad (9)$$

Mayor and Stowe (13) offer a theoretical breakthrough pressure which takes into account the fact that the porosity of the bed and the

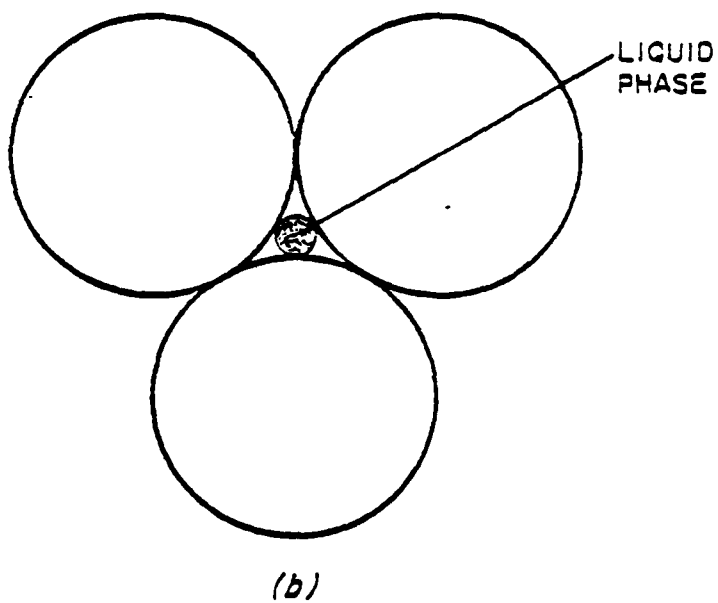
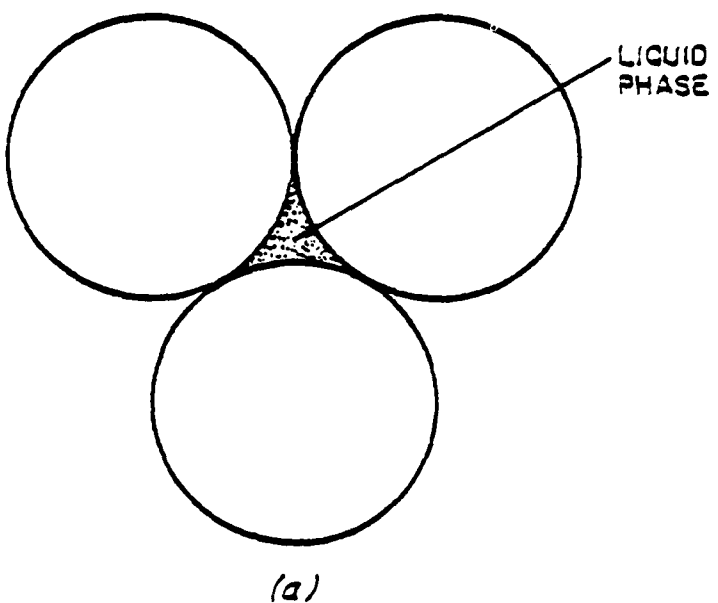


Figure 2. Model of triangular orifice and liquid phase geometries considered in calculating the breakthrough pressure using the hydraulic radius concept.

contact angle of the fluid affect the actual geometry of the liquid within the orifice. Assuming a similar triangular orifice as shown in Fig. 2a and a contact angle of 180°, their breakthrough pressure is:

$$P_{BR} = \frac{22.64 \gamma_{LV}}{d} \quad (10)$$

Frevel and Kressley (14) have carried out an extensive analysis of the observed breakthrough pressure in mercury porosimetry, and offer an expression for the breakthrough pressure as a function of γ_{LV} , bed porosity, radii of curvature, and wetting characteristics such as the extent of interfacial contact between the liquid and spherical particles (Eq. (8), Ref. 14). For a triangular orifice similar to the one considered here, Frevel and Kressley's expression becomes (Eq. (13), Ref. 14):

$$P_{BR} = -17.66 \left(\frac{\gamma_{LV}}{d} \right) \cos \theta \quad (11)$$

The hydraulic radius, m , can easily be calculated when the liquid wets the pore surface as is the case when the triangular orifice is completely filled with the liquid phase. Flow equations thus derived confirm well the experimental results (6). For the case of a non-wetting fluid, a similar approach using the hydraulic radius, m , cannot be satisfactorily used since it has no physical significance, but one must rather consider the surface tension forces which are influenced by the magnitude and sign of the radii of curvature.

The approach taken here accounts for the actual curvatures of the fluid as it goes through the critical constriction site formed by uniform-sized spheres. The triangular constriction site envisioned is

shown in Fig. 3a. Two cross-sectional views of the liquid within the constriction site, one parallel to the plane of the paper and the other perpendicular, are shown in Figs. 3b and 3c, respectively. For this particular liquid surface, the radii of curvature can be approximated at a particular point, point D - Fig. 3b. One radius, R_1 , is fixed by the boundary constraint due to the shape of the beads and is identical to the radius of the beads:

$$R_1 = d/2 \quad (12)$$

At point D, the radius R_2 of the liquid surface can be expressed as a function of the radius of the inscribed circle in the triangular orifice, r_c .

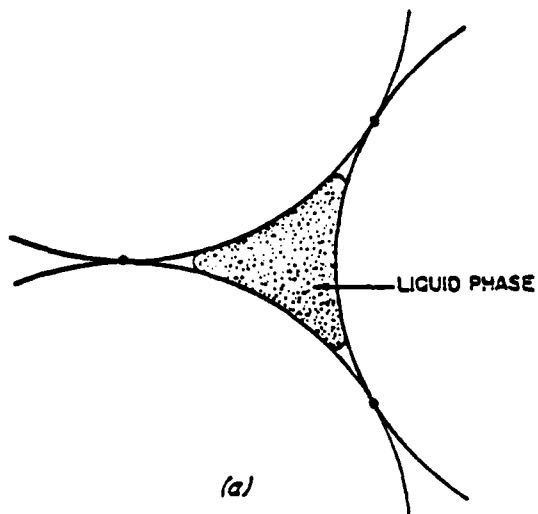
$$R_2 = -r_c \quad (13)$$

However, the radius of the inscribed circle, r_c , can be easily expressed as a function of the diameter of the spherical beads, d . Geometrical considerations lead to the result

$$R_2 = -r_c = -\frac{d}{2} \left(\frac{4}{3} \sin \frac{\pi}{3} - 1 \right) \quad (14)$$

Applying the above values in the fundamental expression, Eq. (2), gives:

$$P_{BR} = -10.928 \left(\frac{\gamma_{LV}}{d} \right) \cos \theta_A' \quad (15)$$

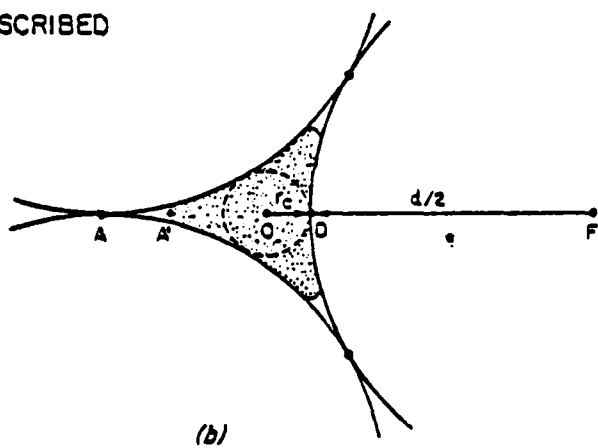


$\frac{d}{2}$ = RADIUS OF SPHERICAL PV PARTICLE

r_c = RADIUS OF INSCRIBED CIRCLE

$$R_1 = \frac{d}{2}$$

$$R_2 = -r_c$$



(b)



(c)

Figure 3. Model of liquid phase geometry used to develop the breakthrough pressure via the radii of curvature approach.
 (a) Triangular orifice and assumed liquid phase geometry;
 (b) Cross-sectional view of liquid parallel to the plane of the paper;
 (c) Cross-sectional view of liquid perpendicular to the plane of the paper.

3.3 EXPERIMENTAL PROCEDURE

Tin and mercury were chosen as the model liquids since both are non-wetting to Al_2O_3 , relatively reliable surface tension data is available, and the required experimental setup was greatly facilitated by the low melting point of both tin and mercury.

Sn/ Al_2O_3 System

A schematic diagram of the apparatus used is shown in Fig. 4. The graphite crucible containing the PV and the melt had two openings at the bottom. The first opening contained an open-ended thermocouple wired to a recorder, which signaled liquid infiltration of the PV when the thermocouple became short circuited. The second opening was connected to a tube open to the atmosphere. The crucible was enclosed in a pressure vessel and was then evacuated and backfilled with argon. The pressure differential between the top of the melt and the bottom of the PV was measured by a manometer placed between points 10 and 11, Fig. 4.

Commercial grade A tin was used. Both irregular and spherical Alcoa tabular alumina particles of various sizes were used to construct the PV. These particles were carefully machine sieved and then hand sieved into different mesh size ranges. A layer of fiberfrax* and -325 mesh ($<45\mu\text{m}$) alumina powder below the PV protected the two bottom openings of the crucible against clogging with liquid tin following breakthrough. Similarly, -325 mesh ($<45\mu\text{m}$) alumina powder

* Manufactured by The Carborundum Company, Niagara Falls, N.Y.

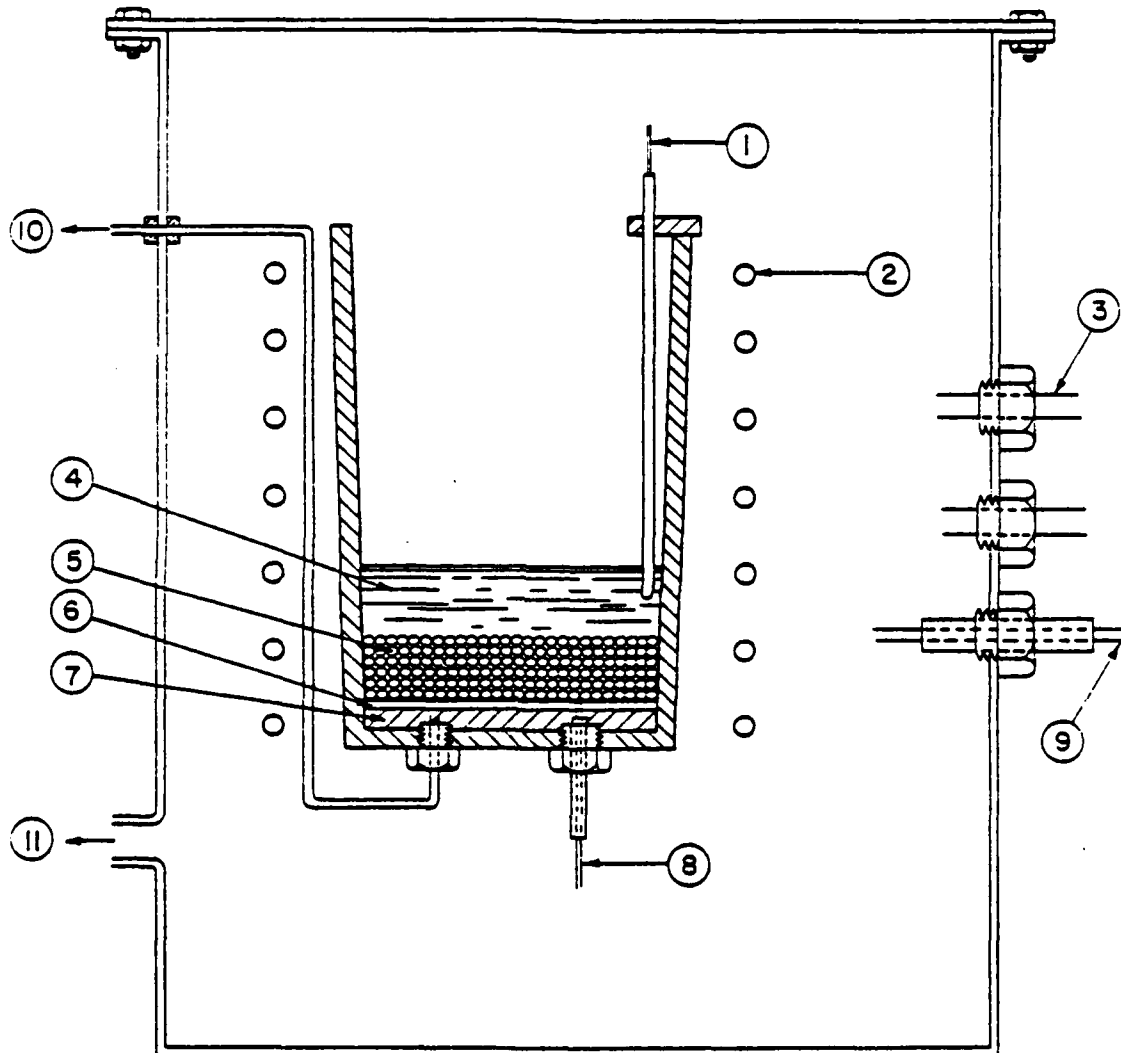


Figure 4. Schematic diagram of the apparatus used for measuring breakthrough pressures for the Sn/Al₂O₃ system. 1. Thermocouple; 2. Induction coil; 3. Induction coil leads; 4. Melt; 5. PV (Al₂O₃ beads); 6. Fine Al₂O₃ powder; 7. Fiberfrax; 8. Open-ended thermocouple; 9. Thermocouple leads; 10. Tube open to atmosphere via a valve and bubble tube*; 11. Vacuum and gas pressurization. * Points 10 and 11 are connected by a manometer.

around the edges of the PV insured that the liquid tin did not leak along the smooth sides of the crucible, where the packing of the particles was relatively less efficient.

After assembling a 1.5 cm high PV in the graphite crucible, solid tin was carefully emplaced, connections for the temperature recorder and induction coils were made, and the pressure vessel was evacuated and back filled with argon. Audio frequency induction heating (@ 4.2 kHz) was employed for melting and maintaining the temperature of the liquid tin at 300°C. A chromel/alumel thermocouple was used for recording and monitoring the temperature of the melt. During melting and equilibrating, the pressure inside the vessel was maintained at one atmosphere. Temperature of the melt was kept constant at 300°C in all the experiments. Upon temperature equilibration the bottom of the crucible was opened to the atmosphere via the valve and bubble tube - point 10, Fig. 4. The argon pressure inside the vessel was increased until the open-ended thermocouple indicated breakthrough of the liquid through the PV. The required pressure was duly noted at the manometer.

Hg/Al₂O₃ System

Since the Hg/Al₂O₃ system did not require heating or temperature monitoring, a different setup was used with essentially the same logic as in the Sn/Al₂O₃ experiments. The PV was assembled in a long quartz cylinder of 3.8 cm diameter and argon was used for pressurization.

3.4 RESULTS AND DISCUSSION

Particle Valve Performance

i) Required Breakthrough Pressures

Experimentally measured breakthrough pressures with different Al_2O_3 particle size ranges are given in Tables I and II, respectively, for the $\text{Sn}/\text{Al}_2\text{O}_3$ and $\text{Hg}/\text{Al}_2\text{O}_3$ systems.

In the available literature no data could be found on contact angles between Hg and Al_2O_3 . Allen and Kingery (15) have measured the contact angles of Sn on Al_2O_3 in vacuum at temperatures ranging from 800°C to 1470°C. They report values of θ (stationary contact angle) as 162° at 800°C, 167° at 1100°C, and 166° at 1200°C. The contact angle of Sn on Al_2O_3 at 300°C cannot be extrapolated from Allen and Kingery's data. Moreover, they have measured the stationary contact angle - a stationary drop resting on a finely polished surface - which is quite different from the apparent advancing contact angle, θ'_A . In a dynamic situation the advancing contact angle is always greater than the stationary contact angle, and the receding contact angle is smaller than the stationary contact angle (9). Furthermore, the surface roughness of the solid substrate should be considered since it also influences the apparent contact angle. For liquids with contact angle greater than 90° the effect of surface roughness is to increase the apparent advancing contact angle, θ'_A (8,9,10). Thus, the apparent advancing contact angle can be as much as 50° to 60° greater than measured stationary contact angle (8). For purposes of calculations here, the value of the apparent advancing contact angle, θ'_A , is

assumed to be 180° , so that $\cos \theta'_A = -1$ (if θ'_A had an actual value of 165° , the error in the value of $\cos \theta'_A$ would only be 3.4% since $\cos 165^\circ = -0.966$).

For the $\text{Sn}/\text{Al}_2\text{O}_3$ system, using a value of 580 dyne/cm (580 mN/m) (15) for γ_{LV} and taking the advancing contact angle, θ'_A , to be 180° , a linear regression for analysis of the experimentally measured breakthrough pressures, P_{BR} , as a function of the average particle diameter, d , yields (Table I) a factor of 11.1 versus the theoretical factor of 10.928 in Eq. (15). Similarly, for the $\text{Hg}/\text{Al}_2\text{O}_3$ system using values of 485 dyne/cm (485 mN/m) (16) for γ_{LV} and 180° for θ'_A , a linear regression analysis of the experimentally measured breakthrough pressures, P_{BR} , as a function of the average particle diameter, d , yields (Table II) a factor of 10.9. Measured breakthrough pressures for both the $\text{Sn}/\text{Al}_2\text{O}_3$ and $\text{Hg}/\text{Al}_2\text{O}_3$ systems as a function of particle size are plotted and shown in Figs. 5 and 6, respectively.

Calculated theoretical breakthrough pressures from Eq. (15) and the corresponding percent difference from the experimental values are given in columns 6 and 7 of Tables I and II for the $\text{Sn}/\text{Al}_2\text{O}_3$ and $\text{Hg}/\text{Al}_2\text{O}_3$ systems respectively. The maximum error for the $\text{Sn}/\text{Al}_2\text{O}_3$ system is 13.86% and for the $\text{Hg}/\text{Al}_2\text{O}_3$ system is 10.0%. The maximum errors occurred at low breakthrough pressures where large diameter particles were employed. The inherent experimental error involved in measuring the metallostatic head above the PV and the manometer reading is ± 0.15 inHg (0.51×10^3 Pa). At 2.0 inHg (6.5×10^3 Pa), this would imply a 7.5% error. In light of the error inherent to the experimental setup itself, the existing maximum errors between the theoretical and

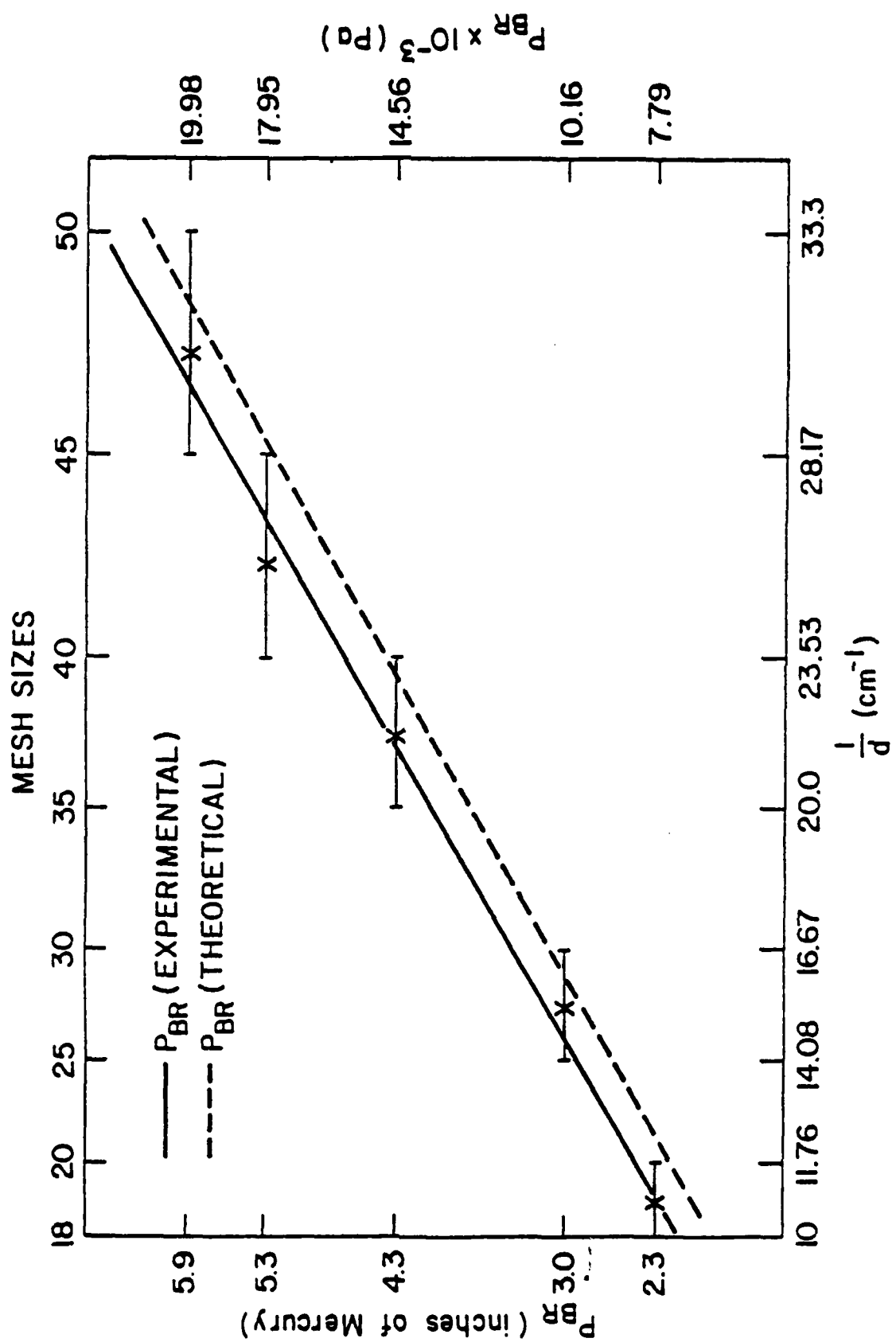


Figure 5. Theoretical and experimental breakthrough pressure for the Sn/Al₂O₃ system.

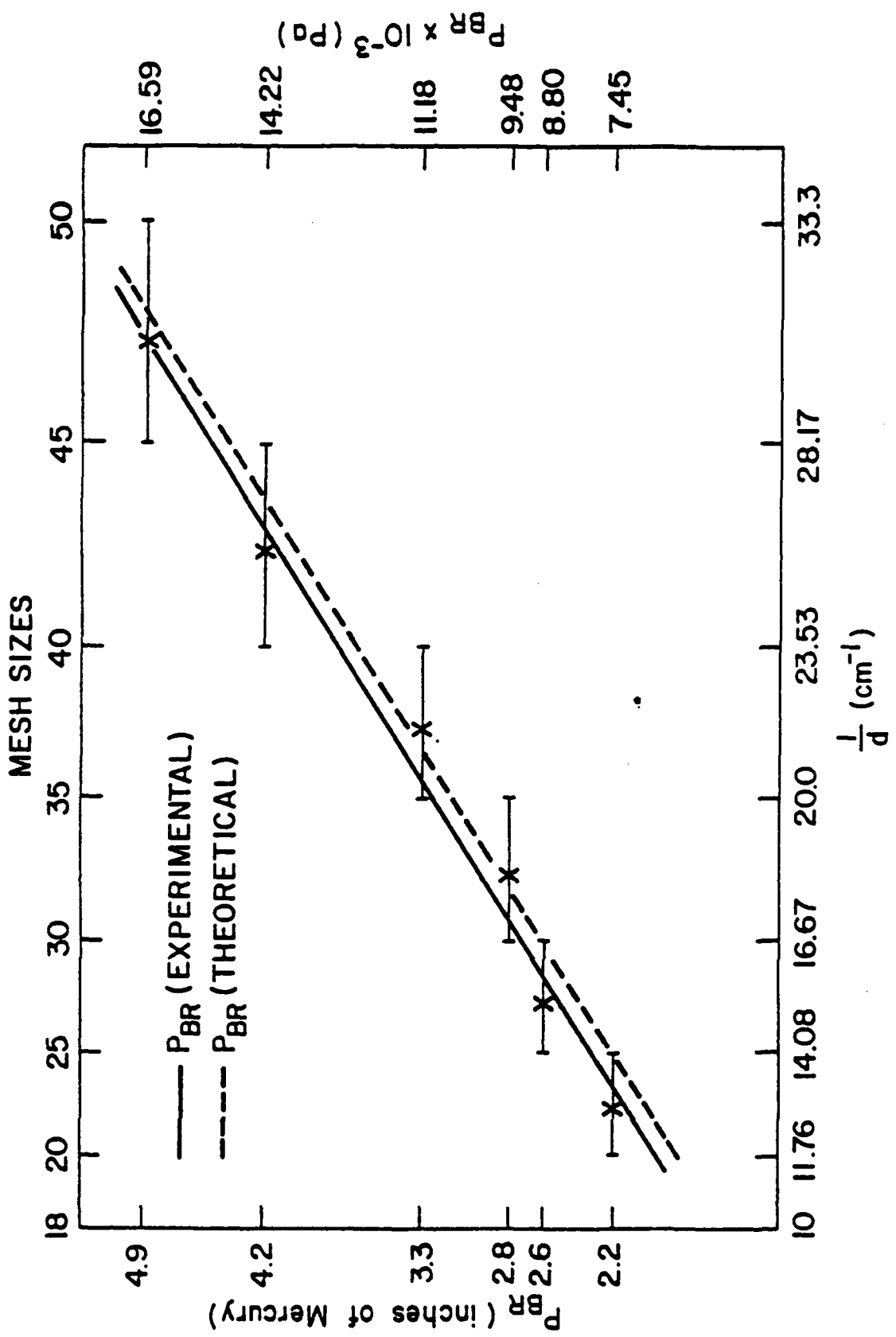


Figure 6. Theoretical and experimental breakthrough pressure for the $\text{Hg}/\text{Al}_2\text{O}_3$ system.

experimental values, 13.86% and 10.0% for the Sn/Al₂O₃ and Hg/Al₂O₃ systems, are acceptable.

Frevel and Kressley (14) have carried out mercury porosimetry studies on the Hg/glass microbeads system. Their experimentally measured and derived breakthrough pressures (Eq. (8), Ref. 14) are respectively given, columns 3 and 4, Table III. Better agreement between experimental and theoretical values is obtained when comparing Frevel and Kressley's experimental data with the breakthrough pressure derived in the present study, Eq. (15); see Table III. This further confirms the validity of the theoretical analysis of the required breakthrough pressure.

Figure 7 is a graphical representation of the theoretical breakthrough pressure P_{BR} as a function of particle diameter, for the steel/Al₂O₃ system. The breakthrough pressure, P_{BR} , is expressed in "inches of steel", and hence corresponds to the maximum supportable metalloc-static head, h_c , for steels. The values used for γ_{LV} and ρ are 1500 dyne/cm (1500 mN/m) and 7 gm/cm³ respectively.

ii) Reliability of the Particle Valve

To evaluate whether the measured breakthrough pressures were reproducible in terms of packing efficiency of the particles, four experiments using -16, +20 mesh (850 to 1180μm) irregular particles and two experiments in each size range with -18, +20 mesh (850 to 1000μm) and -25, +30 mesh (600 to 710μm) spherical particles were carried out. Measured breakthrough pressures varied by only ±0.1 inHg (0.34 x 10³Pa) for each of the above size ranges, whereas

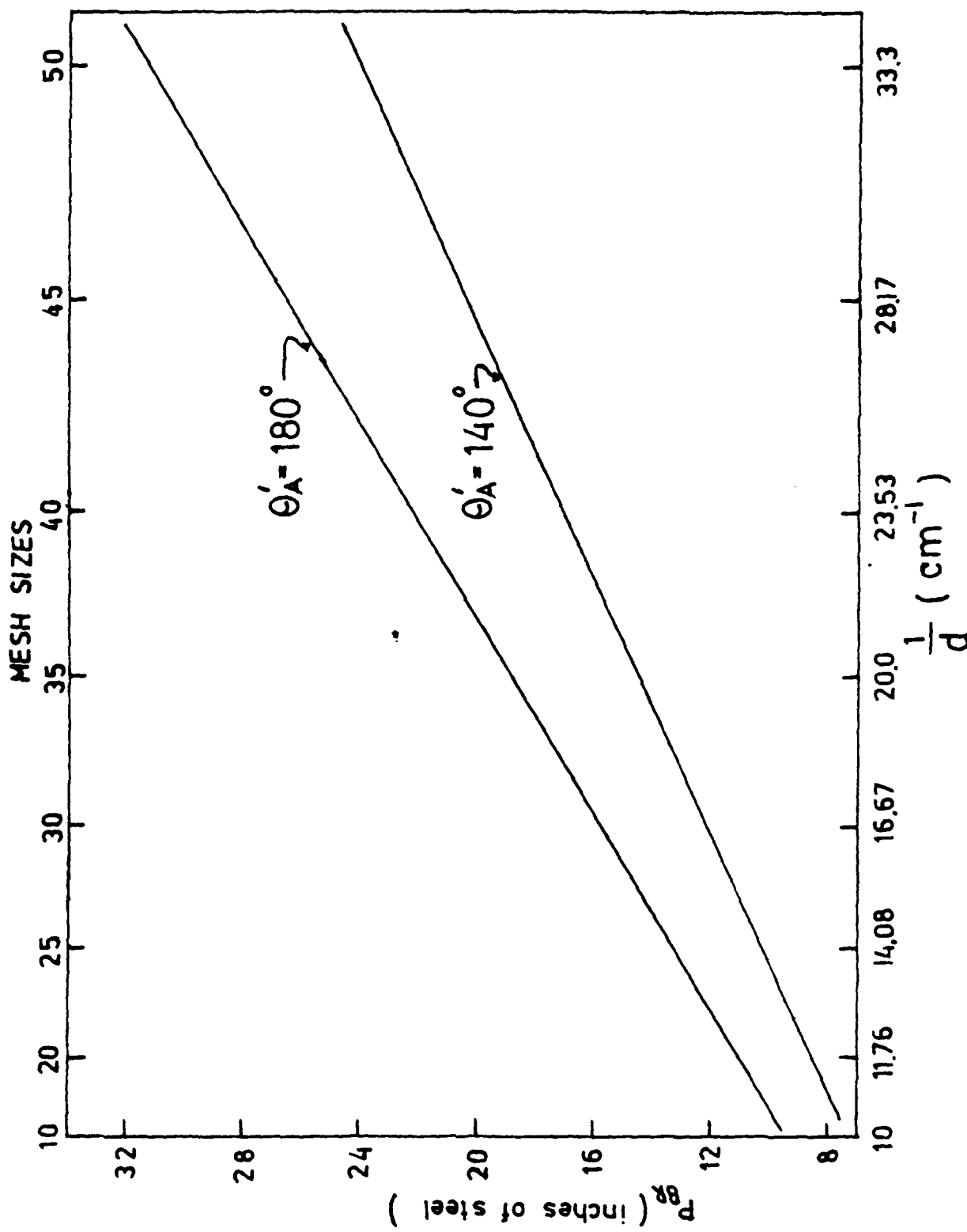


Figure 7. Calculated breakthrough pressures for Fe-based melt/Al₂O₃ system. Breakthrough pressure, P_{BR} , is expressed in "inches of steel" and corresponds to maximum supportable metallostatic head, h_c .

the accuracy of the experimental setup was ± 0.15 inHg (0.51×10^3 Pa).

Hence, under static conditions the PV gives repeatable results.

iii) Spherical vs. Irregular Particles

Irregular and spherical particles of the same size range, -18, +20 mesh (850 to 1000 μ m) were used in experiments #1 and #10 (Table I) with the Sn/Al₂O₃ system. The required breakthrough pressure for irregular particles has been found to be 10% lower than that for spherical particles. Theoretically it is difficult to model breakthrough pressure for nonspherical particles since the radii of curvature cannot be easily defined or measured.

iv) Particle Valve Height

Particle valve height does not affect the breakthrough pressure as long as there exist a few layers of well packed particles which remain undisturbed by the motion of the liquid above the particles. By the same reasoning the cumulative porosity of the bed is immaterial as long as the liquid has to pass through constricted triangular openings of the type shown in Fig. 3a. In run #8 (Table I - Sn/Al₂O₃ system with -16, +20 mesh (850 to 1180 μ m) particles) doubling the height of the PV did not cause any significant change in the breakthrough pressure (1.9 inHg (6.4×10^3 Pa) as compared to 1.8 inHg (6.1×10^3 Pa), the variation being within the experimental error).

Flow of the liquid through the PV is sudden rather than gradual. This was verified experimentally by slowly cooling liquid Sn from 300°C while maintaining a constant pressure of 1.5 inHg (5.1×10^3 Pa) equal

to 83% of the actual failure pressure for -16, +20 mesh (850 to 1180 μ m) irregular particles. Inspection of the system after solidification of the tin showed no sign of leakage into the PV.

Disruption Mechanism of the Particle Valve

A bed of packed (unbonded) particles may be disrupted via mechanical and/or buoyancy forces causing premature leakage of the liquid through the PV. Three disruption mechanisms have been identified and modeled. For each mechanism the required critical variables to avoid failure are given.

i) Failure Due to Direct Impingement of Liquid Droplets on the Particle Valve (Splash Mechanism)

The small spheres forming the PV behave as a thixotropic fluid because of their smooth surfaces and open packing and can easily be disturbed by mechanical forces. Assuming that a pool of metal does not exist above the particle bed, on first filling the vessel the liquid metal droplets falling onto the top surface layer of the PV can easily disrupt it, causing leakage. Particularly for the case when the liquid metal possesses a much higher density than the Al₂O₃ particles (as in the case of molten steel), the momentum of the falling droplets may cause mechanical disruption of the particles. When a small liquid pool rests on the particle bed, a droplet impinging on the pool will cause splashing of the liquid and will thus lose part of its energy in doing so; however, the droplet may still possess enough energy to cause mechanical disruption of the particles.

To avoid failure by this mechanism requires that the energy needed to displace (splash away) a volume of liquid, whose depth is equal to the height of the liquid pool, h , be greater than the energy of the falling liquid droplet, see Fig. 8. The energy of a drop of radius, R , falling from a height H above the liquid pool is $4\pi R^3 \rho g H / 3$, where ρ and g are the density of the liquid and the acceleration due to gravity, respectively.

Two different energy terms need to be considered: (i) the energy required to create a new surface taking into account surface tension forces, and (ii) the energy spent during displacement of the liquid. The energy required to form a new surface, an exposed area having an equivalent diameter h , is given by $\pi h^2 \gamma_{LV}$. The energy required to displace the liquid pool during the formation of the exposed area of diameter, h , is given by (weight of displaced liquid) \times (the displaced distance). The energy spent in displacing the liquid can then be expressed as: $\frac{4}{3}\pi(\frac{h}{2})^3 \rho g(\frac{h}{2})$. Thus the criterion to avoid failure of the PV becomes

$$\frac{4}{3}\pi R^3 \rho g H \leq \pi h^2 \gamma_{LV} + \frac{4}{3}\pi(\frac{h}{2})^3 \rho g(\frac{h}{2}) \quad (16)$$

The height, H , from which a liquid droplet of radius, R , can fall without causing failure of the PV via the splash mechanism is given by:

$$H_{splash} \leq 0.25 h^2 R^{-3} \left(\frac{3\gamma_{LV}}{\rho g} + 0.25 h^2 \right) \quad (17)$$

Figure 9 is a graphical representation of the fail/safe boundary as given by Eq. (17) for three different droplet radii impinging onto

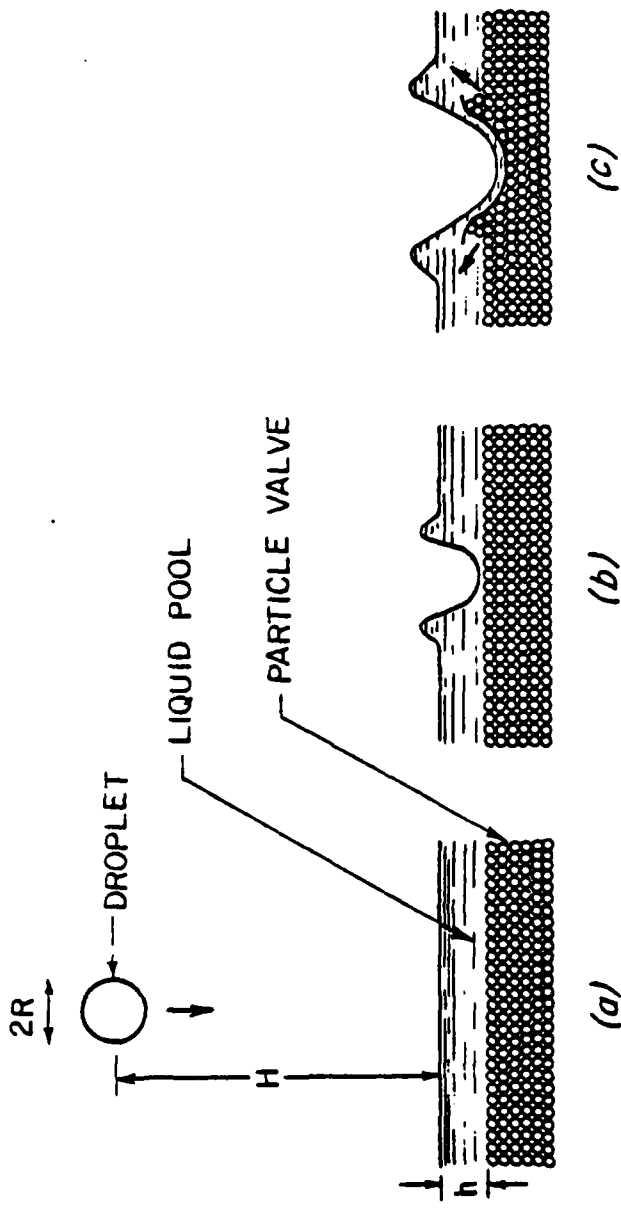


Figure 8. Splash mechanisms: Liquid droplet splashing the liquid pool and disturbing the particle bed mechanically causing failure of the PV.

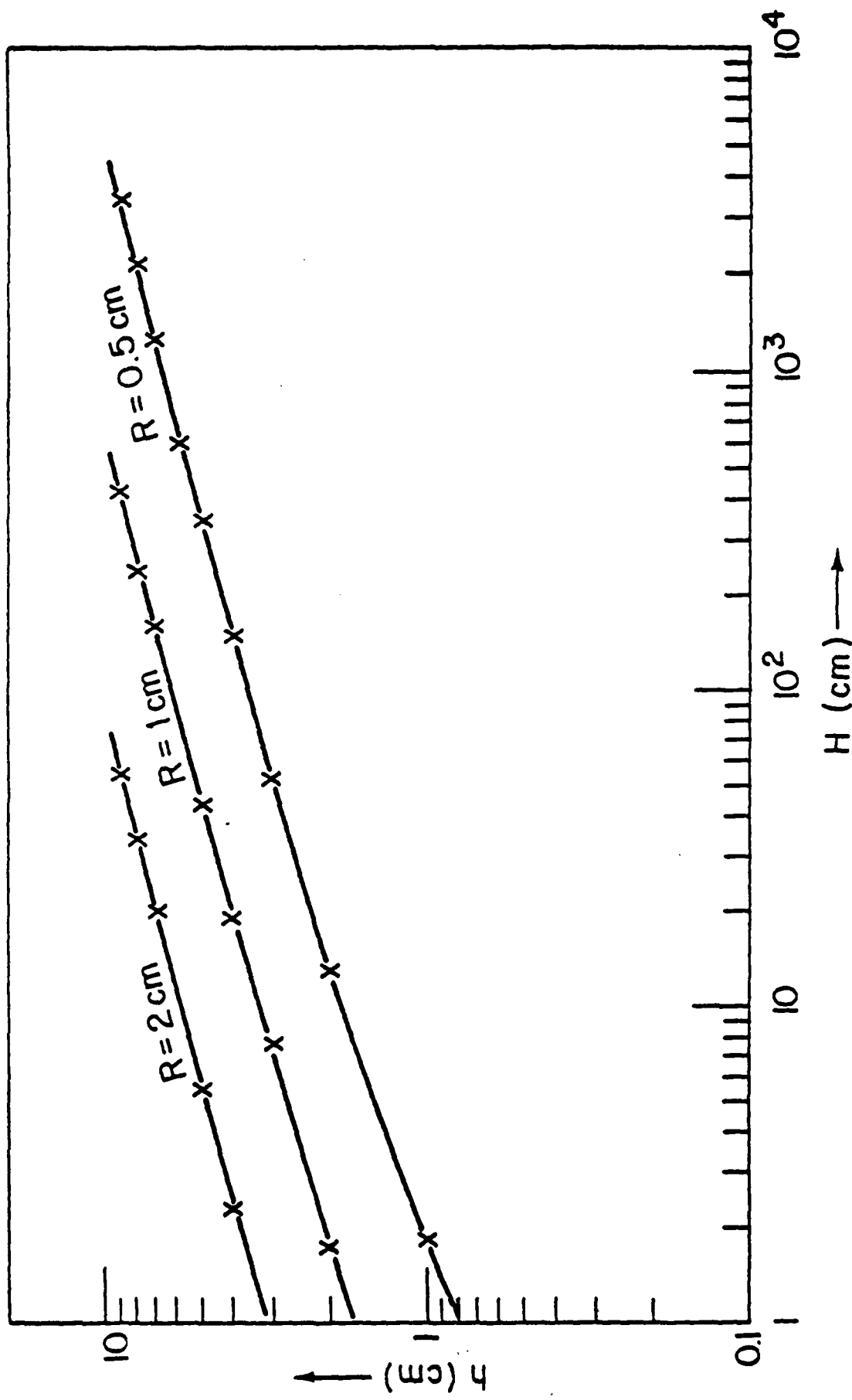


Figure 9. Graphical representation of the governing criterion to avoid failure of the PV via splash mechanism, Eq. (17). For a droplet of radius, R , combinations of allowable pool depth, h , and height from which the droplet falls, H , are to the left of the curve.

a liquid steel pool. The values used are $\gamma_{LV} = 1500 \text{ dyne/cm}$ (1500 mN/m) and $\rho = 7 \text{ gm/cm}^3$. The area to the left of each curve gives combinations of pool depth, h , and height of the impinging droplet, H , that will allow for a safe operation of the PV. Any combination of process variables to the right of each curve will cause failure of the PV by the splash mechanism.

ii) Failure by Augmented Hydrostatic Pressure Caused by an Impinging Liquid Droplet

In this mechanism it is assumed that the impinging droplet does not splash away the liquid but transmits all its energy to the liquid pool by formation of a hemispherical pressure wave which propagates through the entire pool depth. The total pressure acting on the PV is the sum of the static pressure head due to the liquid above it and a dynamic pressure head caused by the propagating pressure wave.

To avoid failure, the total pressure (static plus dynamic), $P_{(S+D)}$, should be less than the maximum supportable static pressure, ρgh_c . The imposed criterion is:

$$P_{(S+D)} \leq \rho gh_c \quad (18)$$

The maximum kinetic pressure of the droplet on the liquid pool is given by ρgH , where H is again the droplet fall height. When the radius of the droplet, R , is greater or equal to the pool depth, h , there is no enough liquid in the pool for propagation of a pressure wave, and hence at the PV the dynamic pressure is equal to ρgH .

Applying the criterion as given by Eq. (18) yields the height from which droplets can impinge on the liquid pool without causing failure:

$$H_{\text{augmented}} \leq h_c - h \quad (\text{for } R \geq h) \quad (19)$$

When the radius of the droplet, R , is less than or equal to the pool depth, h , the resultant dynamic pressure component will vary inversely as the square of the distance from the impact area (property of propagating spherical waves). The total (static + dynamic) head, $P_{(S+D)}$, at the PV will be:

$$P_{(S+D)} = \rho g H \left(\frac{R}{h}\right)^2 + \rho gh \quad (\text{for } R \leq h) \quad (20)$$

where ρ is the density of both the liquid pool and the droplet, R is the radius of the droplet, and h is the depth of the liquid pool. The existing pool depth, h , can be expressed as some fraction of the maximum supportable static head or the critical height, h_c (i.e., $h = f h_c$). By use of Eq. (18) the maximum height H from which a liquid droplet of radius R can fall without causing failure of the PV is:

$$H_{\text{augmented}} \leq \left(\frac{h_c}{R}\right)^2 f^2 (1 - f) h_c \quad (\text{for } R \leq h) \quad (21)$$

Figure 10 is a graphical representation of the fail/safe boundary as given by Eqs. (19) and (21) for three different droplet radii. The values used for steel are $\gamma_{LV} = 1500 \text{ dyne/cm}$ (1500 mN/m), $\rho = 7 \text{ gm/cm}^3$, and $h_c = 10 \text{ cm}$ (corresponding to a PV with particles of diameter, $d = 0.24 \text{ cm}$, θ_A' assumed to be 180°). The area to the left of each curve gives combinations of pool depth, h , and height of the

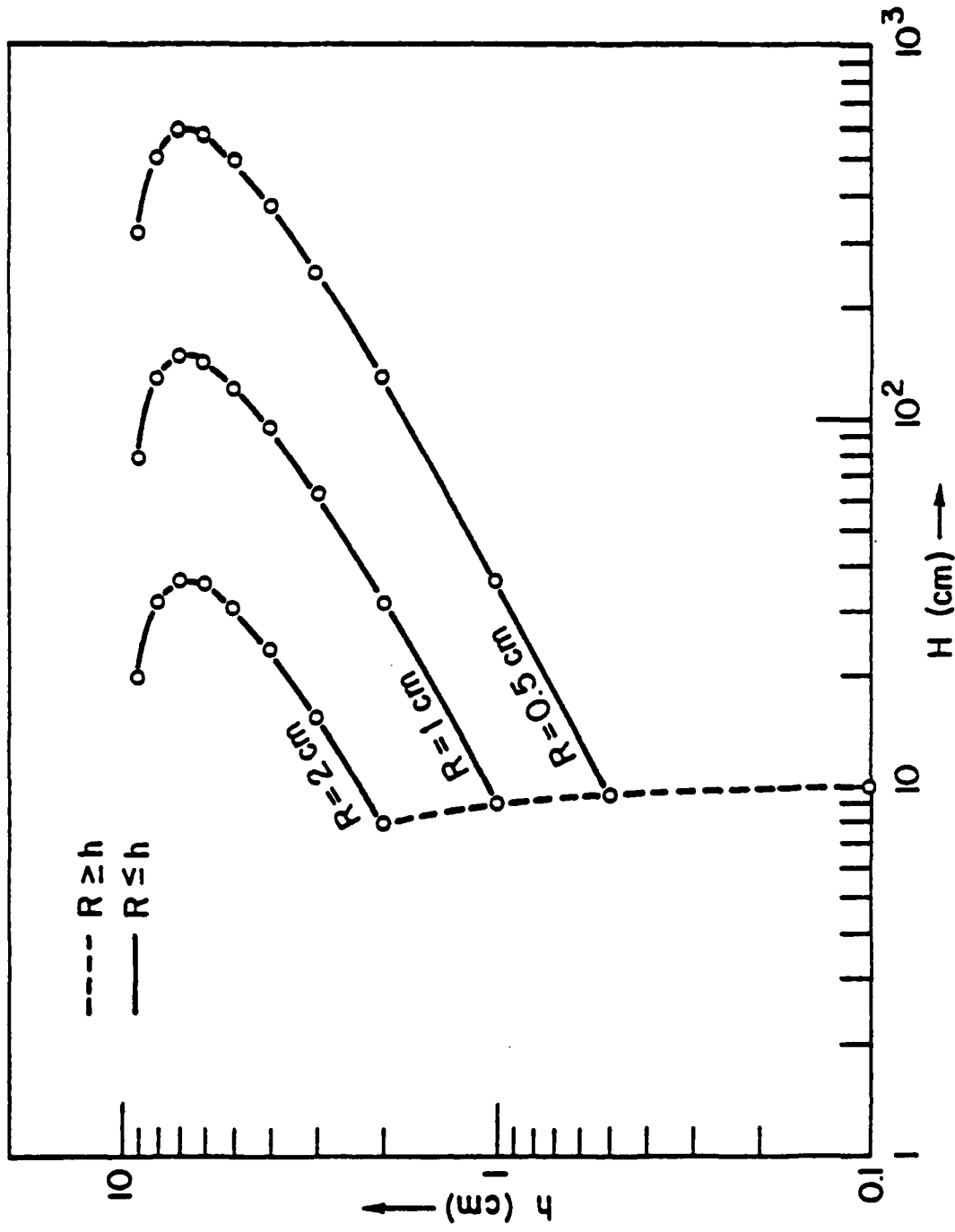


Figure 10. Graphical representation of the governing criterion to avoid failure of the PV via augmented pressure mechanism, Eqs. (19) and (21). For a droplet of radius, R , combinations of allowable pool depth, h , and height from which the droplet falls, H , are to the left of the curve. Maximum supportable metollostatic head, $h_c = 10 \text{ cm}$.

impinging droplet, H, that will allow for safe operation of the PV. Any combination of process variables to the right of each curve will cause failure of the PV by the augmented pressure mechanism.

A PV can either be bonded or unbonded. That is, the PV can either be a porous sintered mass or an aggregate of loosely packed particles. When the PV is bonded, the particles cannot be dislodged by mechanical forces and thus only the augmented failure mechanism need be considered. However, for an unbonded PV, both of these mechanisms should be considered as plausible failure mechanisms.

Figure 11 shows the behavior of Eqs. (17), (19) and (21) for a droplet of radius $R = 0.5$ cm. The values used for steel are $\gamma_{LV} = 1500$ dyne/cm (1500 mN/m), $\rho = 7$ gm/cm³, and $h_c = 10$ cm (corresponding to a PV with particles of diameter $d = 0.24$ cm, θ'_A assumed to be 180°).

Regions of allowable combinations of h and H for both bonded and unbonded particle valves are shown. The plots of Fig. 11 indicate that, for an unbonded PV during the initial stages when the liquid pool depth is still low, the splash mechanism is controlling. At higher pool depths the augmented pressure mechanism takes over. In contrast, for a bonded PV the safe operable region is the area enveloped by the plot for the augmented pressure mechanism of failure.

Figure 12 is a graphical representation similar to Fig. 11 of the two failure mechanisms for droplets of radius, $R = 1.0$ cm and 2.0 cm. The maximum supportable head, h_c , is taken as 10 cm ($d = 0.24$ cm, $\theta'_A = 180^\circ$) and 100 cm ($d = 0.024$ cm, $\theta'_A = 180^\circ$).

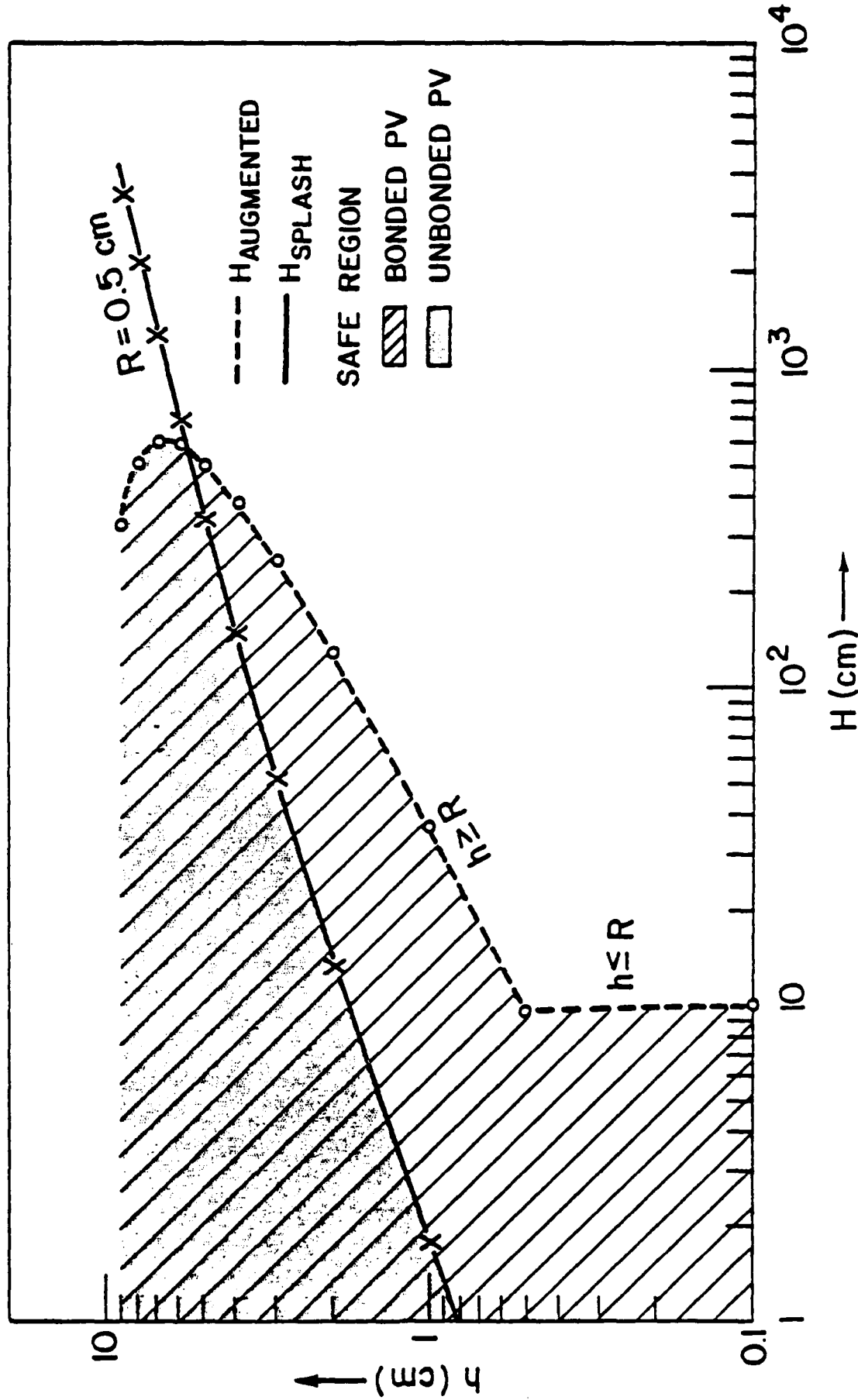


Figure 11. Fail-safe region of process variables for bonded and unbonded particle valves when both splash and augmented pressure mechanism are operable. The radius of the droplet, $R = 0.5 \text{ cm}$, and the maximum supportable metallocstatic head, $h_c = 10 \text{ cm}$.

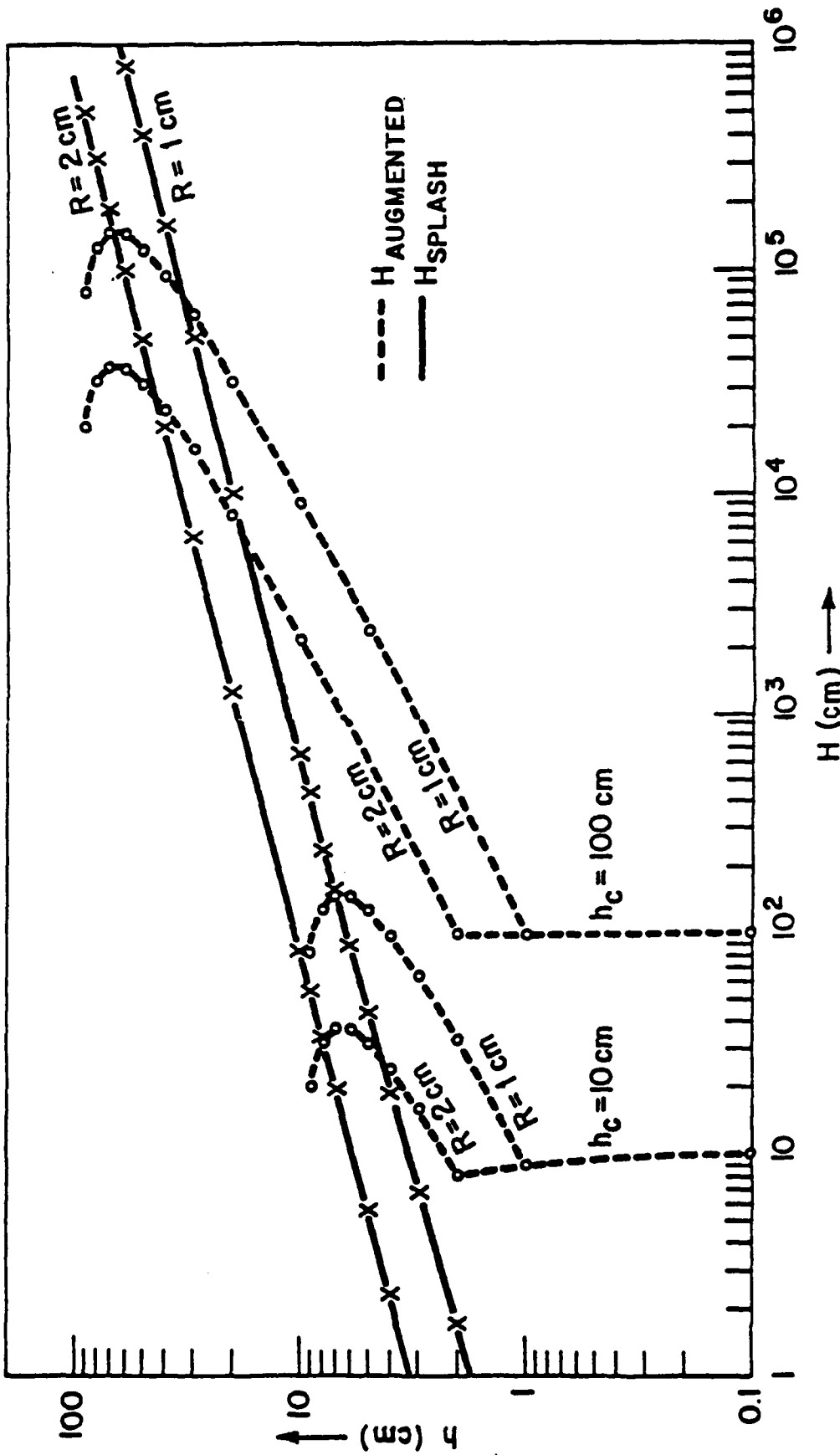


Figure 12. Criteria for failure of PV by splash and augmented pressure failure mechanism for different droplet radii, R , and maximum supportable metallocstatic head, h_c .

iii) Failure Due to Buoyancy Forces Acting on Individual Particles - Flotation

Disintegration of the PV following breakthrough can occur due to density differences between the liquid phase and the particles. At breakthrough, the volume of pores between the particles is not completely filled with the liquid phase, resulting in an imbalance of forces and thus a net downward force on each particle. However, when pressures greater than the required breakthrough pressure are applied, the envelopment of each particle by the liquid phase will increase, and thus there may be a possibility of disruption of the PV due to the unbalanced buoyancy forces.

The pertinent forces have been calculated and are shown in Appendix 3A. The results indicate that the greater the applied infiltration pressure (expressed as a multiple N of the required breakthrough pressure), the greater the force holding down the particles. However, the larger the particles are, the more is the buoyant force, so that there is a critical size of particles above which the particles will float as soon as infiltration begins.

The restriction on d, diameter of the particles used, as derived in Appendix 3A, is:

$$d \leq \left(\frac{40.154 \gamma_{LV} N \sin^2 \alpha}{\Delta \rho g} \right)^{1/2} \quad (22)$$

where

$$N = \frac{\text{applied infiltration pressure, } P_i}{\text{breakthrough pressure, } P_{BR} \text{ (Eq. (15))}}$$

α = half angle describing the area of the particle not in contact with the liquid phase, see Fig. A2.

$\Delta\rho$ = density differential between the liquid phase and the alumina beads.

Table IV shows the calculated values of d , the critical particle diameter for the steel/ Al_2O_3 system below which disintegration of the PV will not occur following infiltration, for different values of $P_i = N \cdot P_{BR}$ (calculated by the use of Eqs. (A11) to (A14) as derived in Appendix 3A). It should be noted that for the steel/ Al_2O_3 system and for $P_i = P_{BR}$, the critical particle diameter is 1.73 cm (Table IV).

Effect of Impurity Contents in the Liquid

As has previously been shown, the breakthrough pressure for a particular size of refractory particles is a function of both the surface tension and contact angle. Hence, the surface tension and the apparent advancing contact angle for a particular melt/PV system need to be known fairly accurately for the correct estimation of the supportable metallostatic head. This is particularly important when the effect of alloying elements is considered; small traces of surface active elements in the melt may cause considerable reductions in the surface tension and contact angles.

Halden and Kingery (17) studied the effect of C, N, O and S on the liquid iron surface tension and interfacial energy with Al_2O_3 and arranged them as S > O > N > C in order of decreasing surface activity. They reported the value of surface tension, $\gamma_{LV} = 1632 \text{ dyne/cm}$

Table IV. Theoretical maximum particle diameter allowed, d , as a function of applied pressure, P_i , to avoid failure of the PV by flotation-steel/ Al_2O_3 system.

$n = \frac{d/2}{ R_1 }$	$\alpha(\text{degrees})$ $\cos^{-1} \left[\frac{n}{n+1} \right]$	$N^+ = f(\alpha)$	$d \text{ (cm)}^*$ critical particle diameter
7.6009	27.904	1.000	1.729
10	24.620	1.391	1.816
25	15.942	3.909	2.007
100	8.069	16.998	2.139
250	5.116	43.702	2.179
1000	2.561	178.921	2.209
2000	1.811	360.243	2.217

$$^+ N = P_i / P_{BR}$$

* Calculated using Eq. (A14).

Note: γ_{LV} (steel) = 1500 dyne/cm (1500 mN/m)

$$\Delta\rho = 4.5 \text{ gm/cm}^3 (4.5 \times 10^3 \text{ kg/m}^3)$$

$$g = 980 \text{ cm/s}^2$$

(1632 mN/m), and the contact angle $\theta = 147.5^\circ$ for a Fe-0.0077% O - 0.009% C - 0.005% S melt as compared to $\gamma_{LV} = 707$ dyne/cm (707 mN/m) and $\theta = 100.8^\circ$ for a Fe-0.0398% O - 0.004% C - 2.0% S melt. This would correspond to a 90% decrease in the calculated breakthrough pressure. Such drastic lowering of the $|\cos\theta|$ term with varying contact angles can render the PV completely unreliable; therefore, highly surface-active elements like S and O need to be carefully controlled. Elements which by themselves are not surface-active in the melt may be quite surface-active in the presence of each other (18).

Besides changing the surface energies of the system directly, the alloying elements can also cause premature failure of the PV by producing elemental metal vapor or a volatile metal-oxygen compound which can coat the refractory particles and thus change their wetting characteristics. Svoboda and Geiger (19) have shown that for the Fe-Mn system mass transport takes place by formation of volatile polynuclear oxides and that maximum vaporization into a porous aggregate occurs at oxygen partial pressures which are slightly less than those required for the liquid oxide to reach an equilibrium state. Furthermore, the vaporization stops when a liquid oxide layer is present - i.e., when partial pressure of oxygen is greater than the equilibrium pressure. Therefore, to prevent failure of the PV caused by diffusion of vapor species into the porous aggregate, metallic alloying elements that are easily volatized or form an easily volatized oxide are to be avoided.

3.5 CONCLUSIONS

1. An expression for the breakthrough pressure for the liquid to penetrate the PV has been derived: $P_{BR} = -10.928 \left(\frac{\gamma_{LV}}{d} \right) \cos \theta_A'$.
2. Experimental breakthrough pressures were measured in the Sn/Al₂O₃ and Hg/Al₂O₃ systems. Excellent agreement was found between the theoretical and experimental results.
3. Based on numerous experiments, it can be concluded that the PV is reliable; the required breakthrough pressure does not depend on the PV height; and spherical or irregular particles may be employed to construct the PV.
4. Three failure mechanisms of the PV have been observed, characterized and modeled. For each particular mechanism the criterion for safe operation of the PV is given.
5. For pool depths close to the supportable metallostatic head the dominant failure mechanism is by the augmented pressure mechanism, and thus both unbonded and bonded particle valves can be utilized.
6. When the pool depth above the PV is shallow, the dominant failure mechanism is by splashing of the liquid, and thus for shallow pool depths the use of a bonded PV is recommended.

REFERENCES

1. G. Langford and R. E. Cunningham: Met. Trans. B., 1978, Vol. 9B, pp. 5-19.
2. G. Langford and D. Apelian: J. of Metals, 1980, Vol. 32, No. 9, pp. 26-33.
3. G. Langford: Materials Science and Engineering, 1977, Vol. 25, pp. 275-284.
4. A. E. Scheidegger: The Physics of Flow Through Porous Media, 2nd ed., pp. 68-90, The MacMillan Co., New York, 1960.
5. A. E. Scheidegger: The Physics of Flow Through Porous Media, 2nd ed., pp. 115-119, The MacMillan Co., New York, 1960.
6. P. C. Carman: Trans. Inst. Chem. Eng. (London), 1937, vol. 15, pp. 168-188.
7. L. E. Murr: Interfacial Phenomena in Metals and Alloys, pp. 87-90, Addison-Wesley Publishing Co., Massachusetts, 1975.
8. N. K. Adam: Discuss. Faraday Soc., 1948, No. 3, pp. 5-11.
9. A. B. D. Cassie: Discuss. Faraday Soc., 1948, No. 3, pp. 11-16.
10. R. Shuttleworth and G. L. J. Bailey: Discuss. Faraday Soc., 1948, No. 3, pp. 16-22.
11. P. C. Carman: Discuss. Faraday Soc., 1948, No. 3, pp. 72-77.
12. L. C. Graton and H. J. Fraser: J. Geol., 1935, vol. 43, pp. 785-909.
13. R. P. Mayor and R. A. Stowe: J. Colloid. Sci., 1965, vol. 20, pp. 893-911.
14. L. K. Frevel and L. J. Kressley: Anal. Chem., 1963, vol. 35, pp. 1492-1502.
15. B. C. Allen and W. D. Kingery: Trans. TMS-AIME, 1959, vol. 215, pp. 30-37.
16. D. W. J. White: Metall. Rev., 1968, vol. 13, pp. 73-96.
17. F. A. Halden and W. D. Kingery: J. Phys. Chem., 1955, vol. 59, pp. 557-559.
18. P. Kozakevitch: Surface Phenomena of Metals, pp. 223-245, SCI Monogr. No. 28, London, 1968.
19. J. M. Svoboda and G. H. Geiger: Trans. TMS-AIME, 1969, vol. 245, pp. 2353-2371.

APPENDIX 3A

PARTICLE SIZE REQUIREMENT TO AVOID FAILURE OF THE PV BY BUOYANCY FORCES

APPENDIX 3A

PARTICLE SIZE REQUIREMENT TO AVOID FAILURE OF THE PV BY BUOYANCY FORCES

Consider a particle which is resting above three other particles as shown in Fig. A1. Following infiltration of the liquid phase through the PV, the forces acting on this individual particle are the buoyant force, B , and the resultant downward vertical force, F , resulting from the applied infiltration pressure, P_i .

The buoyant force is given by

$$B = \frac{4}{3}\pi \left(\frac{d}{2}\right)^3 \Delta\rho g \quad (A-1)$$

where $\Delta\rho$ = density differential between the liquid phase and the particles

d = diameter of the particles.

The total downward force F must take into account the force F_i at each contact point of a particle with respect to the other particles. In the case when a particle is resting above three other particles, then we have three contact points. Therefore,

$$F = 3 F_i \cos \beta = (3) (P_i A_i) \cos \beta \quad (A-2)$$

where P_i = applied infiltration pressure

A_i = cross-sectional area of spherical cap not in contact with the liquid phase and equals πR_2^2 - Fig. A2.

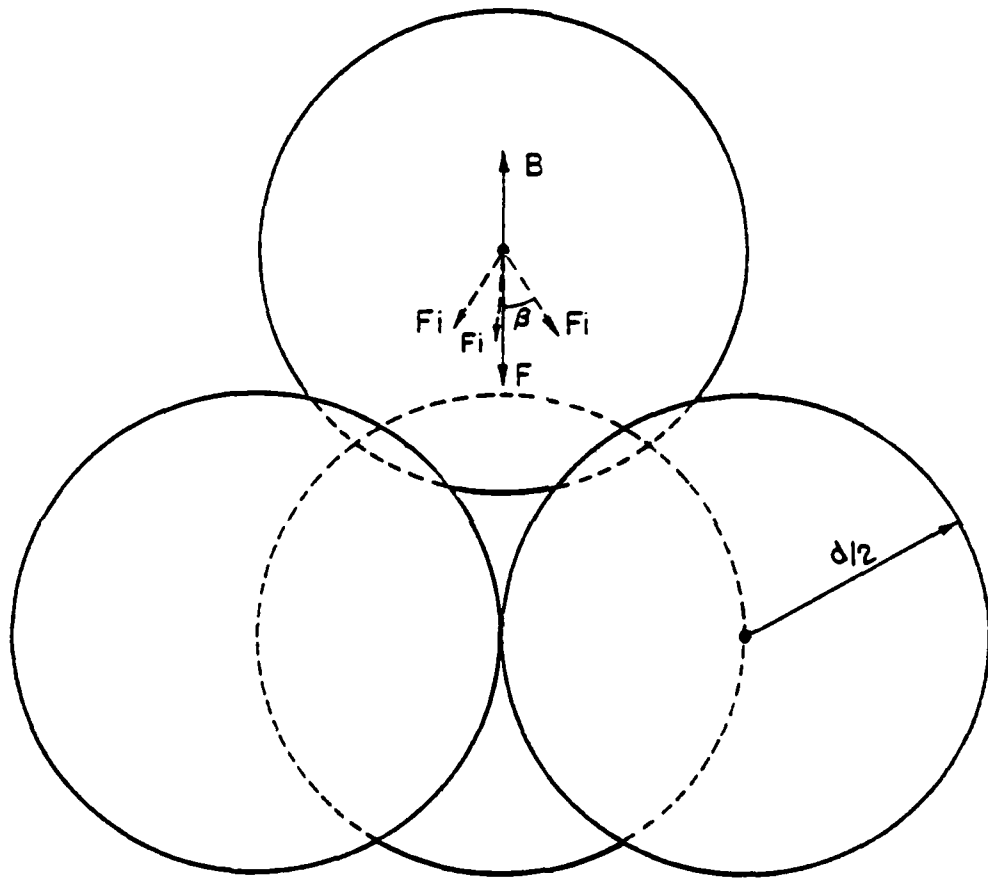


Figure A1. Forces acting on a particle (which is resting on three other particles) after the liquid has infiltrated the PV.

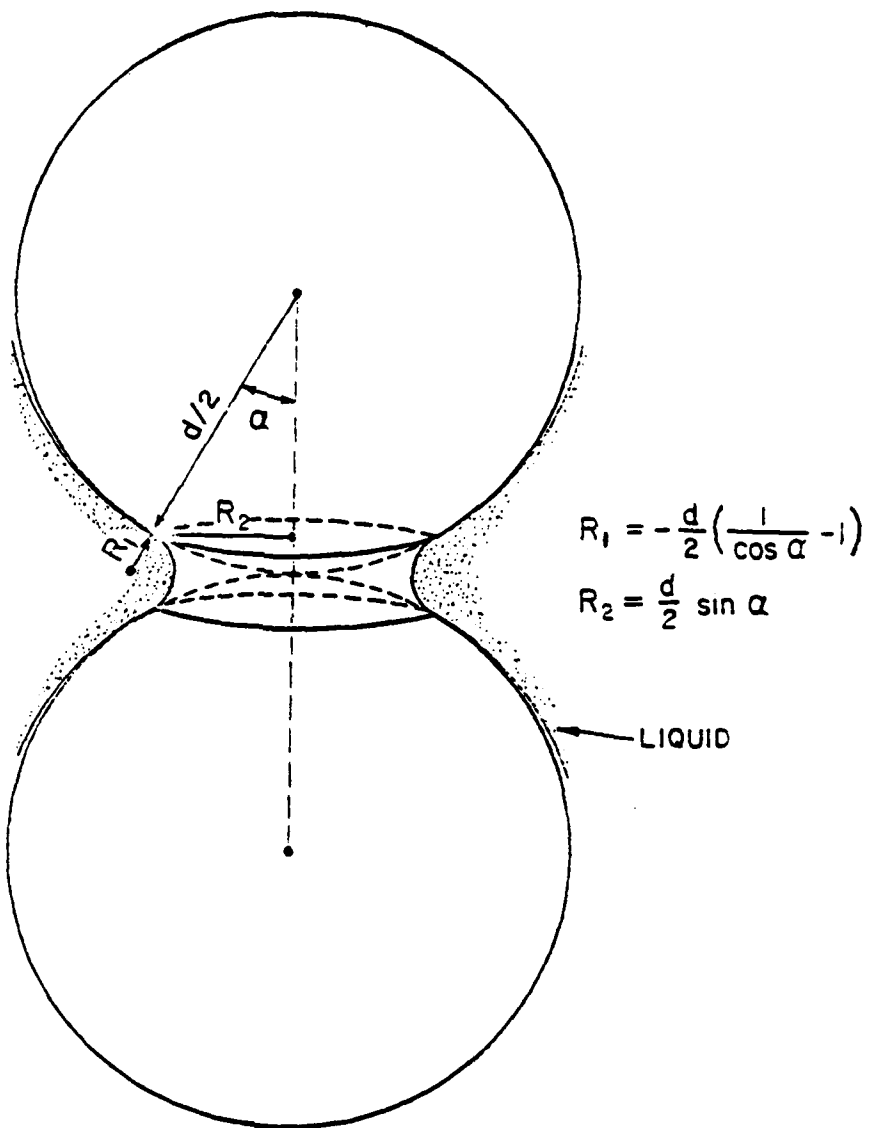


Figure A2. Geometry of liquid, around two particles, following infiltration of the PV.

$\cos \beta$ = direction cosine; β being the angle between the net downward force and the force applied at each contact point. In this case $\beta = 35.26^\circ$.

To express the applied infiltration pressure, P_i , as a function of the particle size of the beads and the required breakthrough pressure, one must first calculate the pertinent radii of curvature. Figure A2 shows the assumed geometry of the liquid meniscus at each particle contact point. From geometrical considerations, the radii of curvature, R_1 and R_2 , can be expressed as a function of α , the half angle sustained by the portion of the particles not in contact with the liquid.

$$R_1 = -\frac{d}{2} \left[\frac{1}{\cos \alpha} - 1 \right] \quad (A-3)$$

$$R_2 = \frac{d}{2} \sin \alpha \quad (A-4)$$

Substitution of Eqs. (A3) and (A4) in Eq. (2) gives the applied infiltration pressure, P_i . For the case when $\theta'_A = 180^\circ$

$$P_i = \frac{2\gamma_{LV}}{d} \left[\frac{\cos \alpha}{1 - \cos \alpha} - \frac{1}{\sin \alpha} \right] \quad (A-5)$$

For the same infiltration pressure, and when θ'_A is less than 180° the liquid meniscus will penetrate further, i.e., α will decrease. On the other hand, the theoretical breakthrough pressure, P_{BR} , as a function of the bed particle size is given by Eq. (15). The applied infiltration pressure can now be expressed as some multiple N of the required theoretical pressure

$$P_i = N \cdot P_{BR} \quad (A-6)$$

The use of the Eqs. (15), (A5) and (A6) yields N as a function of the half angle α :

$$N = \frac{\cos \alpha}{1 - \cos \alpha} - \frac{1}{\sin \alpha} \quad \text{(A-7)}$$

Substitution of the above in Eq. (A-2) yields the total downward force

$$F = 6.692 N \pi \gamma_{LV} d \sin^2 \alpha \quad \text{(A-8)}$$

To avoid failure by flotation of the beads, the net downward force, F, must be greater than the upward buoyancy force, B. Use of Eqs. (A-1) and (A-8) yields the criterion:

$$d \leq \left(\frac{40.154 \gamma_{LV} N \sin^2 \alpha}{\Delta \rho g} \right)^{1/2} \quad \text{(A-9)}$$

When N equals unity, then P_1 equals P_{BR} , and the angle α equals 27.904° - Eq. (A-7). Subsequently, for values of N greater than unity the angle α will be less than 27.904° .

Alternatively, we can define a variable n, the ratio of particle radius, $d/2$ to the magnitude of the radius, R_1 :

$$n = \frac{d/2}{|R_1|} = \left(\frac{1}{\cos \alpha} - 1 \right)^{-1} \quad \text{(A-10)}$$

(when N equals unity, α is equal to 27.904° and thus n, equals 7.6009).

The working relations are:

$$n = \frac{d/2}{|R_1|} \quad \text{(A-11)}$$

$$\alpha = \cos^{-1} \left(\frac{n}{n + 1} \right) \quad \text{(A-12)}$$

$$N = \frac{\left(\frac{\cos \alpha}{1 - \cos \alpha} - \frac{1}{\sin \alpha} \right)}{5.464} \quad \text{and} \quad (\text{A-13})$$

$$d \leq \left(\frac{40.154 \gamma_{LV} N \sin^2 \alpha}{\Delta \rho g} \right)^{1/2} \quad (\text{A-14})$$

4.

MANUFACTURE OF LOW CARBON STEEL SHOTOF CONTROLLED PURITY

C. LALL

H. SRESHTA

G. LANGFORD

SUMMARY

Apparatus for the gas atomization of liquid metals and decarburization of impure (high carbon, high oxyten) steel shot using CO/CO₂ mixture was designed and constructed. The operation and main features of the units are briefly described. The atomization unit was used to manufacture both the low carbon shot and the high carbon melt charge for use in the SD Process.

TABLE OF CONTENTS: Section 4. Manufacture of Low Carbon Steel Shot
of Controlled Purity

	<u>Page</u>
4.1 Introduction.	209
4.2 Gas Atomization of Liquid Metals.	209
4.3 Decarburization of Steel Powders.	215
References.	218
Appendices.	219
Appendix 4A: Degassing of Melts by Bubbling with Argon	220
Appendix 4B: Thermodynamics and Kinetics of Decarburization. . .	224

4. MANUFACTURE OF LOW CARBON STEEL SHOT OF CONTROLLED PURITY.

4.1 INTRODUCTION

Several phases of the present research program required high quality spheroidal metal particles as the starting raw material. The ability to produce the shot at Drexel University offered many advantages. The most important reason being that the metal particles must be of a consistently high quality which mandates that the manufacturing process be rigorously controlled and monitored. In SD castings it is important to minimize the total amount of oxygen as the ductility of the casting decreases with increasing content of oxides⁽¹⁾. A further reason for having our own facility is that it offers much more flexibility; virtually any metal or alloy may be atomized and the chemical composition of the shot may be modified as required. The ability to make alloy additions is also required since both the liquid and the shot will be prealloyed when making tool steels or high strength low alloy steels. There are many techniques for producing metal powders as described in recent reviews (e.g. Dixon⁽²⁾ and Lawley⁽³⁾). The method adopted at Drexel University involved the atomization of a liquid metal stream by a cross-current stream of inert gas and is described below in section 4.2.

Alternatively, methods by which high quality particles can be derived from commercially available impure shot have also been investigated. As described in section 4.3, a decarburization apparatus has been built in which impure shot is heated under a suitable atmosphere to decarburize or deoxidize and thus produce good quality shot.

4.2 GAS ATOMIZATION OF LIQUID METALS

Overall views of the gas atomization unit are shown in Figs. 1 and 2. The apparatus consists of two chambers (Fig. 2); an upper one to melt the charge and a lower one to break up the liquid stream and cool the atomized particles. A more detailed sketch of the melting furnace in the dome or upper chamber assembly is shown in Fig. 3.

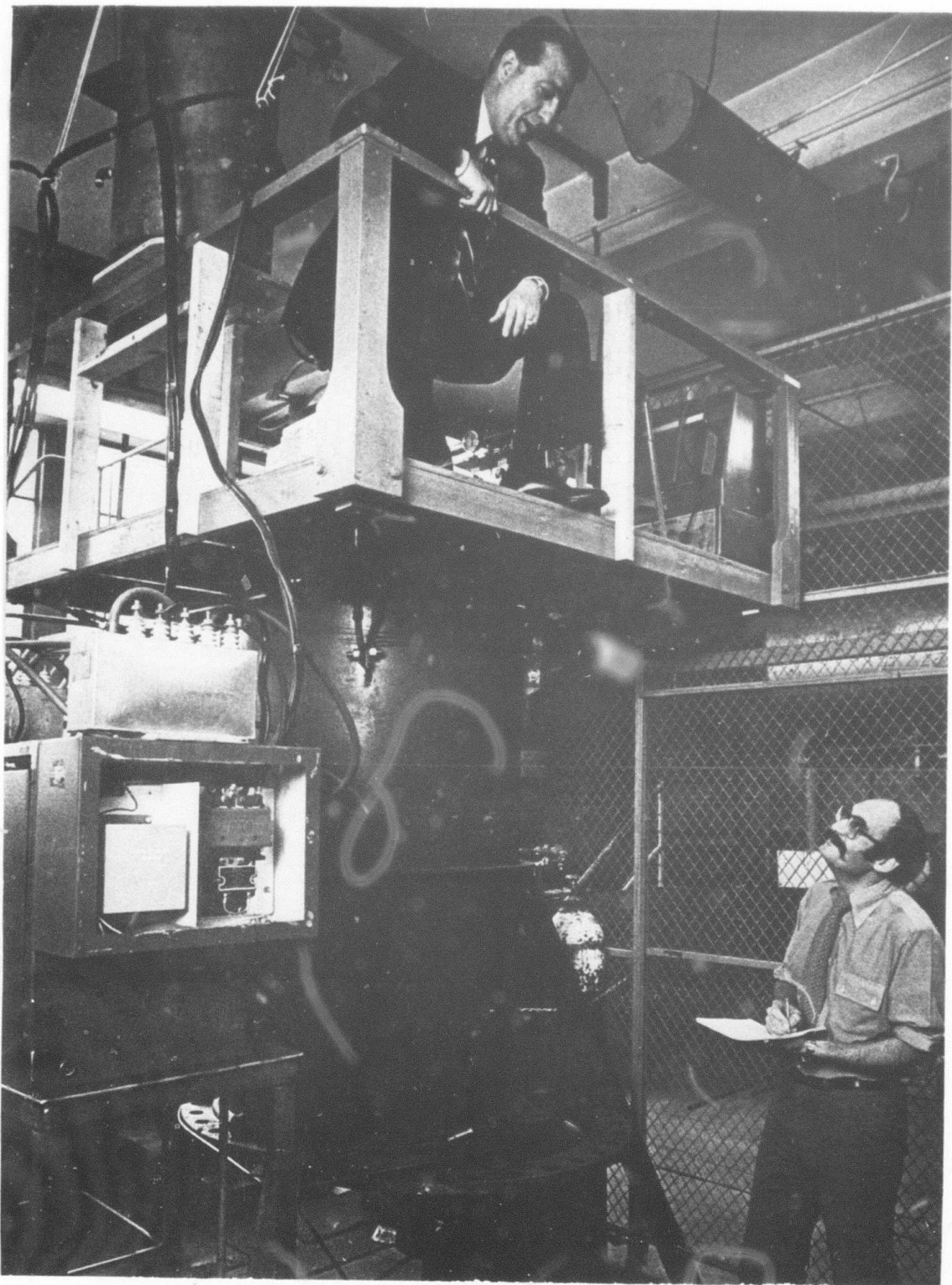
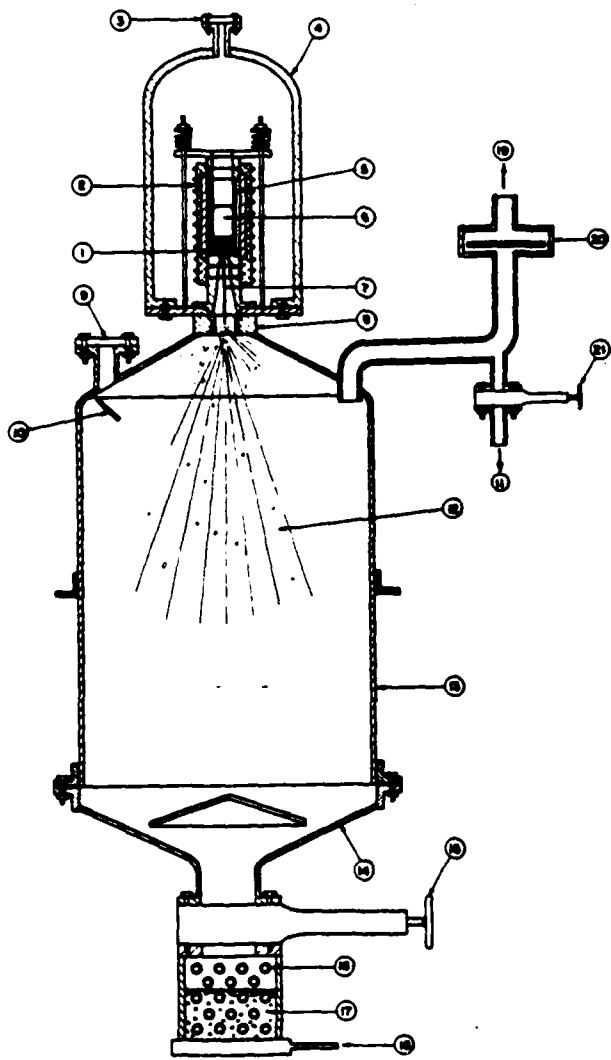


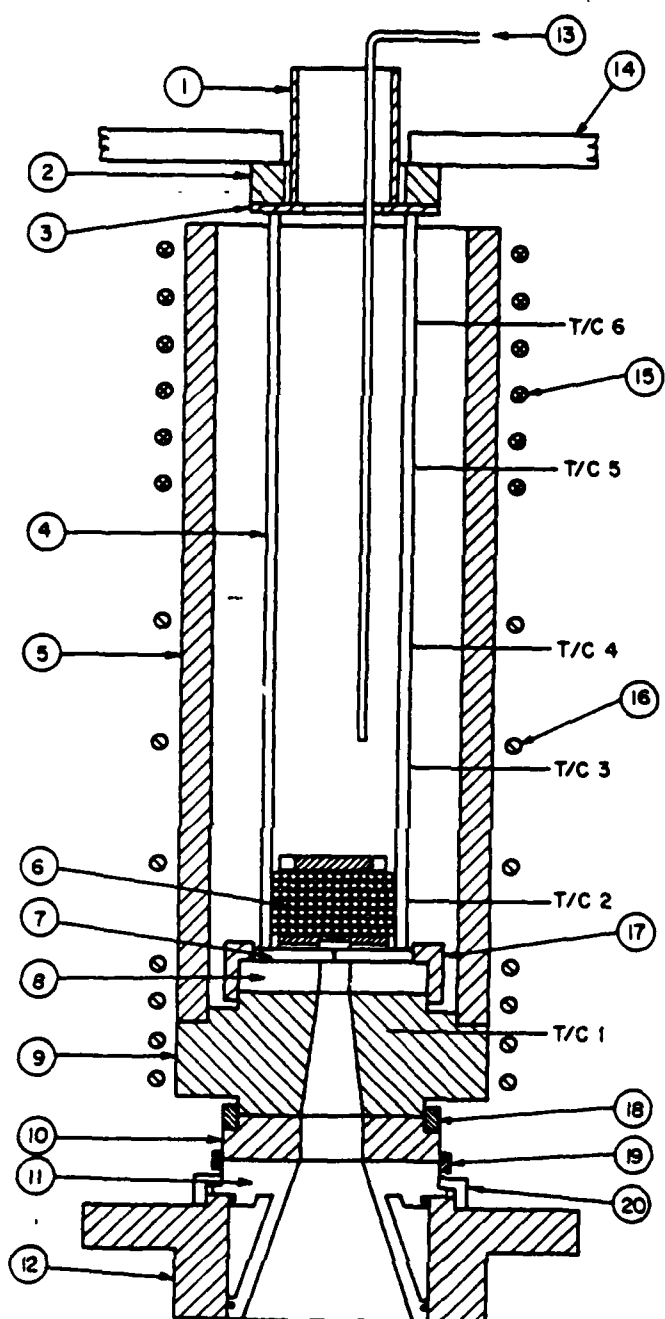
Figure 1. General view of the atomization unit showing the lower atomization or cooling chamber and the work stage.



KEY to Figure 2:

1. Orifice plate and particle valve.
2. Graphite-insulated, graphite cored 10 kHz induction furnace.
3. Sight glass and metal feed port.
4. Stainless steel bell jar (vacuum - and pressure - tight, 1.5 ft. diameter, 2.5 ft. tall)
5. Alumina crucible.
6. Iron alloy melt.
7. Stream of liquid metal.
8. Inert-gas atomization nozzles and manifold.
9. Sight glass.
10. Movable mirror.
11. Pipe to vacuum system.
12. Atomized shot and stream of inert gas.
13. Atomization chamber (vacuum-tight, 3 ft. diameter, 6 ft. tall).
14. Shot collection cone and baffle.
15. Vacuum valve.
16. Cooling-water tubes.
17. Fluidized bed of shot in cooling chamber.
18. Fluidizing-gas manifold.
19. Pipe to exhaust system.
20. Check valve (vacuum-tight).
21. Vacuum valve.

Figure 2. Schematic diagram of the atomization unit.



KEY to Figure 3:

1. Alumina protection tube.
2. Pyrolytic graphite insulator.
3. Alumina protection cover.
4. Alumina crucible.
5. Main graphite susceptor.
6. Particle valve.
7. Alumina orifice disc.
8. Alumina support plate.
9. Base susceptor (graphite).
10. Pyrolytic graphite insulator.
11. Stainless steel pedestal.
12. Pedestal base (water-cooled).
13. Alumina bubble tube.
14. Stainless steel clamp.
15. Upper induction coils.
16. Lower induction coils.
17. Graphite centering ring.
18. Graphite centering ring.
19. Stainless steel centering ring.
20. Hold-down ring.

Figure 3. Schematic diagram of the assembly inside the dome of the atomization unit.

The first step in the atomization process is to completely evacuate the whole system and back fill with inert gas. This is done twice to minimize the residual air in the system. A continuous, low, flow-rate of inert gas is maintained thereafter to keep the inside pressure greater than atmospheric.

The assembly inside the dome is heated by two induction coils which couple to the graphite suscepter (#5, Fig. 3). The heat is transferred to the alumina crucible, and thereby the melt, by radiation and gaseous conduction. When the crucible temperature is near 1600°C the charge, consisting of a half inch (13mm) diameter rod, is lowered through a teflon gland into the crucible. As the tip of the rod is melted off, more and more charge is introduced until a sufficient amount of melt is obtained.

The melt is accumulated above the particle valve (#6, Fig. 3), which consists of carefully graded alumina particles. This valve has two layers: 0.5 in (13mm) depth of coarse particles on top of which is 1.0 in (25mm) of fine particles. The size of the fine particles must be carefully chosen so as to sustain the pressure of the molten metal head but not so fine as to need excessive pressure to force liquid through to the orifice. The required breakthrough pressures as a function of particle size is derived in Chapter 3. The size of the coarse particles is not critical but should be less than seven times the diameter of the small particles so that the latter will not filter through. Metallostatic head of 6 inches (150mm) of 1018 steel was safely supported by -30, +35 mesh ($500\mu\text{m} < x < 600\mu\text{m}$) tabular alumina particles. The coarser layer consisted of -16, +18 mesh ($1000\mu\text{m} < x < 1180\mu\text{m}$) particles. The top of the particle valve is protected by a loose-fitting alumina disc, and the orifice is protected by an alumina baffle to prevent blockage by the coarse particles. A pressure of 15 psi (110 kPa) above the melt is more than adequate to push the liquid through the alumina bed.

When a sufficient amount of melt has been obtained, the steel may be deoxidized by bubbling with high purity argon, which also ensures vigorous mixing of the melt. Details of the deoxidation process and practice are given in Appendix 4A. At this stage any necessary alloy additions may also be made; FeO or CO may be added to control inclusion content.

The temperature variation along the length of the crucible has to be carefully controlled. To monitor the temperature, several thermocouples are inserted through the graphite susceptor and touch the outside of the crucible tube at various positions along its length. Another thermocouple is located below the orifice disc, in the graphite susceptor base. A potential problem is the precipitation of alumina in the orifice during atomization, since the liquid steel dissolves the crucible material. This may be overcome by keeping the steel slightly undersaturated with respect to alumina at the orifice, which is achieved by simply keeping the orifice slightly warmer than the melt. This leads to another problem which is encountered in the continuous casting of steels - orifice erosion (Singh⁽⁴⁾). However, in the present application the orifice diameter is not a crucial parameter so that the same orifice may be used for several runs, as long as the orifice temperature is maintained as low as possible during atomization.

Once the correct temperatures have been obtained the melt is ready to be pushed through the particle valve for subsequent atomization. This is achieved by collecting high pressure inert gas in an accumulator and opening it to the dome (rapid pressurization prevents "dribbling" at the orifice). The pressure differential between the dome and the lower chamber forces the liquid steel through the particle valve, the orifice and into the lower chamber. Inert gas at high pressure is emitted through radially positioned nozzles to break up the stream of liquid steel. Most of the metal particles solidify during their free fall and bounce their way to the bottom, cooling off as they do so. The cooling

rate of the steel particles may be altered by using gases of different conductivities (e.g. argon, nitrogen or helium) in the lower chamber. Excess gas is expelled through a large check valve (#20, Fig. 2).

A stainless steel baffle is used to prevent the shot or unatomized liquid from falling directly into the stainless steel container (catcher) at the bottom (Fig. 2). The latter is filled with inert gas, a fluidized bed with water-to-gas heat exchanger, or cooled with liquid nitrogen in order to cool the shot to room temperature. Representative steel shot produced via the above described atomization process are shown in Fig. 4.

4.3 DECARBURIZATION OF STEEL POWDERS

As an alternative to the gas atomization process, high quality steel particles can be made from less pure forms which are readily available commercially. The high levels of carbon and/or oxygen present in the commercial material must be removed before it is useful for SD casting. This may be achieved by use of a decarburization furnace, shown schematically in Fig. 5. A suitable ratio of gases ($\text{CO}/\text{CO}_2/\text{N}_2$) is premixed and forced through a bed of iron particles which serves to preheat the incoming gas mixture. The mixture passes through a tube and then into the region where the impure shot is contained. The unit is designed to allow analysis of both the incoming and the outgoing gases. Appendix 4B gives the reactions involved in the decarburization process and presents calculations on the thermodynamics and kinetics of the process.

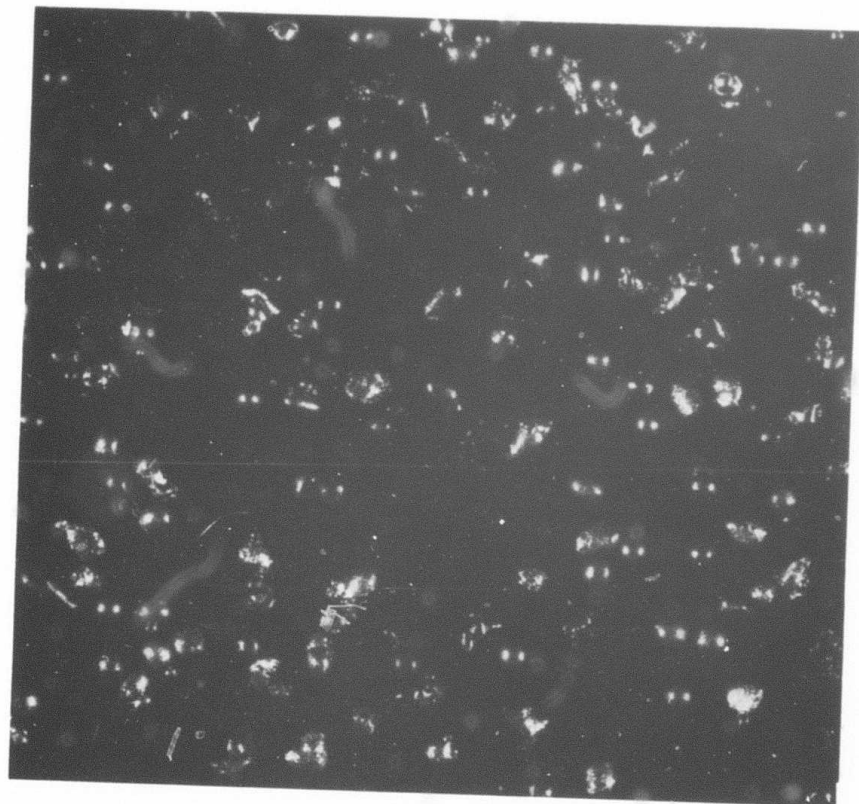


Figure 4. 1018 steel shot produced in one of the preliminary atomization tests (Run #5b). Magnification 10X.

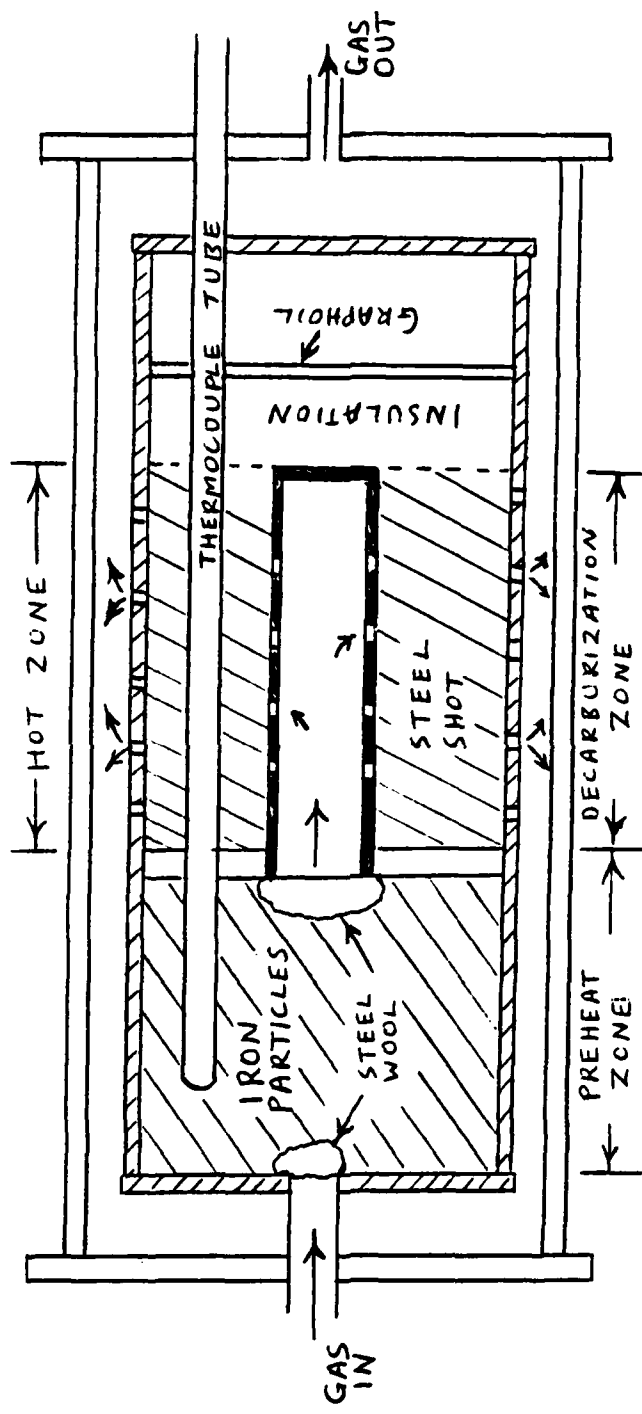


Figure 5. Schematic diagram of the decarburization furnace.

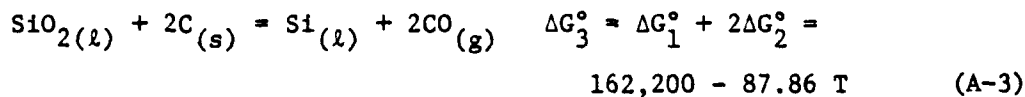
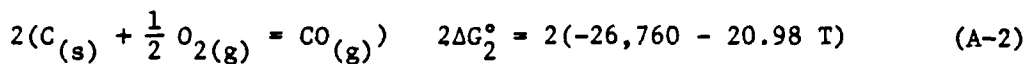
REFERENCES

1. D. Apelian and G. Langford: Rapid Cycle Steel Casting, Proposal submitted to ARPA, January 24, 1977.
2. C. F. Dixon: Can. Met. Quart. (1973), 12, 309.
3. A. Lawley: Int. J. Powder Met. and Powder Tech. (1977), 13, 169.
4. S. N. Singh: Met. Trans. (1974), 5B, 2165.
5. J. F. Elliot, M. Gleiser, V. Ramakrishna: "Thermochemistry for Steel-making" (1963) Addison-Wesley, U.S.A.
6. D. R. Gaskell: "Introduction to Metallurgical Thermodynamics", McGraw-Hill, New York (1973) 497.
7. S. Ban-ya, J. F. Elliot, J. Chapman: Met. Trans. (1970), 1, 1313.
8. W. Jost: "Diffusion in Solids, Liquids, Gases", Academic Press, New York (1960), p. 45.

APPENDICES

APPENDIX 4A DEGASSING OF MELTS BY BUBBLING WITH ARGON

The limiting factor on oxygen removal by bubbling of the melt is the stability of SiO_2 and Al_2O_3 . The initial step is to determine the partial pressures of CO at which reduction of these oxides occurs.

a) Silica

$$\Delta G^\circ = -RT \ln K$$

$$\text{or} \quad K = \exp \left(-\frac{\Delta G^\circ}{RT} \right) \quad (\text{A-4})$$

$$\text{For reaction (A-3)} \quad K = \frac{(a_{\text{Si}})(P_{\text{CO}})^2}{(a_{\text{C}})^2} = \frac{2 \times 10^{-6} (P_{\text{CO}})^2}{(2.5 \times 10^{-3})^2}$$

(Assume $a_{\text{SiO}_2} = 1$)

$$\text{Also,} \quad K = \exp \left(-\frac{162,200}{1.987T} + \frac{87.86}{1.987} T \right)$$

$$= \exp \left(-\frac{8.1622 \times 10^4}{T} + 44.21 \right)$$

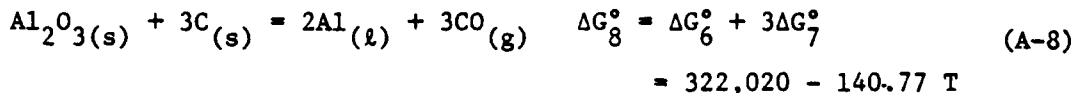
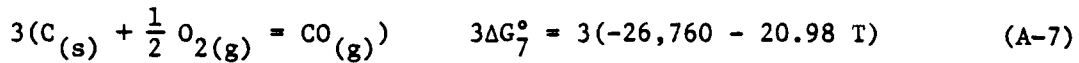
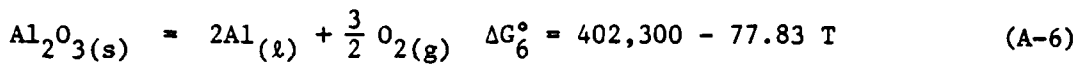
$$(P_{\text{CO}})^2 = \frac{(2.5 \times 10^{-3})^2}{2 \times 10^{-6}} \cdot (K)$$

$$P_{\text{CO}} = \left[\frac{(2.5 \times 10^{-3})^2}{2 \times 10^{-6}} (K) \right]^{1/2} = 1.768\sqrt{K} \quad (\text{A-5})$$

T, °C	T, °K	K	P _{CO} (atm)
1450	1723	0.04234	0.36
1500	1773	0.16104	0.71
1550	1823	0.56924	1.33
1600	1873	1.88096	2.42
1650	1923	5.84077	4.27
1700	1973	17.12453	7.32

Activities are taken from Elliot et al (5), assuming 0.1 w/o Si, 0.05 w/o C, balance Fe and $a_{SiO_2} = 1$.

b) Alumina



$$K = \exp \left(-\frac{\Delta G_8^\circ}{RT} \right) \\ = \exp \left(-\frac{322,020}{1.987 T} + \frac{140.77}{1.987 T} \right) \\ = \exp \left(-\frac{162,047}{T} + 70.84 \right)$$

Also, for reaction (A-8)

$$K = \frac{(a_{Al})^2 (P_{CO})^3}{(a_C)^3} = \frac{(19 \times 10^{-6})^2 (P_{CO})^3}{(2.5 \times 10^{-3})^3}$$

(Assume $a_{Al_2O_3} = 1$)

Therefore $P_{CO}^3 = \frac{(2.5 \times 10^{-3})^3}{(19 \times 10^{-6})^2} [\exp \left(-\frac{162,047}{T} + 70.84 \right)]$

$$P_{CO} = \left[\frac{(2.5 \times 10^{-3})^3}{(19 \times 10^{-6})^2} \cdot (K) \right]^{1/3} \\ = 3.511 \sqrt[3]{K}$$

T, °C	T, °K	Eq. Const., K	K ^{1/3}	P _{CO} (atm)
1450	1723	8.32 x 10 ⁻¹¹	4.366 x 10 ⁻⁴	1.53 x 10 ⁻³
1500	1773	1.18 x 10 ⁻⁹	1.057 x 10 ⁻³	3.71 x 10 ⁻³
1550	1823	1.44 x 10 ⁻⁸	2.438 x 10 ⁻³	8.56 x 10 ⁻³
1600	1873	1.55 x 10 ⁻⁷	5.376 x 10 ⁻³	1.88 x 10 ⁻²
1650	1923	1.47 x 10 ⁻⁶	1.138 x 10 ⁻²	4.00 x 10 ⁻²
1700	1973	1.24 x 10 ⁻⁵	2.319 x 10 ⁻²	8.14 x 10 ⁻²

These calculations assume 0.01 w/o Al, 0.05 w/o C, balance Fe and $a_{Al_2O_3} = 1$. Activities are taken from Elliot et al. (5)

These calculations indicate that SiO₂ and other oxides (MnO, FeO, etc.) of lesser stability are easily reduced by the carbon present in the melt; inert gas bubbling merely improves the kinetics of the process by eliminating the necessity of nucleating CO bubbles in the melt itself, which is not an easy process. More stable oxides such as the Al₂O₃ used as an example here require flushing of the melt with sufficient inert gas to maintain an open system; the inert gas must have an oxidizing potential less than the partial pressures of CO above an oxide-saturated melt.

As a practical matter, less stable oxides than Al₂O₃ are reduced by carbon with the inert gas bubbles acting as a kinetic aid; Al₂O₃ is removed mainly by precipitation followed by flotation, agglomeration, and (slow) reduction by dissolved carbon; the inert gas acts to stir the melt and provide an infinite sink for the CO generated. Bubbling rates of about 1 l/min are currently being used; excessive bubbling is likely to lead to excessive dissolution of the Al₂O₃ crucible and particle valve, especially at very high temperatures (1600°C and above for steels). This latter effect is troublesome during recharging of

the melt, during which temperatures of 1680°C are reached; the melt must subsequently be carefully cooled to 1500-1550°C to ensure that precipitation of dissolved Al₂O₃ is complete enough to minimize deposition of Al₂O₃ in the orifice during atomization.

APPENDIX 4B THERMODYNAMICS AND KINETICS OF DECARBURIZATIONa) Carbon Content

The decarburization reaction is



The free energy (ΔG_1°) for this reaction may be derived from the free energies of the following reactions (From Gaskell⁽⁶⁾).



$$\Delta G_1^\circ = 2\Delta G_2^\circ - \Delta G_3^\circ$$

$$= - 53,400 - 41.90T + 94,200 + 0.2 T$$

$$\underline{\Delta G_1^\circ = 40,800 - 41.70 T.}$$

For a decarburization temperature of 1000°C (1273°K) the partition coefficient, K_p , is given by

$$\begin{aligned} K_p &= \exp \left[-\frac{\Delta G^\circ}{RT} \right] \\ &= \exp \left[-\frac{(40,800 - 41.70 \times 1273)}{1.987 \times 1273} \right] \end{aligned}$$

$$\underline{K_p = 124.56}$$

Since, for reaction (B-1) $K_p = \frac{P_{CO}^2}{P_{CO_2} a_C}$

and

$$P_{CO} + P_{CO_2} = 1$$

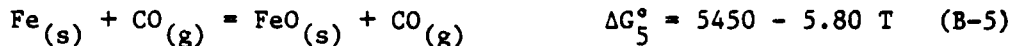
$$K_p = \frac{(1 - P_{CO_2})^2}{P_{CO_2} a_C} = 124.56$$

Where a_C is the activity of carbon, in the γ -Fe field, and is given by (Ban-ya et al.⁽⁷⁾) as:

$$\log_e a_C = \frac{3770}{T} + 2.72 \log_e T - 10.525 + \frac{3860 Y_C}{T} + \log_e \left(\frac{Y_C}{1-Y_C} \right) \quad (B-4)$$

where Y_C is the atomic ratio of carbon to iron; $\frac{n_C}{n_{Fe}}$.

The P_{CO}/P_{CO_2} ratio at which oxidation of the iron will occur sets a lower limit on the carbon content that can be achieved by decarburization.



$$K_p = \frac{P_{CO}}{P_{CO_2} a_{Fe}} = \exp - \frac{(5450 - 5.80 \times 1273)}{1.987 \times 1273} = 2.13$$

The activity of iron in the austenite phase field is given by:

$$\log_e a_{Fe}^\gamma = - \frac{(1970) Y_C^2}{T} + \log_e (1 - Y_C) \quad (B-6)$$

Using this equation it was found that the percentage of CO_2 in the gas should not exceed 32% to prevent oxidation of iron. Therefore, if we use 30% CO_2 in the gas mixture we can estimate the carbon content of the shot after decarburization. If the total gas pressure is 1 atmosphere and

$$P_{CO_2} = 0.3 \text{ atmospheres}$$

$$P_{CO} = 1 - P_{CO_2} = 0.7 \text{ atmospheres.}$$

$$\text{For reaction (B-1)} K_p = \frac{P_{CO}^2}{P_{CO_2} a_C}$$

$$a_C = \frac{P_{CO}^2}{P_{CO_2} \times K_p}$$

$$= \frac{0.7^2}{0.3 \times 124.54}$$

$$a_C = 0.01311$$

From equation (B-4)

$$\log_e 0.01311 = \frac{3770}{1273} + 2.72 \log_e 1273 - 10.525$$

$$+ \frac{3860 Y_C}{T} + \log_e \left(\frac{Y_C}{1-Y_C} \right)$$

$$-1.8824 = 2.9615 + 8.4451 - 10.525 + 3.0322 Y_C + \log_e \left(\frac{Y_C}{1-Y_C} \right)$$

$$3.032 Y_C + \log_e \left(\frac{Y_C}{1-Y_C} \right) = -2.764$$

Substituting values for Y_C of 0.0020 and 0.0015, the left hand side of this equation works out to be -2.692 and 2.817, respectively. Therefore, taking

$$Y_C = 0.002,$$

$$0.002 = \frac{n_C}{n_{Fe}}$$

$$= \frac{n_C}{(1-n_C)}$$

$$n_C = 0.002 (1-n_C)$$

$$n_C = 0.002 - 0.002 n_C$$

$$n_C = \frac{0.002}{1.002} = 0.001996$$

$$\text{Therefore, weight fraction } C = \frac{n_C \times 12}{(1-n_C) 55.85 + n_C \times 12}$$

Therefore, carbon content attainable by this method of decarburizing is estimated to be 0.04295 wt. %.

b) Decarburization Time

Diffusion out of a sphere of radius r_o is given by the following equation (from Jost⁽⁸⁾):

$$\frac{\bar{C} - C_f}{\bar{C}_i - C_f} = \frac{6}{\pi^2} \exp [-t \pi^2 \frac{D}{r_o^2}] \quad (\text{B-7})$$

$$0.5 = \frac{6}{\pi^2} \exp [-t \pi^2 \frac{D}{r_o^2}]$$

$$\exp [-t \pi^2 \frac{D}{r_o^2}] = \frac{1}{2} \times \frac{\pi^2}{6} = \frac{9.8696}{12} = 0.82247$$

$$-t \pi^2 \frac{D}{r_o^2} = \log_e 0.82247 = -0.19545$$

$$t = \frac{0.19545}{\pi^2 D} \times r_o^2$$

$$t = \frac{1.9803 \times 10^{-2}}{D} r_o^2 \text{ secs.}$$

Using different experimental data (from Elliot et al.⁽⁵⁾). values of the diffusion coefficient for C in γ -Fe near 1000°C lie in the range 2.24×10^{-7} to $3.11 \times 10^{-7} \text{ cm}^2 \text{ sec}^{-1}$. The decarburization times calculated from these values of D and various particle sizes are given in Table B-1.

TABLE B-1. Decarburization of Fe-C Shot at 1000°C; calculated range of times for decarburization.

r_0 , cm	r_0^2 , cm ²	t , * s	t' , ** s
1.0	1	8.84×10^4	6.37×10^4
0.1	0.01	8.84×10^2	6.37×10^2
0.05	0.0025	$2.21 \times 10^{+2}$	1.59×10^2
0.01	0.0001	8.84	6.37
0.005	0.000025	2.21	1.59
0.001	0.000001	8.84×10^{-2}	6.37×10^{-2}

* Value of diffusion coefficient used

$$D = 2.24 \times 10^{-7} \text{ cm}^2/\text{s}$$

** Value of diffusion coefficient used

$$D = 3.11 \times 10^{-7} \text{ cm}^2/\text{s}$$

5. KINETICS OF INTERACTIVE LIQUID METAL
INFILTRATION AND DIFFUSION SOLIDIFICATION

H. Sreshta
G. Langford
D. Apelian

SUMMARY

The Diffusion Solidification process is a complex phenomena involving simultaneous mass, momentum and heat transfer. The momentum and mass transfer aspects of the SD process were studied experimentally and results compared to theoretical models. The experimental results, coupled with theoretical models, were used to develop equations quantifying the required time for diffusion solidification, the rate of diffusion solidification, the limits of macrosegregation in the SD process, and the effect of gases in the shot region on the casting quality.

TABLE OF CONTENTS: Section 5. Kinetics of Interactive Liquid Metal
Infiltration and Diffusion Solidification.

	<u>Page</u>
5.1 Introduction	233
5.2 Process Components.	235
5.3 Independent Process Variables	236
5.4 Dependent Process Variables	237
5.5 SD Infiltration	238
5.5.1 SD Infiltration Time for a Packed Bed with no PV using the LC Model	241
5.5.2 Pressure Drop in Packed Beds.	242
5.5.3 The SD Infiltration Times	243
5.5.4 Particle Valve Correction for SD Infiltration Time.	246
5.5.5 Experimental Verification of the SD Infiltration Kinetics .	254
5.5.6 Accuracy of Infiltration Models	254
5.6 Mass Transfer	261
5.6.1 Boundary Movement in the SD Process	261
5.6.2 Solidification Time	265
5.6.3 Homogenization Time	266
5.6.4 Total Solidification Time	267
5.6.5 Solidification Rate for SD Steel Castings	269

	<u>Page</u>
5.7 Macrosegregation in SD Steel Castings	273
5.7.1 LC Theory	273
5.7.2 Modified LC Theory	275
5.7.3 Pressure Requirements for Laminar and Turbulent Flow Conditions	276
5.7.4 Macrosegregation Parameter	277
5.7.5 Macrosegregation for Non-Ideal Thermal Conditions	278
5.7.6 Discussion of Macrosegregation Results	284
5.7.7 Macrosegregation and Total Solidification Time	295
5.8 Gases in Shot Region	297
5.9 Conclusions	298
References	300
Appendices	301
Appendix 5A: Experimental Verification of SD Infiltration Kinetics	302
Appendix 5B: Measurement of Liquid-Solid Interface Motion	310
Appendix 5C: Relationship between Solidified Thickness and Volume of Melt Solidified for Shot	320
Appendix 5D: Experimental Procedure and Results for Macrosegregation in the Fe-C System	330
Appendix 5E: Experimental Procedure and Results for SD Casting Manufacture with Gases in the Shot Region	339
Appendix 5F: Experimental Setup Used for Making 6.35mm Castings, Measuring Shot Resistivity and Movement of Melt in the Packed Bed	345
Appendix 5G: Characterization of SD Components used for the Experiments	362
Appendix 5H: Nomenclature used in Chapter 5	372

5. KINETICS OF INTERACTIVE LIQUID METAL INFILTRATION AND DIFFUSION SOLIDIFICATION

5.1 Introduction

Diffusion solidification kinetics is a study of the infiltration and solidification rates in the process. Infiltration, the first step in the process, involves transfer of a high solute melt into a packed bed of shot essentially devoid of solute at the casting temperature.* During infiltration the kinetics are influenced by mass, momentum and heat transfer. After infiltration is completed, the casting can be considered as a composite of shot and melt and solidification of the melt is considered as the second step in the process. During solidification, the kinetics are governed by mass and heat transfer in the melt-shot composite.

Langford and Cunningham⁽¹⁾ proposed a kinetic model (henceforth referred to as the LC model) for the infiltration step in the process. Momentum transfer in the LC model was based on a fluid flow equation for turbulent flow in a non-interacting packed bet of shot. Mass transfer during this step was predicted using an approximate relationship for liquid-solid interface motion resulting from diffusion of solute into the shot. Heat and mass transfer was

*Casting temperature refers to the temperature at which the melt is saturated with solvent and the shot at the melt temperature.

combined in terms of a macrosegregation parameter, α , to give a kinetic equation in terms of the process variables for the infiltration step in the process. The value of the macrosegregation parameter was used to predict the macrosegregation limits in the SD process.

The second step in the process includes solidification of melt and casting homogenization after solidification has been completed. A kinetic equation has yet to be established to estimate fractional solidification rates and solidification time in terms of the relative amounts of solid and liquid for the SD process. The homogenization time has already been derived approximately by Langford and Cunningham⁽¹⁾ for the SD process.

The objective of this research was to:

- (1) adapt the existing LC macrosegregation theory to Burke-Plummer, Ergun and Blake Kozeny equations for fluid flow in packed beds⁽²⁾,
 - (2) obtain kinetic equations for the solidification step in the process,
 - (3) compare the theoretical infiltration kinetics with experimental results,
 - (4) estimate macrosegregation limits for ideal* and non-ideal SD thermal conditions, and
 - (5) estimate the effect of gas pressure in the shot region on casting quality.
-

*Ideal thermal conditions refers to melt saturated with solvent and shot at the casting temperature.

5.2 Process Components

The SD process has four components: melt charge, shot, particle valve and mold. In comparison to the conventional casting process, the SD process has two additional components: shot and particle valve.

i. Shot

Shot in the SD process refers to low solute solid which occupies the casting volume prior to melt transfer. Irregular and spherical particles could be used as the solid, but spherical particles permit a higher initial fraction of solid. The shot for SD of steels has a low carbon content which deoxides the surface oxide on the particles at casting temperature. (1)

ii. Melt Charge

The melt charge has a composition fixed by the desired casting composition. At the casting temperature, the melt (charge) must be at the liquidus temperature.

iii. Particle Valve

The particle valve is used to isolate the melt charge and shot during the heating period. The valve is essentially an aggregate of non-wetting refractory particles inert to the melt charge and shot. The size of the particles must be adequate to prevent failure of the valve prior to melt transfer. (3)

iv. Mold

The choice of mold for manufacturing SD castings is restricted to the method used to heat the components to process temperature. Three suitable candidates⁽⁴⁾ are:

- investment molds
- permanent molds
- sand molds

5.3 Independent Process Variables

The independent process variables are:

- Shot size (d_p); the average particle size of the solid region.
- Infiltration Pressure (P_A); the applied pressure for transfer of melt into the solid region.
- Pressure in Solid region (P_S); the gas pressure in the shot region just prior to melt transfer.
- Casting temperature (T_C); temperature at which a solvent saturated melt is transferred into the solid region.
- Casting length (L); the length of the solid region parallel to the melt flow direction. Cylindrical geometry is assumed.

5.4 Dependent Process Variables

The dependent process variables are:

- Infiltration Time (t_I)
- Solidification Time (t_S)
- Homogenization Time (t_h)

i. Infiltration Time (t_I)

The infiltration time is defined as the time taken by the melt to fill up the entire solid region. It is a function of the variables given by:

$$t_I = f(P_A, P_S, L, T_C, \epsilon, d_p) * \quad (1)$$

In the above equation the casting temperature represents the melt viscosity and density.

ii. Solidification Time

The solidification time is defined as the time taken to solidify the entire melt. It is a function of the variables given by:

$$t_S = f(k, C_S, D, d_p) \quad (2)$$

*A list of notations is given in Appendix 5H.

where:

C_s - composition of solid

D - diffusivity of solute in solid

k - distribution coefficient

iii. Homogenization Time (t_h)

The homogenization time is time taken for solute homogenization in the casting after the melt has solidified and is given by:

$$t_h = f(\% \text{homogenization}, D, d_p) \quad (3)$$

5.5 SD Infiltration

Once the SD components are heated to casting temperature, the next process step is to transfer the melt into the shot. This is accomplished by instantaneous pressurization of melt. Prior to pressurization the melt is isolated from the shot by the particle valve (PV).

Melt infiltration in the SD process is characterized by simultaneous mass, momentum and heat transfer. Mass transfer during infiltration results from solute rejection from the melt into the shot; the shot essentially is devoid of solute and the melt is saturated with solvent. The mass transfer rate is controlled by diffusion rate of solute in the shot. The net effect of the diffusion is solidification of the melt on the shot surface. The latent heat evolved as a result of solidification leads to non-isothermal flow conditions.

Diffusion solidification melt infiltration can be considered as fluid flow in an interacting packed bed. The extent of interaction is a function of the diffusion rate and the time of contact between shot and melt. In terms of fluid flow, an interacting packed bed is one where the void fraction or cross-sectional area available for flow changes as a function of time during infiltration; the flow area decreasing with time.

To obtain the SD infiltration time or the time taken by the melt to fill a given casting length as a function of the process variables, it is necessary to simplify the transport formulation of SD infiltration. This is done by obtaining infiltration times for packed bed subject to the following conditions:

- non-interacting packed bed with no PV
- non-interacting packed bed with PV
- interacting packed bed with no PV

The SD infiltration time for an interacting packed bed will be expressed in terms of infiltration time for a non-interacting packed bed, (NIPB), with no PV, using time correction functions. The time correction function for PV relates the infiltration time for a non-interacting packed bed with PV to that for a non-interacting packed bed and can be expressed as:

$$f(PV) = \frac{t_I(PV)}{t_I} \quad (4)$$

where: t_I is the infiltration time for a NIPB with no PV, $t_I(PV)$ is the infiltration time for a NIPB with PV and $f(PV)$ is the time correction function for the particle valve. The time correction function for interaction relates the infiltration time for a interacting packed bed with no PV to that for a NIPB with PV and can be expressed as:

$$f(I) = \frac{t_I(I)}{t_I(PV)} \quad (5)$$

where $t_I(I)$ is the infiltration time for an interacting PB with no PV and $f(I)$ the time correcton function for interaction. The infiltration time for an interacting PB with PV, $t_I(IPV)$ is obtained by combining Eqs. (4) and (5) and is given by:

$$t_I(IPV) = f(PV)f(I)t_I \quad (6)$$

The infiltration time, $t(IPV)$, will give a reasonable estimate for the filling time in the SD process. The interaction time function is always greater than 1 and is a function of the process variables having a strong dependence on casting temperature and casting length.

It will be shown later in this section that acceptable casting quality (± 10 percent variation in composition) can be obtained only when the infiltration time is equal to or less than .005 times the solidification time, thereby limiting the amount of SD to approximately 17 percent of the original liquid at the casting top. When the ratio of infiltration to solidification time is equal to .005, the SD thickness is 3.7 percent of the particle radius, which reduces the flow-limiting minimum throat area between shot particles by 42 percent. As interaction at the casting top is limited to 17 percent during infiltration, the value of $f(I)$ will not be significantly greater than 1. Hence infiltration time based on a non-interacting packed bed will give a reasonable estimate of the actual infiltration time.

5.5.1 SD infiltration time for a packed bed with no PV using the LC model.

The LC (Langford and Cunningham) model assumes turbulent flow conditions in the packed bed during infiltration. The infiltration velocity and time for the LC model are given by⁽¹⁾:

$$v^{LC} = \left(\frac{P_A d_p}{60 \epsilon^2 x p_L} \right)^{\frac{1}{2}} \quad (7)$$

$$t_I^{LC} = (5.16 \frac{L^3 \epsilon^2 p_L}{P_A d_p})^{\frac{1}{4}} \quad (8)$$

The infiltration velocity and time given by Eqs. (7) and (8) are for the case where the melt wets the shot surface and vacuum conditions are maintained in the shot region during melt transfer. For a non-wetting melt-shot system, P_A in Eqs. (7) and (8) is replaced by $P_A - P_\gamma$, where P_γ is the pressure required to overcome the surface tension forces. The pressure to overcome surface forces is given by⁽³⁾:

$$P_\gamma = 11 \gamma_L / d_p \quad (9)$$

where γ_L is the surface tension of the melt.

5.5.2 Pressure Drop In Packed Beds

The pressure drop in packed bed depends on the flow conditions in the packed bed. The Reynolds number for fluid flow in packed bed is given by⁽²⁾:

$$Re = \frac{d_p \rho_L v}{(1-\epsilon) \mu_L} \quad (10)$$

The flow is laminar for $Re < 10$ and turbulent for $Re > 1000$. For Reynolds numbers in the range of 100 to 1000 the flow is a transition between laminar and turbulent flow.

The pressure drop for laminar flow in packed beds, $Re < 10$ is given by the BK (Blake-Kozeny) equation⁽²⁾:

$$\frac{\Delta P}{x} = \frac{150 \mu_L (1-\epsilon)^2 v}{d_p^2 \epsilon^3} \quad (11)$$

The pressure drop for turbulent flow in packed beds is given by the BP (Burke-Plummer) equation⁽²⁾:

$$\frac{\Delta P}{x} = \frac{1.75 \mu_L (1-\epsilon) v^2}{d_p \epsilon^3} \quad (12)$$

The pressure drop for laminar, laminar-turbulent transition, and turbulent flow in packed beds is given by Ergun's equation⁽²⁾:

$$\frac{\Delta P}{x} = \frac{1.75 \mu_L (1-\epsilon) v^2}{d_p \epsilon^3} + \frac{150 \mu_L (1-\epsilon)^2 v}{d_p^2 \epsilon^3} \quad (13)$$

5.5.3 The SD infiltration times based on the preceding pressure drop equations.

The following assumptions are made to use the packed bed PB pressure drop equations for estimating SD infiltration times:

- . the packed bed is non-interacting
- . the pressure drop in the PV is negligible
- . the pressure drop in PB results only from frictional (inertial and viscous) forces between the packed bed and melt
- . bulk acceleration and gravitational terms are negligible.
- . the melt wets the shot surface but not the PV

The SD infiltration velocity and time for laminar flow in packed beds can be obtained using the Blake-Kozeny equation and are given by:

$$V^{BK} = \frac{P_A d_p^2 \epsilon^3}{150 \times \mu_L (1-\epsilon)^2} \quad (14)$$

$$\begin{aligned} t_I^{BK} &= \int_0^L \frac{dx}{V^{BK}} \\ &= \frac{75 \mu_L (1-\epsilon)^2 L^2}{d_p^2 \epsilon^3 P_A} \end{aligned} \quad (15)$$

The SD infiltration velocity and time for turbulent flow in packed beds can be obtained by using the Burke-Plummer equation and are given by:

$$v^{BP} = \left(\frac{P_A d_p \epsilon^3}{1.75 \times \rho_L (1-\epsilon)} \right)^{\frac{1}{2}} \quad (16)$$

$$t_I^{BP} = \int_0^L \frac{dx}{v^{BP}} = 0.88 \left(\frac{L^3 \rho_L (1-\epsilon)}{P_A d_p \epsilon^3} \right)^{\frac{1}{2}} \quad (17)$$

The SD infiltration velocity and time for laminar, laminar-turbulent transition and turbulent flow can be obtained using the Ergun equation and are given by Equations (18) and (21).

$$v^E = \frac{-F_1 + (F_2 + (4 F_1 P_A / x))}{2F_2} \quad (18)$$

where F_1 and F_2 are given by:

$$F_1 = \frac{150 L (1-\epsilon)^2}{d_p^2 \epsilon^3} \quad (19)$$

$$F_2 = \frac{1.75 \rho_L (1-\epsilon)}{d_p \epsilon^3} \quad (20)$$

$$t_I^E = \int_{10^{-5}}^L \frac{dx}{v^E} \quad (21)$$

*The lower limit of integration is taken as 10^{-5} m, at $x = 0$, $V = \infty$

Although Eq. (18) must be solved using numerical techniques, it is desirable to obtain an Ergun infiltration time in terms of process variables. Using Eq. (21), the infiltration time was estimated for ten sets of process conditions given in Table I. The data was fitted to the expression:

$$t_I = C_1 t_I^{BK} + C_2 t_I^{BP} + C_3 (t_I^{BK} t_I^{BP})^{-\frac{1}{2}} \quad (22)$$

giving constants; $C_1 = 1.08$, $C_2 = 1.14$ and $C_3 = -0.6$. Hence the infiltration time in terms of process variables is given by:

$$t_I^E = 1.08 t_I^{BK} + 1.14 t_I^{BP} - 0.6 (t_I^{BK} t_I^{BP})^{-\frac{1}{2}} \quad (23)$$

The error in using the above equation for estimating infiltration time was less than ± 2 percent.

5.5.4 Particle valve correction for SD infiltration time.

The PV correction, $f(PV)$, for infiltration time can be obtained by accounting for the pressure drop in the PV during infiltration. The PV correction function will be derived for the different fluid flow equations.

Table I. Process conditions used to obtain an empirical Ergun's infiltration time (t_I^E).

t	d_p	P	T_c	μ_L	ρ_L	L	$(t_I^E)^*$	$(t_I^E)^{**}$	Error
10^4 xm	10^5 kPa	$^{\circ}\text{C}$	Pa.5	kg/m^3	m	s	s	s	%
0.30	3	9	1190	0.0108	7060	0.15	4.501	4.544	0.96
0.60	9	4	1250	0.0082	7045	0.75	3.868	3.799	-1.79
0.55	7	10	1300	0.0067	7030	0.35	1.031	1.022	-0.86
0.35	2	3	1350	0.0058	7015	0.40	58.792	58.704	-0.15
0.40	10	7	1390	0.0055	7000	0.05	0.099	0.101	1.97
0.45	5	4	1190	0.0108	7060	0.90	17.884	17.891	0.03
0.60	8	5	1250	0.0082	7045	0.65	2.855	2.829	-0.90
0.25	4	2	1300	0.0067	7030	0.25	36.837	36.887	0.14
0.40	1	6	1350	0.0058	7015	0.70	283.670	283.646	-0.01
0.35	6	8	1390	0.0055	7000	0.50	9.316	9.490	1.00

* calculated using Eq. (21)

** calculated using Eq. (23)

i. LC Model

Fig.1 shows the melt movement during infiltration, where the melt has moved a distance x in the packed bed of shot. Let the pressure at the PV-shot interface be P_1 . The melt velocity in the PV region is given by:

$$v_{PV} = \left(\frac{(P_A - P_1) d_{PV}}{60 L_{PV} \epsilon_{PV}^2 \rho_L} \right)^{\frac{1}{2}} \quad (24)$$

where d_{PV} is the diameter of the particles in the PV, L_{PV} is the height of the PV and ϵ_{PV} is the void fraction of PV.

The melt velocity in the shot region is give by:

$$v_x = \left(\frac{P_1 d_p}{60x \epsilon^2 \rho_L} \right)^{\frac{1}{2}} \quad (25)$$

where; d_p is the shot diameter, x is the melt penetration distance and ϵ is the void fraction of the shot region.

Assuming that the void fraction of the PV region is equal to the void fraction of the shot region, then from the equation of continuity, the melt velocity in the shot region is equal to the melt velocity in the PV region:

$$v_x = v_{PV} \quad (26)$$

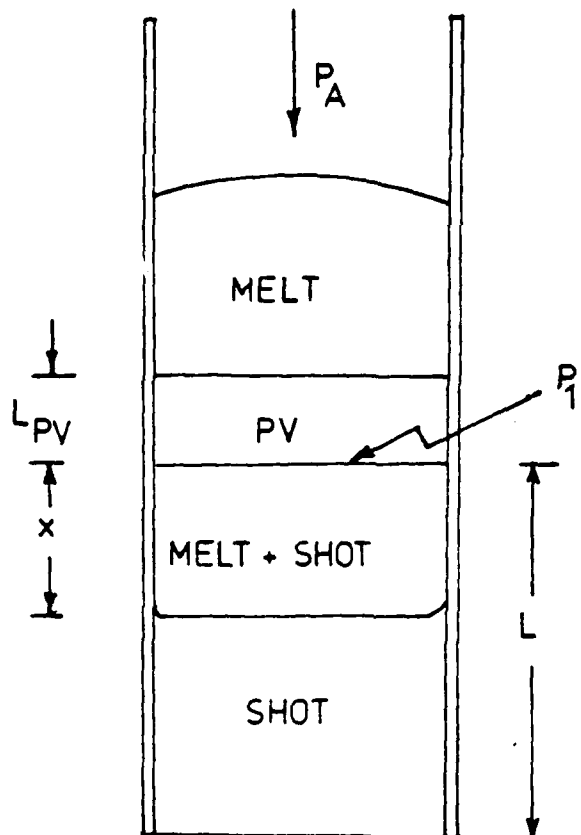


Figure 1. Schematic diagram of melt movement in the SD process; P_A is the applied pressure and P_1 is the pressure at PV-shot interface.

Substituting for v_x and v_{PV} in Equation (26) and rearranging the terms, the PV-shot interface pressure is given by:

$$P_1 = \left(\frac{P_A \left(\frac{d_{PV}}{60 L_{PV} \epsilon^2 \rho_L} \right)}{\frac{d_p}{60 \times \epsilon^2 \rho_L} + \frac{d_{PV}}{60 L_{PV} \epsilon^2 \rho_L}} \right) \quad (27)$$

The velocity of the moving front is obtained by substituting for P_1 in Equation (25).

$$v_x = \frac{\left(\frac{d_{PV} P_A}{60 L_{PV} \epsilon^2 \rho_L} \right)}{\left(1 + \frac{d_{PV}}{d_p} x \right)} \quad (28)$$

The infiltration time for melt transfer is obtained by integrating Eq. (28).

$$\begin{aligned} t_I^{LC} (PV) &= \int_0^L \frac{dx}{v_x} \\ &= 5.16 \left(\frac{L_{PV}^3 \epsilon^2 \rho_L}{P_A d_p} \right)^{1/2} \frac{d_p}{d_{PV}} \left(\left(1 + \frac{d_{PV} L}{d_p L_{PV}} \right) \right)^{3/2} \end{aligned} \quad (29)$$

where $t_I^{LC} (PV)$ is the infiltration time for a non-interacting packed bed with PV.

The PV correction function for the LC model is given by:

$$\begin{aligned}
 (PV)^{LC} &= \frac{t_I^{LC}}{t_I} (PV) \\
 &= \left(\frac{L_{PV} d_p}{L d_{PV}} \right)^{3/2} \left(\left(1 + \frac{d_{PV} L}{d_p L_{PV}} \right)^{3/2} - 1 \right) \\
 &= (\beta + 1)^{3/2} - \beta^{3/2}
 \end{aligned} \tag{30}$$

where β is given by:

$$\beta = L_{PV} d_p / L d_{PV} \tag{31}$$

ii. PV correction for the BP model

Using the same assumptions and procedure for obtaining $f(PV)$ for the LC model, it can be shown that $f(PV)$ is the same for the LC and BP model. The infiltration time for the BP model with PV is given by:

$$t_I^{BP}(PV) = 0.88 \left(\frac{\frac{L_{PV}^3 (1 - \epsilon) p_L}{P_A d_{PV} \epsilon^3}}{} \right)^{1/2} \left(1 + \frac{d_{PV} L}{d_p L_{PV}} \right)^{3/2} - 1 \tag{32}$$

iii. PV correction for the BK model

The melt velocity in the PV region is given by:

$$v_x = \frac{(P_A - P_1) d_{PV}^2 \epsilon_{PV}^3}{150 L_{PV} \mu_L (1 - \epsilon_{PV})^2} \tag{33}$$

The melt velocity in the shot region is given by:

$$v_x = \frac{P_1 d_p^2 \epsilon^3}{150 \times \mu_L (1 - \epsilon)^2} \quad (34)$$

Assuming that $\epsilon = \epsilon_{PV}$, then from the equation of continuity:

$$v_x = v_{PV} \quad (35)$$

Combining Eqs. (33), (34) and (35) and rearranging terms, the PV-shot interface pressure is given by:

$$P_1 = \left(\frac{\frac{P_A d_{PV}^2 \epsilon^3}{150 L_{PV} \mu_L (1 - \epsilon)^2}}{\left(\frac{d_p^2 \epsilon^3}{150 L \mu_L (1 - \epsilon)^2} + \frac{d_{PV}^2 \epsilon^3}{150 L_{PV} \mu_L (1 - \epsilon)^2} \right)} \right) \quad (36)$$

The velocity of the moving front is obtained by substituting for P_1 in Eq. (34).

$$v_x = \frac{\frac{P_A d_{PV}^2 \epsilon^3}{150 L_{PV} (1 - \epsilon)^2 \mu_L}}{\left(1 + \frac{d_{PV}^2 x}{d_p^2 L_{PV}} \right)} \quad (37)$$

The infiltration time for melt transfer is obtained by integrating Eq. (37).

$$\begin{aligned}
 t_I^{BK} &= \int_0^L \frac{dx}{v_x} \\
 &= 75 \left(\frac{\frac{L_{PV}}{d_{PV}}^2 (1 - \epsilon)^2 \mu_L}{\frac{P_A}{d_{PV}}^2 \epsilon^3} \right) \left(\frac{d_p}{d_{PV}} \right) \left(\left(1 + \frac{d_{PV}^2 L}{d_p^2 L_{PV}} \right) - 1 \right)
 \end{aligned} \tag{38}$$

The PV correction function for the BK model is given by:

$$\begin{aligned}
 f(PV)^{BK} &= \frac{t_I^{BK}(PV)}{t_I^{BK}} \\
 &= \left(\frac{\frac{L_{PV}}{d_{PV}}^2}{L d_{PV}} \right) \left(\left(1 + \frac{d_{PV}^2 L}{d_p^2 L_{PV}} \right)^2 - 1 \right) \\
 &= 1 + 2 \left(\frac{d_p}{d_{PV}} \right) \beta
 \end{aligned} \tag{39}$$

iv. Ergun Model

The PV correction function for the Ergun model can be obtained only by numerical methods. However the PV correction function for the Ergun model, $f(PV)^E$ must be between the limits of the PV correction for laminar and turbulent flow. The PV correction for laminar flow, $f(PV)^L$ is given by:

$$f(PV)^L = f(PV)^{BK} = 1 + 2 \left(\frac{d_p}{d_{PV}} \right) \beta \tag{40}$$

The PV correction for turbulent flow, $F(PV)^T$, is given by:

$$\begin{aligned} f(PV)^T &= f(PV)^{LC} = f(PV)^{BP} \\ &= (1 + \beta)^{3/2} - \beta^{3/2} \end{aligned} \quad (41)$$

The PV correction for the Ergun model, $f(PV)^E_T$, must have a value that lies inbetween $f(PV)^L$ and $f(PV)^T$. The effect of dp/d_{PV} ratio on the laminar and turbulent time correction functions is shown in Fig.2. for $L_{PV}/L=.05$.

5.5.5 Experimental verification of the SD infiltration kinetics

The experimental procedure and results are given in Appendix 5A. The infiltration curves (time vs distance) for two experimental runs I1 and I2, are compared to those predicted by the LC, BP and Ergun models in Figs. 3 and 4. Figs. 5 and 6 compares the experimental results with the LC and BP model corrected for pressure drop in the particle valve.

5.5.6 Accuracy of INFILTRATION Models

The infiltration times for the experimental runs are less than a second and solidification time is of the order

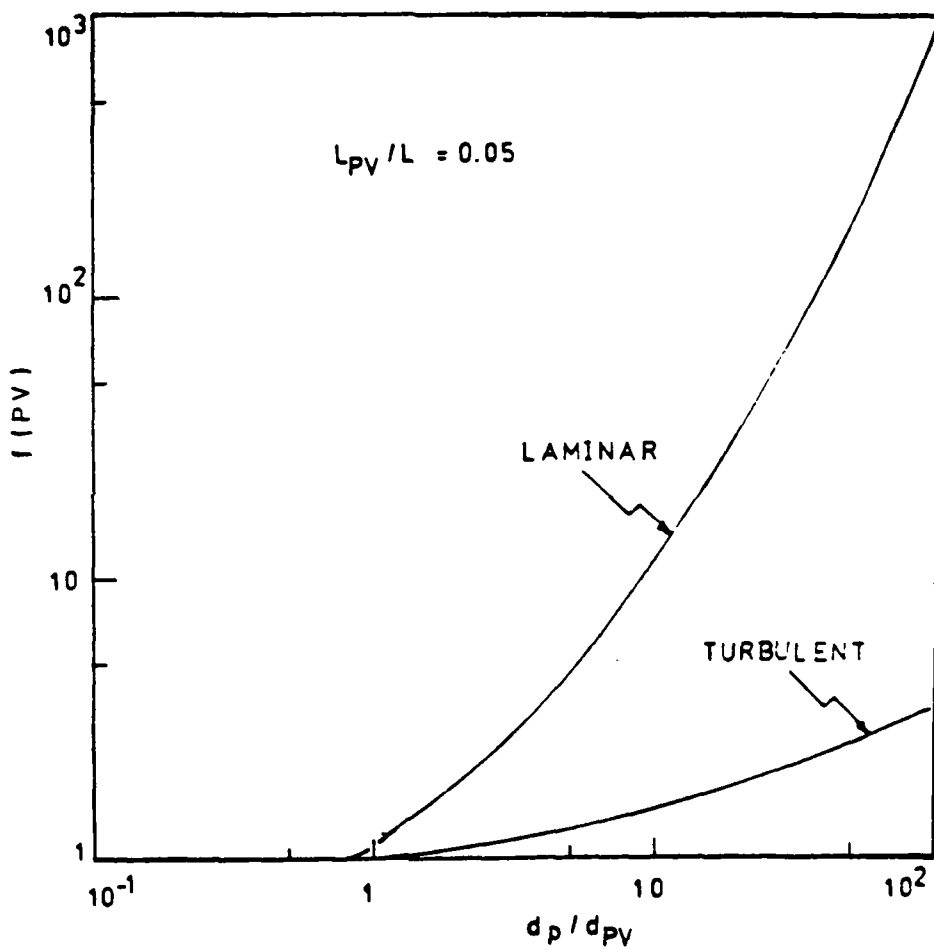


Figure 2. Time correction for PV as a function of d_p/d_{PV} ratio.

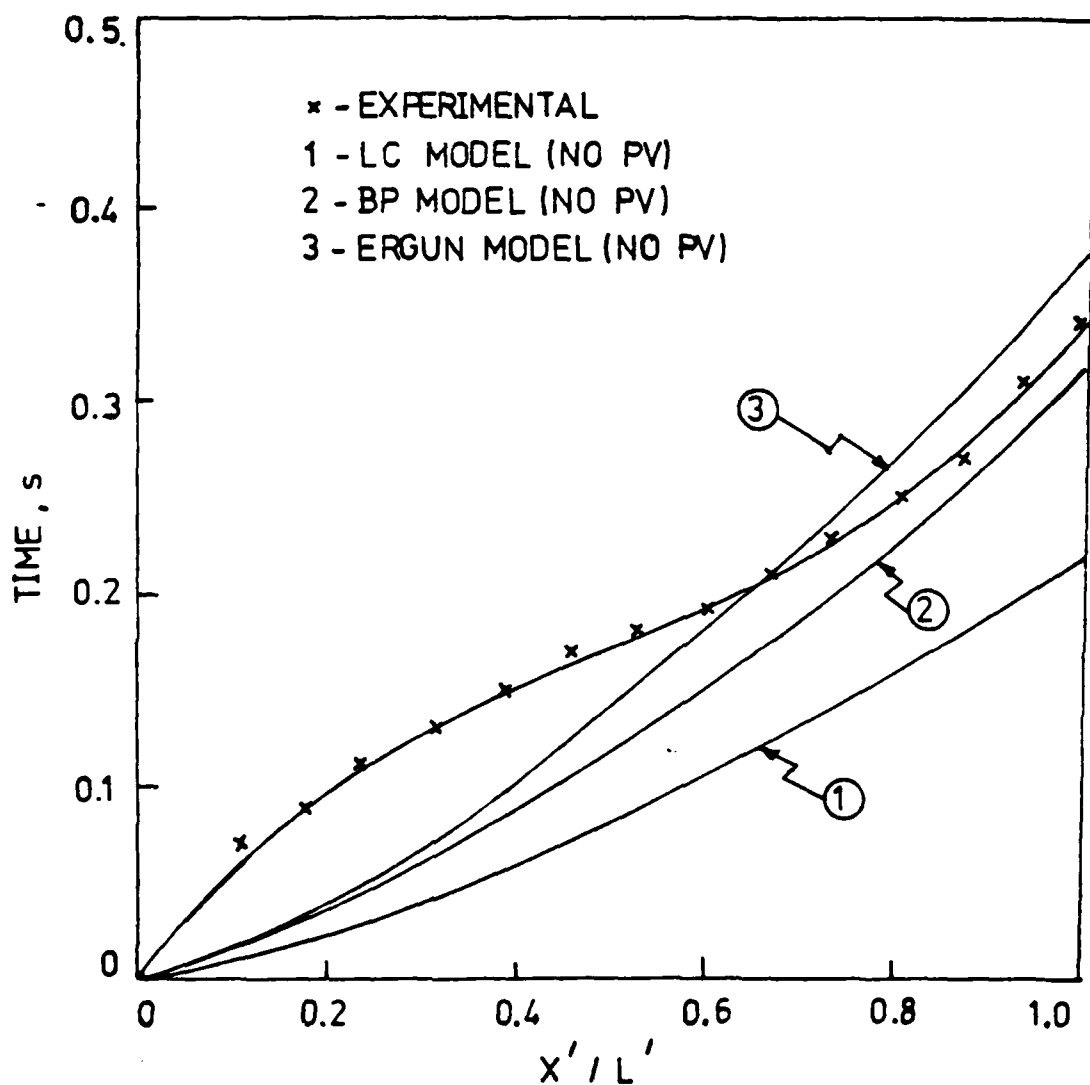


Figure 3. Comparison of experimental and theoretical infiltration curves (infiltration time vs penetration distance) for Run II.

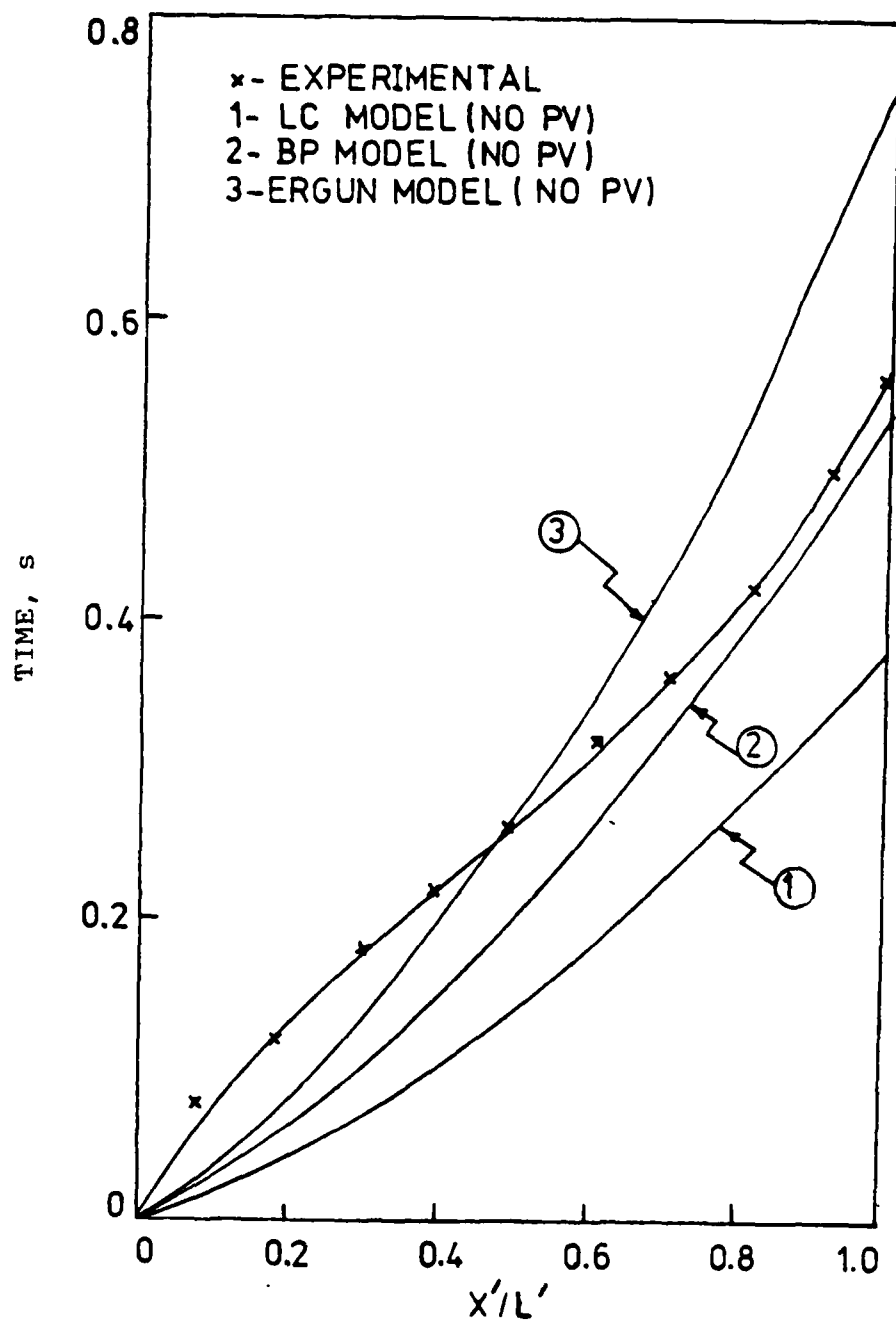


Figure 4. Comparison of experimental and theoretical infiltration curves (infiltration time vs penetration distance) for Run I2.

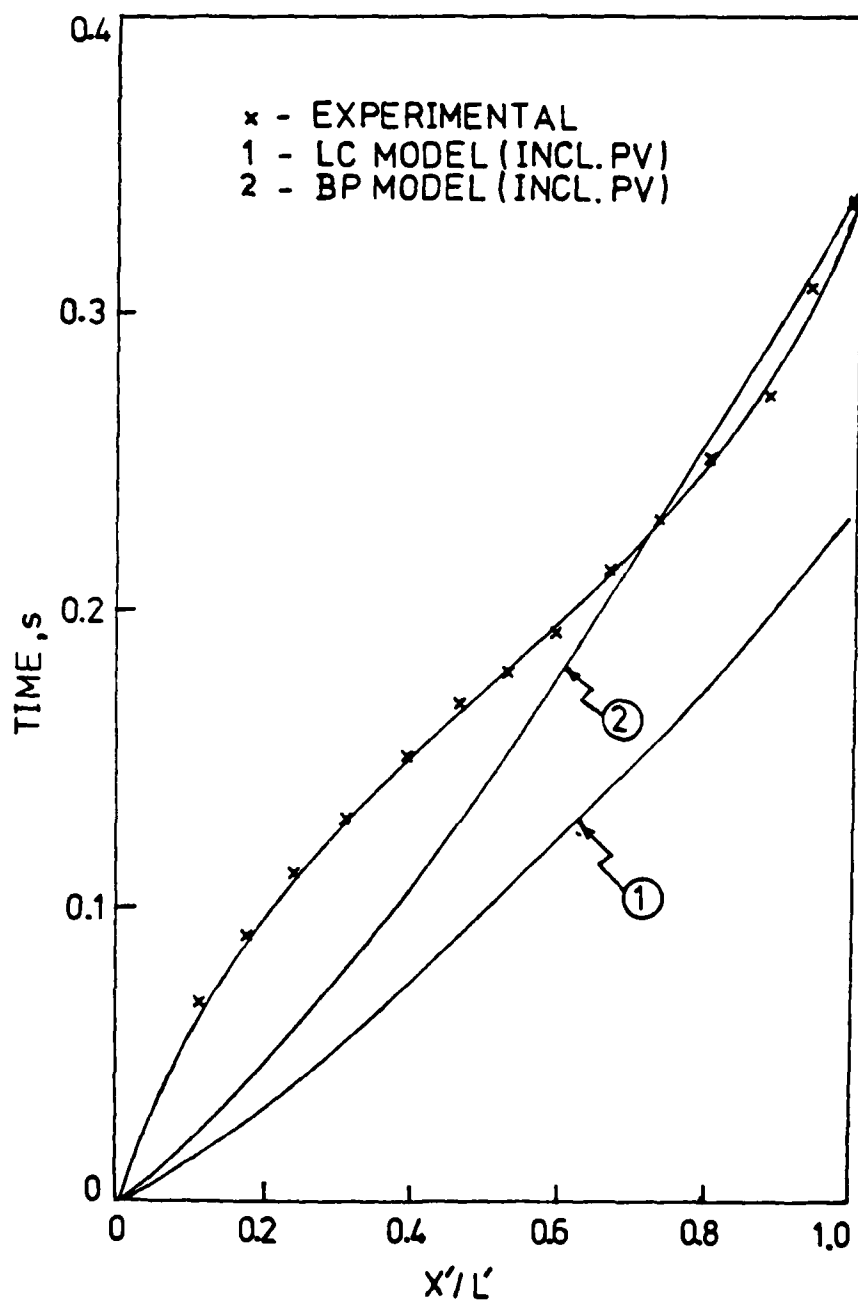


Figure 5. Theoretical infiltration curves with PV correction compared to the experimental infiltration curve for Run II.

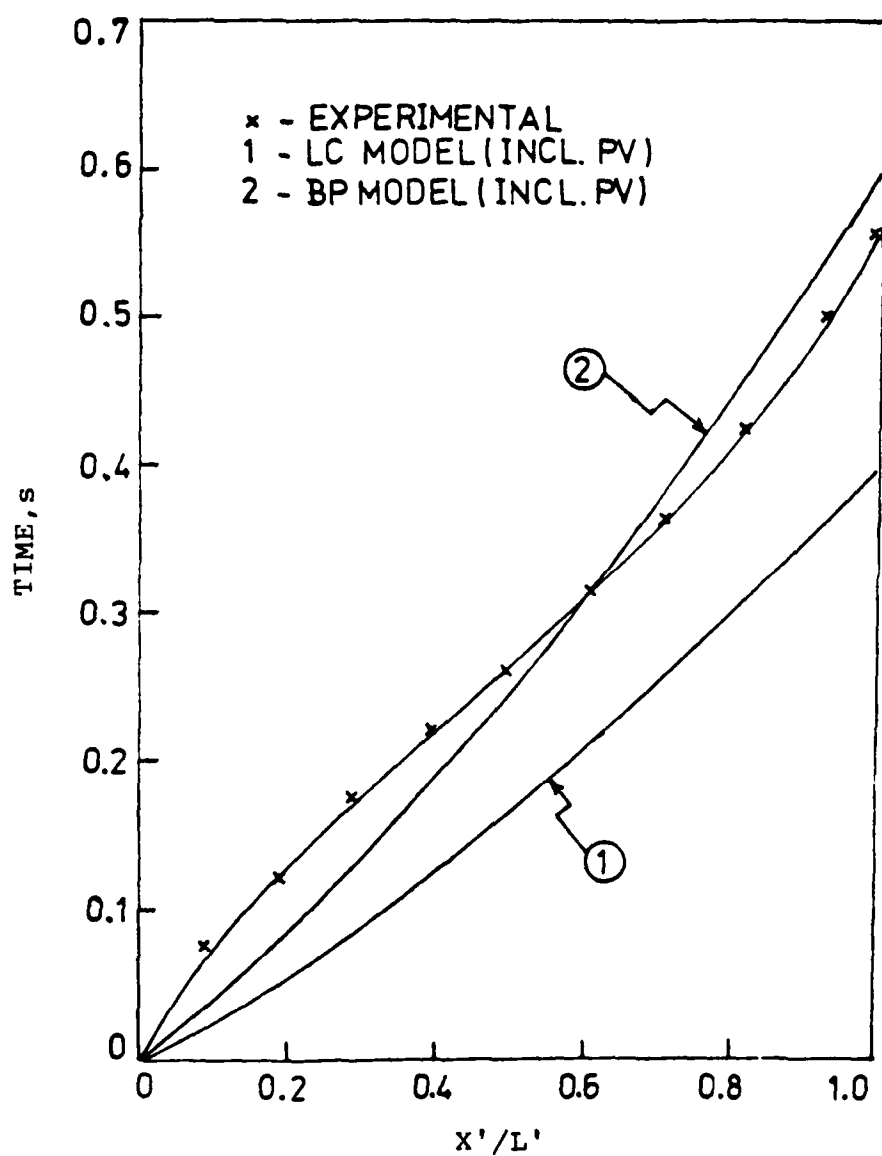


Figure 6. Theoretical infiltration curves with PV correction compared to experimental infiltration curve for Run I2.

of 425 seconds*. The small magnitude of infiltration time to solidification time justifies the use of fluid flow equations for non-interacting packed beds. The experimental results are not compared with the BK model because the flow conditions were not laminar for the process variables used in runs I1 and I2. The Reynolds number based on the average velocity, $(L_{PV} + L)/t_I$, of the melt was 300 for run I1 and 190 for run I2, justifying that the flow was not laminar for runs I1 and I2. It is found that the theoretical infiltration models deviate from the experimental results. The deviation is maximum for the LC fluid flow model which estimates an infiltration time much less than the actual infiltration time. The Ergun model deviates negatively during the initial stages of infiltration and positively during later stages of infiltration. The BP model deviates negatively during the early stages of infiltration but approaches the actual infiltration time during the later stages of infiltration. The negative deviation during the early stages of infiltration arises due to the assumption that steady state is achieved during infiltration. This is not the case as experimental results indicate that the velocity increases initially, reaches a maximum value and then decreases. Hence a more accurate theoretical model must include the acceleration term in the fluid flow equation.

*Calculated using Eq. (50).

When the casting length is greater than 90 mm it is found that the BP model is accurate enough to predict the infiltration time as shown in Figs. 3 and 4 for runs I1 and I2. Hence the SD infiltration time can be accurately predicted by the BP model for casting lengths greater than 90 mm.

The PV correction for the BP model (turbulent flow conditions) decreases the deviation of the predicted and experimental results as shown in Figs. 5 and 6. The PV correction can be neglected provided the β is much less than 1. For the experimental runs β was of the order of 0.125.

Of the four theoretical models used to describe SD infiltration kinetics it is found that the BP model is most accurate in predicting the infiltration for SD of steels.

5.6 Mass Transfer

5.6.1 Boundary movement in the SD process

Langford and Cunningham⁽¹⁾ derived an approximate relationship for liquid-solid interface displacement given by:

$$\delta = 1.25 K_L (Dt)^{1/3} \quad (42)$$

The constant K_L in Eq. (42) is defined by:

$$K_L = \frac{C_S^* - C_S}{C_L^* - C_S} \quad (43)$$

A more accurate expression relating liquid-solid interface displacement to diffusion time for diffusion of solute occurring in a single phase region, coupled to an alloy whose composition lies in the adjacent two phase region is given by⁽⁵⁾:

$$\delta = 2 K (Dt)^{\frac{1}{2}} \quad (45)$$

The constant K in Eq. (44) is defined by:

$$F(K) = \frac{C_S^* - C_S}{C_L^* - C_S^*} = K (\pi)^{\frac{1}{2}} e^{K^2} (1 + \operatorname{erf} K) \quad (45)$$

The relationship between K and F(K) is graphically illustrated in Fig. 6. The diffusion time required to obtain a given displacement is given by:

$$t = 0.25 \frac{1}{D} \left(\frac{\delta}{K}\right)^2 \quad (46)$$

The above equation is valid for isothermal conditions and for one dimensional boundary shift resulting from solute diffusion into a semi-infinite solid.

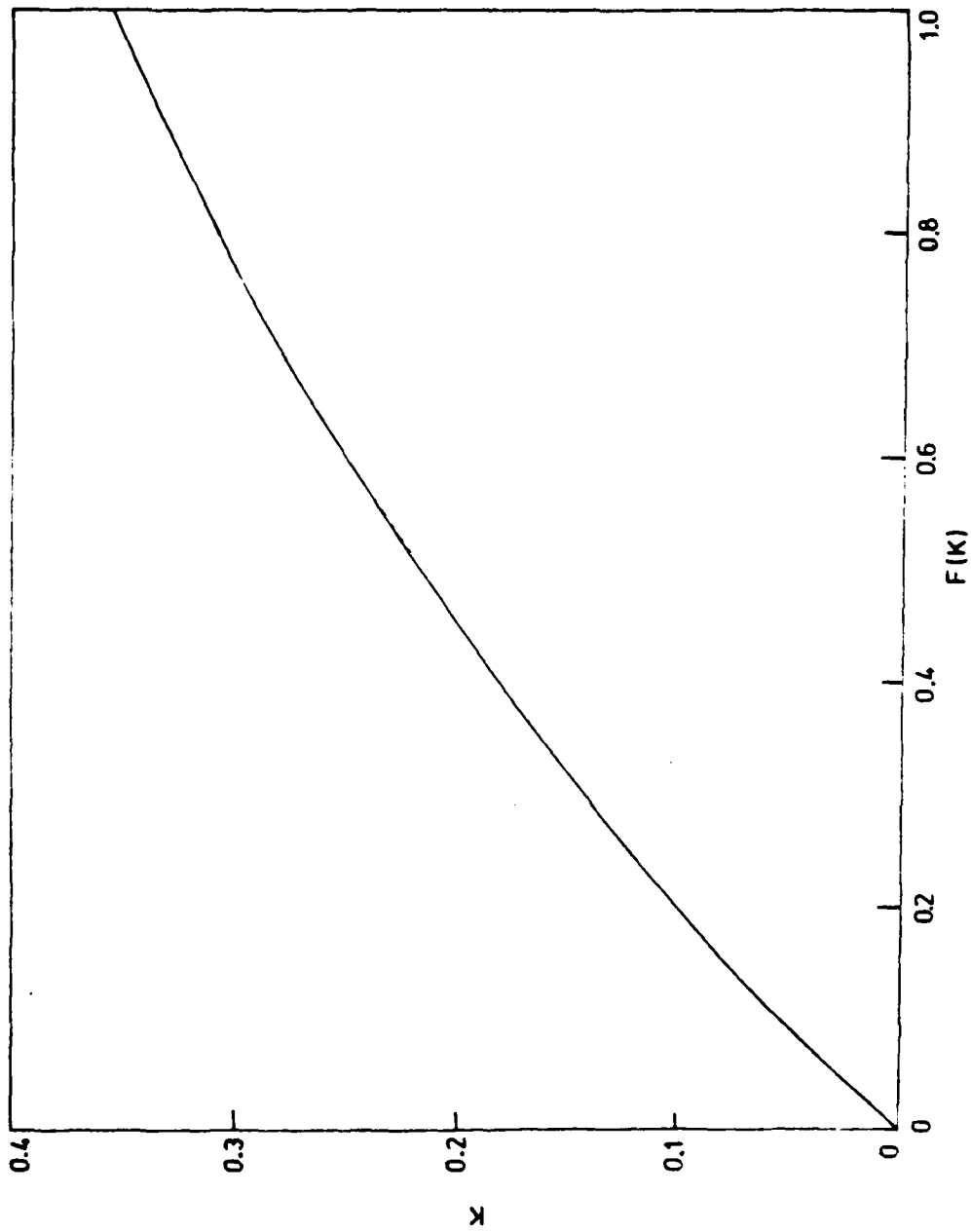


Figure 7. The value of K in equation (44) as a function of $F(K)$; $F(K) = \frac{(C_S^* - C_S)}{(C_L^* - C_S)}$

In the SD process, mass transfer occurs under non-isothermal conditions. The phase change from liquid to solid, raises the temperature of the solid-melt composite. The boundary shift, constrained by five planes, is three dimensional and results from solute diffusion into a solid with finite dimensions; half the shot diameter. A mathematical solution to boundary movement in the SD process will not be attempted because of the complexity involved in obtaining a solution. The constant in Eq. (46) has been verified experimentally. The experimental procedure and results are given in Appendix 5B. Plots of t vs (δ^2/K^2D) gave slopes of 0.184 and 0.140 for shot and rod charge respectively leading to time-displacement relationships given by:

$$\text{Shot: } t = 0.184 \frac{\delta^2}{K^2 D} \quad (47)$$

$$\text{Rods: } t = 0.140 \frac{\delta^2}{K^2 D} \quad (48)$$

Equation (47) accurately predicts the time displacement relationship for shot and is valid for diffusion times less than 126 seconds. At a diffusion time of 126 seconds the (δ/d_p) ration for shot was 0.192 which corresponds to approximately 90% of melt solidifying.* Equation (48) accurately predicts time-displacement relationship for rods when the diffusion time is less than 400 seconds. For diffusion times of 800 seconds, Eq. (48) predicts a much higher value of

*Refer Appendix 5C

displacement (boundary shift) than the experimentally observed value as shown in Fig. B.2. The reason for this is that heat losses from the casting mass (the temperature of which increases with solidification) to the furnaces surroundings maintained at the melt transfer temperature decreases the solidification rate at high values of diffusion time.

Since shot is generally used for manufacturing SD castings, the kinetics of liquid-solid interface motion for SD of steels will be predicted using Eq. (47).

5.6.2 Solidification time

The relationship between maximum displacement of the liquid-solid interface (corresponding to 100% solidification of the melt) and shot diameter of orthorhombic packing of shot is derived in Appendix 5C and is given by:

$$\delta_m = 0.264 d_p \quad (49)$$

Substituting for δ from Eq. (49) gives the solidification time for the SD process:

$$t_s = 0.0128 \frac{d_p^2}{K^2 D} \quad (50)$$

Equation (50) can be used to obtain the solidification times once the casting temperature and shot size are fixed for manufacturing SD castings.

5.6.3 Homogenization time

After the melt has solidified, the solute content is minimum at the center of the shot and maximum at the location of the last liquid to freeze. Assuming that the solute has penetrated to the center of the shot, then the concentration profile is approximately sinusoidal and the index of residual microsegregation is given by⁽⁶⁾:

$$\gamma_i = e^{-(\pi^2 D t / l_o^2)} \quad (51)$$

where γ_i is the index of residual microsegregation.

The distance, l_o , across which the solute concentration is maximum and minimum is related to the shot diameter by:

$$l_o = 0.5 d_p + \delta_m \quad (52)$$

$$= 0.764 d_p$$

The % Homogenization, H , is related to the index of micro-segregation by:

$$H = 100 (1 - \gamma_i) \quad (53)$$

Combining and rearranging Eqs. (51), (52) and (53), the homogenization time in terms of percent homogenization and shot diameter is given by:

$$t_h = 0.059 \ln \left(\frac{100}{100 - H} \right) \frac{d_p^2}{D} \quad (54)$$

The LC homogenization time assumed l_0 be equal to $d_p/2$ is given by:

$$t_h^{LC} = 0.038 \ln \left(\frac{100}{100 - H} \right) \frac{d_p^2}{D} \quad (55)$$

Since l_0 is not equal to $d_p/2$, equation (54) is more accurate for predicting the homogenization time.

5.6.4 Total solidification time

The total solidification time, t_{ST} , for the SD process is the sum of the solidification and homogenization time and is given by:

$$\begin{aligned} t_{ST} &= t_s + t_h \\ &= \left(\frac{0.0128}{K^2} + 0.059 \ln \left(\frac{100}{100 - H} \right) \right) \frac{d_p^2}{D} \end{aligned} \quad (56)$$

The above equation is valid only if the phase diagram permits 100 percent SD. The total solidification time is a function

of percentage solute homogenization desired, casting temperature and shot size. Eq. (56) is valid for SD of steels but could be extended to other alloy systems by obtaining the time boundary shift constant for the desired alloy system. In general, an approximate solidification time for any alloy system can be obtained by assuming that the SD solidification occurs under isothermal conditions. This assumption permits the use of Eq. (46) for predicting interface motion in the SD process. The solidification time can be obtained by combining Eqs. (46) and (49) and is given by:

$$t_s = 0.0174 \frac{d_p^2}{K^2 D} \quad (57)$$

Equation (57) is conservative in estimating the solidification time as the actual solidification time is less than the isothermal solidification time. The total solidification time for isothermal conditions is given by:

$$t_{ST} = \left(\frac{0.0174}{K^2} + 0.059 \ln \left(\frac{100}{100 - H} \right) \right) \frac{d_p^2}{D} \quad (58)$$

5.6.5 Solidification rate for SD steel castings

Assuming that the shot packing is orthorhombic, the relationship governing the volumetric fraction melt solidified to normalized liquid-solid interface displacement is derived in Appendix 5C and is given by:

$$f_{LS} = 1 - (1 - \delta^*)^{2.5} \quad (59)$$

The volumetric fraction of solid as a function of normalized liquid-solid interface displacement is given by:

$$f_s = 1 - 0.395 (1 - \delta^*)^{2.5} \quad (60)$$

The normalized diffusion time, the ratio of diffusion times corresponding to displacements of δ and δ_m respectively for SD of steels can be obtained using Eq. (47) and is given by:

$$\tau = \frac{t}{t_s} = \left(\frac{\delta}{\delta_m} \right)^2 = \delta^* \quad (61)$$

where τ is the normalized diffusion time and δ is the normalized liquid-solid interface displacement.

The volume fraction melt solidified at any instant of time during solidification is obtained by combining Eqs. (59) and (61).

$$f_{LS} = 1 - (1 - (\tau)^{\frac{1}{2}})^{2.5} \quad (62)$$

The volume fraction solid at any instant of time during solidification is obtained by combining Eqs. (60) and (61).

$$f_s = 1 - 0.395 (1 - (\tau)^{\frac{1}{2}})^{2.5} \quad (63)$$

The volume fraction melt solidified as a function of normalized diffusion time is shown in Fig. 8. The volumetric fraction of solid as a function of normalized diffusion time is shown in Fig. 9. Assuming that the volume fraction melt is equal to the weight fraction melt, then 50 percent of the melt solidifies in 0.059 times the solidification time, the solidification rate being extremely high during the early stages of solidification. After 90 percent of the melt solidifies, the remaining 10 percent takes 0.64 times the solidification time to freeze, the solidification rate being extremely low during the last stages of solidification.

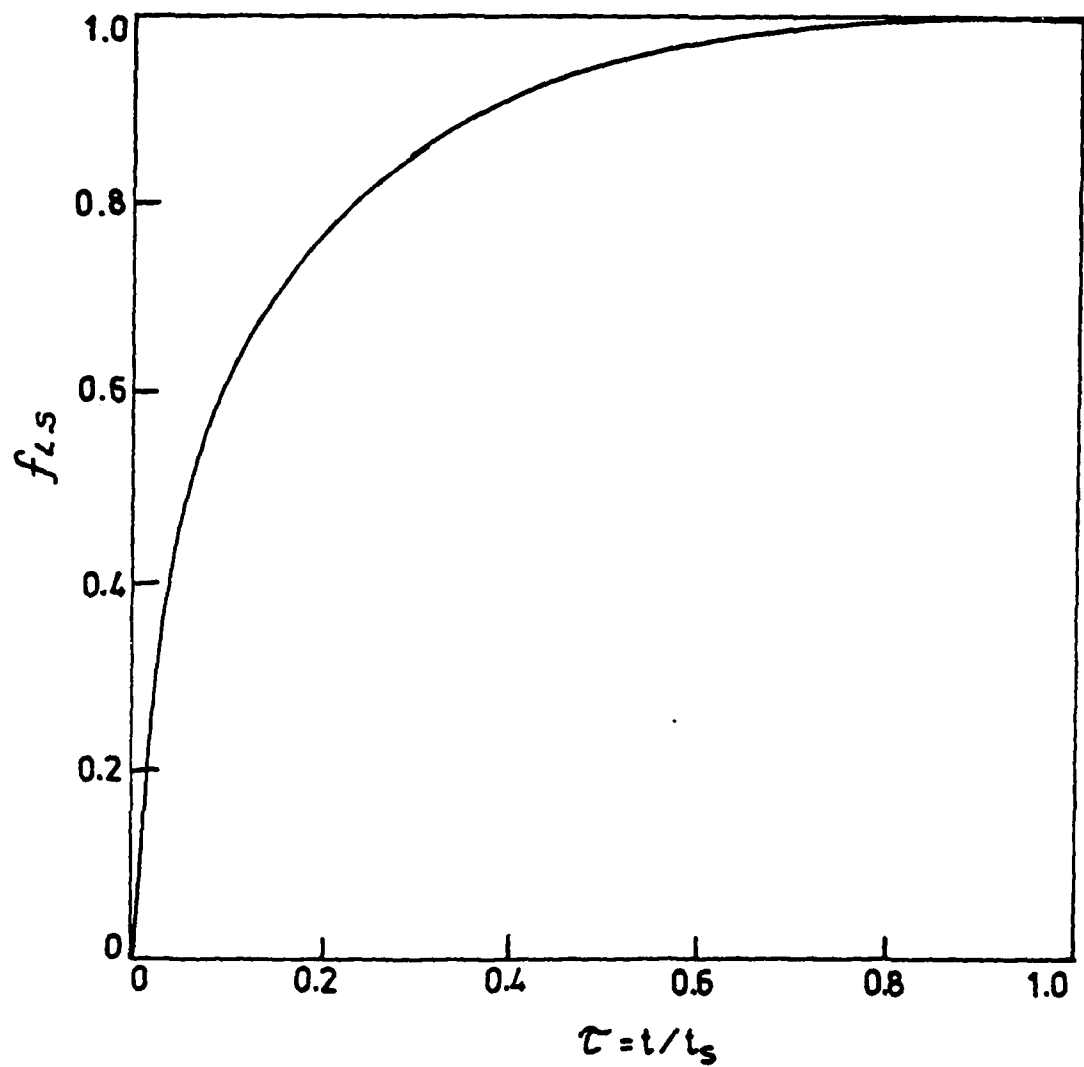


Figure 8. Volumetric fraction melt solidified as a function of normalized diffusion time during SD solidification.

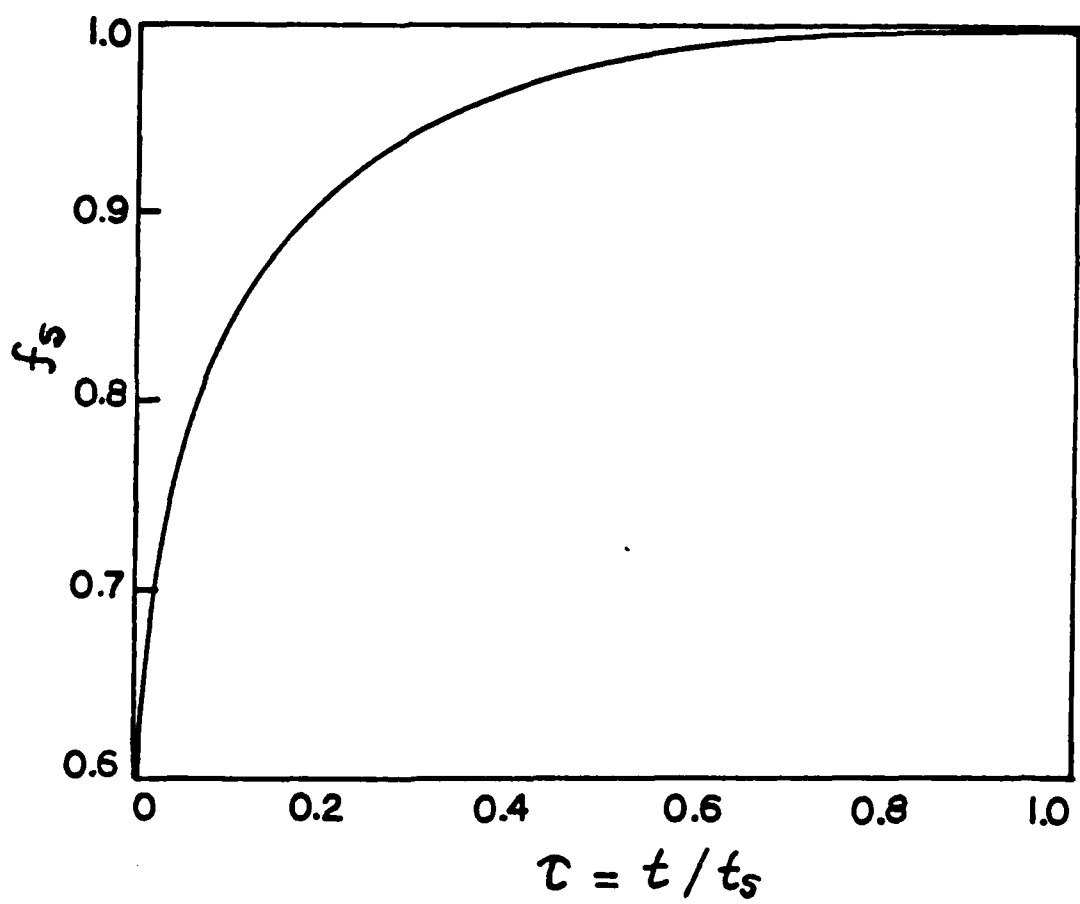


Figure 9. Volumetric fraction solid as a function of normalized diffusion time during SD solidification.

5.7 Macrosegregation In SD Steel Castings

5.7.1 LC Theory

Macro segregation in SD castings results from non-isothermal flow conditions during melt transfer leading to positive solute segregation at the casting top* and negative solute segregation at the casting bottom. The theory assumes that the melt-solid interface is in chemical equilibrium and there is complete mixing of solute in the melt. The temperature rise resulting from latent heat evolution due to SD raises the melt temperature. For a binary alloy system such as the Fe-C, which has a distribution coefficient less than unity, an increase in the melt temperature corresponds to an equilibrium melt solute composition lower than that in the melt (charge); melt located above the PV. When this hotter melt, lower in solute, is forced deeper into the casting, which essentially is a packed bed of shot prior to melt penetration, the average concentration of solute at the casting bottom is much lower than intended. At the casting top, the shot is in contact with undepleted and unheated melt during infiltration and so SD occurs with no depletion in the melt solute content. Under stagnant conditions, i.e., after the melt has been infiltrated, SD can occur only by depletion in the melt solute content.

*Casting top refers to the casting location where the melt first comes into contact with the shot during melt-transfer.

The residence time, analogous to the infiltration time, of undepleted melt in contact with the shot at casting top is responsible for the composition being higher than intended in this region.

Solute segregation along the casting length can be avoided only if SD can be avoided during melt transfer. This is possible only if the infiltration rate is infinite. Since the infiltration rate is finite, the extent of segregation is essentially controlled by the infiltration time or the amount of SD that occurs during this period. The maximum segregation occurs when the infiltration time is equal to the maximum filling time after which melt feeding to the casting interior is abruptly stopped. Hence macrosegregation in the SD process lies between two limits: no segregation at an infinite infiltration rate and maximum segregation when the infiltration time is equal to the maximum filling time. Langford and Cunningham used this concept to combine mass and momentum transfer equations by defining a macrosegregation parameter α , given by⁽¹⁾:

$$\alpha = \frac{t_I}{t_D} \quad (64)$$

where $\alpha = 1$ and t_D is the maximum filling time which corresponds to a solidification thickness of $0.038 d_p$.

The LC maximum filling time is given by⁽¹⁾:

$$t_D = .001 \frac{d_p^2}{K_L^2 D} \quad (65)$$

The LC infiltration pressure obtained by substituting for t_I and t_D in Eq. (64) is given by:

$$p_A^{LC} = \frac{2.5 \times 10^7 \rho_L K_L^4 \epsilon^2 D^2 L^3}{\alpha^2 d_p^5} \quad (66)$$

The above equation was used to define the successful casting criteria: $\alpha = 1$ gives the pressure required to avoid short fills and $\alpha = 0.1$ gives the pressure required to avoid macrosegregation.

5.7.2 Modified LC Theory

The infiltration time given by the LC equation is less than the actual infiltration time and the maximum infiltration time should correspond to the solidification time or to a solidification thickness of $0.264 d_p$. The LC theory can be improved by using a more accurate infiltration model and the solidification time as the criteria for maximum filling time. A new macrosegregation parameter will be defined as the ratio of infiltration to solidification times and is

given by:

$$\alpha_N = \frac{t_I}{t_s} \quad (67)$$

where α_N is the new macrosegregation parameter. The criteria for successful casting manufacture being: $\alpha_N = 1$ to avoid short fills and $\alpha_N \ll 1$ to avoid macrosegregation.

5.7.3 Pressure requirements for laminar and turbulent flow conditions.

The infiltration time for laminar flow conditions during melt transfer is approximately given by Eq. (15). The infiltration pressure can be obtained by combining Eqs. (15), (50) and (67).

$$P_A^{BK} = \frac{5860 \rho_L (1 - \epsilon)^2 K^2 D L^2}{\alpha_N \epsilon^3 d_p^4} \quad (68)$$

where P_A^{BK} is the infiltration pressure required for laminar flow conditions. The infiltration time turbulent flow conditions is approximately given by Eq. (17). The infiltration pressure can be obtained by combining Eqs. (17), (50) and (67).

$$P_A^{BK} = \frac{4725 \rho_L K^4 D^2 (1 - \epsilon) L^3}{\alpha_N^2 \epsilon^3 d_p^5} \quad (69)$$

where P_A^{BP} is the infiltration pressure required under turbulent flow conditions. The infiltration time given by Ergun's equation, valid for all flow regimes does not permit a simplified infiltration pressure equation. It also deviates positively or predicts an infiltration time greater than the actual infiltration time although the average Reynolds numbers for the experimental runs were in the laminar-turbulent flow regime. It is reasonable to assume that flow of liquid metals is turbulent because of inertial effects are more dominant than viscous effects. Hence the successful casting criteria will be based on Eq. (69).

The successful casting criteria for laminar flow may be useful in substitutional alloy systems where small size shot could be used for casting manufacture. For interstitial alloy systems such as Fe-C, the infiltration pressure should be calculated using Eq. (69).

5.7.4 Macrosegregation Parameter

The macrosegregation parameter α_N , for the SD steel casting process will be based on turbulent flow conditions

and can be obtained by rearranging the process variables given in Eq. (69).

$$\alpha_N = \left(\frac{4725 \rho_L K^4 D^2 (1 - \epsilon) L^3}{P_A \epsilon^3 d_p^5} \right)^{\frac{1}{2}} \quad (70)$$

Since α_N is a strong function of the shot size, SD castings were manufactured for shot sizes in ranges of .78 mm to .069 mm at casting temperatures of 1185 and 1360°C . The infiltration pressure and casting length were approximately kept constant in the macrosegregation runs; $L = 100$ mm and $P_A = 700\text{kPa}$. The experimental procedure and results are summarized in Appendix 5D. The values of α_N calculated using Eq. (70) and the corresponding segregation at different casting locations are given in Table II. The constants K , D and ρ_L used for calculating α_N are given in Table III. Figs. 10 and 11 show carbon segregation as a function of α_N at casting temperatures of 1185°C and 1360°C .

5.7.5 Macrosegregation for non-ideal thermal conditions

Ideal thermal conditions refer to the casting temperature. The infiltration pressure given by Eq. (68) and (69) is applicable only to ideal thermal conditions.

Non-ideal thermal conditions refer to deviations of shot

Table II. Macrosegregation for melt and shot at the casting temperature.

Run#	T °C	α_N	Carbon Segregation, %			
			L = 7.5mm	L = 35mm	L = 65mm	L = 90mm
R53	1185	.3900	11	-2	-2	-2
R52	1185	.0860	17	-3	-3	-3
R51	1185	.0178	14	1	-6	-6
R50	1185	.0125	14	1	-6	-6
R54	1185	.0032	3	3	-3	-3
R55	1185	.0008	0	0	0	0
R57	1360	.6700	16	2	-4	-13
R59	1360	.1710	25	15	-18	-24
R60	1360	.0380	14	7	-6	-18
R62	1360	.0068	18	1	-6	-11
R63	1360	.0015	6	0	-2	-1

Table III. Constants K,D and ρ_L used for calculating α_N .

Constant	Casting temperature	
	T = 1360°C	T = 1185°C
K	0.27	0.34
ρ_L kg/m ³	7000	7060
D m ² /s	5.4×10^{-10}	1.54×10^{-10}

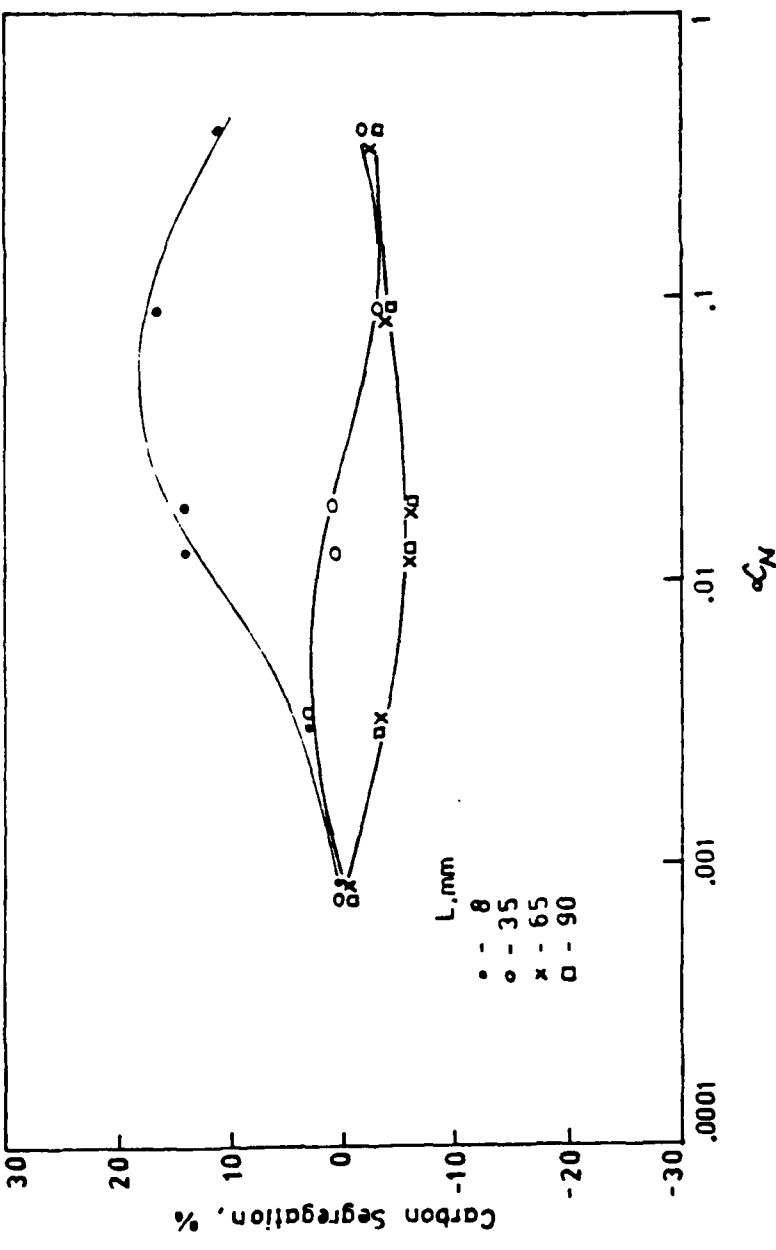


Figure 10. Segregation of carbon as a function of the macrosegregation parameter, α_N , for SD steel castings manufactured at a temperature of 1185°C.

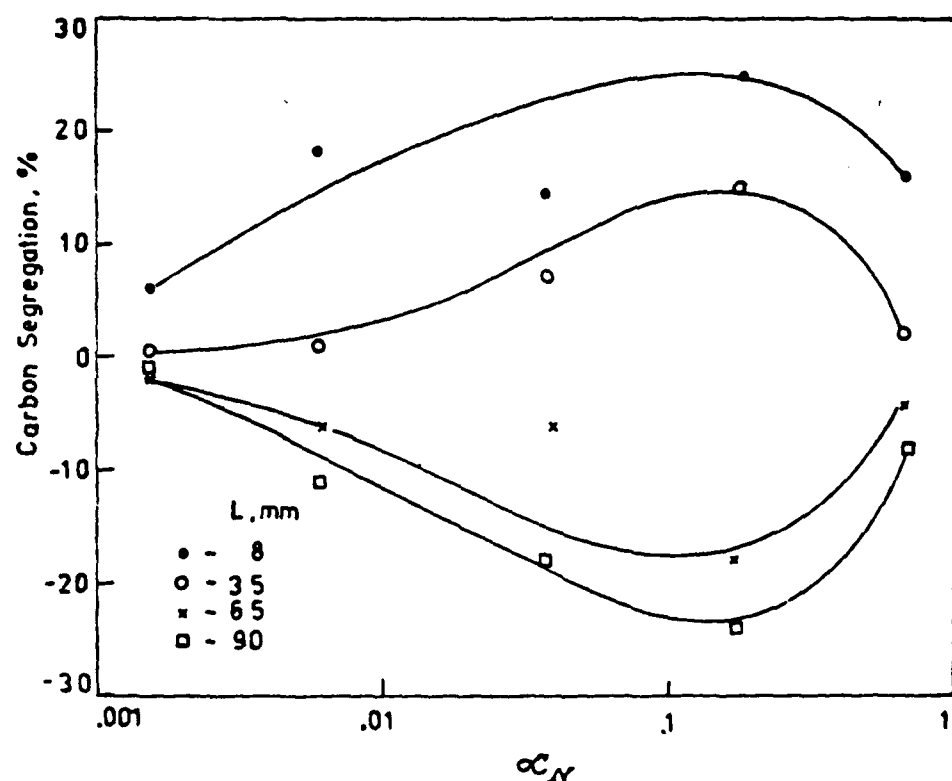


Figure 11. Carbon segregation as a function of the macrosegregation parameter, α_N , at a casting temperature of 1360 $^{\circ}\text{C}$.

and melt temperature from the casting temperature. The two cases that will be discussed under non-ideal thermal conditions are:

1. Superheated melt and shot; melt not saturated with solvent and shot at the melt temperature. This case corresponds to line 2 in Fig. 12.
2. Underheated shot; melt saturated with solvent and shot maintained below the casting temperature.

This case is represented by line 3 in Fig. 12.

1. Superheated melt and shot

The segregation results using a superheated melt and shot are given Appendix 5D. Segregation in this case results from dissolution and so is a function of the superheat, casting temperature and residence time of the melt in contact with the shot during melt transfer. The residence time is analogous to the infiltration time and can be estimated using Eq.(17). Tables IV and V gives the segregation at different casting locations and the corresponding infiltration times for superheat values of 66°C and 19°C respectively; the casting temperature for the runs was 1198°C . To compare the segregation results with ideal thermal conditions α_N for the superheat runs was calculated using Eq.(10). The values of α_N for superheat values of 66°C and 19°C are given in Tables IV and V respectively.

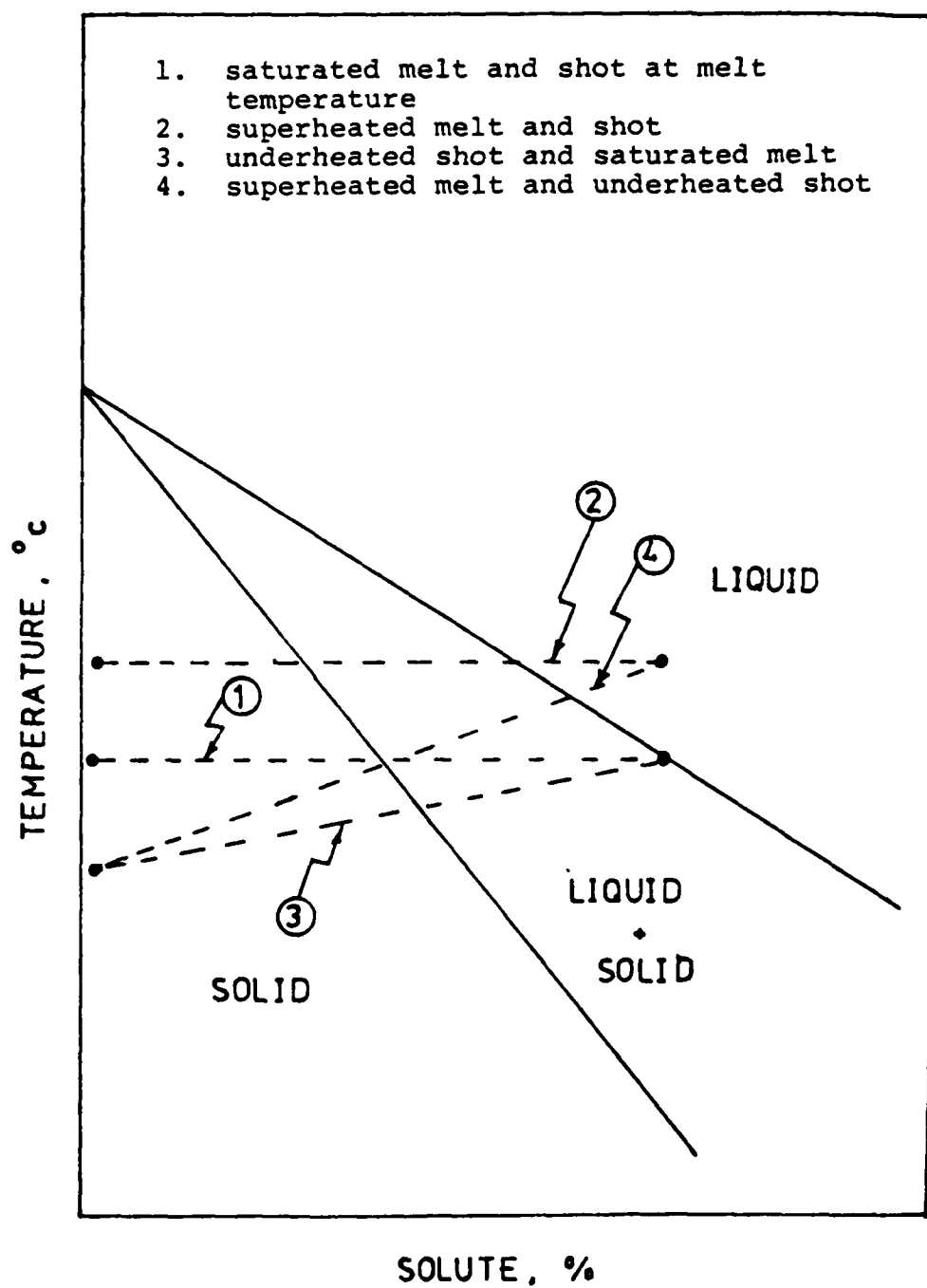


Figure 12. Thermal conditions of shot and melt used for studying macrosegregation in SD castings.

Figures 13 and 14 give the carbon segregation at different casting locations as a function of infiltration time for superheat values of 66°C and 19°C respectively.

2. Underheated shot

The segregation results for underheated shot is given in Table VI. S100 ($d_p = .325$ mm) shot and M20 melt charge were used for casting manufacture. Prior to melt transfer, the melt was maintained at the casting temperature, 1360°C, and the shot at 1335°C corresponding to underheating of 25°C. The maximum liquid penetration was 100 mm at an infiltration pressure of 755 kPa. The average casting composition was 0.94 w/o carbon. The segregation at different casting locations for this case is given in Table VI. The value of α_N is equal to 0.015 for the process conditions used for casting manufacture; the void fraction was assumed to be 0.38.

5.7.6 Discussion of Macrosegregation Results

a) Ideal Thermal Conditions

The segregation curves (segregation vs α_N) attain a maximum value at casting temperatures of 1185°C and 1360°C as shown in Figs. 10 and 11. This contradicts the macrosegregation theory which predicts that segregation should increase with α_N . The segregation pattern deviates from

Table IV. Macrosegregation results for superheated shot and melt; superheat = 66°C and casting temperature = 1198°C.

Run#	t_I	α_N	Carbon segregation, %				
			s	L = 29mm	L = 43mm	L = 80mm	
R1	0.35	.0008		10	4	-9	-16
R2	0.60	.0013		-1	12	-7	-13
R3	0.63	.0125		6	-1	-1	-7
R4	1.08	.0266		8	20	-10	-22

Table V. Macrosegregation results for superheated shot and melt; superheat = 19°C and casting temperature = 1198°C.

Run#	t_I	α_N	Carbon segregation, %				
			s	L = 20mm	L = 35mm	L = 60mm	
R19	0.36	.0008		18	-1	-1	-8
R23	0.44	.0010		15	1	-5	-5
R20	0.59	.0014		9	2	-5	-5
R18	0.66	.0125		10	3	-4	-4
R22	0.71	.0134		9	0	-5	-5
R21	1.05	.0197		16	3	-4	-11

Table VI. Macrosegregation results for an underheated solid

Casting location mm	L_{AV} mm	C(L) w/o	Segregation %
0 - 25	12.5	.93	- 0.01
25 - 50	37.5	.96	0.02
50 - 75	62.5	.97	0.03
75 - 100	87.5	.91	- 0.03

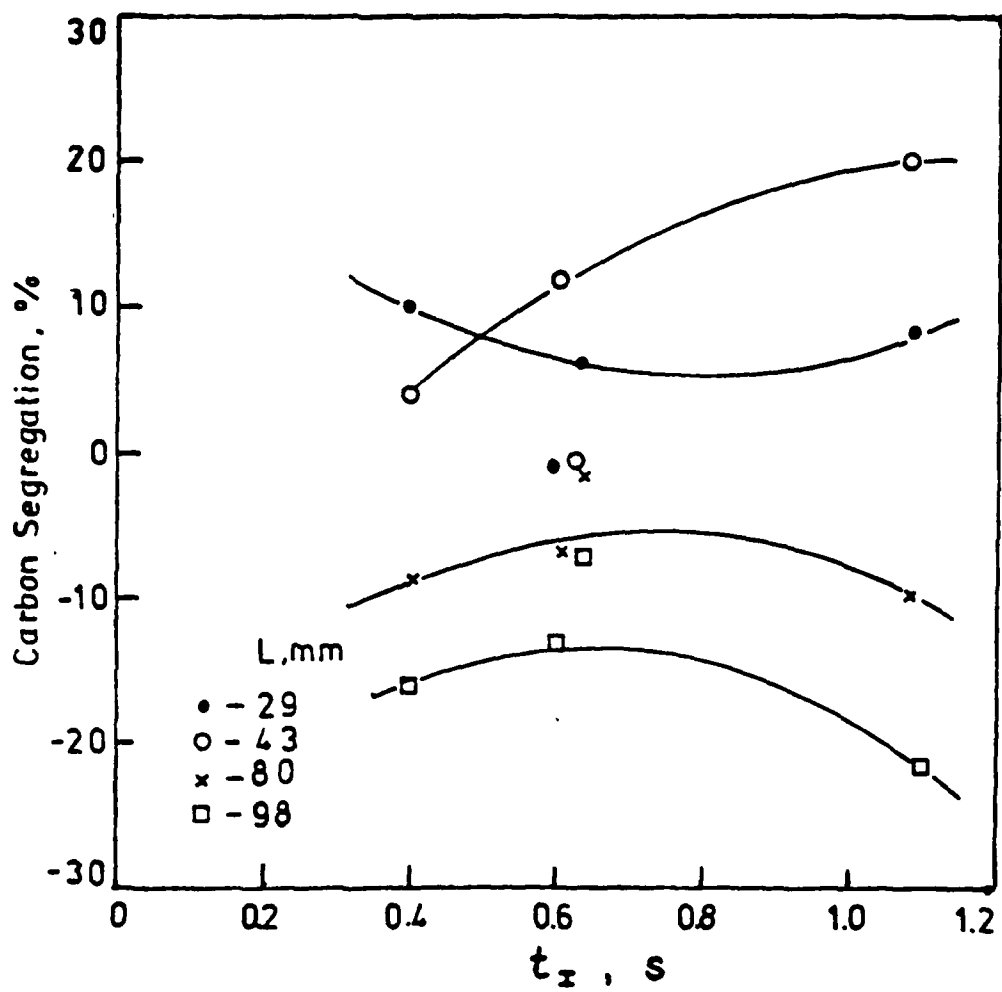


Figure 13. Carbon segregation as a function of infiltration time for SD steel castings using a superheated melt and shot; superheat = 66°C and casting temperature = 1198°C .

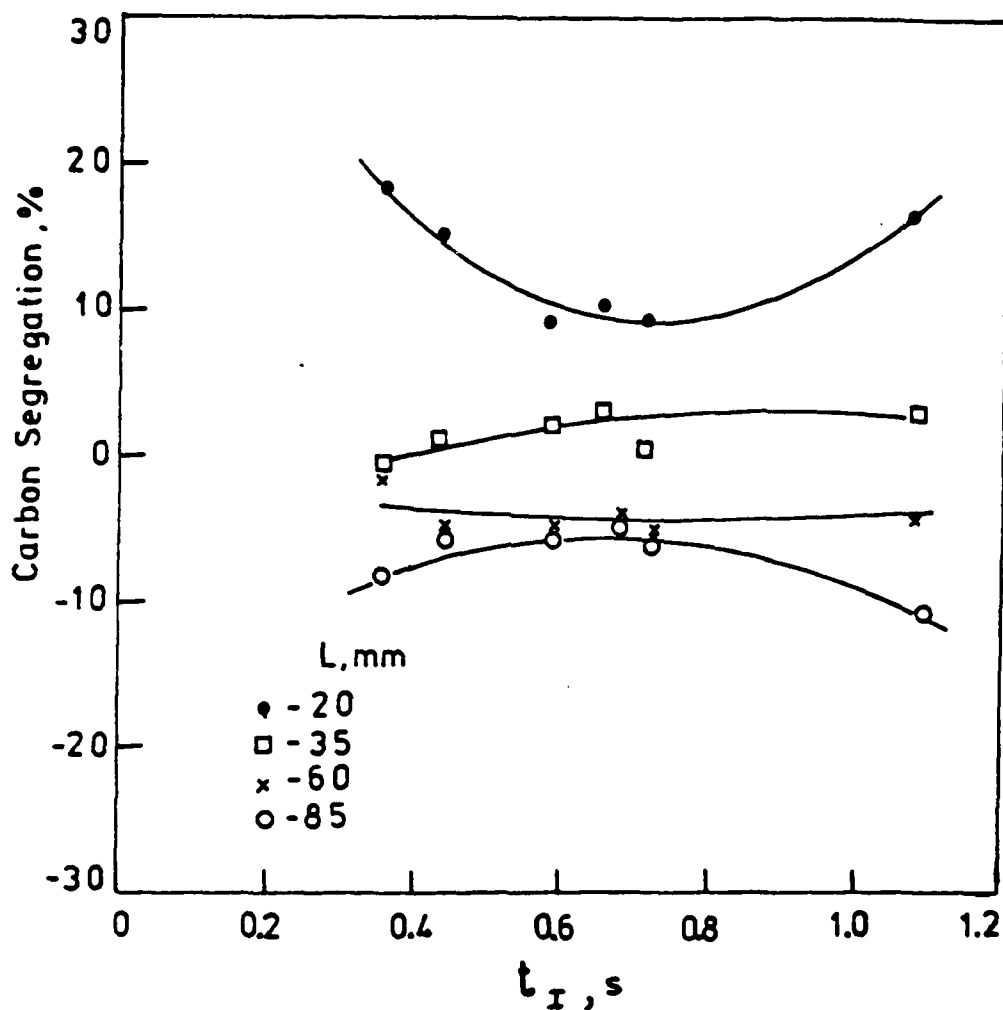
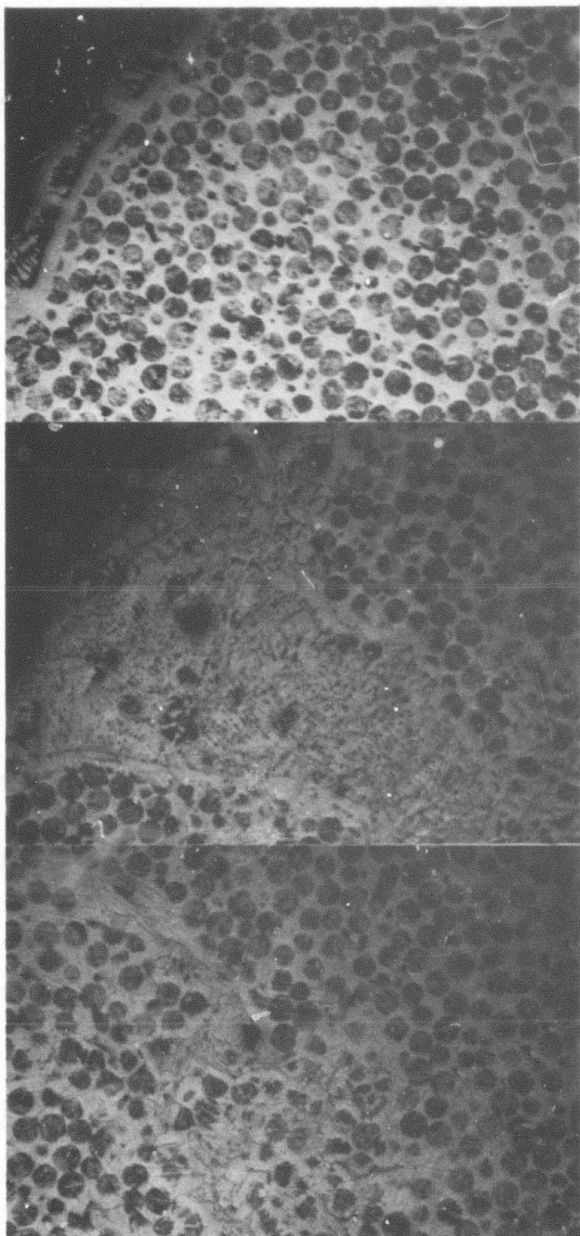


Figure 14. Carbon segregation as a function of infiltration time for SD steel castings using a superheated melt and shot; superheat = 19°C. and casting temperature = 1198°C.

the theory for α_N in the range of .05 to 1. Figures 15 and 16 show the casting microstructure at $\alpha_N = 0.39$ and $\alpha_N = .086$ respectively. The value of α_N was varied by changing the shot size keeping the infiltration pressure and casting length constant for the runs. Hence α_N was increased by decreasing the shot size. The casting microstructure shown in Figs. 15 and 16 indicate that channelling occurs in the packed bed for α_N in the range of .05 to 1. Channels in the packed bed are formed by the melt dissolving the shot in localized regions; the rate of channel formation increasing with decreasing shot size. Once the channel is formed, the bulk of the melt is transported to the packed bed interior through this channel. In the channel, SD is restricted only to the channel walls and so the melt can be fed deeper into the casting with a lower increase in temperature or less segregation than if channelling were absent. The rate of channel formation dictates macrosegregation in the casting; macrosegregation decreasing with increasing channel formation rate. The formation of channel in the packed bed is the reason for the segregation attaining a maximum value. Under channeling conditions, the interacting packed bed theory will not be applicable and hence the maximum penetration distance has no significance.



CASTING
TOP

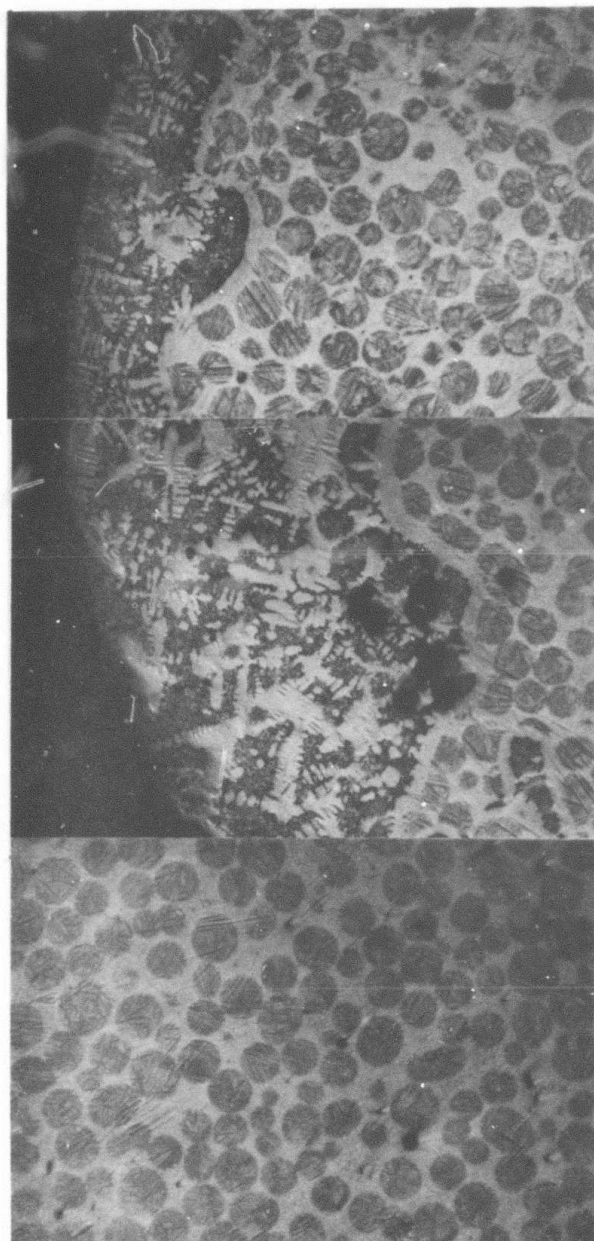
CASTING
MIDDLE

CASTING
BOTTOM

Magnification - 50x

Etch - Nital

Figure 15. Microstructure of a SD casting at different locations manufactured with an $\alpha_N = 0.39$; shot size = 0.069 mm., casting temperature = 1185°C .



CASTING

TOP

CASTING

MIDDLE

CASTING

BOTTOM

Magnification - 50x

F⁴.ch - Nital

Figure 16. Microstructure of a SD casting at different locations manufactured with an $\alpha_N = .036$; shot size = 0.128 mm., casting temperature = 1185°C.

Channelling must be avoided for SD casting manufacture as the casting quality will be poor. The reason for this is that the casting will have localized regions of high solute content where solidification can occur only by thermal freezing. The onset of channelling occurs at $\alpha_N \approx 0.05$ as at this value segregation in the casting attains a maximum value. Hence $\alpha_N > .05$ can be considered as a forbidden region for SD casting manufacture.

High quality castings require that macrosegregation be less than equal to ± 5 percent⁽¹⁾, which requires $\alpha_N = .001$ for SD casting manufacture. At $\alpha_N = .001$, the residence time of the melt in contact with the shot at the casting top is equal to $.001 t_s$. A residence time of $.001 t_s$ corresponds to a normalized liquid-solid interface displacement, (normalized solidification thickness) $\delta^* = 0.03$ and volumetric fraction of melt solidified, $f_{LS} = 0.077$. The macrosegregation parameter was based on an infiltration time for a non-interacting packed bed and for high quality casting, the assumption is valid as only 8 percent of the melt solidified at the casting top. Substituting for $\alpha_N = .001$ in Eq. (69) gives the infiltration pressure for manufacturing high quality SD castings.

$$P_A = \frac{4.9 \times 10^9 \rho_L K^4 D^2 (1 - \epsilon) L^3}{\epsilon^3 d_p^5} \quad (71)$$

Acceptable casting quality, macrosegregation of ± 10 percent is attainable if $\alpha_N^{(1)} = .005$. A residence time of $.005 t_s$ corresponds to $\delta^* = .07$ and $f_{LS} = .17$ at the casting top. Since $\alpha_N = .005$ corresponds to 17 percent of the melt solidifying at the casting top, the deviation of t_I based on a non-interacting packed bed to that of an interacting packed bed will not be significant. A reasonable estimate for infiltration pressure required for attaining acceptable casting quality can be obtained by substituting $\alpha_N = .005$ in Eq. (69).

$$P_A = \frac{1.9 \times 10^8 \rho_L K^4 D^2 (1 - \epsilon) L^3}{\epsilon^3 d_p^5} \quad (72)$$

Equations (71) and (72) give the infiltration pressure required for manufacturing high quality and acceptahle quality SD castings; the infiltration pressure being 25 times greater for a high quality casting then for an acceptable quality casting; the casting temperature, shot size and casting length being identical in the comparision.

The maximum infiltration pressure is dictated by the design pressure of the melt transfer chamber. The minimum shot size that could be used for high quality SD casting manufacture is given by:

$$\begin{aligned}
 d_p(HQ) &= \left(\frac{4.9 \times 10^9 \rho_L K^4 D^2 (1 - \epsilon) L^3}{P_D \epsilon^3} \right)^{1/5} \\
 &= \left(\frac{4.9 \times 10^9 f(T) f(\epsilon) L^3}{P_D} \right)^{1/5} \quad (73)
 \end{aligned}$$

where:

- $d_p(HQ)$ = minimum shot diameter for high quality SD castings.
- $f(T)$ = $\rho_L K^4 D^2$; which is a function of casting temperature.
- $f(\epsilon)$ = $(1 - \epsilon)/\epsilon^3 \approx 11$ for shot packing.
- P_D = design pressure of the melt transfer vessel.

Equation (73) could be used to estimate the minimum shot size for high quality casting manufacture. The minimum shot size for acceptable SD castings is related to $d_p(HQ)$ by:

$$d_p(AQ) = 0.52 d_p(HQ) \quad (74)$$

where $d_p(HQ)$ is the minimum shot size for attaining an acceptable quality casting.

The total solidification time can be obtained by substituting for $d_p(HQ)$ or $d_p(AQ)$ in Eq. (56) to obtain the SD time for acceptable and high quality castings respectively.

b) Non-ideal thermal conditions

1. Superheated Melt And Shot

The segregation in this case results from dissolution⁽⁷⁾ or diffusion melting. The maximum melting occurs at the casting top resulting in a lower solid fraction which gives a higher casting composition in this region. At the casting bottom, the melt is diluted with solute and so the casting composition is higher than intended.

At a superheated value of 66°C it is found that the location of maximum positive segregation is shifted to the casting interior as shown in Fig.12. The segregation is greater than 10 percent and so a superheat of 66°C does not permit SD casting of acceptable quality. At a superheat of 19°C the segregation attains a minimum at infiltration times in the range of 0.5 to 0.7 seconds. Segregation of 10 percent is attainable for infiltration times of 0.5 to 0.7 seconds giving acceptable casting quality with α_N as high as 0.0125.

Lowering the value of superheat should permit SD castings of acceptable quality with larger values of α_N . High casting temperatures should increase the segregation as the dissolution rate is a strong function of temperature.

Since the superheat experiments are limited to values of superheat with reference to a casting temperature of 1198°C, the possibility of using it as a means of controlling macrosegregation is debatable. Superheat values in ranges of 5°C to 10°C may decrease segregation to high quality standards at much higher values of α_N . However from the experimental results it is evident that superheat in excess of 20°C is not permissible for SD casting manufacture.

ii. Underheated Shot

The maximum segregation in this case is \pm 3 percent; negative segregation observed at the casting top and bottom and positive at other locations. The solidification of melt during infiltration occurs due to thermal freezing. This case offers the best means of segregation control as high quality SD castings can be manufactured with α_N values as high as .015, the limitations being the infiltration length being restricted by the shot size and underheating. The results indicate that thermal freezing during infiltration does not significantly change the melt composition as it penetrates the packed bed of shot.

5.7.7 Macrosegregation And Total Solidification Time

Macrosegregation is an index of the casting quality and in common steel making practices must be maintained within

10 percent for acceptable casting quality. The total solidification time includes the solidification and homogenization times and is controlled by the shot size. When SD is used for rapid cycle steel castings then one of the components of the cycle time is the total solidification time. In terms of process economics, it is desirable to obtain high casting quality and operate at low total solidification times for high production rates.

In SD casting manufacture, the casting length is fixed by the casting dimensions, the casting temperature fixed by the composition of melt and shot and the maximum infiltration pressure constrained by the design pressure of the casting machine. Under the above circumstances, the only process variable that can be used to control the casting quality is the shot size and the following relationships between casting quality and total solidification time are valid for ideal and non-ideal thermal conditions:

- . casting quality for ideal thermal conditions can be improved only by increasing the total solidification time; the shot size must be increased to decrease the value of α_N .
- . casting quality for the case of an underheated solid is enhanced at the expense of increasing the total solidification time; the use of large size shot for this case being essential to

compensate for the decrement in void fraction due to thermal freezing.

attaining a limiting casting quality for the case of superheated melt and shot by considerably decreasing the total solidification time; the use of smaller shot being possible as no solidification occurs during melt transfer.

In all the above thermal conditions, improvement in casting quality is achieved at the expense of total solidification time or vice-versa. A non-ideal thermal condition which may provide better casting quality without significantly increasing the total solidification time is by using a superheated melt and a underheated shot as shown by line 4 in Fig. 12. In this case the attainment of thermal equilibrium between the melt and shot during melt transfer prevents diffusion of solute into the shot, which is responsible for macrosegregation under ideal thermal conditions. The thermal freezing which occurs initially is partially restrained by the remelting of the thermally solidified region on the shot at a later period during melt transfer.

5.8 Gases In Shot Region

The influence of gas pressure on casting quality is important for designing a SD die casting machine. The experiemntal procedure and results are given in Appendix 5E.

The specific gravity of the casting as a function of the ratio of gas pressure to driving force for melt transfer, ($P_S/P_A - P_S$) is shown in Fig. E.2. The specific gravity decreases linearly with $P_S/(P_A - P_S)$ and can be expressed as:

$$SG_C = SG_C^0 - 0.27 (P_S/(P_A - P_S)) \quad (75)$$

where:

SG_C - specific gravity of casting

SG_C^0 - specific gravity of casting at $P_S = 0$

P_S - gas pressure in the shot region

P_A - applied gas pressure

The casting quality, measured in terms of specific gravity is not significantly decreased by operating at ($P_S/P_A - P_S$) less than 0.15 indicating that evacuation of gases from the shot region may not be essential for a SD die casting machine.

5.9 Conclusions

The infiltration times for the different fluid flow models were compared with experimental results. It was found that the Burke-Plummer fluid flow model was most accurate in predicting the actual infiltration time for SD castings of steels. The effect of the PV on the infiltration time has been obtained in terms of the time correction function, $f(PV)$, for laminar and turbulent flow conditions.

The solidification time for SD castings of steel in terms of shot sizes derived based on time displacement relationships for SD of steels. An equation was obtained to give the total solidification time, which includes the SD time and the homogenization time. The SD rate was obtained in terms of fraction of solid as a function of diffusion time.

The LC macrosegregation theory was modified and the pressure requirement equations for high quality and acceptable quality SD castings have been derived. The new macrosegregation parameter and experimental results served as the basis for obtaining the pressure requirement criteria.

Gases in shot region did not affect the casting quality significantly. The results indicated that evacuation of gases from the shot region is not essential provided the infiltration pressure is greater than 700 kPa.

REFERENCES

1. G. Langford and R.E. Cunningham: Met. Trans. B, 1978, Volume 9B, pp. 5-19.
2. R.B. Bird, W.E. Stewart and E.N. Lightfoot: Transport Phenomena, John Wiley and Sons, Inc., 1960, pp. 196-200.
3. See Chapter 3 of this report for a detailed analysis of the "Particle Valve."
4. D. Apelian and G. Langford: Rapid Cycle Steel Casting. Proposal for research written for the Defense Advanced Research Program Agency, 1977.
5. D.D. Van Horn: Trans. ASM, 1959, Vol. 51, pp. 185-198.
6. M.C. Flemings: Solidification Processing, McGraw-Hill, 1974, pp. 328-330.
7. J.M. Lommel and B. Chalmers: Trans. Met. Soc. AIME., 1959, Vol. 215, pp. 499.

APPENDICES

APPENDIX 5A

EXPERIMENTAL VERIFICATION OF SD INFILTRATION KINETICS.

1. Experimental Procedure

The set up used for measuring movement of the infiltration melt into the packed bed is described in Appendix 5F. The current through the packed bed was set at an approximate value to ensure a constant current source during infiltration. A few seconds prior to melt transfer, the chart recorder was turned on with a chart speed of 50mm/s and the induction unit was shut off.

2. Relationship between measured voltage and distance.

Figure A.1 shows the movement of the melt in the packed bed at any instant of time. The voltage leads are located at distances of x_1 and L_1 from the top of the bed. Since the experimental infiltration time is measured between the voltage leads, the actual and experimental infiltration time and distance are related by:

$$\begin{aligned} t &= t_I - t_I(x=x_1)^* \\ x' &= x - x_1 \\ L' &= L_1 - x_1 \end{aligned} \quad (A-1)$$

* List of notations are given at the end of this Appendix.

LEGEND

1. external resistance
2. dc voltage source
3. voltage leads
4. current leads
5. voltage recorder
6. shot region infiltrated with melt
7. packed bed of shot
8. mold

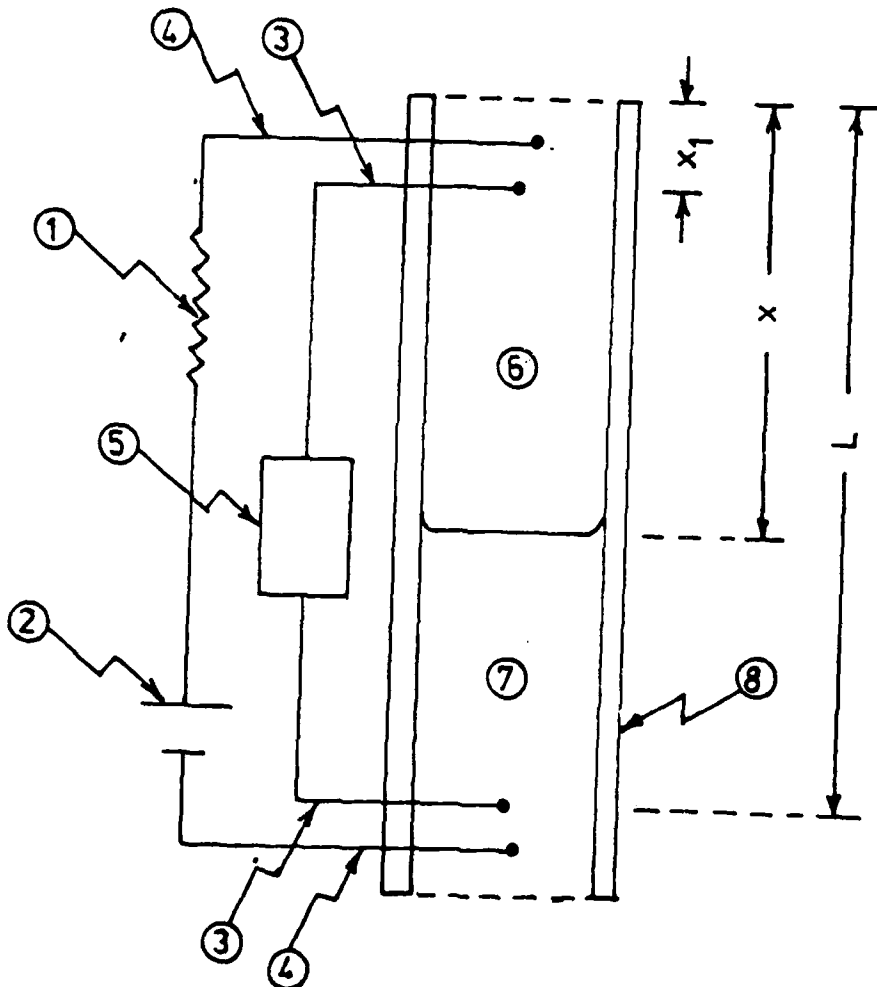


Figure A.1. Schematic diagram of setup measuring melt movement by recording voltage changes in the packed bed during melt transfer.

Boundary conditions for the problem are:

$$\begin{aligned} t &= 0 \text{ at } x' = 0 \\ t &= t^* \text{ at } x' = L_1 \end{aligned} \quad (A-2)$$

The resistance of the advancing melt-packed bed composite can be written as:

$$\begin{aligned} R(t) &= R_C + R_{PB} \\ &= (\rho_C^* x' + \rho_S^* (L' - x'))/A \end{aligned} \quad (A-3)$$

From Equation (A-3) the values of $R(t)$ at $t=0$ and $t=t^*$ are given by:

$$R(0) = \rho_S^* L'/A \quad (A-4)$$

$$R(t^*) = \rho_S^* L'/A \quad (A-5)$$

The voltage at any instant of time is given by:

$$V(t) = I R(t)$$

Combining and rearranging Equations (A-4), (A-5) and (A-6) an expression for distance in terms of voltage can be obtained.

$$\frac{x'}{L'} = \frac{V(0) - V(t)}{V(0) - V(t^*)} \quad (A-7)$$

3. Results

The process conditions, process variables, current through packed bed and location of voltage leads are

given in Tables A-I, A-II and A-III. The voltage, time and distance** data is given in Tables A-IV and A-V.

**Calculated using Equation (A-7).

Table A-1. Process components for infiltration runs.

Run No.	Shot *	Melt	PV
I1	S224	M10	PVS($d_p = 1.55$ mm)
I2	S224	M10	PVS($d_p = 1.55$ mm)

Table A-II. Process variables for infiltration runs

Run No.	$d_p, 10^4 \times m$	$P, 10^{-5} \times Pa$	$T_c, {}^\circ C$	ϵ	L, m	L_{PV}, mm
I1	7.8	6.87	1185	0.38	.115	25
I2	7.8	2.74	1185	0.38	.115	25

Table A-III. Current through packed bed and location
of voltage leads for infiltration runs.

Run No.	I_{ma}	x_1	L_1
I1	69.5	.009	.098
I2	65.6	.015	.105

* The composition of shot and melt used is given in Appendix 5G.

Table A-IV. Voltage vs time data for Run II

$V(x')$ mv	$t(x')$ s	x'/L'
4.65	0	0.00
4.25	0.07	0.111
4.00	0.09	0.181
3.75	0.11	0.250
3.50	0.13	0.319
3.25	0.15	0.389
3.00	0.17	0.458
2.75	0.18	0.523
2.50	0.19	0.597
2.25	0.21	0.670
2.00	0.23	0.736
1.75	0.25	0.805
1.50	0.27	0.875
1.25	0.31	0.944
1.05	0.34	1.000

Table A-V. Voltage vs time data for Run I2

V(x')	t(x')	x'/L'
mv	s	
4.875	0	0
4.500	0.08	0.79
4.000	0.12	0.185
3.500	0.18	0.297
3.000	0.22	0.397
2.500	0.26	0.503
2.000	0.32	0.608
1.500	0.36	0.714
1.000	0.42	0.820
0.500	0.50	0.926
0.150	0.56	1.000

List of Notations

- A - cross-sectional area of packed bed
I - current through packed bed
L - casting length
 L_{PV} - height of particle valve
 L_1 - distance of the bottom voltage lead from the casting top
R - resistance
 R_C - resistance of melt shot composite
 t - experimental infiltration time
 t_I - actual infiltration time
 x - actual melt penetration distance
 x' - experimental melt penetration distance
 x_1 - distance of the upper voltage lead from the casting top
 ρ_C^* - resistivity of melt shot composite
 ρ_{PB}^* - resistivity of shot

APPENDIX 5B

MEASUREMENT OF LIQUID-SOLID INTERFACE MOTION

1. Experimental Procedure

a) Components

Rods (1008 steel) and shot (peening shot decarburized using CO/CO₂ gas mixtures) were used as the solid charge. The melt charge, M10*, was atomized and had a carbon content of 4 percent. The particle valve consisted of spherical alumina particles with an average particle diameter of 1.55 mm. The castings were made in an open end mullite tube, (ID = 6.35 mm), modified to a closed one end tube as described in Appendix 5F.

b) Casting Procedure

The casting procedure involved the following steps:

- The shot, particle valve and melt charge were placed in the mold as described in Appendix 5F.
- The mold was then attached to probe A and flushed with argon
- The mold with its contents attached to the probe was inserted into the vacuum furnace (see Appendix 5F for details). During this period,

*See Appendix 5G for explanation of symbols used to characterize the melt and the shot charges.

the furnace was maintained at 1100°C with a nitrogen gas atmosphere to prevent air from entering the chamber.

- After clamping the probe to the furnace chamber, the valve connecting the probe to the furnace chamber was opened and the chamber and probe were evacuated.
- The furnace temperature was maintained at 1100°C for 1800 seconds for vacuum deoxidation of solid and melt charge.
- The furnace temperature was raised 100°C above the casting temperature and then lowered to the casting temperature.
- Melt transfer was accomplished by closing the valve connecting the probe to the furnace chamber and pressurizing the mold with argon gas.
- The furnace was kept at the casting temperature for homogenization of the melt-solid composite.
- The probe was removed from the furnace by backfilling it with nitrogen gas and releasing the probe chamber clamps.

c) Process Variables

All the castings were made using an infiltration pressure of 700 kPa and at a casting temperature of 1185°C.

d) Measurement of Solidified Thickness

The castings were cut, mounted and polished using standard metallographic procedures. The specimens were then etched with a suitable etchant* to demarcate the solid, solidified and melt regions. The solidified thickness was measured using a travelling microscope. At least three sets of data were taken for each specimen. For shot, the solidification thickness and shot diameter were measured parallel and perpendicular to the melt flow direction. The actual solidification thickness can be obtained using Eq. (B-1).

$$\delta = ((\delta' + d/2)^2 + (d_p^2 - d^2)/4)^{1/2} - d_p/2$$

(B-1)

where:

δ' - measured solidified thickness

d - measured shot diameter

d_p - average particle diameter

δ - actual solidified thickness

* A dilute mixture of Picral and Nital

Equation (B-1) is valid for $d \leq d_p$. For $d > d_p$, δ was assumed to be equal to δ' .

2. Results.

Tables B-I to B-IV summarize the time-solidification thickness measurements for shot and rods. The value of K (defined in section 5.6) and the diffusion coefficient of carbon in austenite for shot and rods are given in Table B-V. Figs. B.1 and B.2 give plots of t vs (δ^2/K^2D) for shot and rods respectively. The best fit straight lines through the origin for the plots in Figs. B.1 and B.2 give the following slopes:

Rods: $m = 0.140$

Shot: $m = 0.184$

Table B-Ia. Measurement of solidification thickness (δ) as a function of time; shot - S225*,
 $d_p = .55$ mm., viewing plane - parallel to melt flow direction.

OBS#	t	d	δ'	δ
	s	mm	mm	mm
1	65	0.550	0.075	0.075
2	65	0.625	0.087	0.087
3	65	0.416	0.085	0.069
4	65	0.472	0.102	0.091
5	126	0.475	0.117	0.106
6	126	0.533	0.120	0.117
7	126	0.533	0.100	0.098
8	126	0.438	0.122	0.104

Table B-Ib. Measurement of solidification thickness (δ) as a function of time; shot - S225,
 $d_p = .55$ mm., viewing plane - perpendicular to melt flow direction.

OBS#	t	d	δ'	δ
	s	mm	mm	mm
1	65	0.500	0.092	0.086
2	65	0.523	0.087	0.084
3	65	0.508	0.077	0.072
4	65	0.530	0.075	0.073
5	126	0.530	0.117	0.114
6	126	0.450	0.118	0.102
7	126	0.540	0.100	0.099
8	126	0.430	0.123	0.104

* The shot is characterized in Appendix 5G.

Table B-IIa. Measurement of solidification thickness (δ) as a function of time; shot - S224,
 $d_p = 0.78$ mm, viewing plane - parallel to melt flow direction.

OBS#	t	d	δ'	δ
			mm	mm
1	65	.670	0.112	0.100
2	65	.620	0.092	0.076
3	65	.758	0.070	0.068
4	65	.648	0.090	0.077
5	126	.565	0.130	0.102
6	126	.573	0.128	0.102
7	126	.667	0.131	0.116
8	126	.742	0.122	0.117

Table B-IIb. Measurement of solidification thickness (δ) as a function of time; shot - S224,
 $d_p = 0.078$ mm, viewing plane - perpendicular to melt flow direction.

OBS#	t	d	δ'	δ
			mm	mm
1	65	0.653	0.106	0.092
2	65	0.690	0.075	0.068
3	65	0.578	0.073	0.057
4	65	0.752	0.088	0.085
5	126	0.667	0.133	0.103
6	126	0.557	0.133	0.103
7	126	0.583	0.140	0.113
8	126	0.551	0.152	0.119

Table B-III. Measurement of solidification thickness (δ)
as a function of time; viewing plane
perpendicular to the melt flow direction.

d_p	t	δ	δ_{AV}
mm	s	mm	mm
.876	60	.113	.105
		.110	
		.103	
		.097	
		.130	.122
	100	.110	
		.127	
		.120	
		.160	.152
		.123	
1.20	200	.172	
		.150	
		.090	.099
		.097	
		.100	
	60	.107	
		.117	.130
		.120	
		.143	
		.143	
1.55	200	.127	.149
		.160	
		.163	
		.147	
		.100	.100
	100	.100	
		.100	
		.117	.123
		.113	
		.110	
400	200	.113	
		.127	.150
		.160	
		.147	
		.163	
	400	.216	.215
		.216	
		.216	
		.210	
		.26	.239
800	800	.257	
		.260	

Table B-IV. Average measured value of δ as a function
of time for shot

Shot	dp mm	t s	$\delta(//)$ _{AV} mm	$\delta(L)$ _{AV} mm	δ_{AV} mm
S224	.780	65	0.080	0.076	0.078
S224	.780	126	0.109	0.110	0.110
S225	.550	65	0.080	0.079	0.080
S225	.550	.26	0.106	0.105	0.106

Table B-V. Values of D and K for shot and rods
at a SD casting temperature of 1185°C.

Charge	C_S^* w/o	C_S^* w/o	C_L^* w/o	F(K)	K	D $\times 10^{10} \text{ m}^2/\text{s}$
S224	0	1.93	4.04	0.914	0.337	1.537
S225	0	1.93	4.04	0.914	0.337	1.537
Rods(1008)	0.05	1.93	4.04	0.891	0.332	1.537

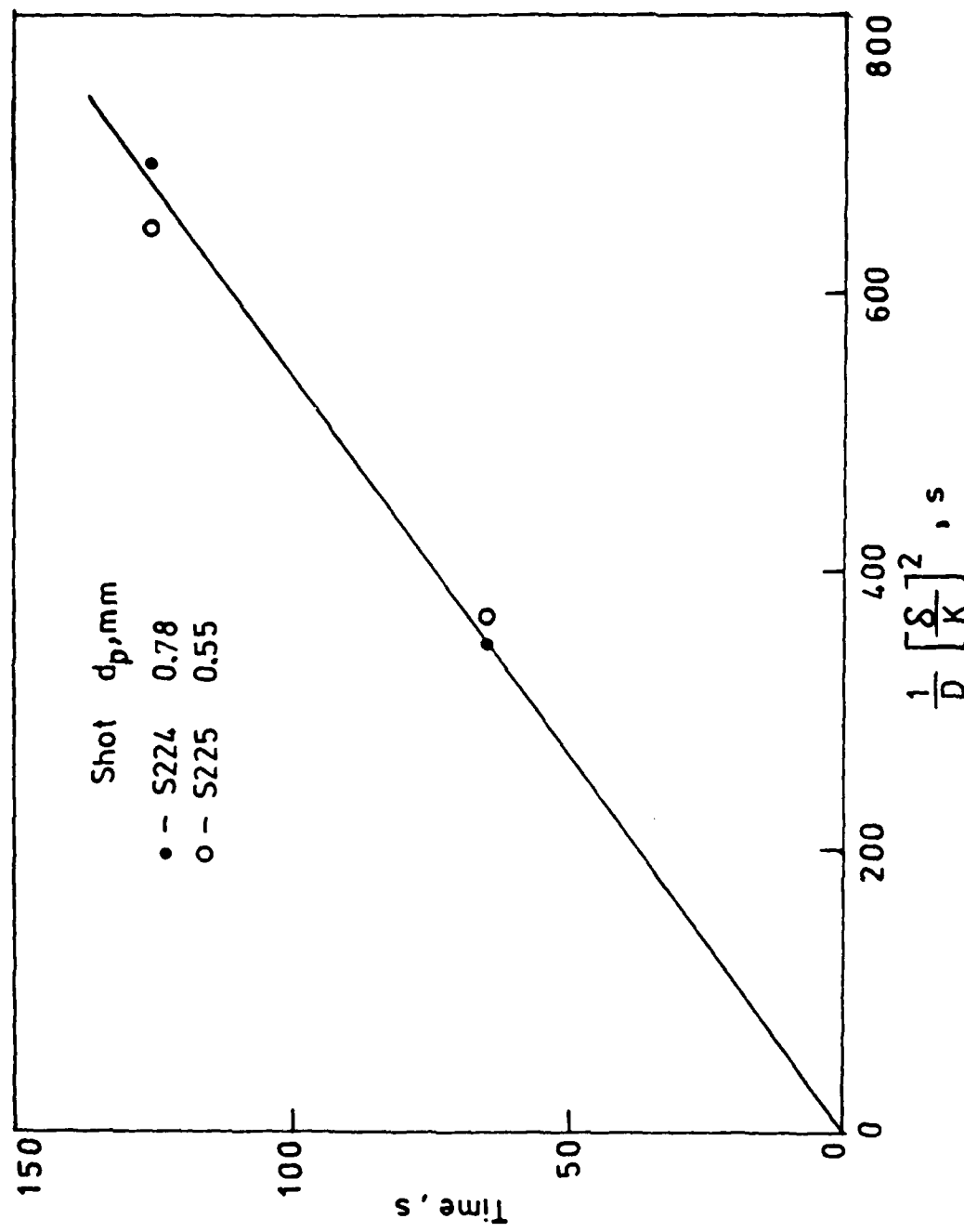


Figure B.1. Plot of diffusion time vs $\delta^2/K^2 D$ for shot at a casting temperature of 1185°C.

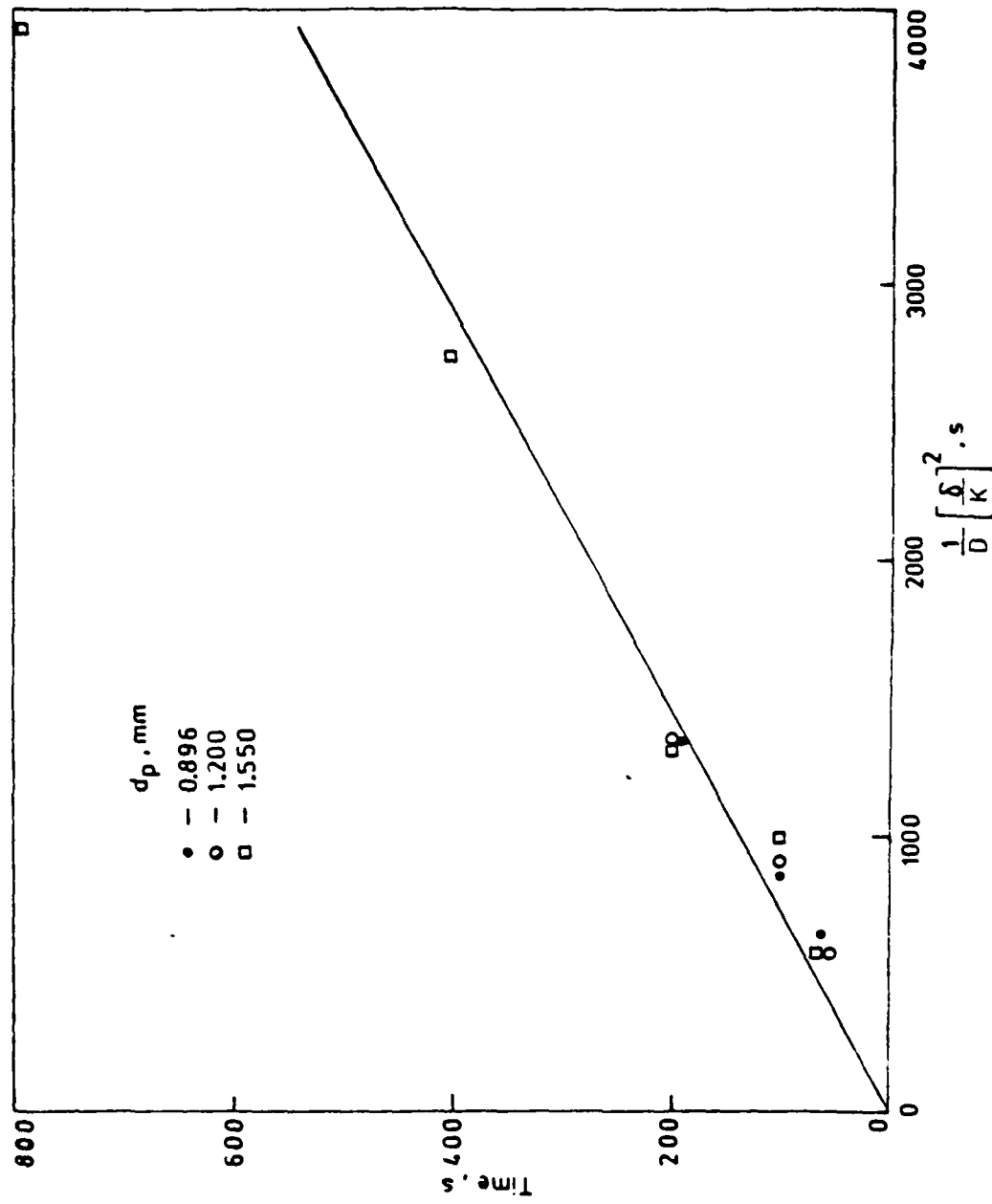


Figure B.2. Plot of diffusion time vs δ^2/K_D^2 for rods at a casting temperature of 1185°C.

APPENDIX 5C

RELATIONSHIP BETWEEN SOLIDIFIED THICKNESS
AND VOLUME OF MELT SOLIDIFIED FOR SHOT

1. Unit Cell

The unit cell for packing of shot is assumed to be orthorhombic. Orthorhombic packing of a single size shot gives a void fraction of 0.395, whereas the observed void fraction for shot with a diameter variation of 10 percent is in the range of 0.37 to 0.400. The unit cell is shown in Fig. C.1.

2. Maximum Solidification Thickness for Shot

After the melt is transferred into the shot region, the last liquid to freeze will be located in the region O' or the centroid of $\Delta A'B'C'$. The solidified thickness, δ for complete solidification can be computed from Fig. C.2 which is a vertical section through line AO in Fig. C.1.

$$\begin{aligned}\delta_m &= AO' - AD \\ &= 0.264 d_p\end{aligned}\quad (C-1)$$

3. Relationship between volumetric fraction solid,
volumetric fraction liquid and solidified thickness.

One twelfth of the unit cell, shown in Fig. C.3, was

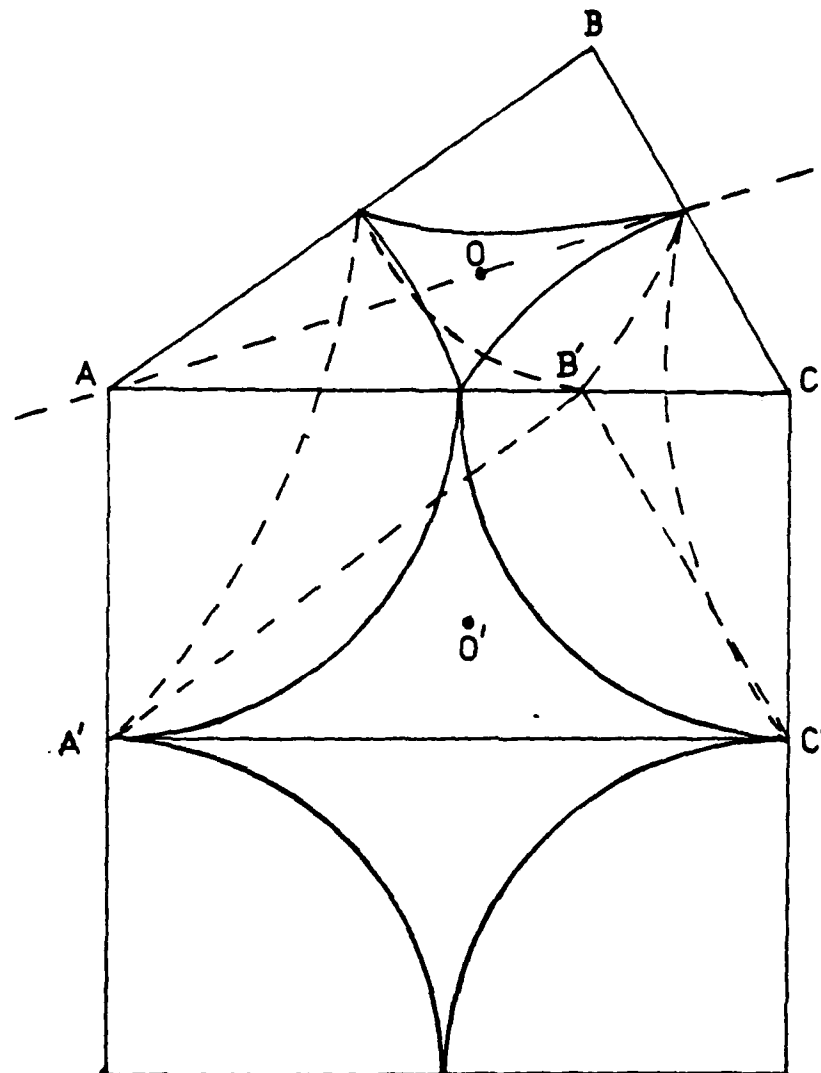


Figure C.1. Unit cell for orthorhombic packing of shot

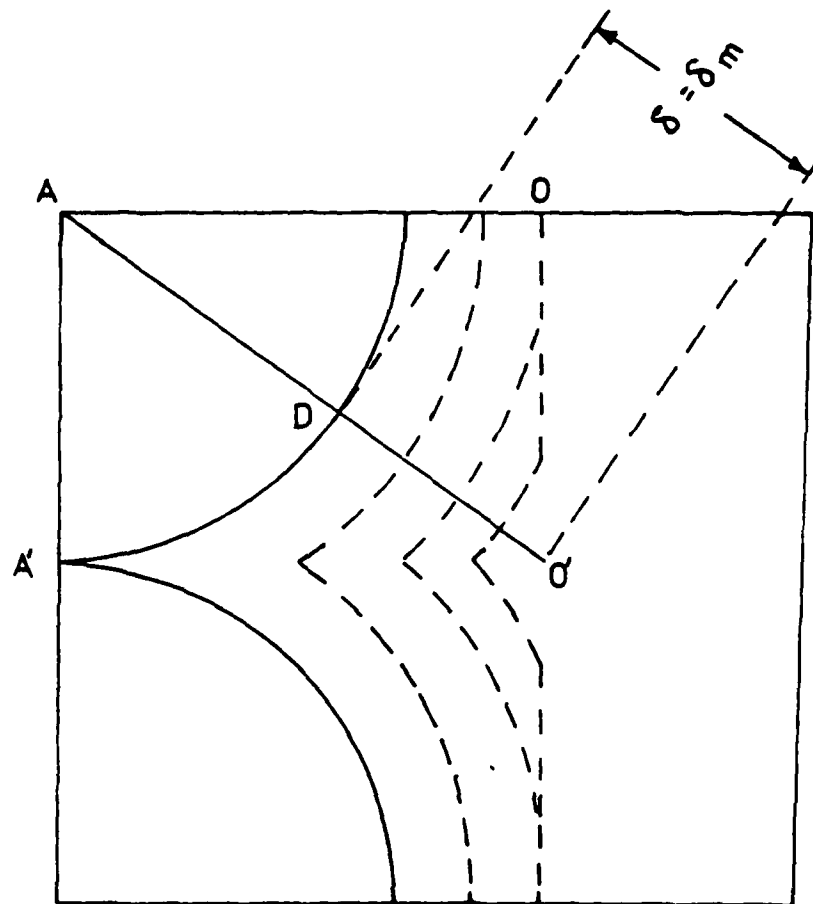


Figure C.2. Vertical section through line AO of unit cell in Fig. 2C.1, showing movement of liquid-solid interface movement during solidification

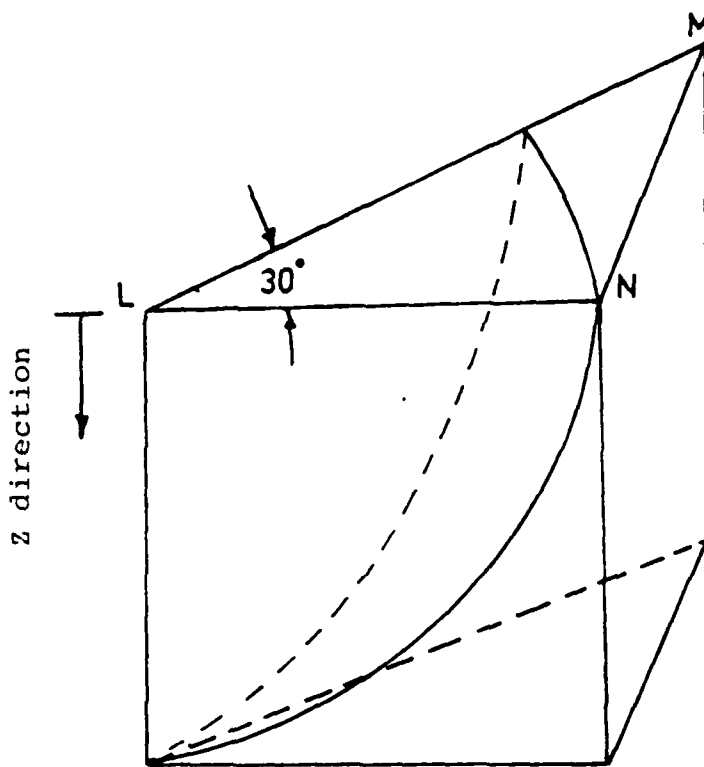


Figure C.3. Unit cell used for calculating volume fraction solid and volume fraction melt as a function of liquid-solid interface motion for shot charge.

used to estimate volumetric fraction of liquid and solid during solidification. As the front moves, the value of δ is zero outside the cell volume, or δ is constrained by the boundaries of the unit cell. The solidification thickness was taken as increment values of particle diameter:

$$\delta = f_1 d_p \quad (C-2)$$

where: f_1 is given by:

$$0 \leq f_1 \leq 0.264 \quad (C-3)$$

Since the cross-sectional area of cell is constant in the Z direction, the solid area, $A_s(\delta)$ for a given δ was calculated for different Z values; 0 to $0.5 d_p$. The volume of solid for a given value of f_1 is given by:

$$V_s(f_1) = \int_0^{0.5} A_s(f_1) dz \quad (C-4)$$

The volume of the unit cell is given by:

$$V_c = A_c d_p / 2 \quad (C-5)$$

where A_c is the area of ΔLMN in Fig. C.3. The volume fraction solid is obtained by combining Equations (C-4) and (C-5).

$$\epsilon_s(f_1) = v_s(f_1)/v_s = \int_0^1 (A_s(f_1)/A_c) dz' \quad (C-6)$$

where z' is given by:

$$z' = 2z'/d_p \quad (C-7)$$

In Fig. C.4, $(A_s(f_1)/A_c)$ is plotted vs z' for different f_1 values. The area under each curve gives the value of the integral in Eq. (C-7) and hence the value of $\epsilon_s(f_1)$. The relationship between $\epsilon_s(f_1)$ and $\epsilon_L(f_1)$ is given by:

$$\epsilon_L(f_1) = 1 - \epsilon_s(f_1) \quad (C-8)$$

where $\epsilon_L(f_1)$ is the volume fraction of liquid. The relationship between δ/d_p and δ/δ_m can be obtained using Eq. (C-1)

$$\delta^* = (\delta/\delta_m) = (\delta/.264 d_p) = (f_1/.264) \quad (C-9)$$

Table C-I gives the values of $\epsilon_L(\epsilon_L at f_1/0.264)$, $\epsilon_s(\epsilon_s at f_1/0.264)$ and δ^* obtained using Eqs. (C-6), (C-8) and (C-9). Mathematical expressions relating δ^* to ϵ_L and ϵ_L to δ^* are given by:

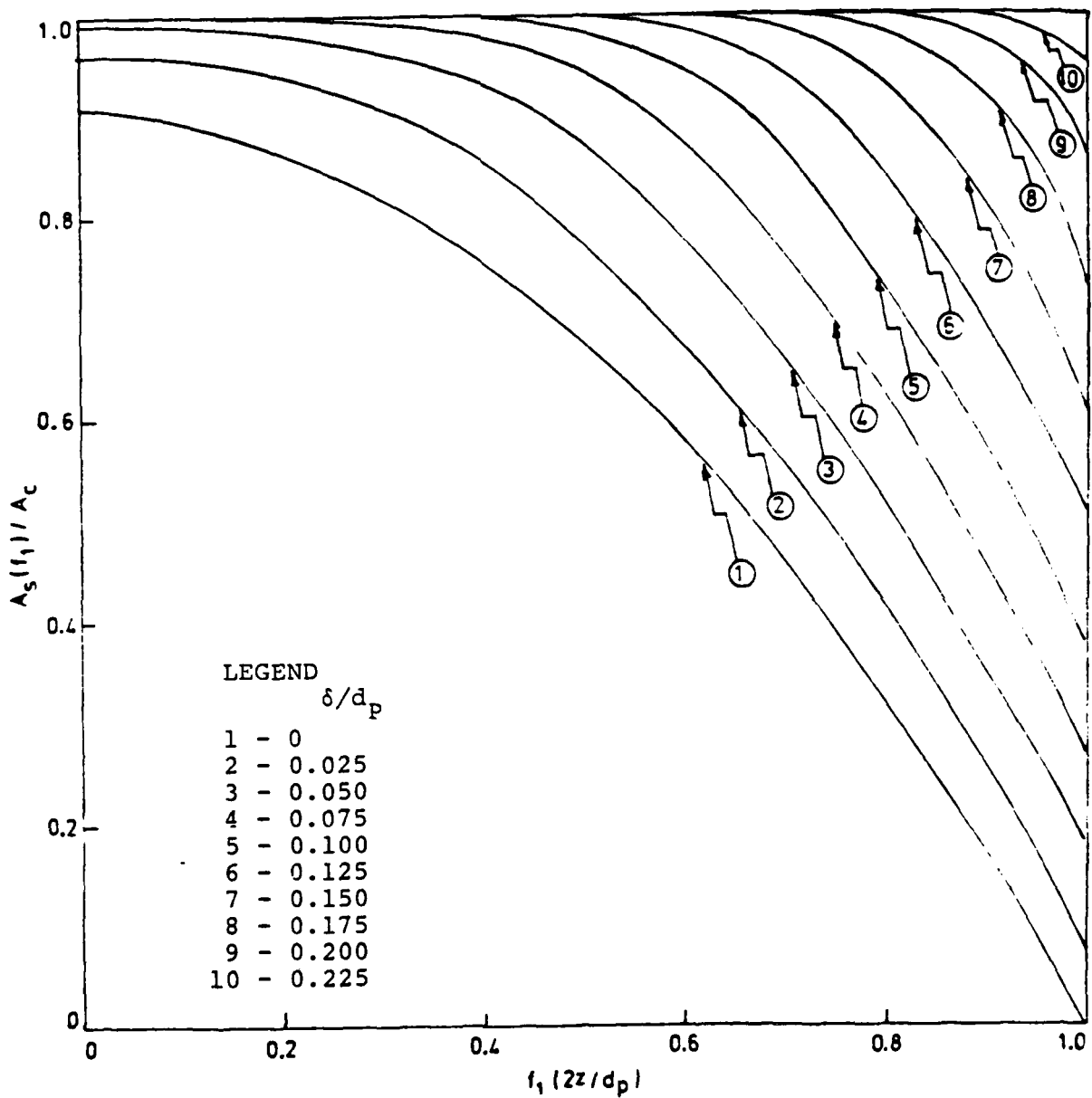


Figure C.4. Fraction of cross-sectional area occupied by solid as a function of z for different displacement values during SD.

Table C-I. - Volumetric fraction of liquid and solid
 as a function of dimensionless displacement,
 δ^* , for orthorhombic packing of shot.

δ^*	ϵ_L	ϵ_S
0	.395	.605
0.0948	.309	.691
0.1895	.234	.766
0.2843	.170	.830
0.3791	.119	.881
0.4738	.077	.923
0.5686	.063	.937
0.6634	.049	.951
0.7582	.029	.971
0.8529	.015	.981
0.9477	.005	.995
1.000	0	1.000

$$\epsilon_L = 0.395 (1 - \delta^*)^{2.5} \quad 0 \leq \delta \leq .526$$

$$= 0.1774 (1 - \delta^*)^{2.5} \quad .526 \leq \delta^* \leq 1 \quad (C-10)$$

$$\delta^* = 1 - (\epsilon_L / .395)^{.4} \quad .395 \geq 1 \geq .077$$

$$= 1 - (\epsilon_L / .1774)^{.77} \quad .077 \geq \epsilon_L \geq 0 \quad (C-11)$$

The volume fraction melt solidified at any instant of time, f_{LS} , is given by:

$$f_{LS} = (\epsilon_0 - \epsilon_L) / \epsilon_0 \quad (C-12)$$

where ϵ_0 is 0.395 for orthorhombic packing of shot.

The relationship between f_{LS} and δ^* is obtained by:

$$f_{LS} = 1 - (1 - \delta^*)^{2.5} \quad .0 \leq \delta \leq .526$$

$$= 1 - 0.45 (1 - \delta^*)^{1.3} \quad .526 \leq \delta \leq 1 \quad (C-13)$$

At $\delta^* = .526$ the value of $f_{LS} = 0.845$ or approximately 85 percent of melt has solidified. To simplify the relationship between f_{LS} and δ^* , it will be assumed that the value of $\delta^* = .526$ corresponds 100 percent solidification of the melt. This leads to an approximate relationship between f_{LS} and δ^* given by:

$$f_{LS} = 1 - (1 - \delta^*)^{2.5} \quad (C-14)$$

The fraction of melt solidified as a function of normalized boundary shift solidification thickness can be predicted accurately for $0 \leq \delta^* \leq .526$ and with an error of less than 5 percent for $.526 \leq \delta^* \leq 1$ using Eq. (C-14). The relationship is valid only for orthorhombic packing of shot.

The volume fraction solid at any instant of time is given by:

$$f_s = f_{s(t=0)} + \epsilon_0 f_{LS} \quad (C-15)$$

where $f_{s(t=0)} = .605$ and $\epsilon_0 = \epsilon_L(t=0) = .395$

Substituting for $f_{s(t=0)}$ and ϵ_0 in Eq. (C-15) gives the volume fraction solid (f_s) in the casting as a function of δ^* .

$$f_s = 1 - .395 (1 - \delta^*)^{2.5} \quad (C-16)$$

APPENDIX 5D

EXPERIMENTAL PROCEDURE AND RESULTS FOR
MACROSEGREGATION IN THE FE-C SYSTEM

1. Experimental Procedure

The solid and melt charge used for the macrosegregation runs are given in Table D-I. Spherical alumina particles with an average diameter of 1.55mm were used for the particle valve. A mullite tube, ID = 6.35 mm, open both ends, was used for casting manufacture. The tube was modified to a closed one end as described in Appendix 5F. The casting procedure was the same as that described in Appendix 5B. The process variables and variables used to estimate the void fraction are given in Tables D-II and D-III. The castings were cut and analysed for carbon content* at four casting locations.

2. Results

The casting composition (carbon content) as a function of casting location is given in Table D-IV. The average casting composition, was obtained from the casting composition location data using Eq. (D-1).

$$\bar{c}_c = \frac{1}{L} \int_0^L c(x) dx \quad (D-1)$$

* The author is indebted to Bethlehem steel for chemical analysis

Table D-I. SD components for Macrosegregation runs

Run#	Shot	Melt
R1	S221	M10
R2	S221	M10
R3	S100	M10
R4	S100	M10
R18	S100	M10
R19	S221	M10
R20	S221	M10
R21	S100	M10
R22	S100	M10
R23	S221	M10
R50	S100	M10
R51	S100	M10
R53	S100	M10
R54	S225	M10
R56	S224	M10
R57	S100	M20
R59	S100	M20
R60	S100	M20
R62	S225	M20
R63	S224	M20

Table D-II. Process variables for macrosegregation runs.

Run#	d_p mm	ϵ	L mm	T_c °C	ΔT °C	P_A kPa	t ** s
R1	0.780	0.393*	114	1264	66	833	200
R2	0.780	0.393*	114	1264	66	284	200
R3	0.275	0.380*	114	1264	66	833	200
R4	0.275	0.380*	114	1264	66	284	200
R18	0.275	0.365	108	1217	19	738	185
r19	0.780	0.402	113	1217	19	738	1185
R20	0.780	0.382	102	1217	19	239	1185
R21	0.275	0.376	104	1217	19	239	150
R22	0.275	0.372	100	1217	19	480	150
R23	0.780	0.393	110	1217	19	480	1185
R50	0.275	0.387	115	1185	0	701	175
R51	0.231	0.391	114	1185	0	701	130
R52	0.128	0.376	104	1185	0	701	50
R53	0.069	0.374	108	1185	0	701	50
R54	0.463	0.370	104	1185	0	701	500
R55	0.780	0.419	113	1185	0	701	1185
R57	0.069	0.378	94	1360	0	701	50
R59	0.128	0.365	102	1360	0	701	50
R60	0.231	0.392	109	1360	0	701	50
R62	0.463	0.387	108	1360	0	701	60
R63	0.780	0.402	101	1360	0	701	165

* Values estimated from other runs

**Solidification and homogenization time used for casting manufacture

Table D-III. Variables used for estimating void-fraction.

Run#	d_{PB} mm	L mm	W gms	ρ_s kg/m^3
R1	-	114.3	-	7650
R2	-	114.3	-	7650
R3	-	114.3	-	7800
R4	-	114.3	-	7800
R18	6.30	107.5	16.7	7800
R19	6.18	113.0	15.5	7650
R20	6.38	102.0	15.4	7650
R21	6.41	103.5	16.3	7800
R22	6.45	100.0	16.1	7800
R23	6.42	110.0	16.1	7650
R50	6.25	114.5	16.8	7800
R51	6.30	113.5	16.8	7800
R52	6.35	103.5	16.0	7800
R53	6.35	109.0	16.7	7800
R54	6.36	104.0	15.9	7650
R55	6.35	113.0	15.9	7650
R57	6.45	96.0	15.0	7800
R59	6.27	101.5	15.5	7800
R60	6.35	108.5	16.3	7800
R62	6.32	108.0	15.9	7650
R63	6.30	101.0	14.4	7650

Table D-IV. Casting composition and percent deviation from mean casting composition for macrosegregation runs.

Run#	Casting Location	L_{AV}	L_{AV}/L	$c(x)$	S^*
				w/o	%
R1	19 - 38	29	0.25	1.7	10
	70 - 57	48	0.42	1.6	4
	70 - 89	80	0.86	1.3	- 9
	89 - 108	98	0.86	1.3	-16
R2	19 - 38	29	0.25	1.6	- 1
	38 - 57	48	0.42	1.8	12
	70 - 89	80	0.70	1.5	- 7
	89 - 108	98	0.86	1.4	-13
R3	19 - 38	29	0.25	1.7	- 6
	38 - 57	48	0.42	1.6	- 1
	70 - 89	80	0.70	1.6	- 1
	89 - 108	98	0.86	1.5	- 7
R4	19 - 38	29	0.25	1.8	8
	38 - 57	48	0.42	2.0	20
	70 - 89	80	0.70	1.5	-10
	89 - 108	98	0.86	1.3	-22
R18	0 - 20	10	0.09	1.6	10
	25 - 45	35	0.33	1.5	3
	51 - 70	60	0.56	1.4	- 4
	76 - 92	86	0.80	1.4	- 4
R19	0 - 20	10	0.09	1.8	18
	25 - 45	35	0.31	1.5	- 1
	50 - 70	60	0.53	1.5	- 1
	76 - 92	86	0.76	1.4	- 8
R20	0 - 20	10	0.10	1.6	9
	20 - 45	35	0.34	1.5	2
	50 - 70	60	0.59	1.4	- 5
	76 - 92	86	0.84	1.4	- 5
R21	0 - 20	10	0.10	1.7	16
	20 - 45	35	0.34	1.5	3
	50 - 70	60	0.59	1.4	- 4
	76 - 92	86	0.84	1.3	-11
R22	0 - 20	10	0.10	1.6	9
	25 - 45	35	0.35	1.5	0
	50 - 70	60	0.60	1.4	- 5
	76 - 92	86	0.86	1.4	- 5

* Segregation of carbon given by Eq. (D-2).

Table D-IV. Continued

Run#	Casting Location	L _{AV}	L _{AV} /L	c(x)	S
	mm	mm		w/o	%
R23	0 - 20	10	0.09	1.7	15
	25 - 45	35	0.32	1.5	1
	56 - 70	60	0.55	1.4	- 5
	76 - 92	86	0.78	1.4	- 5
R50	5 - 10	75	0.07	1.7	14
	30 - 40	35	0.31	1.5	1
	60 - 70	65	0.57	1.4	- 6
	85 - 95	90	0.79	1.4	- 6
R51	5 - 15	75	0.07	1.7	14
	30 - 40	35	0.31	1.5	1
	60 - 70	65	0.57	1.4	- 6
	85 - 95	90	0.79	1.4	- 6
R52	5 - 15	75	0.07	1.7	17
	30 - 40	35	0.34	1.4	- 3
	60 - 70	65	0.63	1.4	- 3
	85 - 95	90	0.87	1.4	- 3
R53	5 - 15	75	0.07	1.7	11
	30 - 40	35	0.32	1.5	- 2
	60 - 70	65	0.60	1.5	- 2
	85 - 95	90	0.83	1.5	- 2
R54	5 - 15	75	0.07	1.5	3
	30 - 40	35	0.34	1.5	3
	60 - 70	65	0.63	1.4	- 3
	85 - 95	90	0.79	1.4	- 3
R55	5 - 15	75	0.07	1.5	0
	30 - 40	35	0.31	1.5	0
	60 - 70	65	0.57	1.5	0
	84 - 95	90	0.79	1.5	0
R57	5 - 15	75	0.08	1.10	25
	30 - 40	35	0.35	0.97	2
	60 - 70	65	0.65	0.91	- 4
	85 - 95	90	0.90	0.83	-13
R59	5 - 15	75	0.08	1.20	25
	30 - 40	35	0.35	1.10	15
	60 - 70	65	0.65	0.79	-18
	85 - 95	90	0.90	0.73	-24
R60	5 - 15	75	0.07	1.00	14
	30 - 40	35	0.32	1.94	7
	60 - 70	65	0.60	0.83	- 6
	85 - 95	90	0.83	0.72	-18

Table D-IV. Continued

Run#	Casting Location	L _{AV}	L _{AV} /L	c(x)	S
	mm	mm		w/o	%
R61	5 - 15	75	0.07	1.00	18
	30 - 40	35	0.32	0.86	1
	60 - 70	65	0.60	0.80	- 6
	85 - 95	90	0.83	0.76	-11
R62	5 - 15	75	0.08	0.91	6
	30 - 40	35	0.35	0.86	0
	60 - 70	65	0.65	0.84	- 2
	85 - 95	90	0.90	0.85	- 1

where $c(x)$ is the composition at casting location x , \bar{c}_c is the average casting and L is the casting length. The value for the integral in Eq. (D-1) was obtained using the trapezoidal rule. Carbon segregation expressed as the percentage deviation from the average casting composition was calculated using Eq. (D-2).

$$S = \left(\frac{c(x) - \bar{c}_c}{\bar{c}_c} \right) 100 \quad (D-2)$$

Where S is the carbon segregation in percent. The average casting composition is given in Table D-V. The carbon segregation for the different runs are given in Table D-IV.

Table D-V. Average casting composition for macrosegregation runs.

Run #	\bar{c}_c
	w/o
R 1	1.54
R 2	1.61
R 3	1.61
R 4	1.67
R18	1.46
R19	1.52
R20	1.47
R21	1.46
R22	1.47
R23	1.48
R50	1.49
R51	1.49
R52	1.45
R53	1.53
R54	1.45
R55	1.50
R57	0.95
R59	0.96
R60	0.88
R62	0.85
R63	0.86

APPENDIX 5E

EXPERIMENTAL PROCEDURE AND RESULTS FOR SD CASTING
MANUFACTURE WITH GASES IN THE SHOT REGION

1. Experimental Procedure.

a) Components.

All castings were made using S224 ($d_p = 0.78\text{mm}$) shot and M31 melt charge. Spherical alumina particles ($d_p = 1.55\text{ mm}$) were used for the particle valve. The castings were made in a mullite tube modified to a closed one end tube as described in Appendix 5F.

b) Casting Procedure

The casting procedure was similar to that described in Appendix 5B, except that after vacuum deoxidation at 1100°C , the chamber was back filled with Helium gas in runs E2 and E3. The process variables for the different runs are given in Table E-1.

c) Density Measurement

Each casting was cut into nine pieces of equal length ($l=10\text{ mm}$). The density was measured using the standard weighing-in-air/weighing-in-fluid technique. Carbon tetrachloride was used as the immersion fluid.

Table E-I. Process variables for the gas pressure runs.

Run#		L mm	T _C °C	d _p mm	P _A kPa	P _S kPa
E1	0.4	90	1329	0.780	700	0
E2	0.4	90	1329	0.780	700	40
E3	0.4	90	1329	0.780	700	105

Table E-II. Specific gravity of casting at different casting locations.

Casting Location	L _{AV} mm	L _{AV/L}	Specific Gravity		
			E1	E2	E3
0 - 10	5	0.056	7.760	7.760	7.717
10 - 20	15	0.167	7.750	7.696	7.671
20 - 30	25	0.278	7.714	7.670	7.678
30 - 40	35	0.389	7.685	7.657	7.668
40 - 50	45	0.500	7.689	7.671	7.639
50 - 60	55	0.610	7.682	7.676	7.663
60 - 70	65	0.722	7.679	7.686	7.641
70 - 80	75	0.833	7.659	7.678	7.656
80 - 90	85	0.944	7.669	7.687	7.660

2. Results.

The specific gravity as a function of casting location is given in Table E-II and plotted in Fig. E.1. The specific gravity of the casting for different $P_s/(P_A - P_s)$ ratios is given in Table E-III and plotted in Fig. E.2.

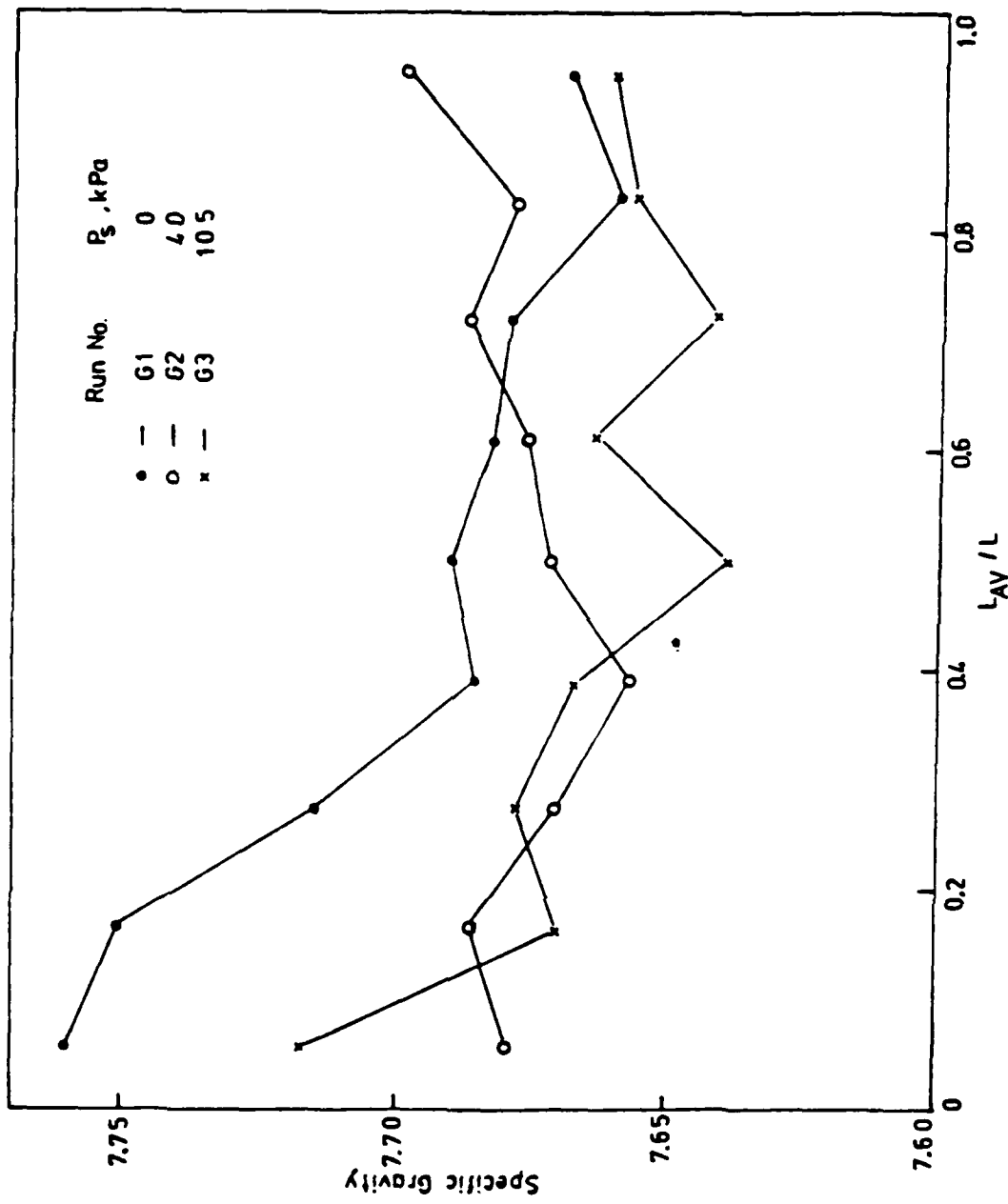


Figure E.1. Specific gravity as a function of casting location for different gas pressures in the shot region just prior to melt infiltration.

Table E-III. Effect of $P_A/(P_A - P_S)$ ratio on specific gravity of casting.

Run	$P_A/(P_A - P_S)$	Specific gravity
G1	0	7.70
G2	0.057	7.68
G3	0.150	7.66

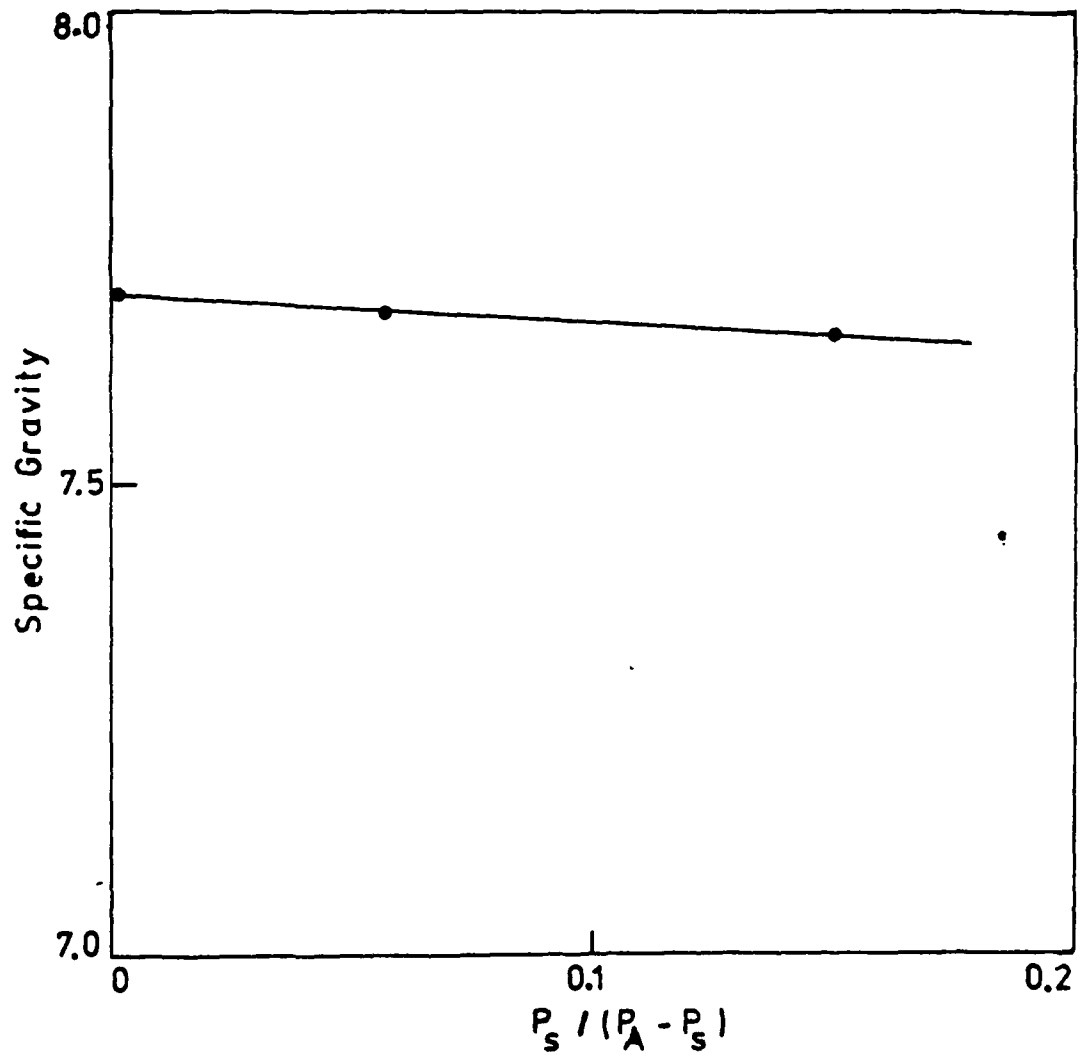


Figure E.2. Specific gravity of casting as a function of the ratio of gas pressure in shot region to the driving force for melt transfer.

APPENDIX 5F

EXPERIMENTAL SET UP USED FOR MAKING 6.35 MM
CASTINGS, MEASURING SHOT RESISTIVITY AND
MOVEMENT OF MELT IN THE PACKED BED.

The set up used was similar to the one described by Langford and Cunningham⁽¹⁾. However the furnace chamber, components and probe used were modified and so the set up will be described in detail.

1. Furnace Chamber

The purpose of the chamber was to isolate the furnace from the surroundings. The furnace chamber consisted of an mild steel vessel and an aluminium blind flange.

a) Mild Steel Vessel

A schematic of the vessel is shown in Fig. F.1. A blind mild steel plate, 12.7 mm thick and 406 mm in diameter was welded* to one end of a 16" (406 mm) S10 mild steel pipe, 974 mm in length. The other end of the pipe was welded to a mild steel flange, 19 mm thick, ID = 394 mm and OD = 508 mm. The bottom flange had 12, $\frac{1}{2}$ " (12.5 mm) standard threaded holes on a bolt circle of 457 mm. Copper tubing,

* The author is indebted to Mr.E.Tees and the Drexel univerisity physical plant personnel for their assistance in apparatus construction.

LEGEND

1. mild steel blind flange
2. mild steel pipe
3. window
4. main opening
5. cooling coils
6. flange
7. opening to connect chamber to probe

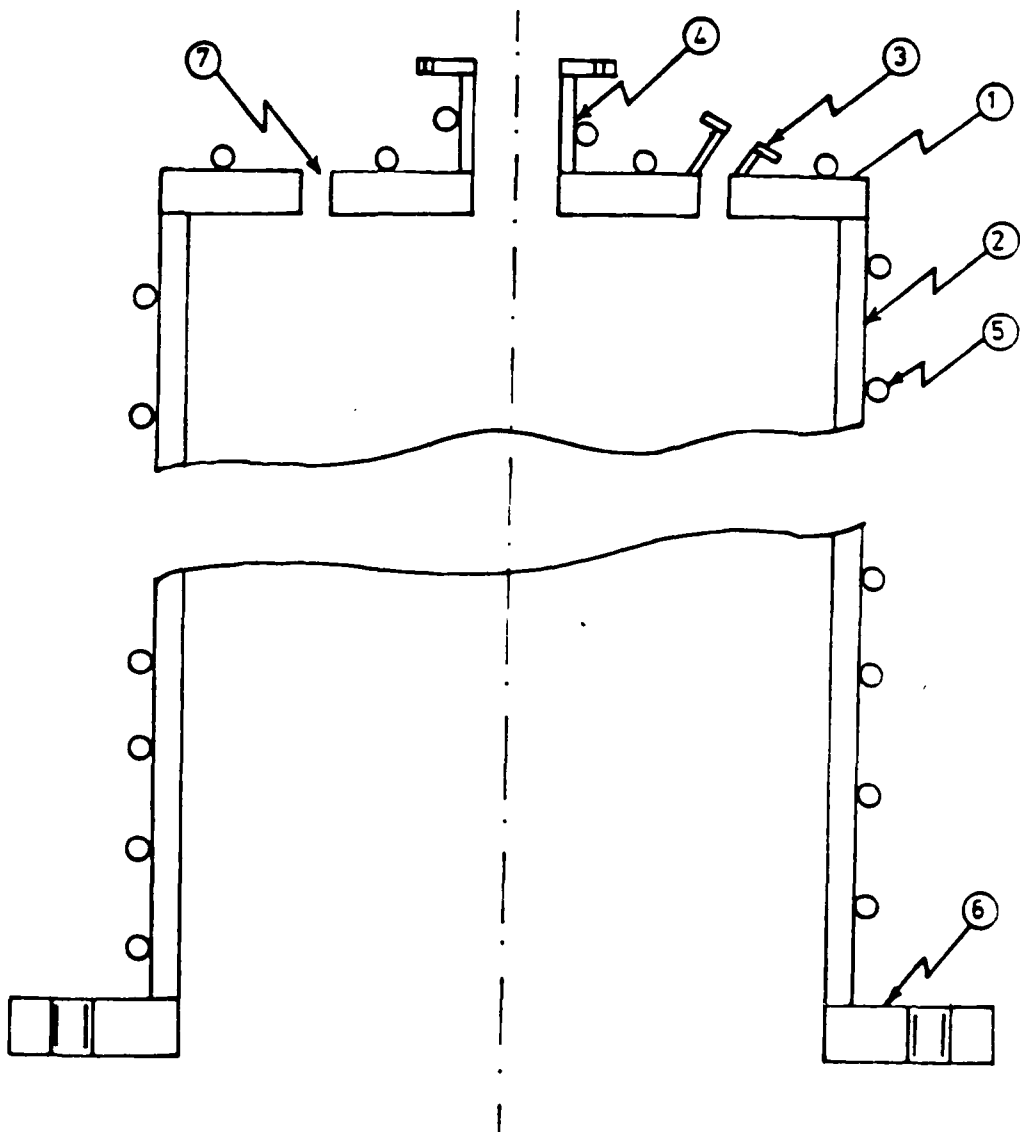


Figure F.1. Vacuum furnace chamber.

9.50 mm in diameter was soldered to the mild steel vessel for cooling purposes.

The blind flange at the top of the vessel had five openings. The main opening, 63.6 mm in diameter, was used to insert the probe. The flange on the main opening had an 'O' ring groove and four 3/8" (9.5 mm) standard threaded holes to clamp and seal the probe to the furnace vessel.

The other openings were used for:

- . Gas inlet to chamber
- . Gas connection from vessel to probe
- . Pressure guage
- . Furnace view window.

b) Bottom Flange.

The bottom flange was an aluminium (6061) plate having the following dimensions: 25.4 mm, 508 mm, 508 mm. Fig F.2 shows the top view of the bottom flange.

An 'O' ring, 462 was used to seal the blind flange to the main vessel. The vacuum inlet, induction leads, thermocouple leads and cooling water outlet were all introduced from the bottom flange. The flange was water cooled to prevent excessive heating during furnace operation. A stainless steel ring on which the furnace components were mounted, rested in a

LEGEND

1. water outlet
2. groove for centering furnace components
3. inlet for induction coils
4. 1/2" blind holes for clamping system
5. thermocouple inlets
6. vacuum port
7. water outlet
8. 'O' ring for sealing chamber to bottom flange
9. 1/2" hole for bolting flange to chamber
10. 1/2" holes for supporting vacuum furnace

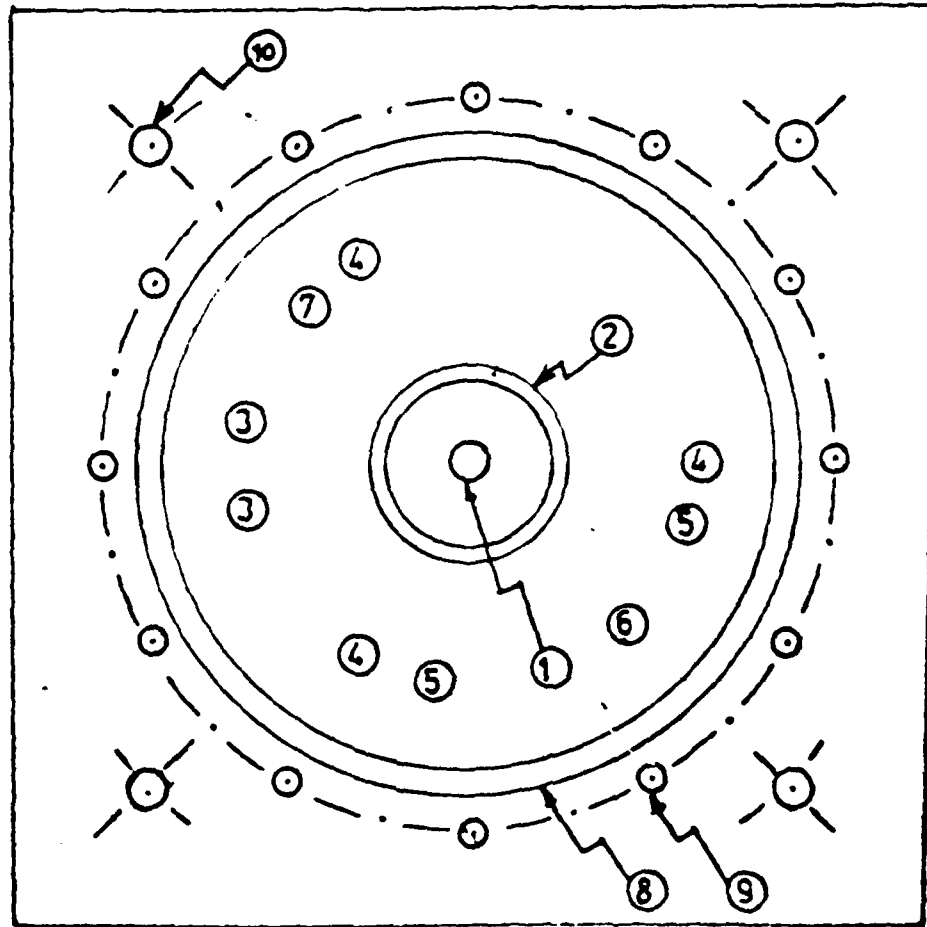


Figure F.2. Bottom flange layout for the vacuum furnace.

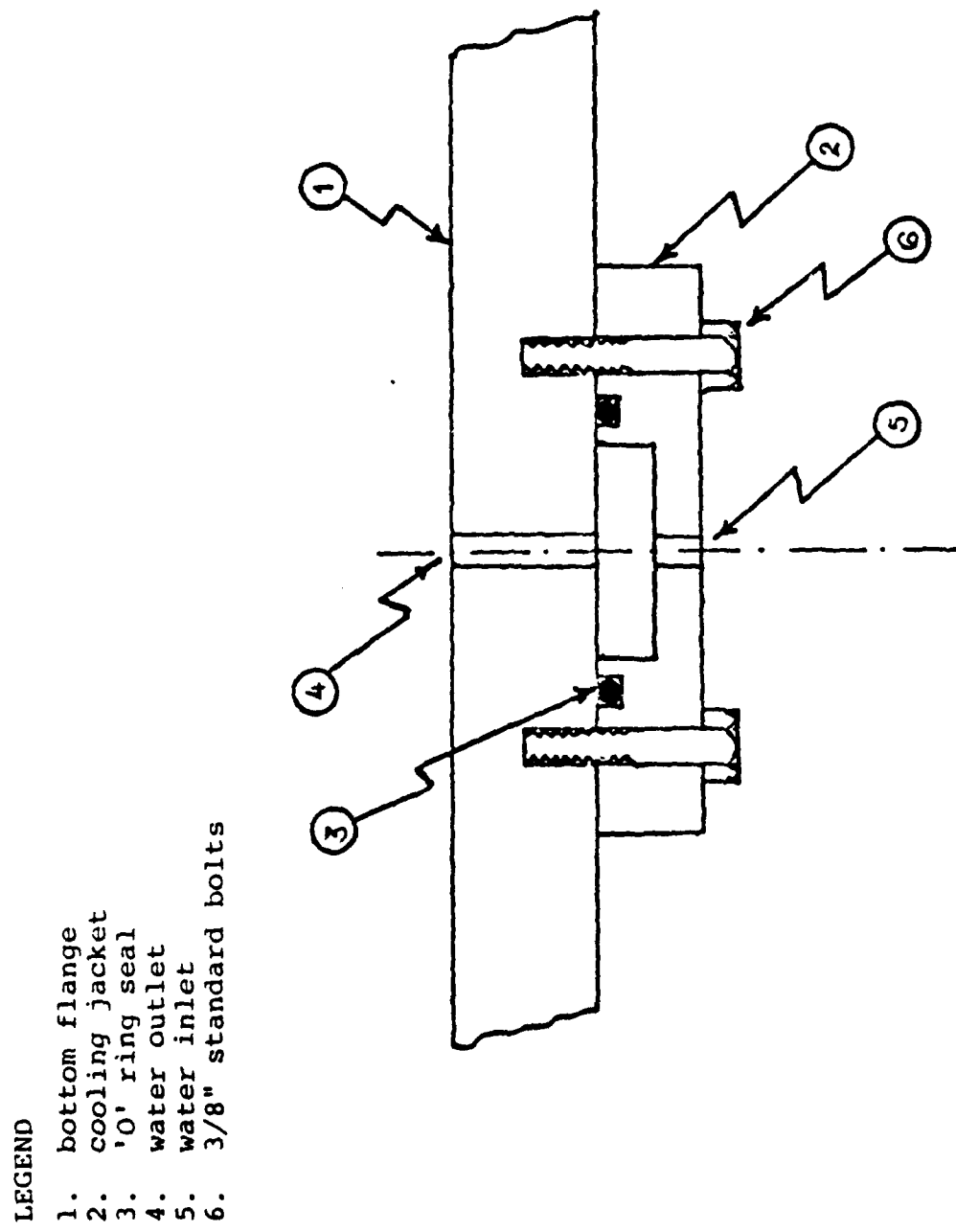


Figure F.3. Cooling jacket for bottom flange

groove in the center of the flange. Three 1/2" (12.5 mm) standard threaded blind holes, 120° apart on a bolt circle of 318 mm were used to clamp the furnace components to the bottom flange. The threaded rod used for the clamping system also served as mounts for thermocouple connectors.

2. Furnace Components.

A sketch of the furnace is shown in Fig F.4. The heating zone was 457 mm long and 75 mm in diameter. The opening at the top was 50 mm in diameter permitting molds with diameters upto 50 mm to be introduced into the furnace.

The graphite components were adequately insulated using graphite felt and fiberfrax. The induction coil 203 mm in diameter, 508 mm long with 14 turns was made from soft refrigeration copper tubing 9.5 mm in diameter. The coil turns were concentrated at the furnace top so as to attain an uniform temperature in the furnace.

The furnace components were clamped to the bottom flange using three 1/2" (12.5 mm) standard threaded stainless steel rods.

LEGEND

- | | |
|-----------------------------|--------------------------------|
| 1. furnace component clamp | 6. thermocouples |
| 2. pyrolytic graphite (top) | 7. fiberfrax |
| 3. top susceptor | 8. bottom susceptor |
| 4. cylindrical susceptor | 9. pyrolytic graphite (bottom) |
| 5. graphite susceptor | 10. stainless steel ring |

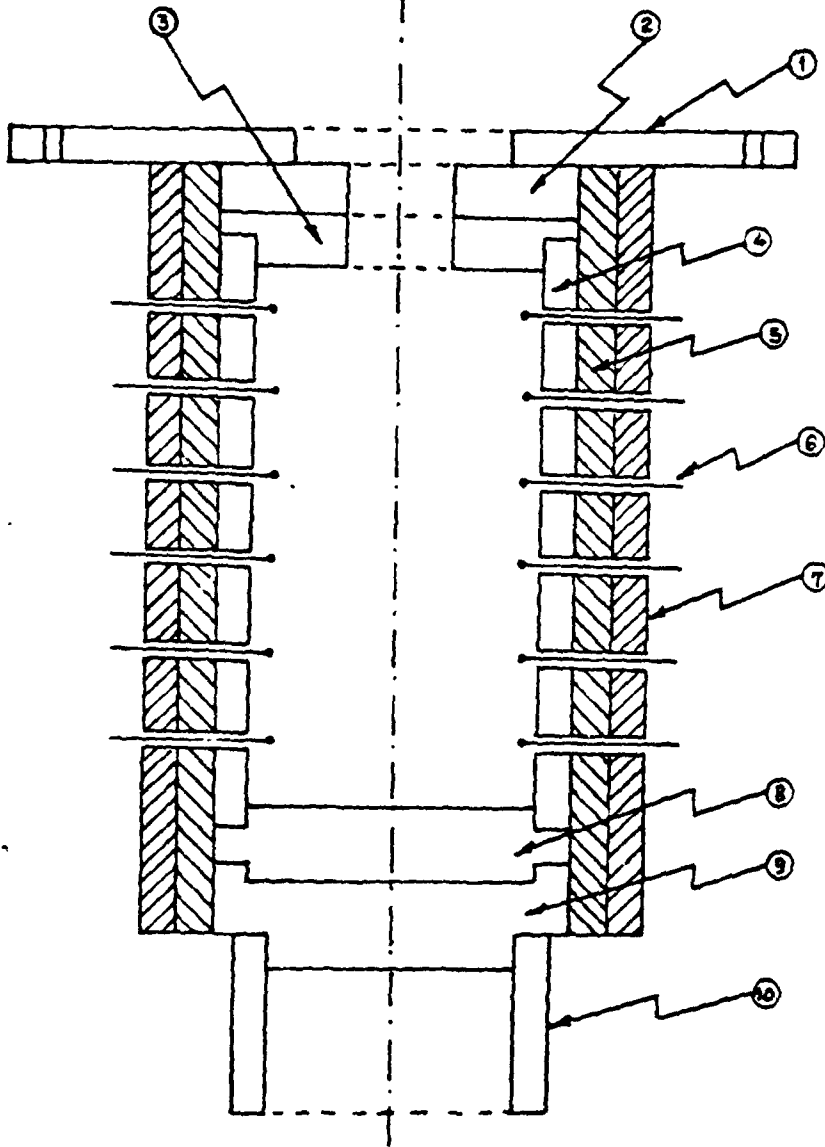


Figure F.4. Furnace components for vacuum furnace.

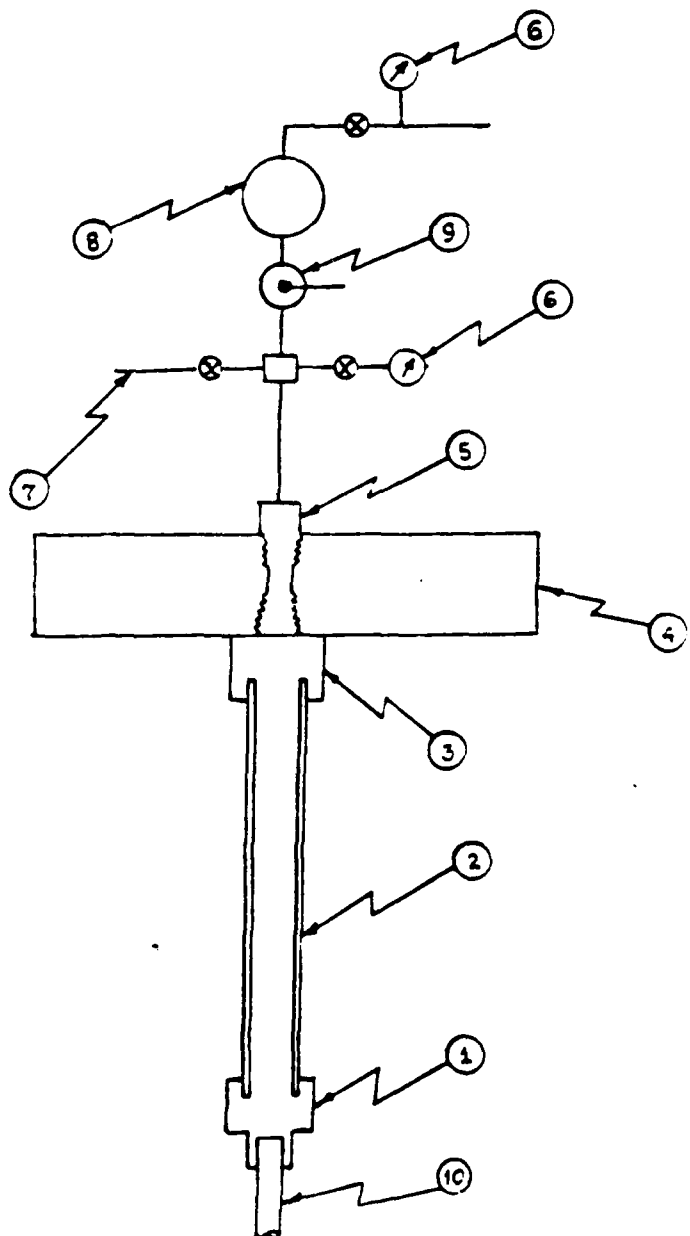
3. Energy Source and Temperature Control.

Power was supplied to the furnace from an Integral 30 TM 4.2 kcycles, 30 kW, induction unit. Temperature control was achieved manually by recording the temperature using a potentiometer and adjusting the power input to the furnace. The maximum possible power input to the furnace was 30 kW. A power input of 3kW was required to maintain the furnace temperature at 1200°C.

4. Probe

The main opening was closed using a blind flange during heat up and shut down operations. A probe was attached to the main opening for casting manufacture, resistivity measurements and measuring melt movement in the packed bed during infiltration.

Casting manufacture was done using Probe A, shown in Fig. F.5. Experiments for measuring resistivity and melt movement in packed bed were done using Probe B, shown in Fig. F.6. Probe B was a modified version of Probe A, having connectors for two thermocouples and four electrical contact points that could be connected to the shot charge for measuring the voltage in the shot region.

**LEGEND**

1. fitting (318" - 1/2")
2. S.S. tube (1/2" OD)
3. fitting (1/2" - 1/4" NPT)
4. aluminium flange
5. fitting (1/4" NPT - 1/4" NPT)
6. pressure guage
7. gas connection to main chamber
8. accumulator
9. ball valve
10. mullite specimen tube

Figure F.5. Probe A, used for SD casting manufacture.

LEGEND

- | | |
|-------------------------------|------------------------------------|
| 1. fitting | 12. valve |
| 2. S.S.tube | 13. pressure gage |
| 3. electrical connector | 14. gas connection to main chamber |
| 4. voltage/current leads | 15. ball valve |
| 5. fitting (1/2" - 1/4" NPT) | 16. accumulator |
| 6. thermocouple leads | 17. gas inlet line |
| 7. aluminium d lange | 18. pressure gage |
| 8. conax fitting | 19. dc source |
| 9. conax fitting | 20. standard resostor |
| 10. fitting (1/4" - 1/4" NPT) | voltage recorder |
| 11. mv recorder | 21. mullite specimen tube |

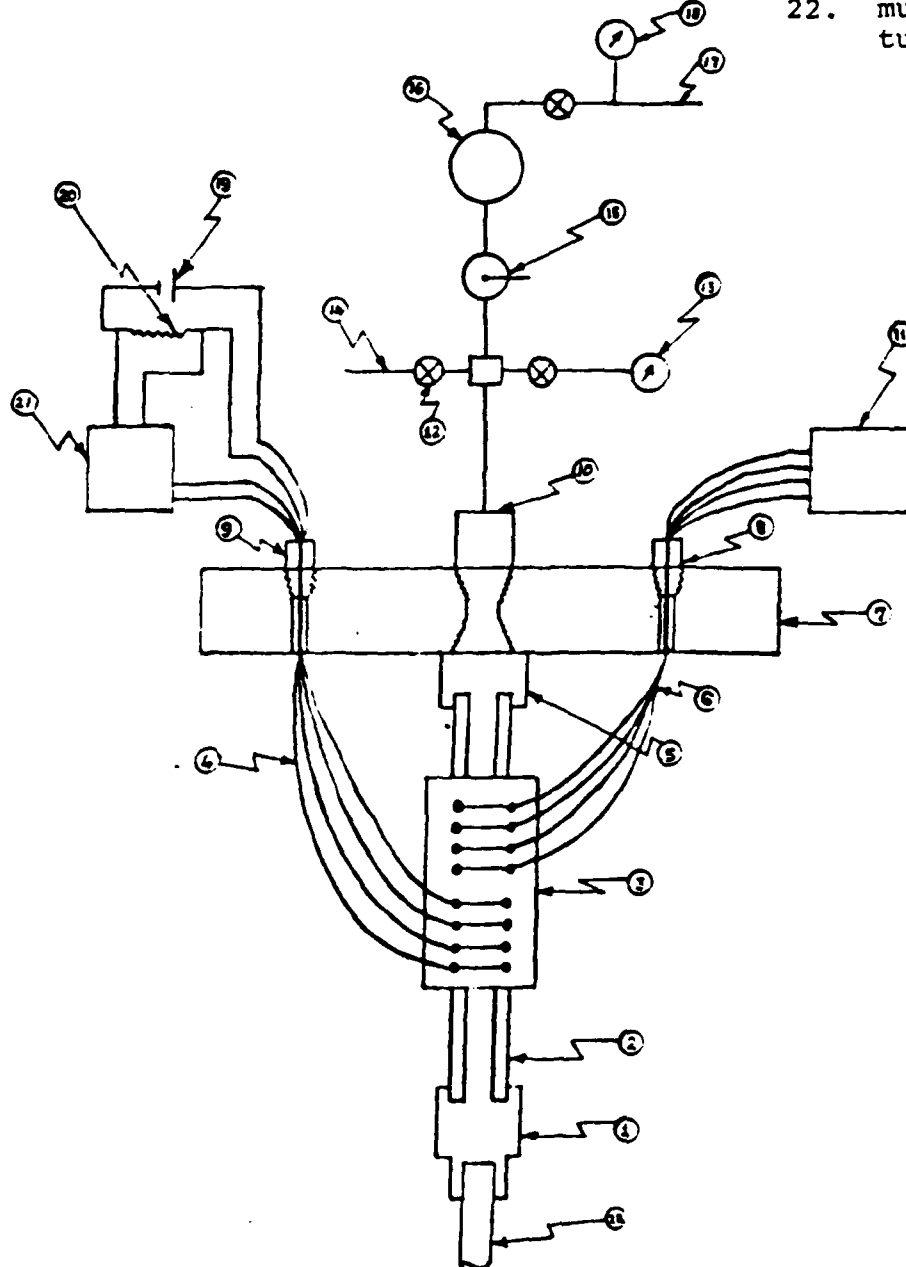


Figure F.6. Probe B used for resistivity and melt movement measurements

5. Molds for 6.35 mm Castings.

A mullite tube, open at both ends, 6.35 mm ID, 9.53 mm OD and 609 mm long, was modified to a closed one end tube as shown in Fig. F.7. Saurisen No.8 cement was used to close one end of the mullite tube. A 1/65 mm hole was drilled above the cement plug to flush out the air from the charge using argon prior to inserting the probe into the furnace. Two layers of alumina powder ($< 45 \mu\text{m}$) were sandwiched between steel wool using a steel rod with a diameter of 6 mm. The purpose of the alumina porous plug was to stop the melt charge from leaving the mold during infiltration.

For resistivity measurements of shot, one end of the mold was closed using a 50 mm layer of steel wool.

6. SD Component Assembly for Casting Manufacture.

After modifying the open both ends tube as described above, the SD components were added to the mold. The location of components is shown in Fig. F.8. An alumina rod, 1.65 mm in diameter was placed on top of the melt charge to prevent the melt from rising up the tube during evacuation and melting. The mold was then attached to the Probe A using a 9.53 mm swagelok fitting. Teflon ferrules were used as the sealing media

LEGEND

1. mullite tube (ID = 6.35 mm., OD = 9.5 mm.)
2. steel wool
3. alumina powder ($<45\mu\text{m}$)
4. 1.65 mm diameter hole
5. Sauerisen No.8 cement

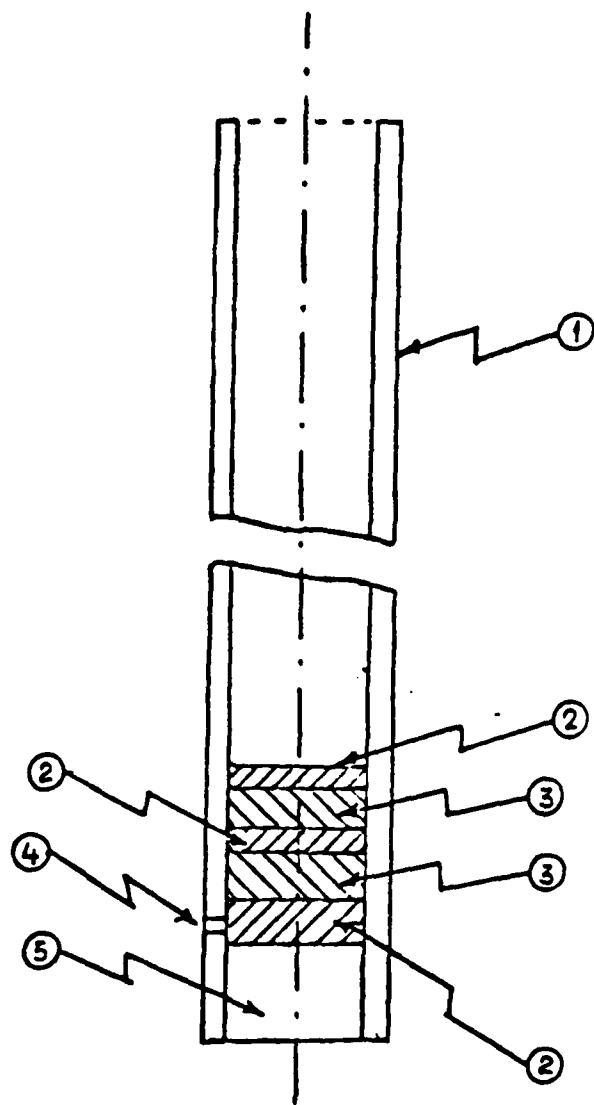


Figure F.7. Porous bottom plug for SD casting manufacture

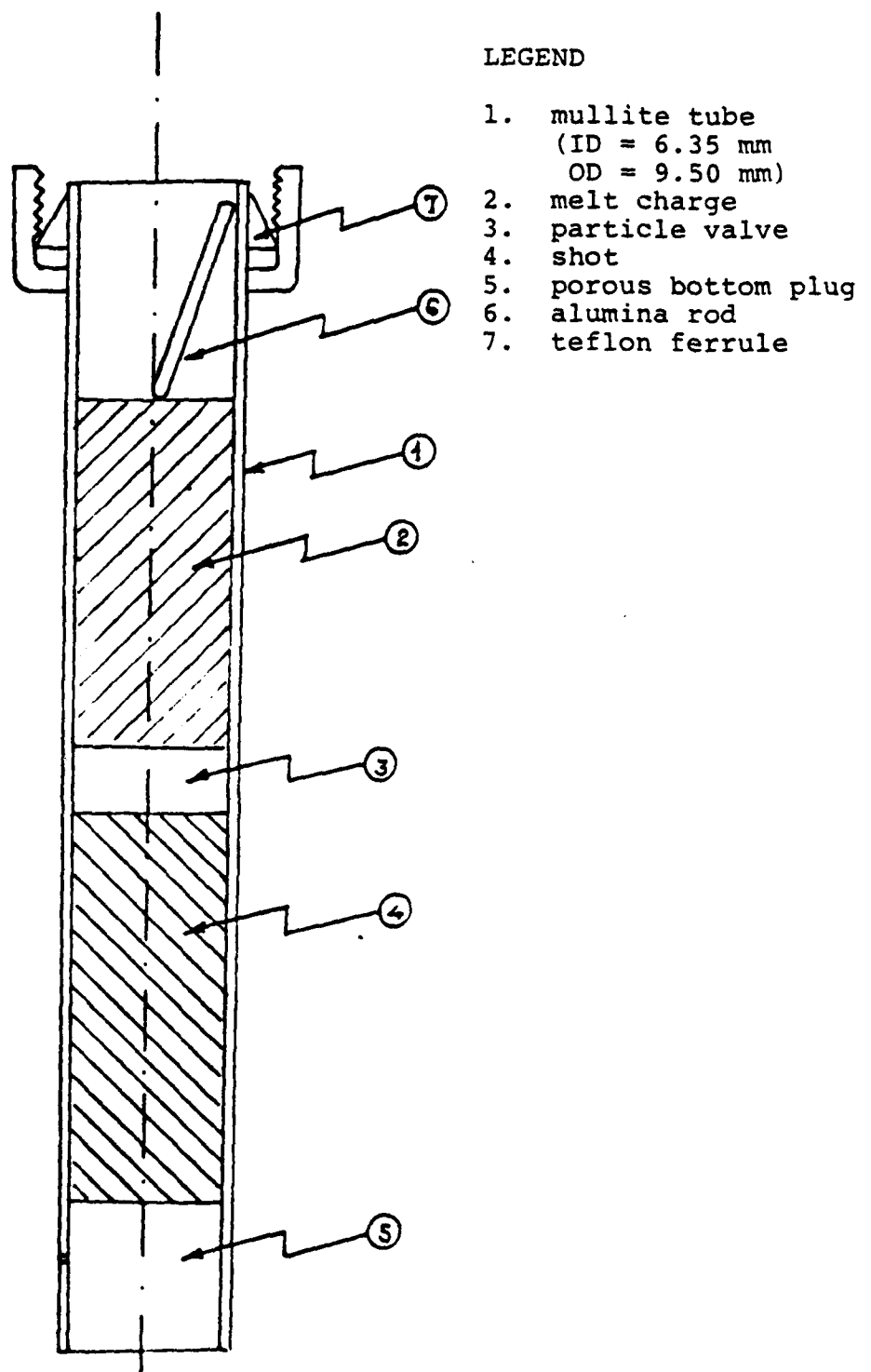


Figure F.8. Location of SD charge components in the mold for manufacturing 6.35 mm castings.

between the fitting and the mold as shown in Fig. F.8.

7. Set up for Measuring Resistivity of Bonded and Unbonded Spherical Steel Powder.

The set up for measuring the resistivity of shot is shown in Fig. F.9. Four iron wires, .508 mm in diameter were used as the leads for measuring the resistivity of the packed bed of shot. The wires were introduced to the packed bed through 1.65 mm holes drilled in the mold. A thermocouple placed in a 6.35 mm ID mullite tube containing shot was used to measure the temperature of the packed bed during the run. The current leads were connected to a DC source and a standard resistor. The voltage leads were connected to a voltage recorder. The voltage drop across the resistor was also measured using a voltage recorder. At any given moment the temperature of the PB was given by the thermocouple output, the current through the PB was proportional to the voltage drop across the standard resistor and the resistance of PB proportional to the voltage drop across the voltage leads.

8. Set up for Measuring the Melt Movement in the Packed Bed.

The set up used for evaluating the melt transfer

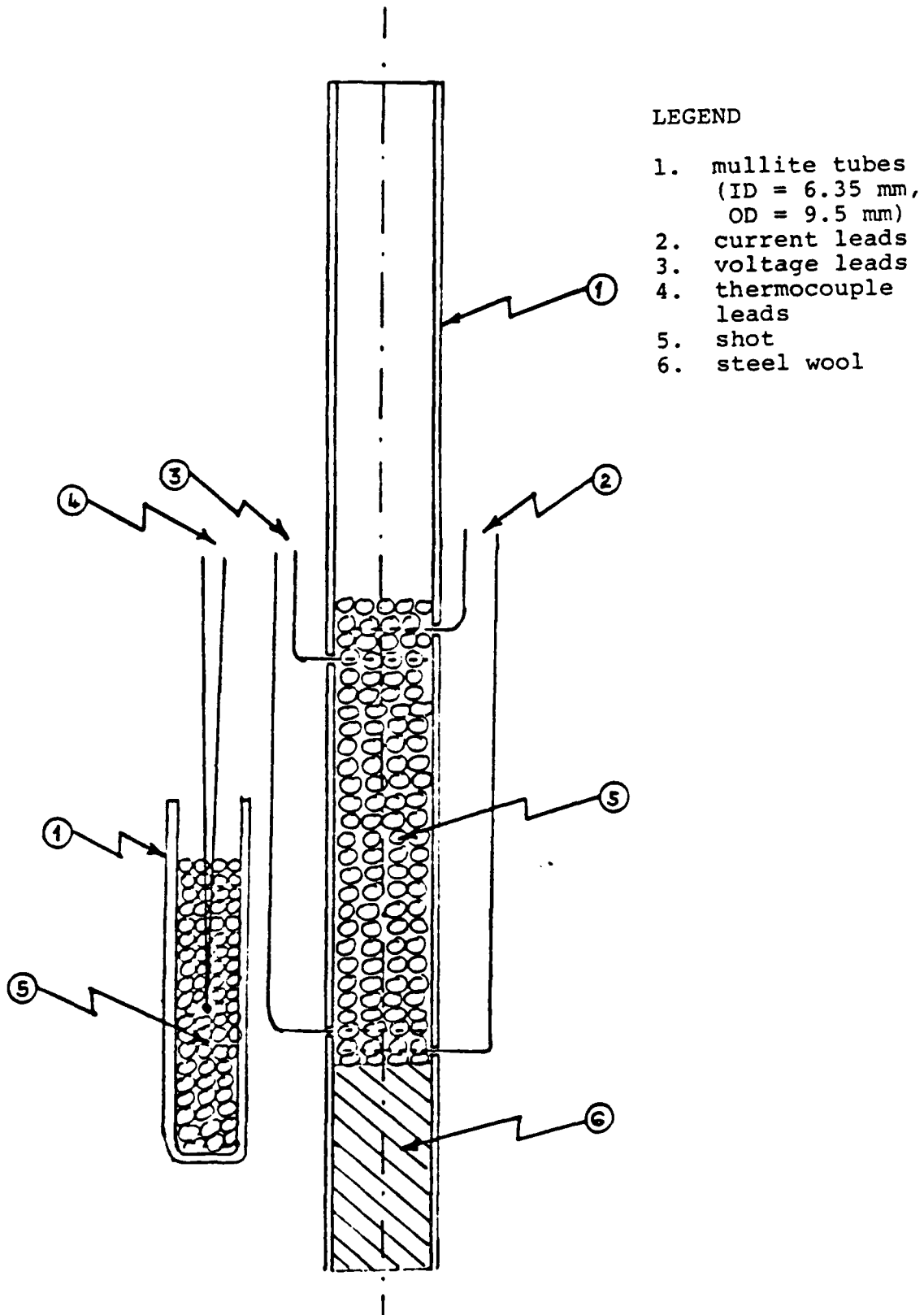


Figure F.9. Setup for measuring resistivity of unbonded shot

kinetics is shown in Fig. F.10. The four point leads consisted of AISI 1008 wire, 1.575 mm in diameter. The leads were introduced into the packed bed of shot via 1.65 mm drilled holes in the mullite mold. The holes were adequately sealed using a mixture of alumina powder ($< 45 \mu\text{m}$) and Sauerisen No. 8 cement contained in a 19 mm ID mullite tube.

After adding the SD components to the mold, the mold was connected to Probe B. The voltage current leads were connected in a similar manner to that described for measuring resistivity of shot.

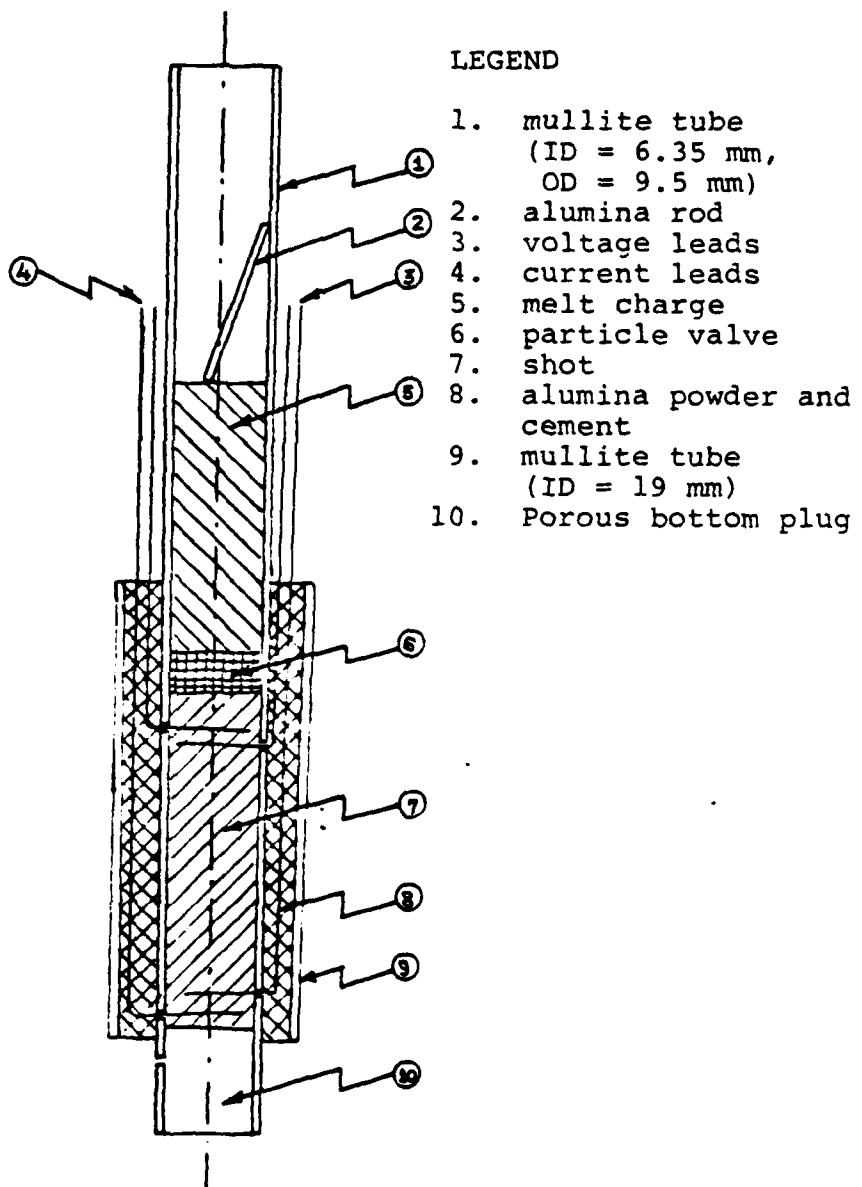


Figure F.10. Setup used for measuring melt movement into the shot.

APPENDIX 5G

CHARACTERIZATION OF SD COMPONENTS USED FOR THE EXPERIMENTS.

1. SHOT CHARACTERIZATION

a) Code.

The powders used in the experiments are characterized by a letter and a number code. The letter refers to the particle shape; S stands for spherical and I stands for non-spherical or irregular particles.

The number is used to give the manufacturing process, chemical operation on the powder after manufacture, and the batch number, if a number of batches were made using the same chemical operation.

The first digit in the number indicates the powder manufacturing process and the correlation between the digit value and the manufacturing process is given in Table G-I. The second digit refers to chemical operation the powder was subject to after manufacture. The relation between the digit value and chemical operation is given in Table G-II. A zero value at the second and third digit is for the case when the powder is not subject to chemical operation. The third digit is used to differentiate batches of powder subject to the same chemical operation. For example, Powder S211 refers to batch 1 of spherical water atomized powder

Table G-I. Correlation between first digit and manufacturing process.

DIGIT VALUE	MANUFACTURING PROCESS
1	Rotating Electrode
2	Steam Atomized
3	Water Atomized

Table G-II. Correlation between second digit and chemical operation.

DIGIT VALUE	CHEMICAL OPERATION
0	No operation
1	Deoxidation
2	Decarburization

deoxidized in an inert atmosphere at 1000°C.

b) Powder Composition.

Tables G-III, G-IV and G-V give the chemical analysis of the different powders used in the experiments.

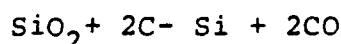
c) Surface Morphology

The surface morphologies of powders S100, S200 and S211 are shown in Figs. G.1, G.2 and G.3.

d) Chemical Operations

i. Deoxidation.

Heat treatment of steel powders in an inert atmosphere at temperatures of about 700°C to 1200°C reduced surface oxides and removed dissolved oxygen from the particles according to the reactions:



ii. Decarburization.

Very low carbon steel particles can be obtained by decarburizing powder with high carbon contents. CO/CO₂ or H₂/H₂O gas mixtures were used as the decarburization media.

Table G-III. Chemical composition of powders as received
in weight percent.

Element	Powder		
	S100	S200	I300
C	.18	1.90 - 0.95	-
Si	,035	0.40 - 0.97	-
Mn	.76	0.40 - 1.00	1.0
O	.022	0.44 - 0.20	-
N	.015	0,14 - 0.13	-
S	.022	0.02 - 0.03	-
Fe	98.973	96.61 - 96.83	98.5
Ni	-		0.5

Table G-IV. Chemical composition of Deoxidized powders
in weight percent.

Element	Powder			
	S211	S212	S213	S214
C	0.84	0.81	0.85	.90
Si	0.42	0.96	0.50	.96
Mn	0.41	1.04	0.65	1.00
O	0.36	0.04	0.16	.076

Table G-V. Chemical composition of decarburized particles in weight percent

Element	Powder			
	S221	S222	S223	S224
C	.26	.005	.033	.038
Si	.42	.42	.42	.42
Mn	.41	.41	.41	.41
O	.40	.40	.44	.36
				.076

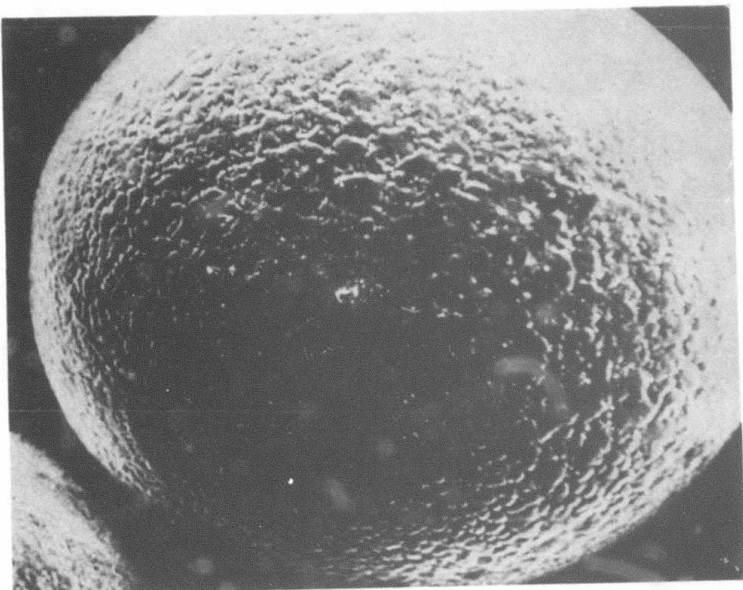


Figure G.1. Scanning electron micrograph of S200 powder (300X).

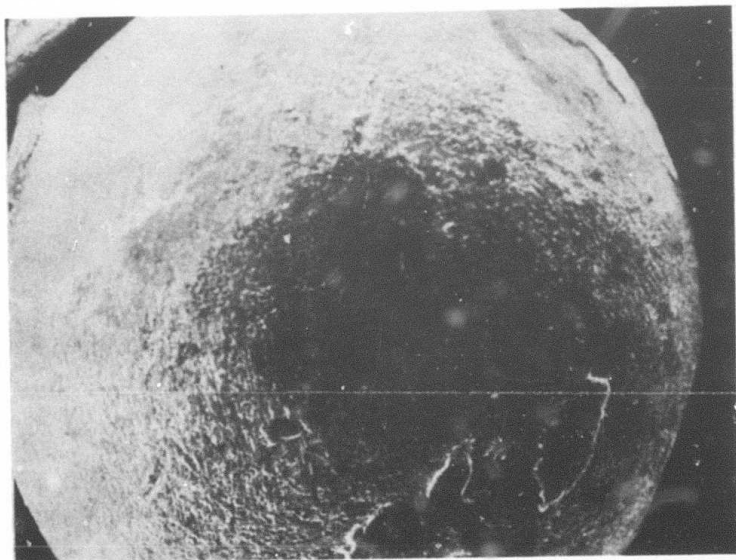


Figure G.2. Scanning electron micrograph of S212 powder (300X).

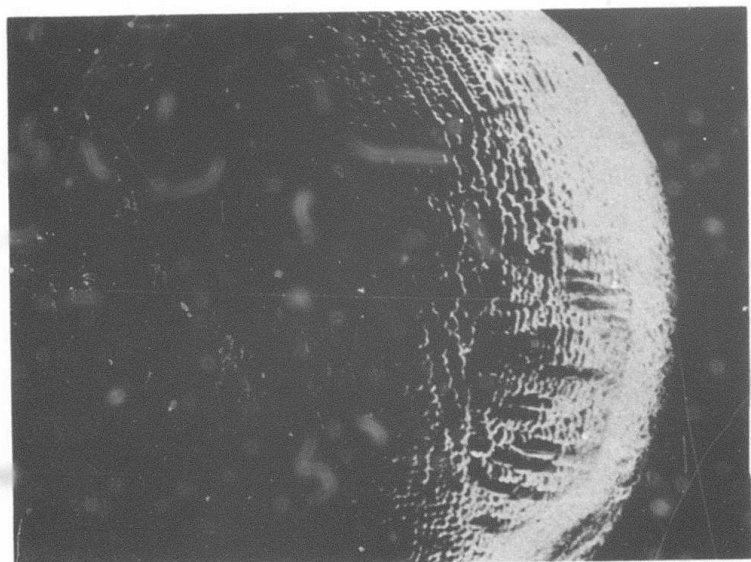


Figure G.3. Scanning electron micrograph of S100 powder (300X).

e) Particle Size Distribution

The size ranges for different powders used in the experiments are given in Table G-VI.

2. CHARACTERIZATION OF MELT CHARGE.

The melt is characterized by a letter and a two digit number code. The letter M refers to the melt. The first digit denotes the type of melt charge and the second digit refers to chemical operations the charge received after manufacture.

Three different melt charges were used in the experiments; M10, M20 and M31. M10 and M20* were argon atomized using a 1018 and graphite charge and had compositions of 4 weight percent and 2.3 weight percent respectively. M31 was Iron Shot** deoxidized at 1000°C. in a nitrogen atmosphere. The chemical compositions of the melt charge are given in Table G-VII.

3. CHARACTERIZATION OF PARTICLE VALVE.

Alumina particles were used for the particle valve. The particle valve was designated as PV. PVS refers to spherical alumina particles and PVI refers to irregular alumina particles.

* The author is indebted to Dr. C. Lall for manufacturing M10 and M20.

** Trade Mark of Metal Blast Inc., Cleveland, Ohio.

Table G-VI. Particle size distribution for the shot

<u>Shot</u>	<u>Particle size range , μm</u>
S100	30 - 335
I100	335 - 2000
S200	250 - 4750
S211	600 - 850
S212	1400 - 2000
S213	850 - 1400
S214	1400 - 2000
S221	600 - 850
S222	600 - 850
S223	600 - 850
S224	600 - 850
S225	335 - 600
S226	1400 - 1200
S300	150

Table G-VII. Chemical composition of the melt charge
in weight percent

Element	Melt Charge		
	M10	M20	M31
C	4.0	2.32	2.70
Si	.035	.03	0.65 - 1.30
Mn	.76	.76	0.4 - .75
S	.022	.02	.65 - 1.00
P	-	-	.12 - 0.23
O	.022	.02	0.15
Cu	-	-	0.88

APPENDIX 5H

NOMENCLATURE USED IN CHAPTER 5

c_s - composition of shot
 c_{s^*} - composition of solidus
 d - average diameter of particles
 d_p - average diameter of shot
 D - diffusivity of solute in the single phase
solid region
 $f(PV)$ - time correction function for particle valve
 $f(I)$ - time correction function for SD interaction
 f_{LS} - volumetric fraction melt solidified
 f_S - volumetric solid fraction
 H - percentage homogenization
 K_L - constant which is a function of c_s , c_{s^*} and c_{L^*}
 K - constant which is a function of c_s , c_{s^*} and c_{L^*}
 l_0 - distance between maximum and minimum solute
concentration in the casting
 L - casting length
 P_A - infiltration pressure
 P_Y - pressure required to overcome surface tension forces
 P_S - gas pressure in the shot region just prior to
melt transfer
 Re - packed bed Reynolds number

SG - specific gravity
 t_I - infiltration time
 t_s - SD time
 t_D - maximum filling time
 t_h - homogenization time
 t_{ST} - total SD time
x - melt penetration distance
 ρ_L - melt denisty
 μ_L - melt viscosity
 γ_L - surface tension of melt
 γ_i - index of residual microsegregation
 δ - liquid-solid interface displacement
 δ^* - normalized liquid-solid interface displacement
 δ_m - maximum displacement of liquid-solid interface
 β - constant used to determine the time correction function for PV
 τ - normalized diffusion time
 α - macrosegregation parameter
 α_N - new macrosegregation parameter
 ϵ - void fraction of shot packing

Subscripts and Superscripts

L - melt
S - solid
PV - particle valve
LC - Langford and Cunningham
E - Ergun
BP - Burke-Plummer
BK - Blake-Kozeny
T - turbulent
L - laminar

6. MICROSEGREGATION OF TERNARY ALLOYING ELEMENTS IN
STEELS CAST BY DIFFUSION SOLIDIFICATION

M. Paliwal

D. Apelian

G. Langford

SUMMARY

The SD process for casting steels is based on diffusion of carbon from a high carbon melt into low carbon austenite. The effect of adding a ternary alloying element to the melt on different process variables is addressed. The segregation of an alloying element in the solidifying melt can be divided into three specific zones:

- i) Initial segregation controlled by the alloying element composition of the original solid.
- ii) A transition zone.
- iii) Normal segregation behavior as governed by the equilibrium phase diagram.

For the alloying elements Ni, Co, Mn and Mo, the first solidifying melt has an alloying element composition which is identical to the composition of the original solid. The initial segregation fits the empirical relationship:

$$C_i^Y = \psi x^2 + C_i^{Y(o)}$$

where, x is the distance from the solid/infiltrant interface, $C_i^{Y(o)}$ is the alloying element composition of the original solid, C_i^Y is the solid alloying element composition at the solid/liquid interface and ψ is an adjustable constant. The alloying elements, for which initial segregation is controlled by the alloying element composition of the original solid, can be made to segregate either positively or negatively by appropriately choosing the alloy composition of the original solid and the melt.

TABLE OF CONTENTS: Section 6. Microsegregation of Ternary Alloying Elements in Steels Cast by Diffusion Solidification

	<u>Page</u>
6.1 Introduction	377
6.2 Theoretical Considerations	380
• Phase Diagram for Ternary Systems	380
• Rate of Interface Motion	382
• Segregation of Ternary Alloying Elements	384
Case A: $C_i^Y(o) = k_i C_i^L(o)$	389
Case B: $C_i^Y(o) < k_i C_i^L(o)$	390
Case C: $C_i^Y(o) > k_i C_i^L(o)$	393
6.3 Experimental Procedure	400
6.4 Results and Discussion	406
6.5 Conclusions	421
References	423
Appendices	424
Appendix 6A: Fraction of Liquid as a Function of Distance, x , for Normal Segregation	425
Appendix 6B: Composition vs. Distance Data	427

6. MICROSEGREGATION OF TERNARY ALLOYING ELEMENTS IN STEELS CAST BY DIFFUSION SOLIDIFICATION.

6.1 INTRODUCTION

The SD casting process for steels is based on the diffusion of carbon from high carbon liquid iron to preheated, low carbon solid austenite (1). A unique advantage of the process is that ternary additions can be made in the shot or the melt individually (1,2,3). Addition of alloying elements to the melt generally will change the solidus and the liquidus compositions.

The diffusivity of common substitutional alloying elements in austenite is four to six orders of magnitude less than that of carbon in austenite. Also the diffusivity of the alloying elements is greater in liquid iron than in austenite; which leads to substantial segregation of the alloying elements, as shown by Langford and Cunningham (1) for an SD weld.

The shrinkage pores in the SD process are more likely to form in the last liquid to freeze (the location of porosity in SD castings is discussed in Chapter 7). Segregation of alloying elements around the pore, i.e., in the last liquid to freeze, can preferentially strengthen or weaken the volume around a pore with respect to the rest of the matrix. Whether the segregation of the alloying element has a positive or a negative effect on the resulting mechanical properties of the casting will depend on the composition of the material around the pore and also on the heat-treatment the casting is subjected to following

solidification. A sufficiently strong area around a pore will retard void growth and thus improve the resulting mechanical properties of the casting. On the other hand, an alloy composition which renders the volume around the pore air hardenable would cause it to be brittle and therefore highly crack-susceptible. Unless the casting is subsequently heat-treated the ductility of the casting as a whole may be adversely affected.

The process variables that will be affected by addition of alloying elements to the melt are:

- a) Metallostatic head supportable by the PV: As discussed already in Chapter 3 the surface tension of a liquid Fe-C melt is composition dependent; addition of alloying elements, will therefore change the metallostatic head that can be supported by the PV.
- b) Carbon composition of the melt: The process requires that the melt composition and temperature correspond to the liquidus. A melt composition above the liquidus is thus superheated and may result in partial remelting of the shot before SD can start (1). Thus, in order to retain the same process temperature, the carbon composition of the melt will have to be changed. Of course for a practical process one could alternatively change the temperature instead to be on the liquidus, and hence retain the desired carbon content of the casting.

- c) Solidification time: The thickness of the solidified layer, and hence the solidification time are dependent on the process temperature via the diffusivity of carbon in austenite and the carbon composition of the liquidus and the solidus. Many ternary alloying elements are known to drastically retard the diffusion of carbon in austenite.
- d) Homogenization time: The homogenization time for an SD casting (1) has been defined as the time required to obtain a flat carbon concentration. If homogenization of alloying elements subsequent to solidification is to be achieved, the homogenization time will be much greater than that calculated for carbon homogenization, due to lower diffusivity of alloying elements in austenite. The extent of segregation of alloying elements is thus required to define homogenization times for alloying elements.

The objective of this part of the study is to understand the partitioning behavior of the common substitutional alloying elements between the solid and liquid under isothermal conditions for the SD process for steels; where diffusion of carbon in austenite controls the solidification rate.

Such a study is fundamentally important since segregation in multicomponent systems is not well understood. Davis (4) justifies the use of binary data for partition coefficients from a theoretical viewpoint up to additions of 2 wt% for solutes which exhibit low

interaction effects and has verified it for a number of systems. For alloy systems in which solute atoms have large interaction coefficients the binary partition coefficients cannot be used; the segregation ratio of Cr is approximately unity in a Fe-1.5 Cr alloy, whereas in a Fe-1.5% Cr-1% C alloy the segregation ratio varies between 3.8 and 4.3 (5).

Extensive work has been done on segregation of alloying elements for thermal freezing of cast irons and it has been observed that the elements which decrease the activity of carbon in the melt (Cr, Mn, Mo, Ti, V, etc.), increase the carbon liquidus composition, and have partition coefficients (k_i) less than unity (6,7). In contrast, alloying elements which increase the activity of carbon in the melt (Co, Cu, Ni, Al, Si, etc.), reduce the solubility of C, and segregate inversely, that is have partition coefficients greater than unity (6,7).

6.2 THEORETICAL CONSIDERATIONS

i) Phase Diagram for Ternary Systems

Most of the experimental data on Fe-C based ternary systems is reported along an isopleth, i.e., Fe-C compositions are plotted for a constant third element composition. An isothermal section from this data can be plotted using the solidus and liquidus compositions at a fixed temperature from different isopleths. To completely define the isotherm one needs to know the connecting tie-lines which unfortunately are not available for most Fe-C based ternary systems.

For dilute addition of an alloying element, (i), the equilibrium partition coefficients and hence the solidus can be approximated from the experimentally determined liquidus compositions. The governing relationships as given by Kirkaldy et al. (8) for carbon (c) and alloying element (i), solidus compositions are:

$$x_c^Y = \frac{x_c^L \exp \left[\frac{\Delta^\circ G_{c}^{Y-L}}{RT} + \epsilon_{cc}^L x_c^L \right]}{1 + \epsilon_{cc}^Y x_c^L \exp \left[\frac{\Delta^\circ G_{c}^{Y-L}}{RT} \right]} \quad (1)$$

$$x_i^Y = \frac{x_i^L \exp \left[\frac{\Delta^\circ G_{i}^{Y-L}}{RT} + \epsilon_{ci}^L x_c^L \right]}{1 + \epsilon_{ci}^Y x_c^L \exp \left[\frac{\Delta^\circ G_{c}^{Y-L}}{RT} \right]} \quad (2)$$

The partition coefficients for carbon (c) and alloying element (i) respectively are therefore:

$$k_c = \frac{x_c^Y}{x_c^L} \quad (3)$$

$$k_i = \frac{x_i^Y}{x_i^L} \quad (4)$$

where:

x_c^Y, x_c^L = mole fraction of carbon in austenite and liquid respectively, when the solid austenite and liquid are in equilibrium with each other.

x_i^Y, x_i^L = mole fraction of alloying element, i, in austenite and liquid respectively, when the solid austenite and liquid are in equilibrium with each other.

$\Delta^{\circ}G_c^{Y-L}$, $\Delta^{\circ}G_i^{Y-L}$ = free energy change for standard state at infinite dilution; $\Delta^{\circ}G_c^{Y-L} = \Delta^{\circ}G_c^L - \Delta^{\circ}G_c^Y$.

ϵ_{ci}^Y , ϵ_{ci}^L , ϵ_{cc}^Y , ϵ_{cc}^L = Wagner interaction coefficients.

k_c , k_i = Partition coefficient for carbon and alloying element, i, respectively.

ii) Rate of Interface Motion:

For the binary Fe-C SD solidification, the movement of the interface with time will be given by the general solution of the binary isothermal diffusion controlled growth equation. The thickness of solidified layer, ϵ , as a function of time, for an austenite region that can be considered infinite is (9):

$$\epsilon = 2K\sqrt{D_c^Y \cdot t} \quad (5)$$

where K is determined by trial and error from,

$$\frac{C_c^Y - C_c^{Y(0)}}{C_c^L - C_c^Y} = K\sqrt{\pi} e^{-K^2} (1 + \operatorname{erf} K) \quad (6)$$

where:

ϵ = thickness of solidified layer.

K = an adjustable constant

D_c^Y = diffusivity of carbon in austenite

t = time

C_c^Y = carbon composition of solid at the solid/liquid interface;
wt percent

C_c^L = carbon composition of liquid at the solid/liquid interface; wt percent

$C_c^{Y(o)}$ = carbon composition of the original solid; wt percent

For the solidification of the ternary Fe-C-i melt, Eqs. 5 and 6, can still be used where only the carbon compositions and diffusivity in austenite is being considered (carbon diffusion will control the rate of solidification since the diffusivity of carbon is much greater than the diffusivity of the ternary alloying elements). However, due to the presence of the ternary alloying element the carbon composition of the solid and liquid at the solid/liquid interface will be affected. Also the diffusivity of carbon in austenite will change due to the presence of the ternary alloying element in the solidifying melt.

A closed form analytical solution of Eqs. 5 and 6 is only possible when diffusivity of the elements and the interface compositions are assumed to remain constant during growth. When interface compositions change with growth numerical techniques have to be employed assuming local equilibrium at the interface, as done by Goldstein and Randich (10) for isothermal ternary diffusion controlled growth.

In a ternary or higher order system when the diffusivity of one of the elements is much greater than the other elements, the concept of local equilibrium at the interface breaks down. The phenomenon has been well documented for decomposition of austenite into ferrite and carbides for Fe-C-i alloys, where i is a substitutional alloying element (the diffusivity of carbon in austenite is 10^4 to 10^6 times

greater than that of the major substitutional elements). The assumption of local equilibrium at the moving interface is usually made to facilitate the analysis of the moving boundary problem of diffusion controlled growth, however it is not an essential condition (11).

In the SD process the depleting phase is the Fe-C-i ternary melt. Complete mixing in the liquid for carbon and the alloying element, i, is a reasonable assumption and as such, non-equilibrium compositions at the solid/liquid interface are neither expected nor can be explained on the basis of differences in diffusivities. The underlying reasons for non-equilibrium compositions at the solid/liquid interface and the segregation behavior of the alloying elements, in the SD casting process, are explained in the following section.

iii) Segregation of Ternary Alloying Elements:

Figure 1 shows the physical situation for the SD process when the Fe-C melt has a ternary alloying addition made to it. The corresponding phase diagram showing an isothermal cut of the ternary iron rich corner is given in Figure 2. A melt at its liquidus composition ($C_c^{L(o)}$, $C_i^{L(o)}$)* is suddenly brought into contact with the

-
- * $C_c^{L(o)}$, $C_i^{L(o)}$: Carbon (c) and alloying element (i) composition of the liquid melt, at start of process.
 - $C_c^Y(o)$, $C_i^Y(o)$: Carbon (c) and alloying element (i) composition of the original austenite.
 - C_i^Y , C_i^L : Alloying element composition of the austenite and liquid at the solid/liquid interface.
 - C_c^Y , C_c^L : Carbon composition of the austenite and liquid at the solid/liquid interface.
 - k_c , k_i : Partition coefficient for carbon and alloying element, i, respectively.

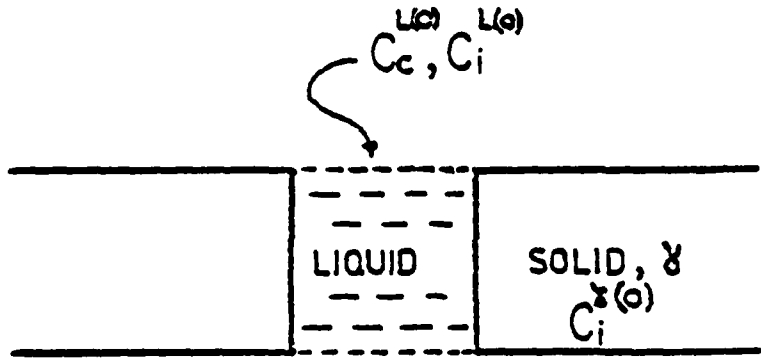


Figure 1. Physical situation representative of the SD process.
A melt of composition $C_c^{L(o)}$, $C_i^{L(o)}$ is suddenly brought
into contact with austenite of composition $C_i^{(o)}$
(assumed zero percent carbon in original solid).

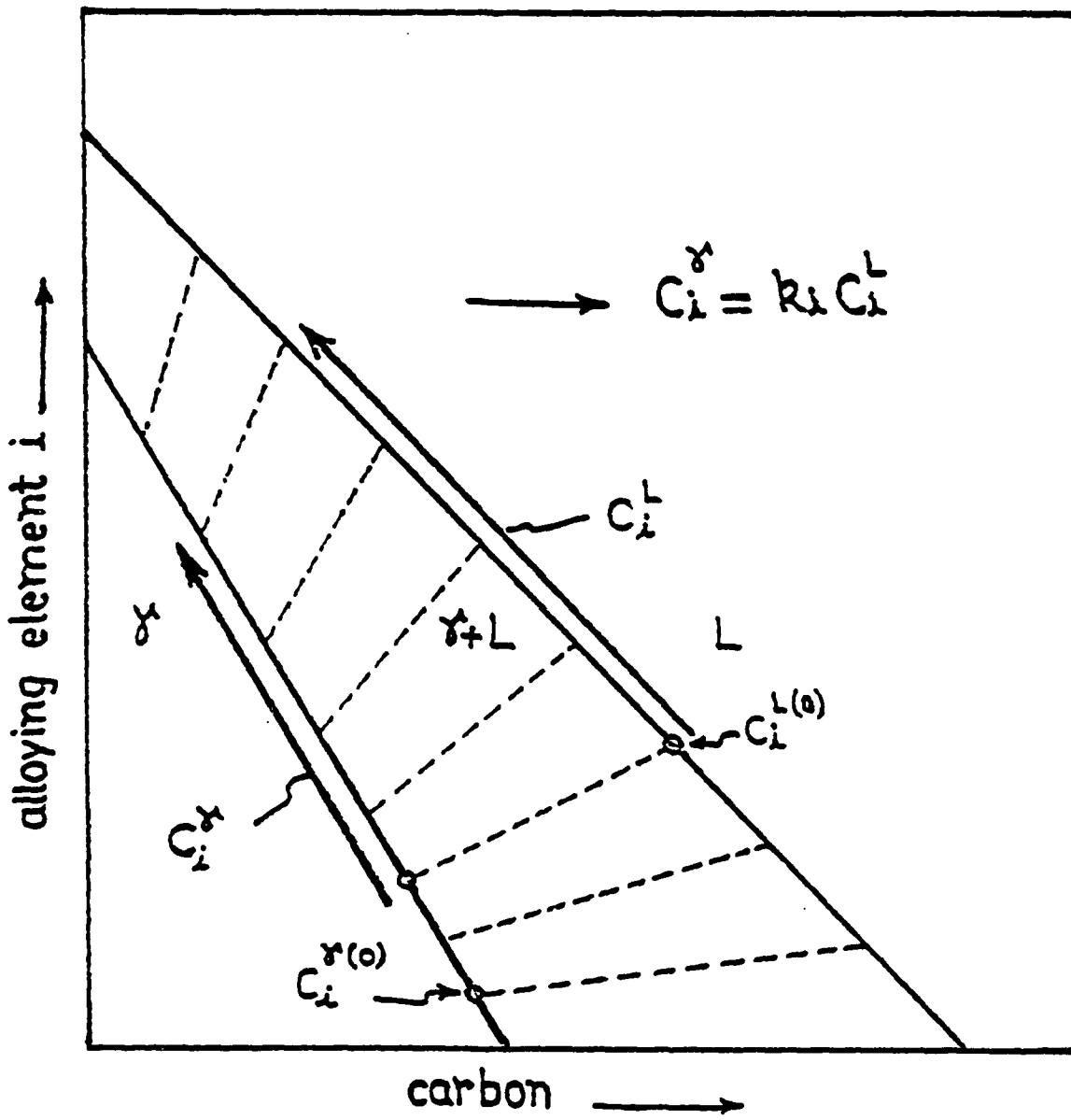


Figure 2. Ternary isothermal section showing carbon and alloying element compositions. Solid and liquid paths (shown by arrows) correspond to expected compositions assuming local equilibrium at the solid/liquid interface.

austenite phase of some composition $C_i^{Y(o)}$ (assumed zero weight % carbon in initial solid). The problem of interest is to define the composition of the solidus at the interface as a function of solidified thickness, ϵ .

One would ideally assume that irrespective of the alloying element composition of the original solid, $C_i^{Y(o)}$, the first solid to form would be given by the equilibrium solidus composition, i.e.,

$$C_i^Y \Big|_{x=0^+} = k_i C_i^{L(o)}$$

and

$$C_c^Y \Big|_{x=0^+} = k_c C_c^{L(o)}$$

as dictated by the phase diagram; or the tie line passing through the initial liquidus composition ($C_c^{L(o)}$, $C_i^{L(o)}$). As solidification proceeds by rejection of carbon into austenite the solid and liquid composition at the solid/liquid interface should vary along the solidus and liquidus as dictated by the tie lines, Fig. 2. Thus, knowing the liquidus composition and partition coefficients for the ternary isotherm, the segregation of the alloying element can be predicted by a Scheil type equation in its differential form (12).

The alloying element composition of the first solid to freeze, as expected from the phase diagram, is dictated by the liquid composition. The composition of the original solid can be chosen rather arbitrarily and is independent of the liquid composition. However in the SD process the first solid to freeze is in juxtaposition to the original solid. If the two compositions are not equal in terms of the

substitutional alloying element this would imply a large coherent strain due to a step change in the composition of the substitutional alloying element. The greater the difference between the atomic radii of Fe and the substitutional alloying element, the greater will be the strain energy. Thus solidification of a layer of composition as dictated by the phase diagram or the chemical free energy would result in a serious penalty in terms of the strain energy. The solidification rate as governed by the diffusion of carbon in austenite, only serves to enhance the effect since there is not enough time to dissipate the stresses (caused due to differences in atomic radii) by high temperature creep. Thus when atomic radii are significantly different, the first solid to freeze will have an alloying element composition which is approximately equal to the alloy composition of the original solid, i.e.,

$$c_i^{\gamma} \Big|_{x=0^+} \approx c_i^{\gamma(0)}$$

Three possible cases can then be considered.

A. $c_i^{\gamma(0)} = k_i c_i^L(0)$

B. $c_i^{\gamma(0)} < k_i c_i^L(0)$

C. $c_i^{\gamma(0)} > k_i c_i^L(0)$

In the following discussion, for the three cases only the alloying element compositions $c_i^{\gamma(0)}$, c_i^{γ} , $c_i^L(0)$ and c_i^L are mentioned for the sake of clarity. As will be shown the alloying element composition of the

original solid dictates the alloying element composition of the solid and liquid at the solid/liquid interface. The carbon compositions can be determined from the isothermal ternary phase diagram and are fixed, once the alloying element compositions at the solid/liquid interface are specified.

Also following solidification carbon is quick to homogenize because of its higher diffusivity whereas the alloying elements retain their composition for significantly longer times. Thus for homogenization studies, only the segregation of the alloying elements need be considered. The discussion and the phase diagrams considered here pertain to alloying elements which exhibit an equilibrium partition coefficient, k_i , less than unity. The segregation behavior for alloying elements with k_i greater than unity can be deduced easily.

$$\text{Case A: } \underline{C_i^Y(o) = k_i C_i^L(o)}$$

When the alloying element composition of the original solid, $C_i^Y(o)$, is equal to $k_i C_i^L(o)$ (the composition of the first solid to freeze as expected from the phase diagram), solidification proceeds normally with equilibrium maintained at the solid/liquid interface. Assuming no back diffusion in the solid for the alloying element, i, complete mixing in the liquid and equilibrium at the interface, the composition of the solidified layer will be given by:

$$C_i^Y = k_i C_i^L(o) (f_L)^{k_i} - 1 \quad (7)$$

If the partition coefficient k_i changes with liquidus composition, the differential form of the Scheil Equation can be solved numerically to

predict the segregation of the substitutional alloying element. The sequence of events is shown in Figure 3.

$$\underline{\text{Case B: } C_i^Y(o) < k_i C_i^L(o)}$$

Figure 4 shows the composition profiles for the solid and liquid composition paths when $C_i^Y(o)$ (original solid composition in terms of the alloying element, i), is less than $k_i C_i^L(o)$ (the expected composition of first solid to freeze as dictated by the phase diagram). The actual composition of the first solid to freeze, in terms of the alloying element, i, corresponds to the original solid composition which is less than the equilibrium composition $k_i C_i^L(o)$. Mathematically:

$$C_i^Y \Big|_{x=0^+} = C_i^Y(o) < k_i C_i^L(o)$$

As solidification proceeds the solid composition at the solid/liquid interface follows the solidus line, and the bulk liquid composition moves along the liquidus, however $C_i^Y \neq k_i C_i^L$. The process continues till some point 2_Y is reached where C_i^Y (the solid composition at the solid/liquid interface) is in equilibrium with the bulk liquid composition C_i^L (point 2_L). The composition range, where equilibrium at the solid/liquid interface between the solid and the bulk liquid composition is not maintained is 1_Y to 2_Y for the solidus and 1_L to 2_L for the liquidus.

During the solidification process, the path between 2_L to 3_L on the liquidus is the region where equilibrium conditions hold at the solid/liquid interface and the corresponding solidus follows the path 2_Y to 3_Y as dictated by the tie lines (Figure 4). Thus the region

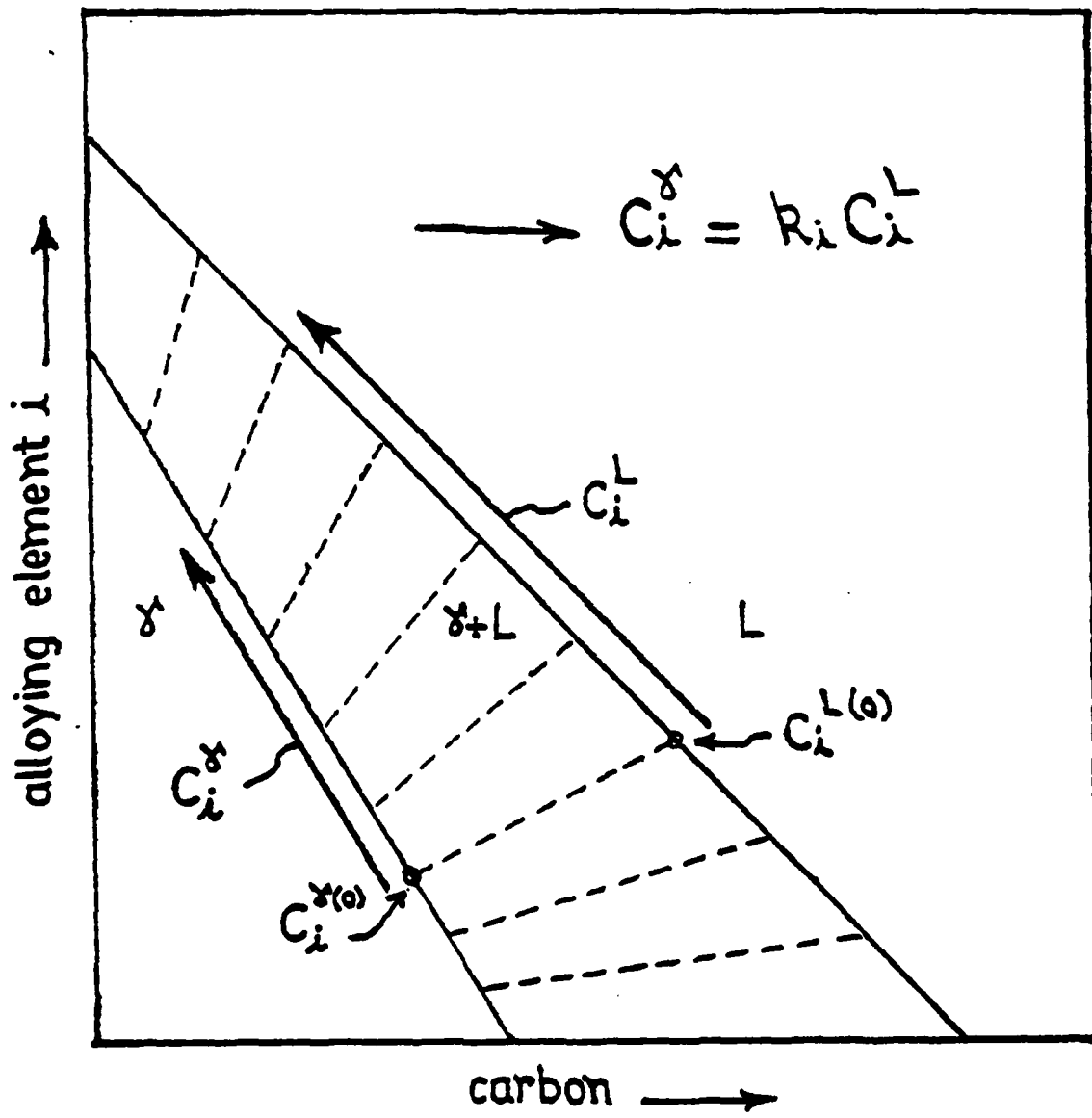


Figure 3. Isothermal section showing solid and liquid compositions paths, as solidification proceeds, for case A: $C_i^{\gamma(o)} = k_i C_i^L(o)$. Equilibrium conditions are maintained at the solid/liquid interface.

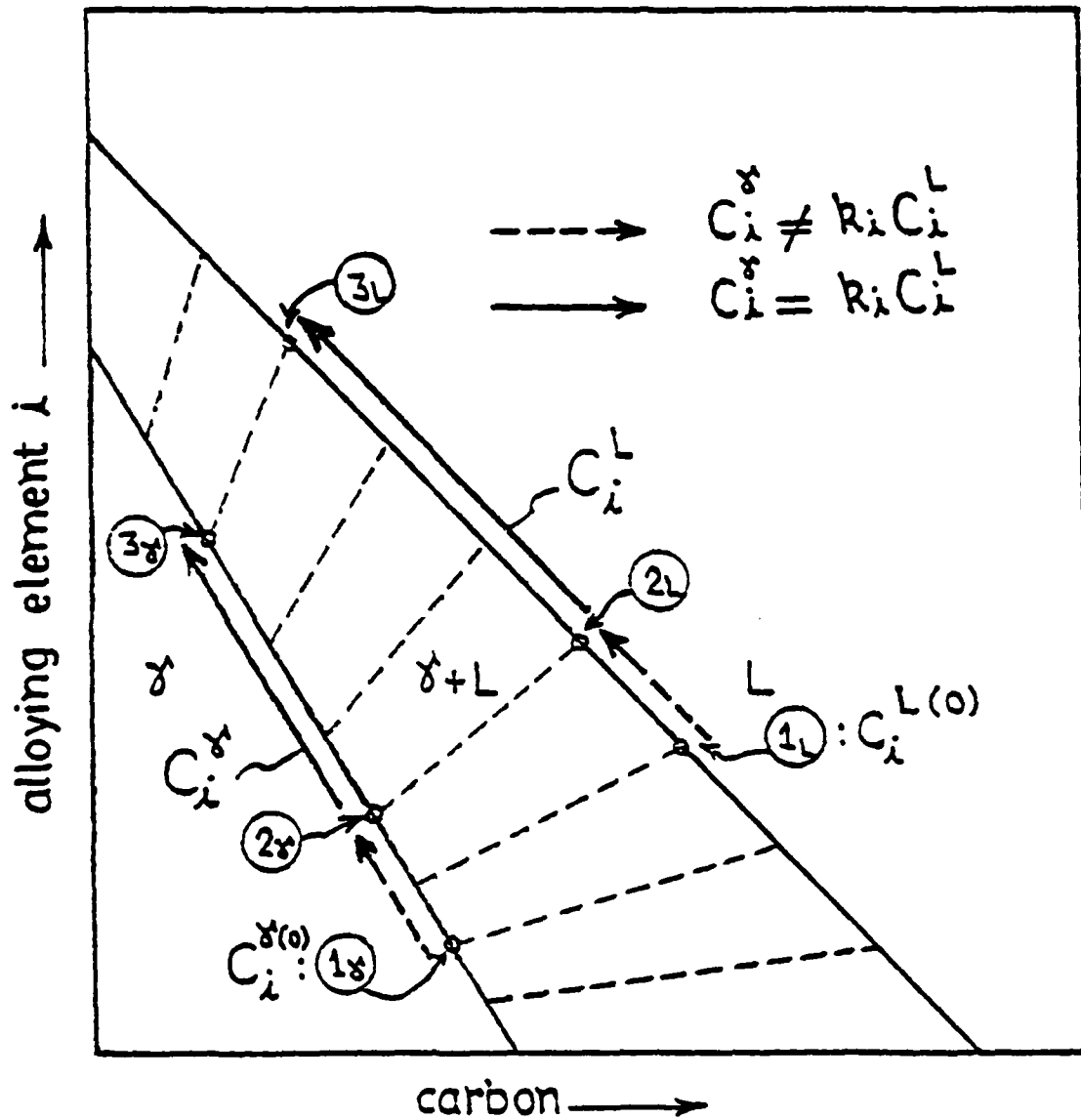


Figure 4. Actual solid and liquid composition paths, as solidification proceeds, for case B: $C_i^g(0) < k_i C_i^L(0)$. The alloying element composition of the first solidifying melt is $C_i^g(0)$. Dashed arrows indicate the region in which equilibrium is not maintained at the solid/liquid interface. Solid arrows represent the region where equilibrium condition hold at the solid/liquid interface.

in which the normal Scheil Equation can be used to predict the segregation of the alloying element starts at 2_L , with $f_L = 1$, and liquid composition corresponding to point 2_L .

Case C: $C_i^Y(o) > k_i C_i^L(o)$

The sequence of events, for the case when the original solid composition $C_i^Y(o)$ is greater than $k_i C_i^L(o)$ (the expected composition of the first solid to freeze as dictated by the phase diagram) is shown in Figures 5 and 6. The first layer to solidify has an alloy composition approximately equal to the original solid composition, $C_i^Y(o)$:

$$C_i^Y \Big|_{x=0^+} \approx C_i^Y(o) > k_i C_i^L(o)$$

As solidification proceeds the solid composition at the solid/liquid interface will follow the solidus path $1_Y - 2_Y$. The solid alloy composition, C_i^Y is initially decreasing in spite of the fact that the equilibrium partition coefficient, k_i , is less than unity. The bulk liquid composition will be increasing when $C_i^Y(o) < C_i^L(o)$, i.e., when the original solid composition is less than the initial liquid composition (1_L to 2_L in Figure 5). When the original solid composition is greater than the initial liquid composition, i.e., $C_i^Y(o) > C_i^L(o)$, the liquid composition will initially decrease (1_L to 2_L in Figure 6). At 2_L the liquid composition is in equilibrium with the solid composition (Point 2_Y , Figures 5 and 6) at the solid/liquid interface and normal solidification will then proceed; the solid and liquid compositions being dictated by the tie lines.

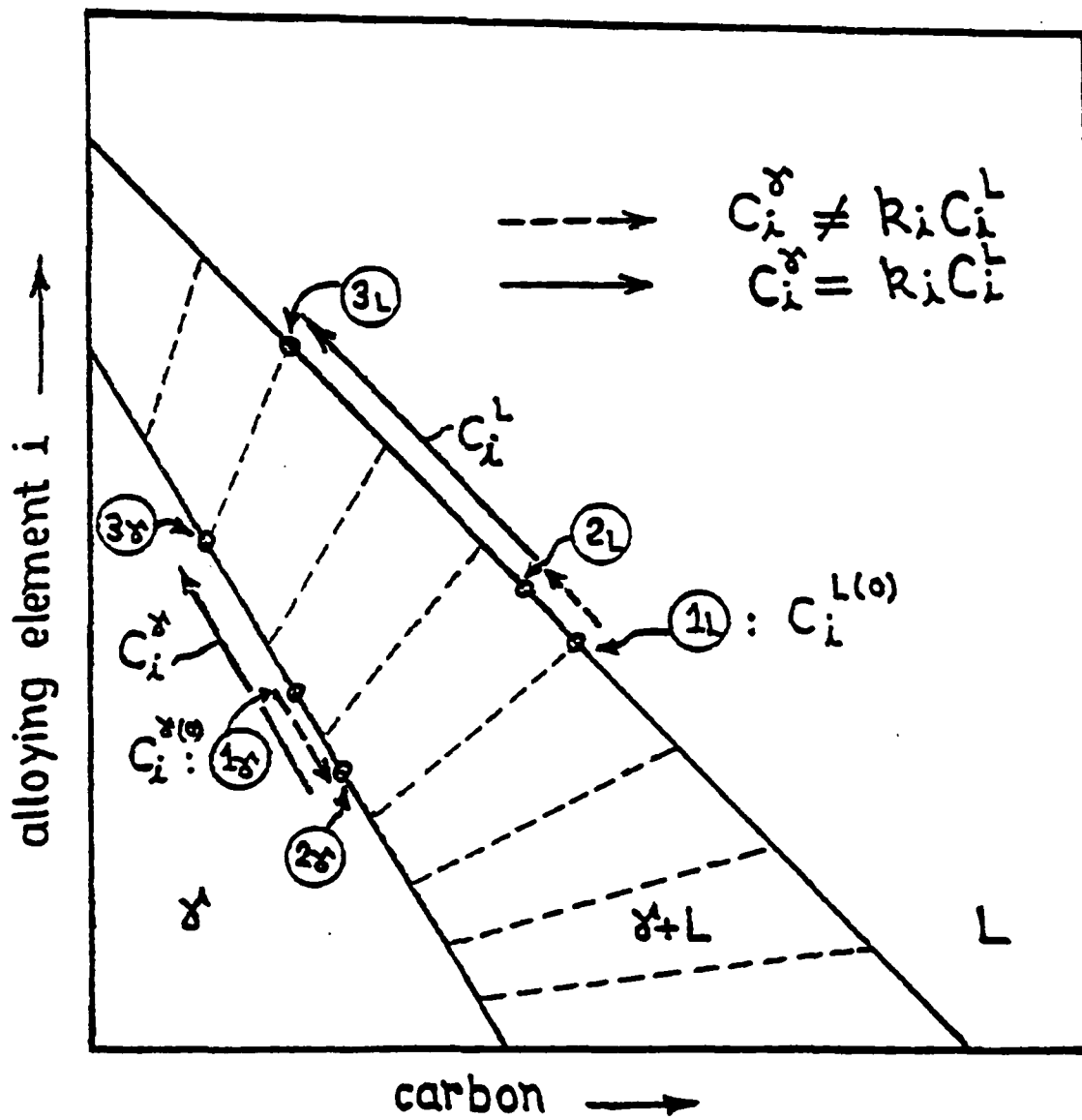


Figure 5. Solid and liquid compositions at the solid/liquid interface for case C: $C_i^Y(o) > k_i C_i^L(o)$, when $C_i^Y(o) < C_i^L(o)$. The alloying element composition of the solid is initially decreasing irrespective of the fact that the partition coefficient, k_i , is less than unity.

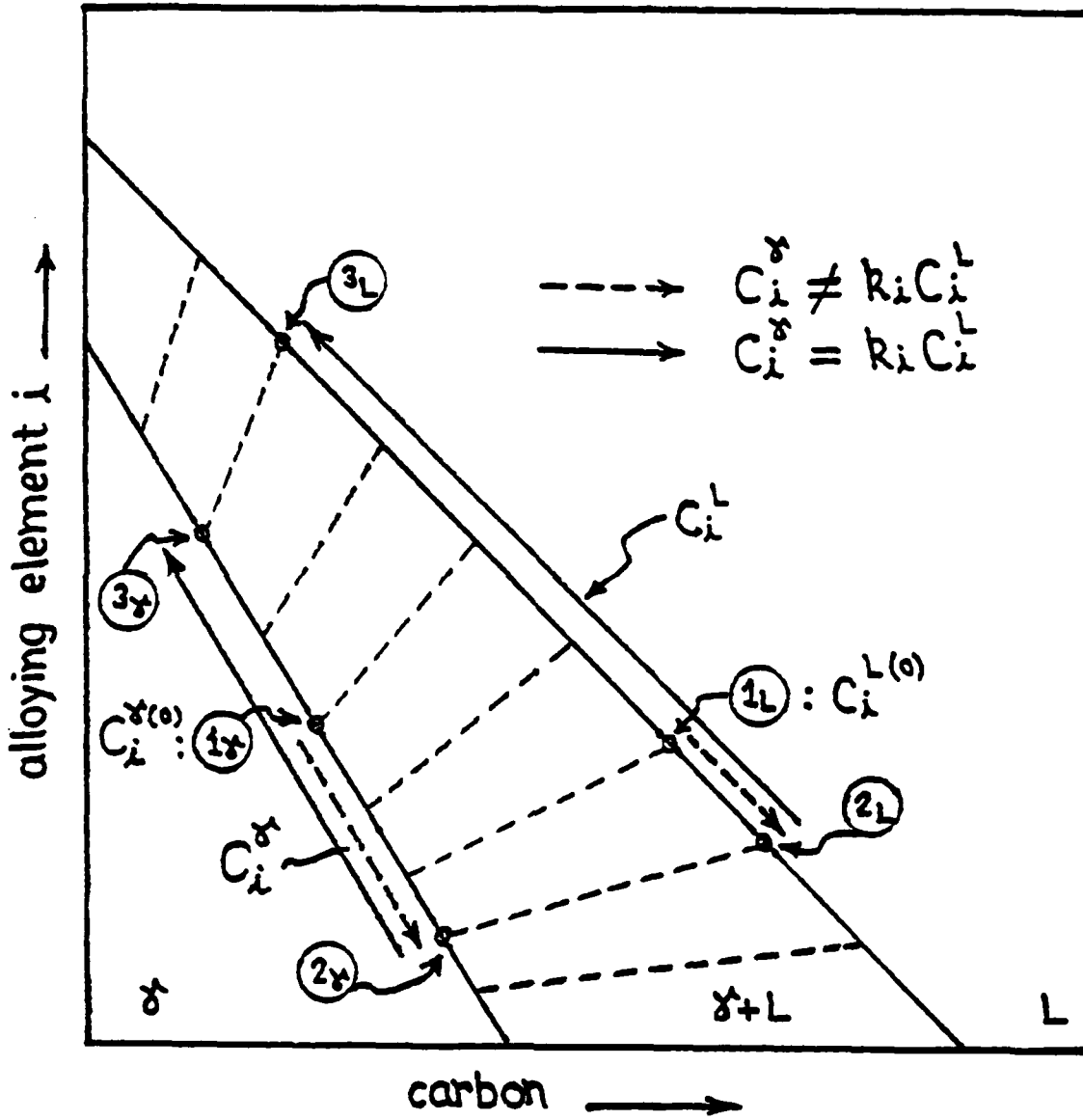


Figure 6. Solid and liquid composition paths for case C: $C_i^y(0) > k_i C_i^L(0)$, when $C_i^y(0) > C_i^L(0)$. The alloying element composition of the solid and the liquid is decreasing initially in spite of the fact that the partition coefficient, k_i , is less than unity.

The above discussion qualitatively describes the segregation behavior of a substitutional alloying element in the SD process for the three cases as dictated by the alloy composition of the original solid, $C_i^{Y(0)}$. During normal solidification, the segregation behavior can be predicted by a Scheil type equation (12) if the partition coefficient k_i is constant. If k_i varies with the liquid composition then a differential form of the Scheil Equation (12) has to be solved numerically. The partition coefficients can be approximated for known liquidus compositions using thermodynamic relationships as given by Kirkaldy et al. (8). However the initial segregation behavior will control the location and liquid composition at which point normal solidification proceeds. Prediction of the initial segregation behavior requires a functional relationship between the alloy composition of the original solid, $C_i^{Y(0)}$; the initial liquid composition, $C_i^{L(0)}$; the length L , required to be solidified; the rate of interface motion, $\frac{de}{dt}$; and the free energy contributions of the chemical energy and strain energy as a function of compositional gradients.

The equilibrium solid and liquid compositions as given by the phase diagram take into account only the chemical potential in a homogeneous phase. For a homogeneous solution, at constant temperature and pressure, the partial molar free energy of a component (Fe, C or i) is equal to its chemical potential, i.e., $\bar{G}_i = \mu_i$. Equations 1 and 2 were derived by equating the partial molar free energy of individual components (Fe, C or i) in the austenite and liquid of homogeneous compositions in equilibrium with each other (8).

$$\bar{G}_i^Y = \bar{G}_i^Y + RT \ln a_i^Y = \bar{G}_i^Y + RT \ln \gamma_i^Y X_i^Y \quad (8)$$

$$\bar{G}_i^L = \bar{G}_i^L + RT \ln a_i^L = \bar{G}_i^L + RT \ln \gamma_i^L X_i^L \quad (9)$$

The Wagner interaction coefficients were introduced by using the Taylor series expansion for $\ln \gamma_i$. The three resulting equations ($\bar{G}_{Fe}^Y = \bar{G}_{Fe}^L$, $\bar{G}_C^Y = \bar{G}_C^L$, and $\bar{G}_i^Y = \bar{G}_i^L$) can then be solved simultaneously to give X_{Fe}^Y , X_C^Y , X_i^Y in terms of the interaction coefficients, equilibrium liquid compositions, and free energy change at the standard state ($\Delta^{\circ}G^{Y-L}$ terms) (8). The above procedure is valid when the equilibrium between unstressed homogeneous solid and liquid phases is considered. In a SD casting the solidifying product is not at a homogeneous composition and additional complexities must be considered. Cahn (13) in his work on spinodal decomposition has pointed out that when a composition gradient exists the free energy will be modified to take into account:

- (i) the chemical free energy change due the composition gradient and,
- (ii) the elastic energy of coherency strains due to this composition gradient.

The partial molar free energy of the components (Fe, C or i) in the austenite is then not equal to its chemical potential, i.e., $\bar{G}_i^Y \neq \mu_i^Y$. The liquid, however is still homogeneous and stress free, $\bar{G}_i^L = \mu_i^L$, and therefore expression for the partial molar free energy of the components in liquid remains unchanged, Equation 9. The partial molar free energies of the components (Fe, C or alloying element i) in austenite should then be written as (only the expression for alloying element, i, is given; similar expressions can be written for carbon and iron):

$$\bar{G}_i^Y = {}^0G_i^Y + f_1 \left(x_j^Y, \frac{\partial x_i^Y}{\partial x}, \phi \left(\frac{\partial x_i^Y}{\partial x} \right) \right), \quad j = \text{Fe, C, and i.} \quad (10)$$

where ${}^0G_i^Y$ = free energy of alloying element i at chosen standard state

x_j^Y = Mole fractions of the components Fe, C, and alloying element, i.

$\frac{\partial x_i^Y}{\partial x}$ = Composition gradients of the components Fe, C and alloying element, i.

$\phi \left(\frac{\partial x_i^Y}{\partial x} \right)$ = Stress field caused due to the composition gradients.

In absence of composition gradients and hence related stresses, Eq. 10 reduces to Eq. 8 with $f_1(x_j^Y) = RT \ln a_i$. The partial molar free energy of the alloying element, i, can be written as:

$$\bar{G}_i^Y = f_{1(i)} (x_j^Y) + f_{2(i)} \left(\frac{\partial x_i^Y}{\partial x} \right) + f_{3(i)} \left(\phi \left(\frac{\partial x_i^Y}{\partial x} \right) \right), \quad j = \text{Fe, C and i} \quad (11)$$

where $f_{1(i)}$ is the chemical contribution to the partial molar free energy of the component i, for a homogeneous solution, $f_{2(i)}$ is the contribution to the partial molar free energy of the component i due to the composition gradient and $f_{3(i)}$ is the elastic contribution to the partial molar free energy of component i. The free energy change at chosen standard state, ${}^0G_i^Y$ is included in $f_{1(i)}$.

One approach of approximating the elastic free energy contribution is to consider an individual atom as an elastic sphere and thus calculate the free energy change, for changing its radius from r_a to r'_a .

For the case when compression is uniform in all directions, and Hooke's Law is applicable the free energy change for compression of an elastic sphere from a radius r_a to r'_a is given by (14):

$$\Delta G^{\text{sphere}} = 6\pi r_a (r'_a - r_a)^2 \cdot B_s \quad (12)$$

where B_s is bulk modulus of the elastic sphere. Assuming that individual atoms can be treated as elastic spheres the free energy contribution due to strain energy will be (15):

$$\Delta G^{\text{elastic}} (\text{per mole}) = 6\pi K r_a (r'_a - r_a)^2 \cdot B_s N \quad (13)$$

where r_a = radius of atom when in an unstressed homogeneous solution

r'_a = radius of atom in solution when compositional gradients exist. Different from r_a since coherency strains have to be accommodated.

N = Avagadro's number

B_s = Bulk modulus of the atom.

In Eq. (13), K is a constant introduced since the assumptions made regarding atoms being elastic spheres and uniform compression in all directions are not realistic. The application of the above equation to estimate elastic contribution to free energy will also require the estimation of the bulk modulus of the atoms, B_s , the individual atomic radii when in an unstressed solution, and the changes in atomic radii when in a stressed solution (for Fe, C, and the alloying element, i) at the process temperature. The pertinent atomic radii are not known

and difficult to approximate from room temperature data. The unstressed radius of an atom (r_a) depends on the temperature, the crystal structure of the phase and its immediate environment (16). The atomic radii of the atoms when coherency strains are taken into account (r'_a) will depend on the composition gradient in the austenite at the solid/liquid interface (besides the crystal structure, and the temperature), since coherency strains developed depend on the composition gradients involved. Specifically, for a given composition gradient, one needs to know the coherent strains involved, and therefore the part of coherent strain energy accommodated by individual atoms (Fe and the substitutional alloying element; the strain energy for the interstitial atom (carbon) can be neglected). Moreover one has also to take into account the contribution to the chemical free energy due to the composition gradient and the stress relaxation mechanisms that might be operable at the solid/liquid interface (formation of vacancies and dislocation via high temperature creep when the rate of interface motion has slowed down).

In this study, due to the complexity of the problem and lack of pertinent data no attempt has been made to quantitatively model the initial segregation behavior from such a fundamental viewpoint.

6.3 EXPERIMENTAL PROCEDURE:

Instead of using spherical shot for the segregation studies cones were used since it is easier to locate the original solid/infiltrant interface with this geometry. Each cone was 0.247 inches (0.627 cm) in diameter, 0.5 inches (1.27 cm) long and had a 5° taper on one end

(Fig. 7). Two 0.01" x 0.01" (0.0254 x 0.0254 cm²) grooves along the side of each cone, insured free flow of melt into the gap between two successive cones. For the experiments where original solid does not have any alloying elements in it the cones were machined from a 0.25" (0.635 cm) iron rod of 99.95% purity. Cones, for experiments in which the solid had varying amounts of Mn, were machined from commercially available C1018 steels or Fe-Mn alloys cast from electrolytic iron and manganese.

The melt alloy compositions were prepared in a two stage process. An iron carbon alloy was prepared by induction melting electrolytic iron and adding spectroscopic grade graphite to it. The melting was done in an argon atmosphere. Ar was bubbled through the melt to minimize dissolved oxygen in the melt before addition of graphite. The Fe-C melt was then atomized using inert gas (argon). The Fe-C powder was analyzed to have 2.2% C. Subsequent melts for the experiments were made from this stock Fe-2.2% C alloy by blending it with ternary alloying element and Fe or carbon to give desired compositions.

The logic and the assembly of the components (cones, PV, and melt charge) in the 0.25" ID Al₂O₃ tube (18" long) is shown in Figure 8. The Al₂O₃ tube after assembling of the components was connected to a steel probe and flushed with Ar for 15 minutes, to avoid oxidation of the cones and the melt charge on insertion of the probe into the hot furnace. The mold along with its contents was heated using cylindrical graphite cored induction heating (10 kHz). Since the melt required to be heated to a higher temperature than the cones initially; a two zone

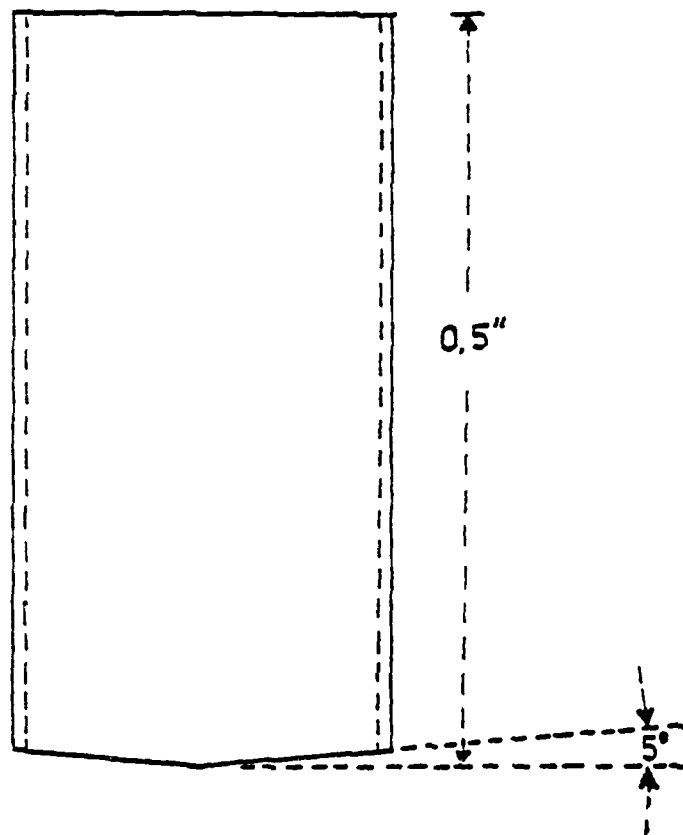
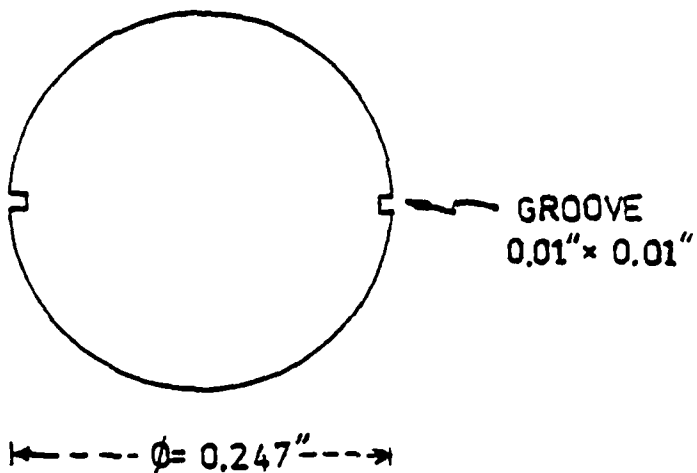


Figure 7. Geometry of cones used in the segregation studies.
(Diagram not to scale.)

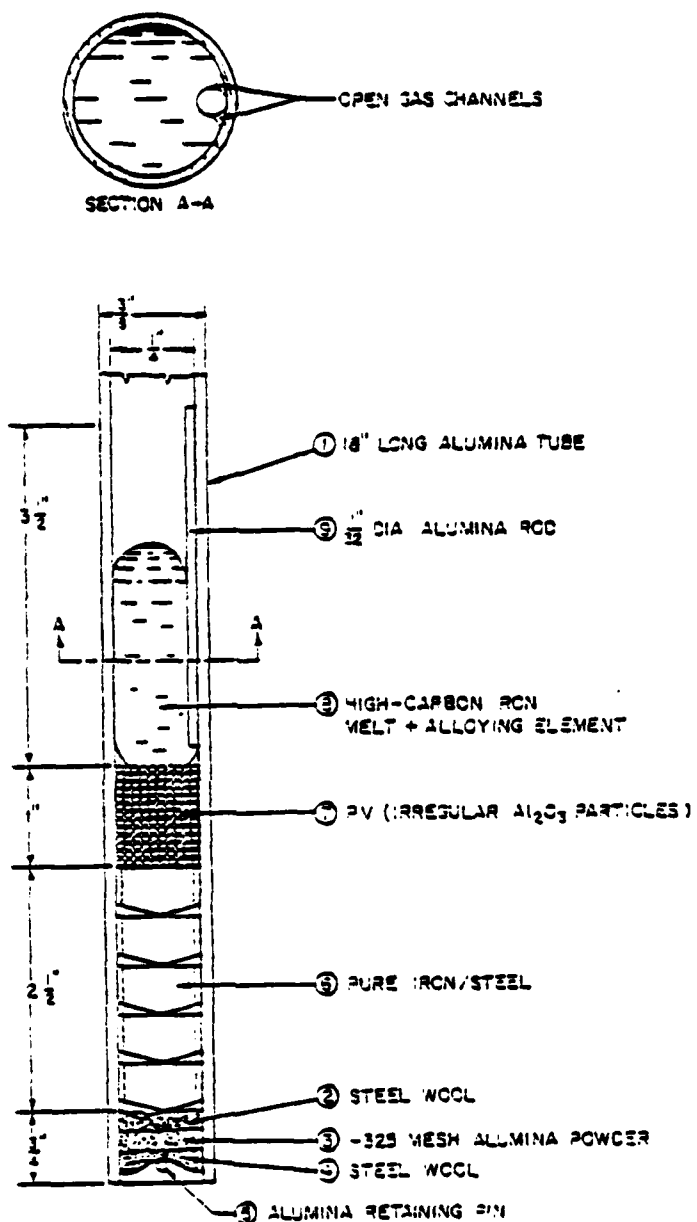


Figure 8. Arrangement of the cones, particle valve, and melt in a 0.25" Al_2O_3 tube for segregation studies. (Mold logic based on Ref. (1).)

furnace construction was used, with separate induction coils, graphite susceptors, and temperature controllers. The two sections of the furnace were insulated from each other by using a 1.25" thick pyrolytic graphite spacer. Radially located W-5 pct Re/W-26 pct Re thermocouples were used to control and measure the temperatures in the furnace. The furnace assembly was enclosed in a steel vessel which could be evacuated and/or pressurized.

At the beginning of the cycle that is when the Al_2O_3 tube is inserted into the furnace, the melt zone and the solid zone are both at the process temperature (1372°C). After inserting the Al_2O_3 tube; a valve which connected the probe to the pressure vessel was opened and the whole assembly was evacuated. After 10 minutes of heating time the temperature of the melt charge region was raised to 1472°C (100°C superheat) and maintained for 30 minutes, followed by a 15 minute cooling period to the melt transfer temperature. The melt and the charge were maintained at the process temperature (1372°C) for 10 minutes after which the probe was pressurized, causing melt transfer, into the solid region. The holding time after melt transfer (at the casting temperature before removal of the mold assembly from the furnace) was six minutes. The melt transfer pressure used was 50 psi gauge.

The cones were cut through the center longitudinally for segregation studies. Microsegregation of the ternary alloying element across the diffusion solidified zone was measured using an ARL electron probe. The cross section of the solidified melt and the direction in which the concentration profiles were taken are shown in Fig. 9.

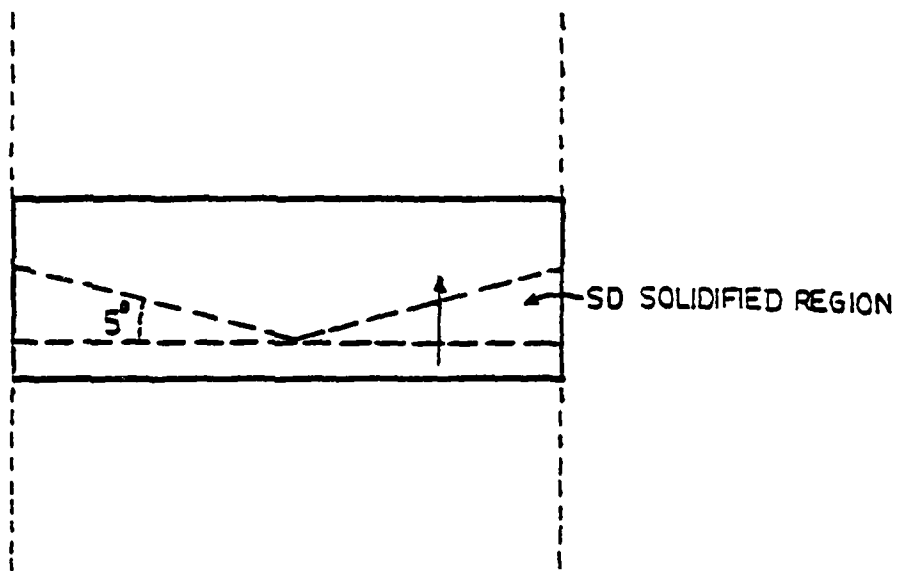


Figure 9. Cross-section through the cones showing the region of solidified melt and the direction of microprobe line scan.

6.4 RESULTS AND DISCUSSION

To determine the effect of the alloy compositions of the original solid on the resulting segregation in the solidifying melt; Mn content of the cone was varied. In all such experiments it was found that the Mn content of the first melt to solidify was equivalent to the original solid Mn composition, $C_{Mn}^{Y(o)}$. Three representative segregation behaviors are shown in Figures 10 through 12. Figures 10 and 11 represent samples where the liquid melt has a much higher Mn content than the original solid ($C_{Mn}^{Y(o)} < k_{Mn} C_{Mn}^{L(o)} < C_{Mn}^{L(o)}$). Of special interest is the segregation behavior depicted in Fig. 12. Mn under equilibrium conditions is supposed to segregate in a positive manner. However, for the case depicted in Figure 12, $k_{Mn} C_{Mn}^{L(o)}$ is less than $C_{Mn}^{Y(o)}$, i.e., the equilibrium solid composition expected to freeze out (from the phase diagram) is less than the Mn content of the original solid. The actual Mn content of the first solidified melt is the same as the original solid and initially decreases continuously till normal segregation occurs which is exhibited by the positive segregation of Mn, Fig. 12. The observed segregation behavior exemplifies the Case C (see theoretical section) where $C_i^{Y(o)} > k_i C_i^{L(o)}$, and showed a decrease followed by an increase in the composition of the solidified melt.

It is obvious then, that the initial segregation behavior is controlled by the alloy content of the original solid. In analyzing the segregation behavior of the alloying elements three specific zones are considered.

- a) Initial segregation as controlled by the alloy composition of the original solid.

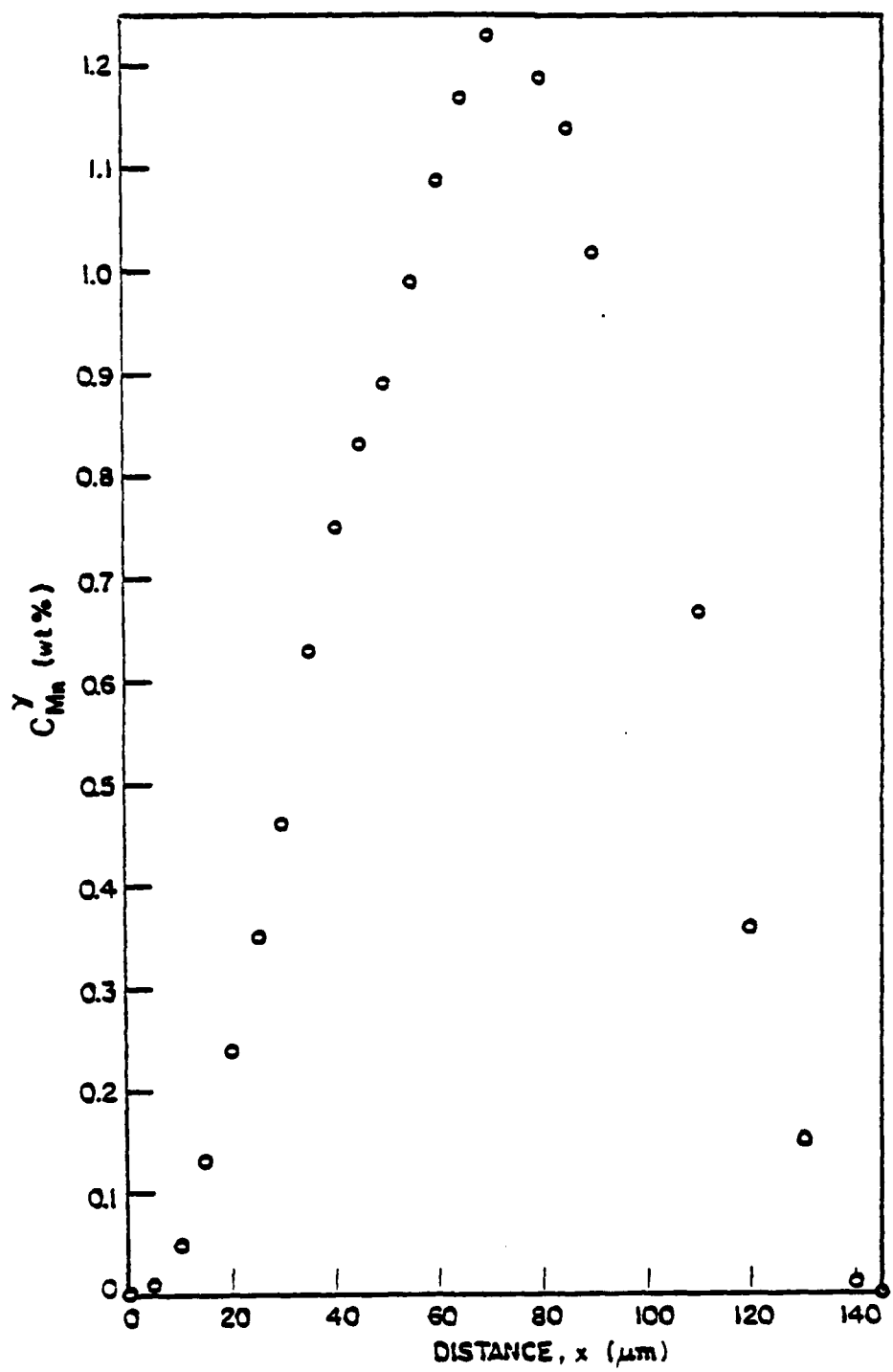


Figure 10. Mn concentration across the solidified melt region.
Original solid was devoid of manganese, i.e. $C_{Mn}^\gamma = 0$.
($C_{Mn}^\gamma \approx 0.6$ wt %)

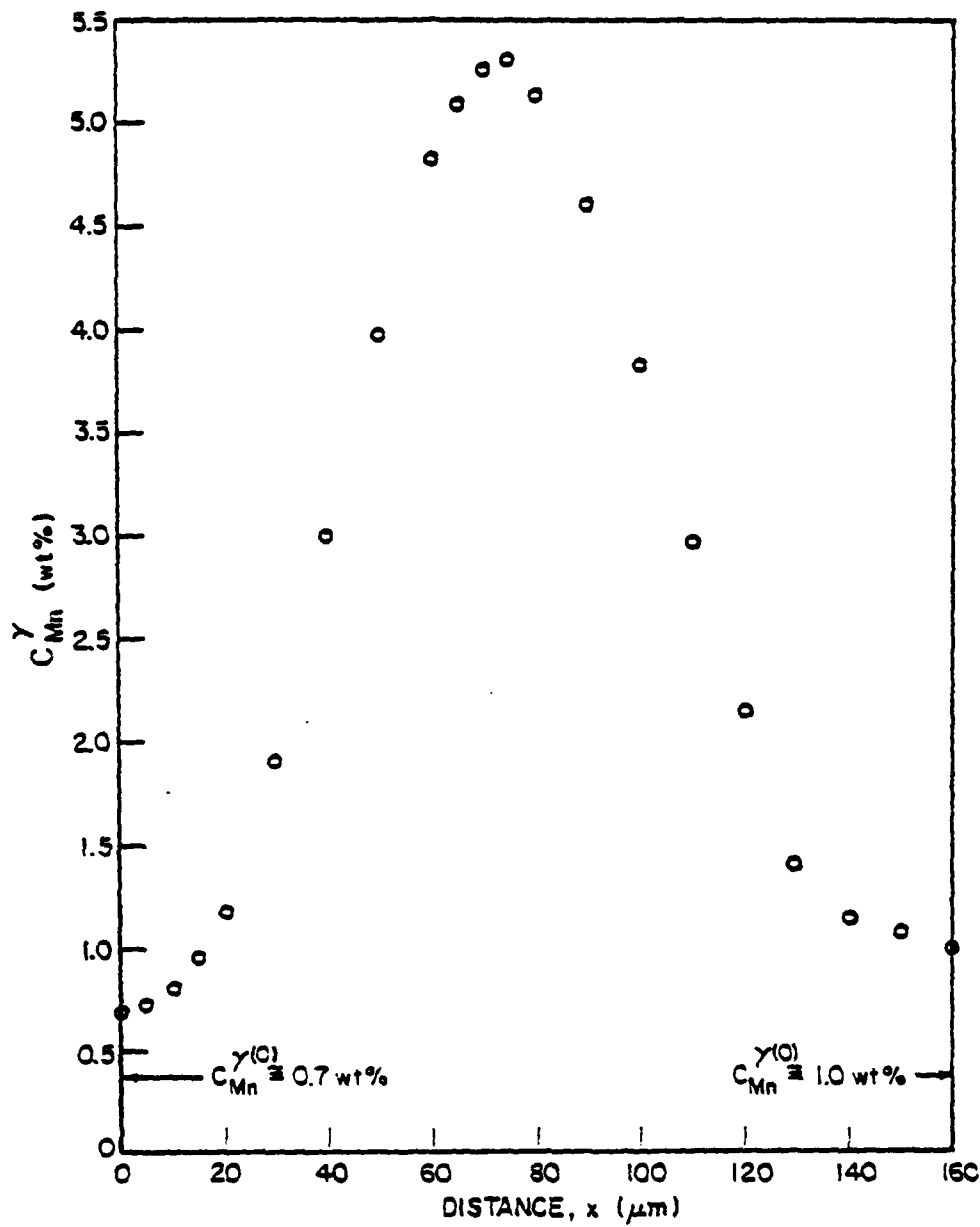


Figure 11. Mn concentration across the solidified melt between two cylinders of composition Fe-0.7 wt % Mn and Fe-1.0 wt % Mn. (C_L^Y is 3.0 wt %)

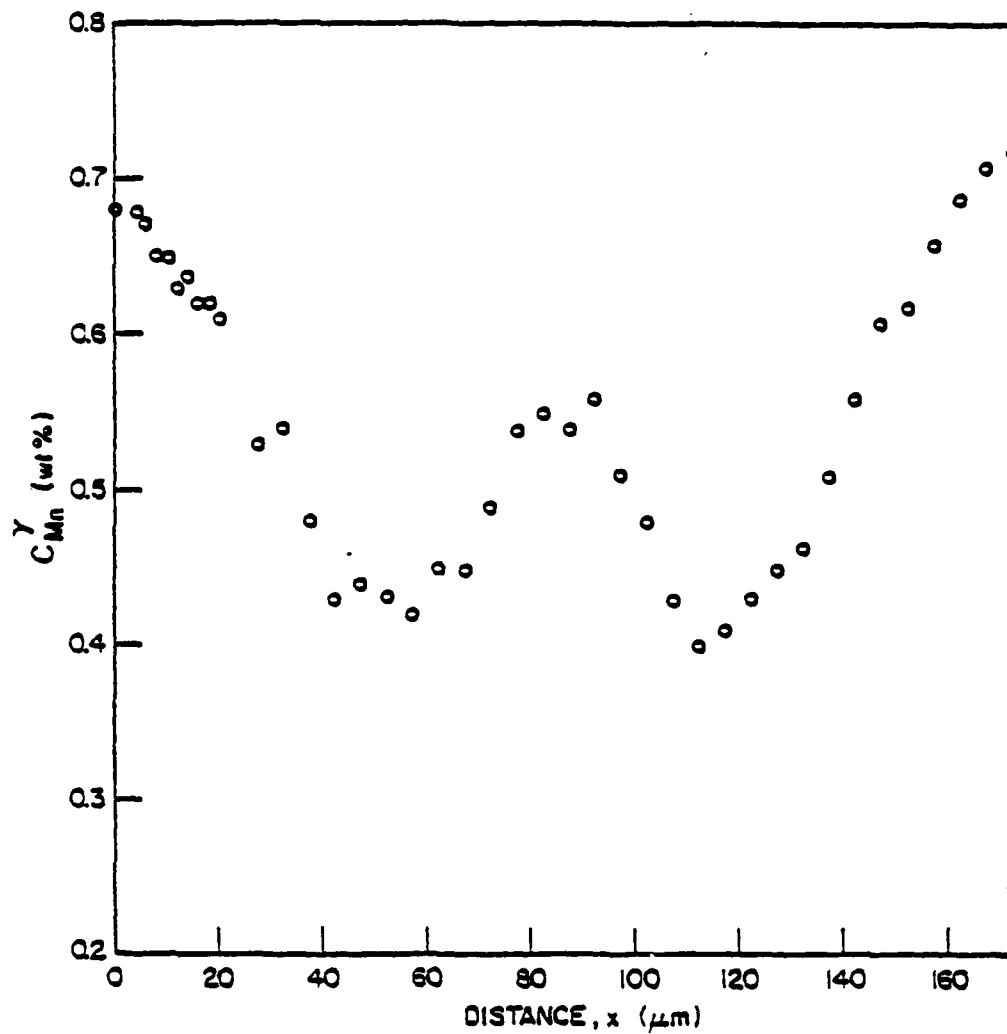


Figure 12. Initial inverse segregation of Mn in the solidifying melt exemplifying case C: $C_i^Y(o) > k_i C_i^L(o)$. ($C_{\text{Mn}}^Y(o) \approx 0.7$ wt %, $C_{\text{Mn}}^L(o) \approx 0.5$ wt %)

b) A transition zone.

c) Normal segregation behavior.

The initial segregation behavior was empirically found to obey the relationship:

$$C_i^Y = \psi \cdot x^2 + C_i^{Y(o)} \quad (14)$$

where x is the distance from the initial solid/infiltrant interface, $C_i^{Y(o)}$ is the alloying element composition of the original solid, ψ is the empirically determined constant for initial segregation, and C_i^Y is the alloying element composition of the solidified melt. To determine ψ , by regression analysis only an initial distance of 35 μm was considered even though the composition profiles for some elements have been plotted for much larger distances using the empirical relationship, Eq. (14).

Each data point on the composition-distance profile (Figures 13 to 18) was assumed to be where normal segregation becomes the dominant mode of segregation. Through curve fitting into a Scheil type equation (Eq. 7) via linear regression analysis a partition coefficient k_i , was determined for the particular point under consideration, from the slope of $\log C_i^Y$ vs. $\log f_L$ data. The hypothesis that normal segregation behavior becomes the dominant mode of segregation at the specific point being considered was tested by evaluating the computed correlation coefficient. The point which yielded the maximum correlation coefficient was determined as the point where the normal segregation becomes the prevalent mode. The fraction of liquid, f_L , as a function of distance, x , for assumed location at which normal segregation starts; is derived

in Appendix 6A. Figures 13 through 17 show the experimentally measured and empirically fitted equations for alloying elements Ni, Co, Mn, Mo and Cr, respectively. (The composition vs. distance data, in tabular form is compiled in Appendix 6B.) A discussion on the segregation behavior of each of these alloying elements follows.

Ni and Co: Under equilibrium conditions, both Ni and Co exhibit negative segregation. The segregation behavior for Ni and Co during the SD process is shown in Figs. 13 and 14 respectively. The original solid in both cases was pure iron and hence the alloy composition of the solidifying melt starts from zero percent and builds up steadily according to Eq. 14. The value of ψ , the constant in Eq. 14 depicting the initial segregation behavior was calculated (using distance of up to, $x = 35\mu\text{m}$) to be $9.28 \times 10^{-4} \text{ wt \%}/(\mu\text{m})^2$ and $8.8 \times 10^{-4} \text{ wt \%}/(\mu\text{m})^2$ for the Ni and Co cases, respectively. At a distance of approximately $40\mu\text{m}$ the solid and liquid compositions have attained their equilibrium values and both systems now exhibit a negative segregation. The value of the equilibrium partition coefficient, k_1 , as determined from the experimental data is 1.106 for Ni and 1.084 for Co.

Mn and Mo: Mn and Mo segregate positively under equilibrium solidification conditions. Again the initial segregation behavior for both Mn and Mo for the SD process was controlled by the alloy composition of the original solid. Figure 15 shows the segregation behavior of Mn when the original shot had zero percent Mn. The first solid to freeze has zero percent Mn and the segregation behavior up to a distance of $35\mu\text{m}$ is dictated by Eq. 14. The value of ψ was

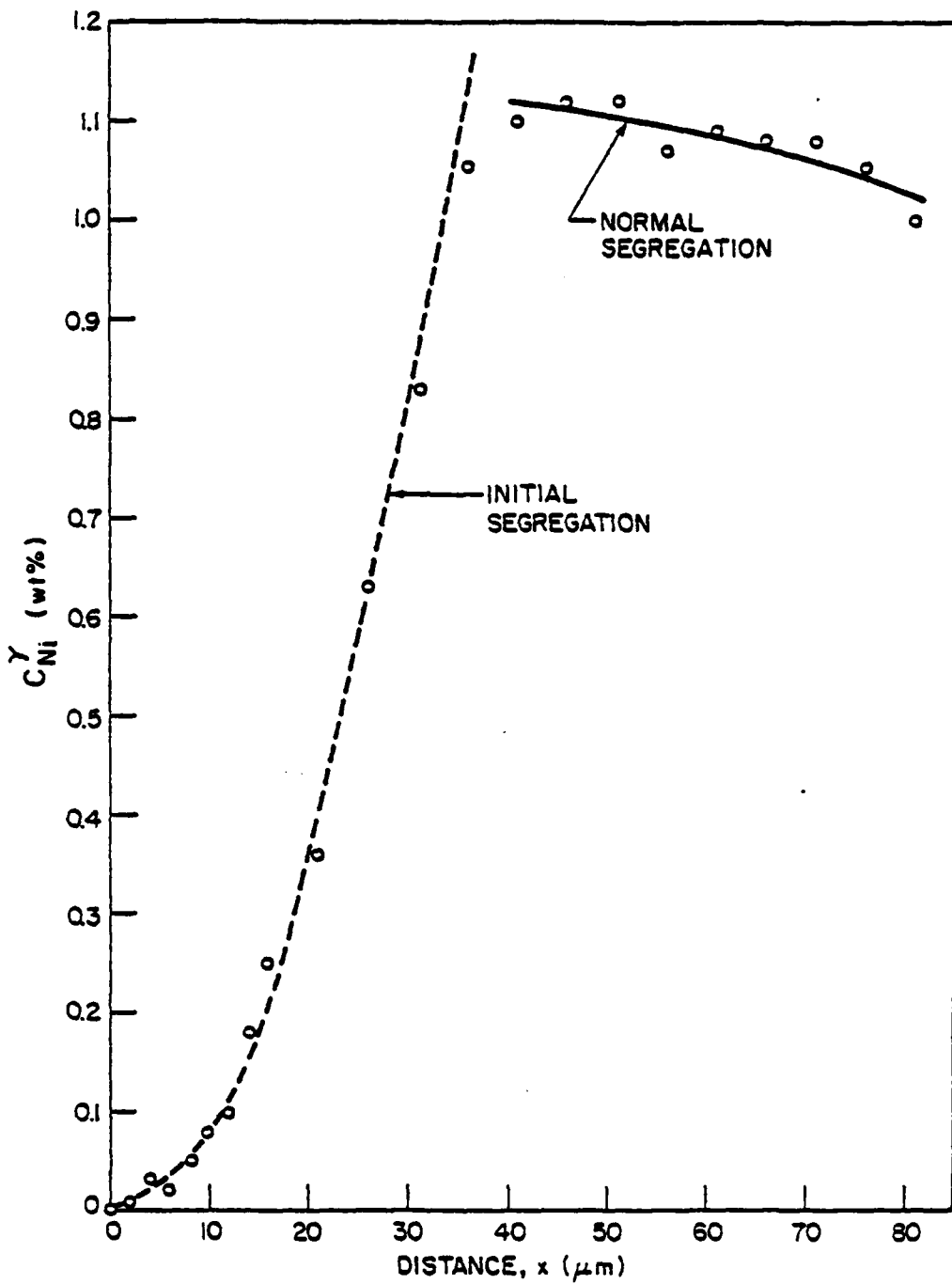


Figure 13. Experimentally measured and empirically fitted composition profiles for Ni segregation across the solidified melt. Only half the distance across the solidified region is plotted. ($C_{Ni}^Y(o) \approx 0$ wt %, $C_{Ni}^L(o) \approx 0.75$ wt %)

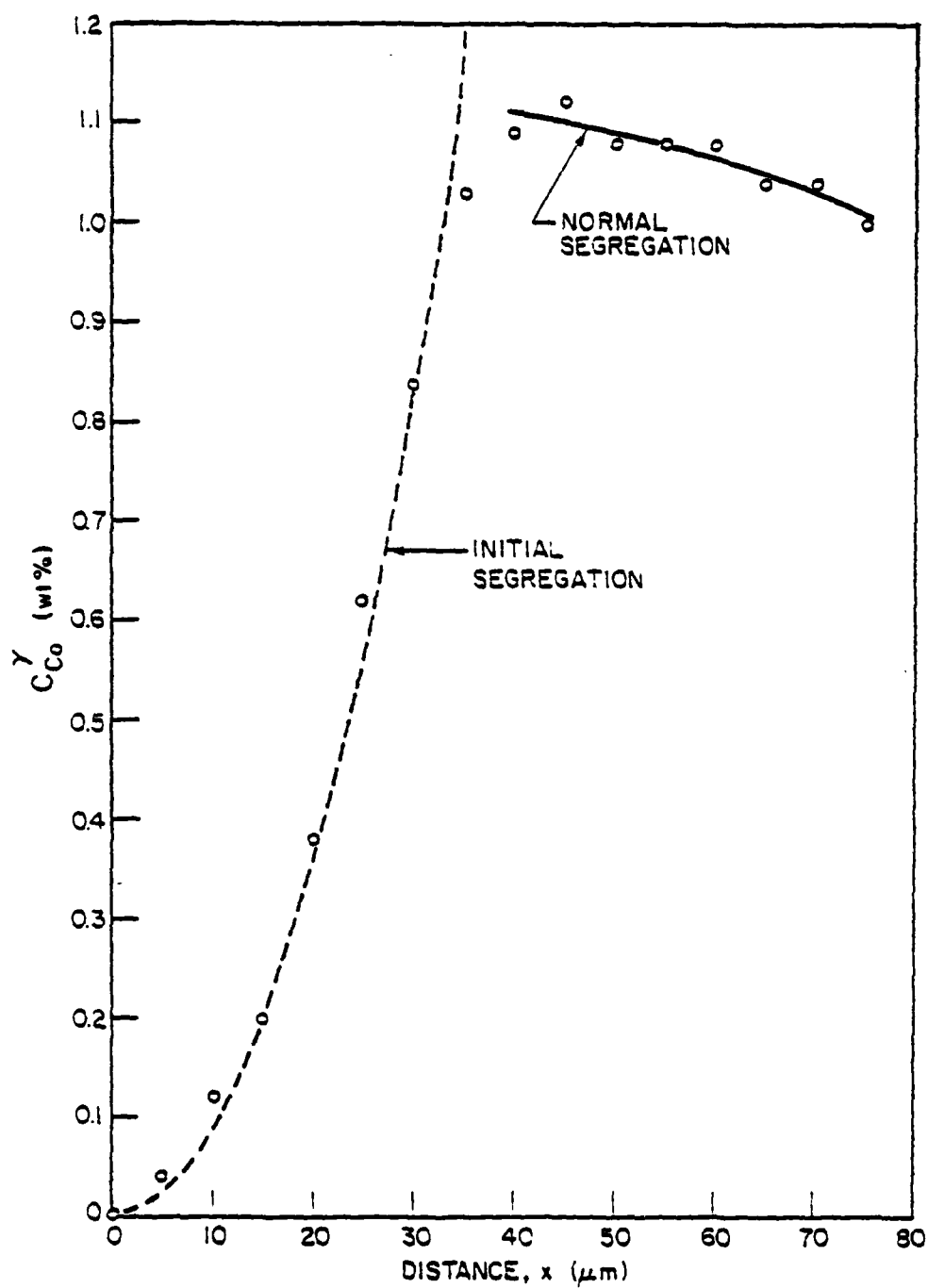


Figure 14. Experimentally measured and empirically fitted composition profiles for Co segregation. ($C_Co^Y(0) = 0$ wt %, $\frac{C_Co^L(0)}{C_Co} \approx 0.8$ wt %)

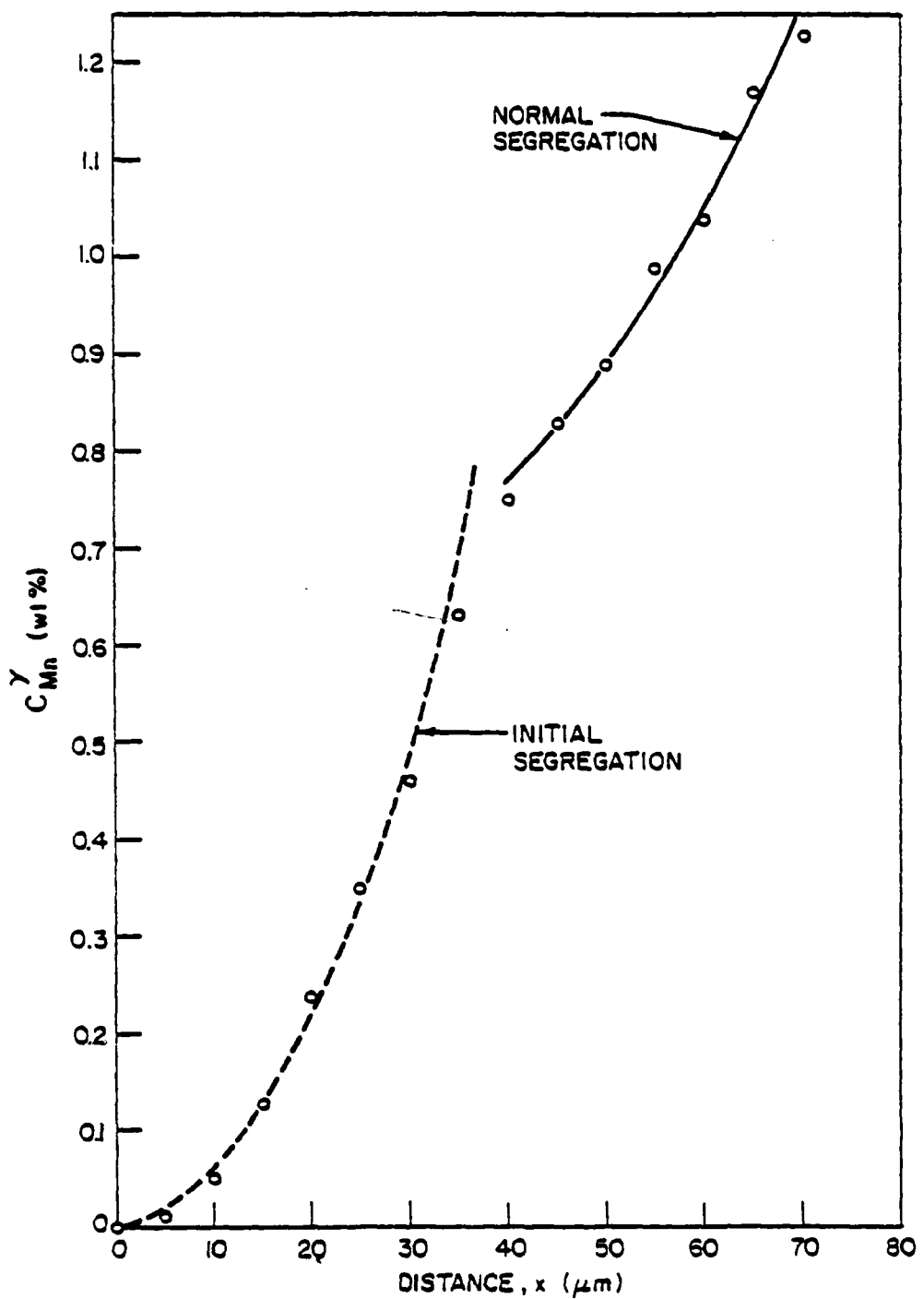


Figure 15. Experimentally measured and empirically fitted composition profiles for Mn segregation. ($C_Mn^Y(o) = 0$, wt %, $C_Mn^L(o) = 0.6$, wt %)

calculated to be 5.74×10^{-4} wt %/(μm)². For distances greater than 40 μm the segregation is governed by the normal Scheil equation and the partition coefficient, k_i , equals 0.299.

Figure 16 shows the segregation behavior for Mo when the original solid was devoid of Mo. The initial solidifying melt has zero percent Mo to begin with and then increases according to Eq. 14, with $\psi = 4.2 \times 10^{-4}$ wt %/(μm)². At distances of 50 μm and larger; significant deviation from the theoretical equation for initial segregation has occurred. The data after a distance of 50 μm could not be suitably fitted to the Scheil equation with a constant k_i , and therefore only the equation for the initial segregation has been plotted.

Cr: The segregation behavior of Cr (Fig. 17) was markedly different from the other alloying elements in the sense that the initial Cr composition of the solidifying melt did not start at zero even though the original solid had no chromium. As such the theoretical curve is plotted using only the Scheil equation with $k_i = 0.5646$ and initial liquid alloy composition of 1.008 wt %.

The fact that the alloy composition of the original solid does not in any way alter the segregation behavior during SD casting would suggest that the radii of Fe and Cr atoms in austenite at the process temperature are approximately the same. The Goldschmidt radii (room temperature atomic radii assuming a coordination number of 12) of Fe and the alloying elements are listed in Table I. On the basis of Goldschmidt radii one would expect that Ni and Co would not show any

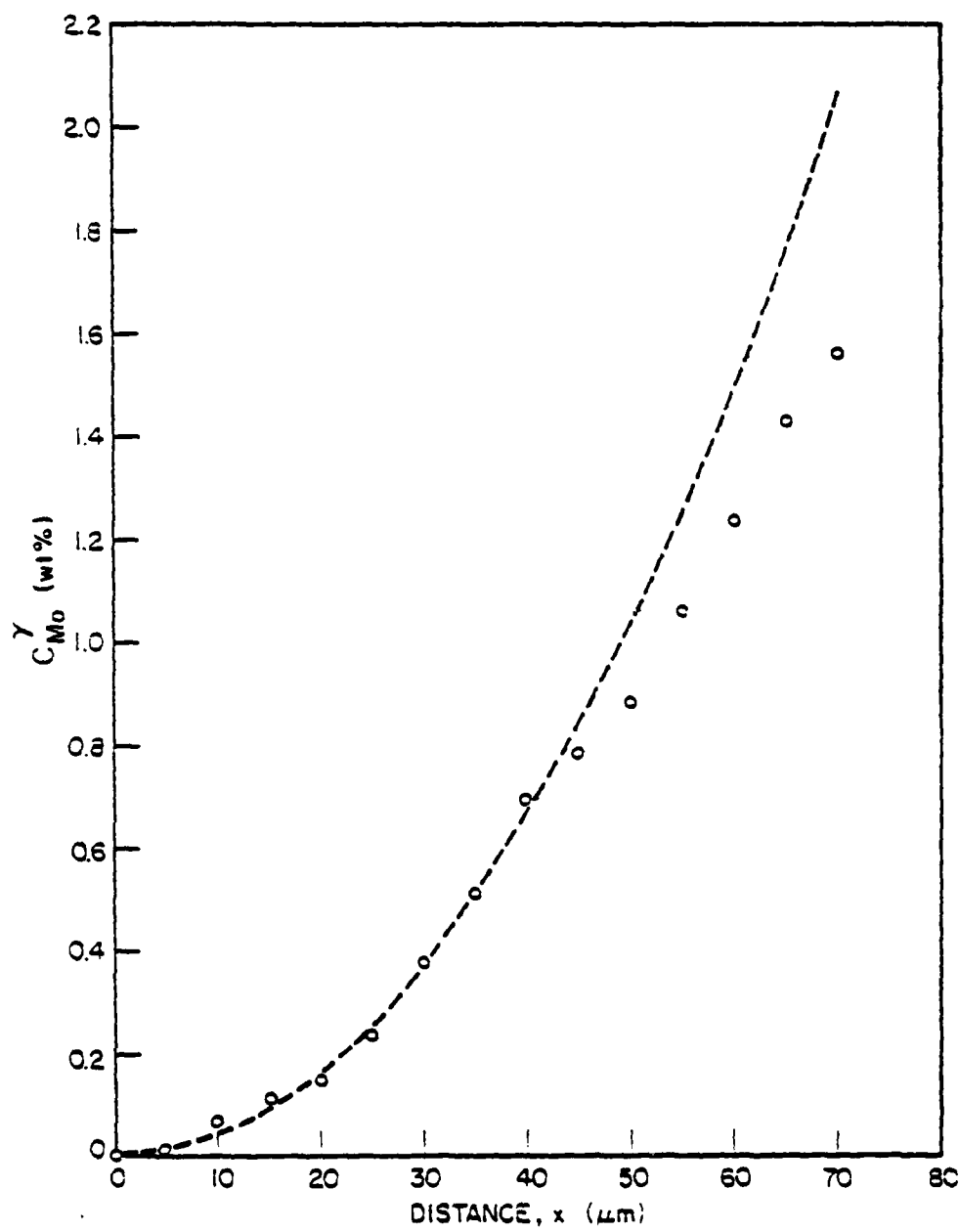


Figure 16. Experimentally measured and empirically fitted composition profiles for Mo segregation. ($C_{Mo}^{\gamma(0)} = 0$ wt %, $C_{Mo}^{L(0)} \approx 0.6$ wt %)

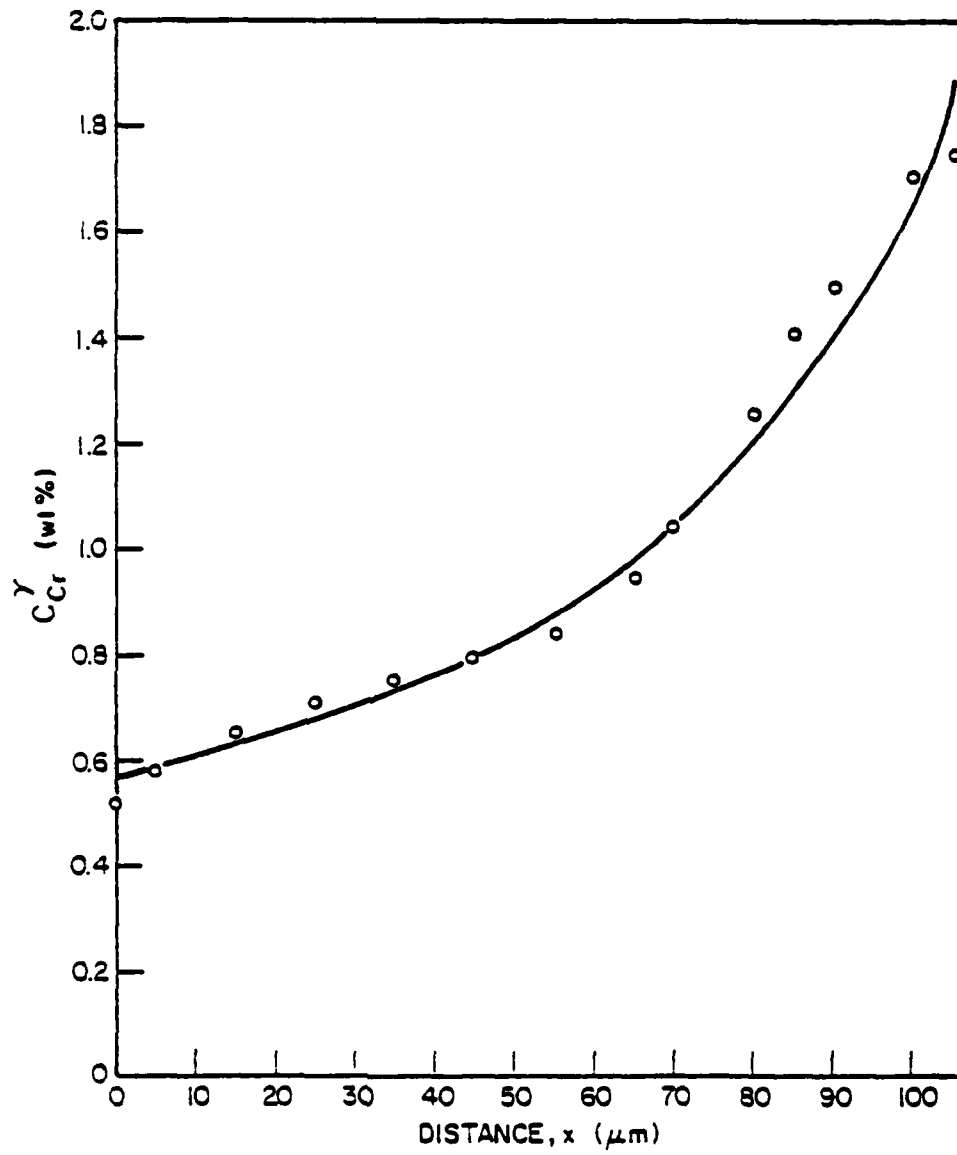


Figure 17. Experimentally measured and empirically fitted composition profiles for Cr segregation. ($C_{Cr}^Y(0) = 0$ wt %, $C_{Cr}^L(0) \approx 1.0$ wt %)

Table I: Goldschmidt Radii of Iron and Common Alloying Elements

<u>Element</u>	<u>Goldschmidt Radii</u>
Fe	1.26
Mo	1.39
Mn	1.35
Ni	1.24
Co	1.25
Cr	1.30

strain energy effects whereas Cr would. It has already been discussed that Goldschmidt radii cannot be used since radii of atoms depend on the crystal structure, temperature and its immediate environment. The studies on the effectiveness of different alloying elements acting as a solute strengthening agent also supports this view. Addition of Cr to ferrite or steels composed of ferrite plus pearlite does not alter their lower yield strength, whereas Ni can increase the lower yield strength of ferrite by 3,000 psi and of steels (ferrite plus pearlite) by as much as 5,000 psi per atomic percent addition (17,18). In contrast, Co should not show strain energy effects since its Goldschmidt radii is close to that of iron. Co, in fact, does not act as an effective strengthener in ferrite (17,18) at room temperature but it showed strong initial segregation in the SD process. Thus the elastic sphere model of atoms using Goldschmidt radii cannot satisfactorily be used to calculate or even qualitatively suggest the strain energy effects of individual atoms when in solution or at a higher temperature.

ψ , in Eq. 14 for the initial segregation behavior, is an adjustable constant and does not have a fixed value even for the same alloy system. Figure 18 shows the initial segregation behavior of Mn, where the initial alloy composition for the original solid was 0.7% Mn and the liquid melt had approximately 3% Mn. The coefficient ψ here has a value of 1.4374×10^{-3} wt %/ $(\mu\text{m})^2$ as compared to 5.74×10^{-4} wt %/ $(\mu\text{m})^2$ for the case for the initial segregation of Mn depicted in Figure 15.

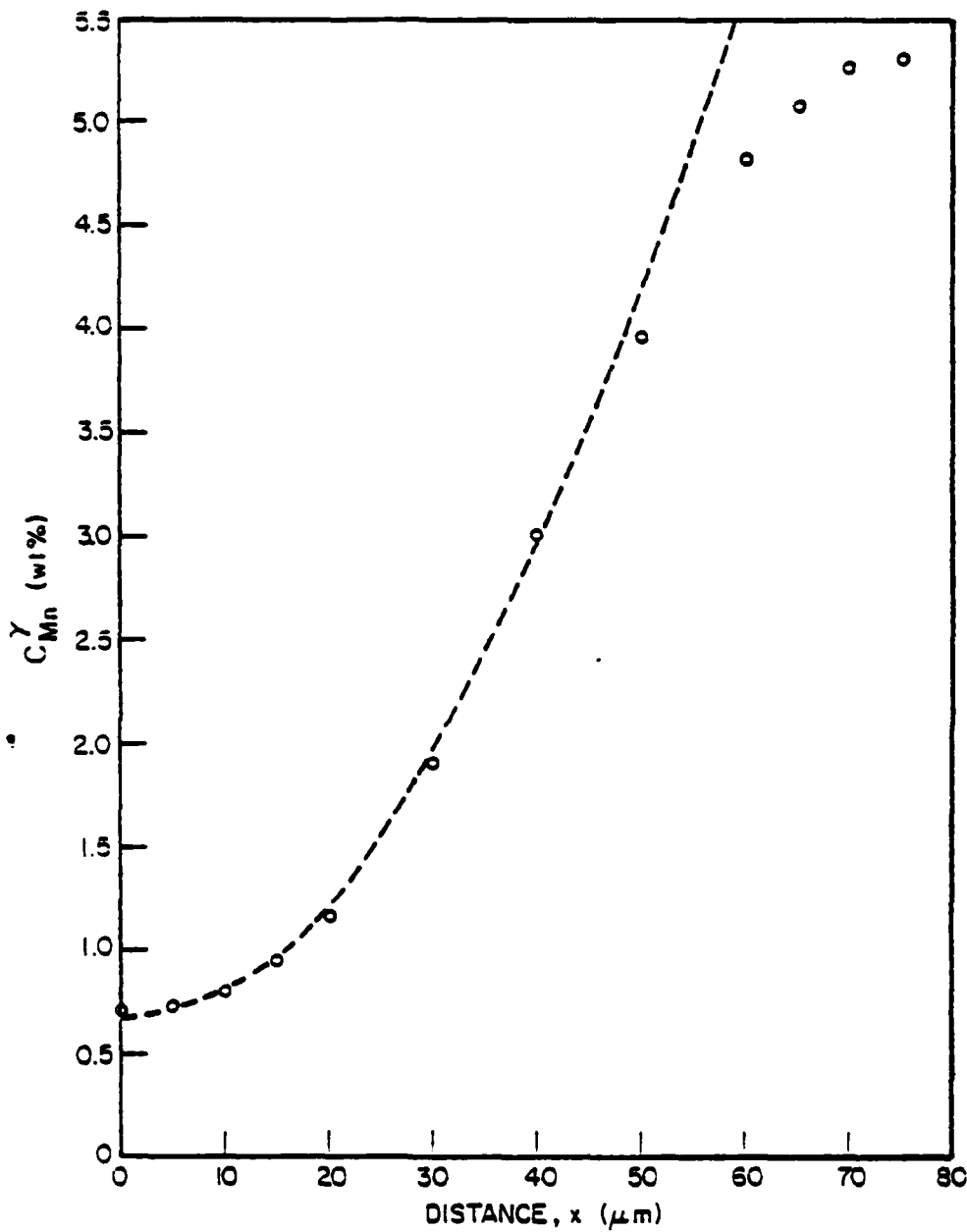


Figure 18. Experimentally measured and empirically fitted composition profile for Mn segregation. ($C_{Mn}^Y(o) = 0.7$ wt %, $C_{Mn}^{L(o)} = 3.0$ wt %)

6.5 CONCLUSIONS:

1. The segregation behavior of common alloying elements in SD cast steels has been studied. The segregation of an alloying element in the solidifying melt can be subdivided into three specific zones:
 - a) Initial segregation, controlled by the alloying element composition of the original solid.
 - b) A transition zone.
 - c) Normal segregation behavior as governed by the equilibrium phase diagram.
2. The initial segregation behavior is controlled by the relative alloying element composition of the original solid and the melt. For the elements Ni, Co, Mn and Mo the first solidifying melt has an alloying element composition which is identical to the composition of the original shot.
3. The initial segregation fits the empirical relationship:

$$C_i^Y = \psi \cdot x^2 + C_i^{Y(0)}$$

where ψ is an adjustable constant.

4. The normal segregation behavior can be predicted by a Scheil type equation. However, the initial segregation behavior controls the location and melt composition at which point normal segregation behavior becomes the dominant mode.
5. The segregation behavior of Cr was found to be an exceptional case, as it did not show an initial segregation behavior.

Cr only showed the normal segregation behavior irrespective of the Cr content of the original solid.

6. The alloying elements which show an initial segregation as controlled by the alloy composition of the original solid (e.g. Ni, Co, Mn, Mo), can be made to segregate either positively or negatively by appropriately choosing the alloy composition of the original solid and the melt.

REFERENCES

1. G. Langford and R. E. Cunningham: Met. Trans. B., 1978, Vol. 9B, pp. 5-19.
2. G. Langford and D. Apelian: J. of Metals, 1980, Vol. 32, No. 9, pp. 26-33.
3. G. Langford: Materials Science and Engineering, 1977, Vol. 25, pp. 275-284.
4. K. G. Davis: Met. Trans., 1971, Vol. 2, pp. 3315-3323.
5. M. C. Flemings, D. R. Poirier, R. V. Barone and H. D. Brody: J. Iron Steel Inst., 1970, 208, pp. 371-381.
6. H. D. Merchant: Recent Research on Cast Iron, H. D. Merchant, ed., Gordon and Breach, New York, 1968, pp. 40-45.
7. J. Charbonnier and J. C. Margerie: Recent Research on Cast Iron, H. D. Merchant, ed., Gordon and Breach, New York, 1968, pp. 391-401.
8. J. S. Kirkaldy, B. A. Thomson and E. A. Baganis: Hardenability Concepts with Applications to Steel, D. V. Doane and J. S. Kirkaldy, eds., TMS-AIME, 1978, pp. 82-125.
9. D. D. VanHorn: Trans. ASM, 1959, Vol. 51, pp. 185-198.
10. J. I. Goldstein and E. Randich: Met. Trans., 1977, Vol. 8A, pp. 105-109.
11. R. F. Sekerka, C. L. Jeanfils and R. W. Heckel: Lectures on the Theory of Phase Transformations, H. I. Aaronson, ed., TMS-AIME, New York, 1975, p. 130.
12. M. C. Flemings: Solidification Processing, McGraw Hill, New York, 1974, pp. 34-36.
13. J. W. Cahn: Acta Met., 1961, Vol. 9, pp. 795-801.
14. J. Friedel: Adv. in Phys., 1954, 3, p. 446.
15. R. A. Swalin: Acta Met., 1957, Vol. 5, pp. 443-448.
16. T. B. Massalski: Physical Metallurgy, R. W. Cahn, ed., North-Holland Publishing Co., Amsterdam, 1965, pp. 163-176.
17. N. S. Stoloff: Fundamental Phenomena in the Materials Sciences, L. J. Bonis, J. J. Duga and J. J. Gilman, eds., Plenum Press, New York, 1967, Vol. 4, pp. 197-245.
18. G. Langford, P. K. Nagata, R. J. Sober, W. C. Leslie: Met. Trans., 1972, Vol. 3, pp. 1843-1849.

APPENDICES

APPENDIX 6A

FRACTION OF LIQUID AS A FUNCTION OF DISTANCE, x, FOR NORMAL SEGREGATION

Figure A1 shows the cross-sectional geometry of the diffusionally solidified zone. Triangle ABC represents the original gap between the two cones in which the melt has been infiltrated. For the microprobe line scan distance, x , is measured across the line O-O' starting at point O (Fig. A1), $x = 0$ at point O. Successive triangles DEF, GHI and JKL represent the area in which liquid is left when the solid liquid interface is at points N (and N'), M (and M') and J respectively. Normal segregation is assumed to start when the solid/liquid interface has reached some point N, i.e. $x_{ns} = ON$. Triangle DEF thus represents the area at which $f_L = 1$ for normal segregation equation to be applicable for distances $x \geq x_{ns}$ (ON).

From geometrical considerations the remanent liquid on an aerial basis at a given point, x , is given by:

$$\frac{(277.8 - 2x)^2}{2 \tan 5^\circ} \pm 0.5\% \text{ (for } x \leq 100\mu\text{m})$$

where x = solidified thickness. As an example, when the solid/liquid interface is at point M, the solidified thickness $x = OM$ and the area of the remaining liquid is GHI which can be calculated using the above expression. The fraction of liquid left, f_L , as a function of distance x for $x \geq x_{ns}$ is then:

$$f_L = \left(\frac{277.8 - 2x}{277.8 - 2x_{ns}} \right)^2 \quad (\text{A-1})$$

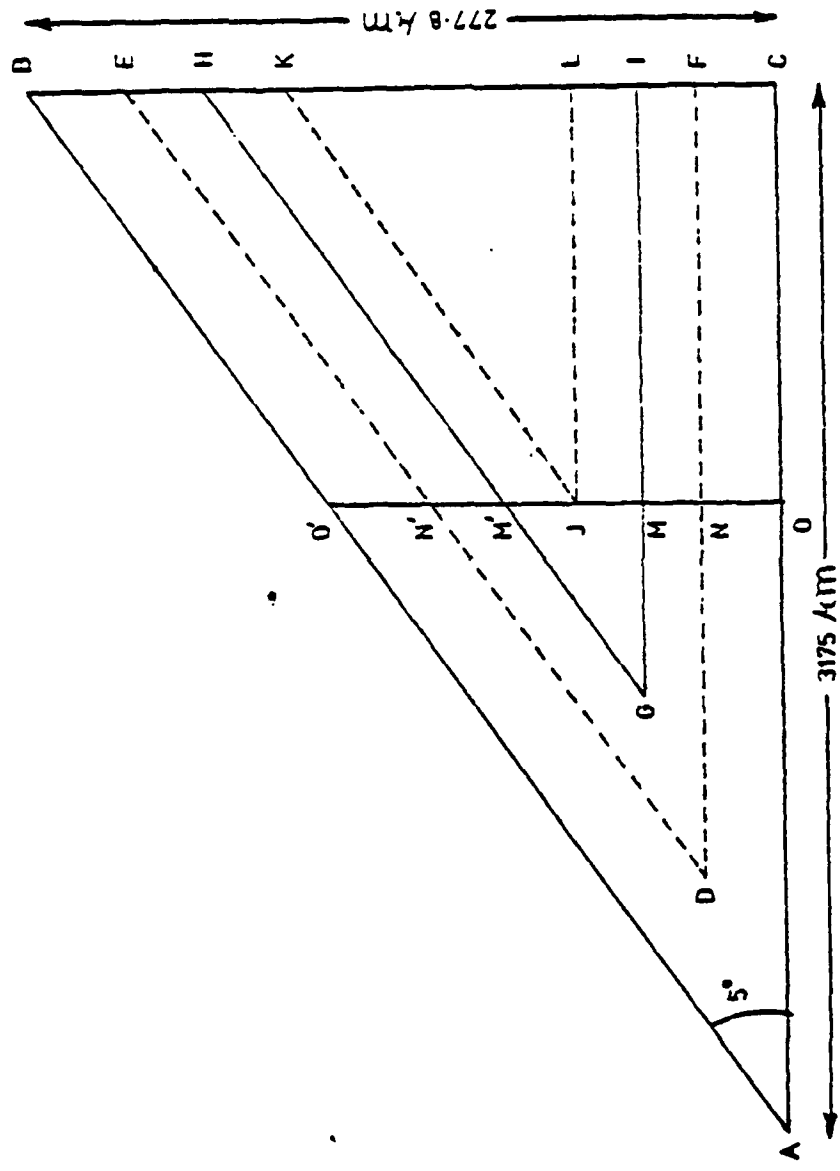


Figure A.1 Cross-sectional geometry of the solidifying melt between two cylinders.

APPENDIX 6B

COMPOSITION vs. DISTANCE DATA

Table B-I: Experimentally measured and calculated compositions for Ni segregation

Distance $x, \mu\text{m}$	Experimental Compositions		Calculated Compositions*
	$C_{\text{Ni}}^Y, \text{wt \%}$	$C_{\text{Ni}}^Y, \text{wt \%}$	
0	0.00	0.000	
5	0.04	0.023	
10	0.12	0.093	
15	0.20	0.209	
20	0.38	0.371	
25	0.62	0.580	
30	0.84	0.835	
35	1.03	1.137	
40	1.09	1.113	
45	1.12	1.100	
50	1.08	1.088	
55	1.08	1.075	
60	1.08	1.061	
65	1.04	1.046	
70	1.04	1.031	
75	1.00	1.014	

$$* C_{\text{Ni}}^{Y(0)} = 0 \text{ wt \%}$$

$$\psi = 9.28 \times 10^{-4} \text{ wt \%}/(\mu\text{m})^2$$

$$k_{\text{Ni}} = 1.106$$

$$x_{ns} = 40 \mu\text{m}$$

$$C_{\text{Ni}}^L (\text{at } x = x_{ns}) = 1.006 \text{ wt \%}$$

Table B-II: Experimentally measured and calculated compositions for Co segregation

Distance $x, \mu\text{m}$	Experimental Composition	Calculated Compositions*
	$C_{\text{Co}}^Y, \text{wt \%}$	$C_{\text{Co}}^Y, \text{wt \%}$
0	0.00	0.000
2	0.01	0.004
4	0.03	0.014
6	0.02	0.032
8	0.05	0.056
10	0.08	0.088
12	0.10	0.127
14	0.18	0.172
16	0.25	0.225
21	0.36	0.388
26	0.63	0.595
31	0.83	0.846
36	1.06	1.140
41	1.10	1.123
46	1.12	1.113
51	1.12	1.103
56	1.07	1.092
61	1.09	1.081
66	1.08	1.069
71	1.08	1.056
76	1.05	1.043
81	1.00	1.028

$$C_{\text{Co}}^{(o)} = 0 \text{ wt \%}$$

$$\psi = 8.8 \times 10^{-4} \text{ wt \%}/(\mu\text{m})^2$$

$$k_{\text{Co}} = 1.084$$

$$x_{ns} = 41 \mu\text{m}$$

$$C_{\text{Co}}^L \text{ (at } x = x_{ns}) = 1.0362 \text{ wt \%}$$

Initial Segregation

Normal Segregation

Table B-III: Experimentally measured and calculated compositions for Mn segregation

Distance $x, \mu\text{m}$	Experimental Compositions		Calculated Compositions*
	$C_{\text{Mn}}^Y, \text{wt \%}$	$C_{\text{Mn}}^Y, \text{wt \%}$	
0	0.00	0.000	
5	0.01	0.014	
10	0.05	0.057	
15	0.13	0.129	
20	0.24	0.230	
25	0.35	0.359	
30	0.46	0.517	
35	0.63	0.703	
40	0.75	0.769	
45	0.83	0.827	
50	0.89	0.893	
55	0.99	0.969	
60	1.09	1.056	
65	1.17	1.158	
70	1.23	1.277	

$$* C_{\text{Mn}}^Y(0) = 0 \text{ wt \%}$$

$$\psi = 5.74 \times 10^{-4} \text{ wt \%}/(\mu\text{m})^2$$

$$k_{\text{Mn}} = 0.299$$

$$x_{\text{ns}} = 40 \mu\text{m}$$

$$C_{\text{Mn}}^L \text{ (at } x = x_{\text{ns}} \text{)} = 2.573 \text{ wt \%}$$

Table B-IV: Experimentally measured and calculated compositions for Mo segregation

Distance $x, \mu\text{m}$	Experimental Compositions	Calculated Compositions*
	$C_{\text{Mo}}^Y, \text{ wt } \%$	$C_{\text{Mo}}^Y, \text{ wt } \%$
0	0.00	0.000
5	0.01	0.011
10	0.07	0.042
15	0.11	0.095
20	0.15	0.168
25	0.24	0.263
30	0.38	0.378
35	0.51	0.515
40	0.69	0.672
45	0.78	0.851
50	0.88	1.050
55	1.06	1.271
60	1.24	1.512
65	1.43	1.775
70	1.56	2.058

* $C_{\text{Mo}}^{(o)} = 0 \text{ wt } \%$

$$\psi = 4.2 \times 10^{-4} \text{ wt } \% / (\mu\text{m})^2$$

Table B-V: Experimentally measured and calculated compositions for Cr segregation

Distance $x, \mu\text{m}$	Experimental Compositions		Calculated Compositions*
	$C_{\text{Cr}}^Y, \text{wt \%}$	$C_{\text{Cr}}^Y, \text{wt \%}$	
0	0.52	0.569	
5	0.58	0.588	
15	0.65	0.629	
25	0.71	0.676	
35	0.75	0.733	
45	0.80	0.800	Normal Segregation
55	0.84	0.883	
65	0.95	0.986	
70	1.05	1.048	
80	1.26	1.201	
85	1.41	1.298	
90	1.50	1.413	
100	1.71	1.724	
105	1.75	1.943	

* $C_{\text{Cr}}^{(o)} = 0 \text{ wt \%}$

$k_{\text{Cr}} = 0.5646$

$x_{ns} = 0 \mu\text{m}$

$C_{\text{Cr}}^L (\text{at } x = x_{ns}) = 1.008 \text{ wt \%}$

7. STRUCTURE AND PROPERTIES OF STEELS CAST BY DIFFUSION SOLIDIFICATION

M. Paliwal
D. Apelian
G. Langford

SUMMARY

The mechanical properties of SD cast steels will depend on the properties of the shot and the subsequently solidified melt. The effect of shot quality on the mechanical properties of the resulting SD casting has been investigated. The accommodation of solidification shrinkage, as the entrapped melt solidifies was also studied. A mechanism for pore formation during SD casting is offered.

TABLE OF CONTENTS: Section 7. Structure and Properties of Steels Cast
by Diffusion Solidification

	<u>Page</u>
7.1 Introduction.	435
7.2 Cavitation Due to Solidification Shrinkage - Literature Review	437
7.3 Experimental Procedure.	442
7.4 Results and Discussion.	445
• Effect of Shot Quality on Casting Ductility.	445
• Peening Shot	445
• Argon Atomized Shot.	451
• Accommodation of Solidification Shrinkage	457
• Ternary Alloying Element as Strengtheners.	463
7.5 Conclusions	464
References	466

7. STRUCTURE AND PROPERTIES OF STEELS CAST BY DIFFUSION SOLIDIFICATION

7.1 INTRODUCTION

An SD casting is basically a composite of pre-cast solid and the later solidifying melt. The resulting mechanical properties of the casting will be controlled by either one of these components. The location and nature of imperfections in the shot and the solidifying melt will thus dictate the initiation of and mode of failure of the resultant casting. The different situations that can arise are:

a) Failure of casting due to melt porosity: The infiltrant or the solidifying melt can form porosity caused by evolving gases or solidification shrinkage. The solubility of gases is higher in liquids than in solids and thus evolution of gases will cause porosity in the solidifying melt unless these constituents are converted to condensed phases (e.g. $\text{Si} + \text{O}_2 \rightarrow \text{SiO}_2$ as in the standard deoxidation reactions in steels).

When the region between three touching spheres (the highest local planar packing for a random packing of spheres) has solidified, feeding of the melt into the casting will be halted. The solidification of the remaining melt left between the shots will lead to solidification shrinkage which has to be accommodated by formation of porosity in the shot, the solidified melt or the remaining melt (unless the casting as a whole deforms plastically to accommodate the solidification shrinkage).

b) Interface weakness: The shot/infiltrant interface can be a spot of local weakness due to two basic reasons:

- i) The shot surface if covered with an oxide scale which is not reduced during the casting process, will result in localized distribution of weakening inclusions. The surface oxides can also act as heterogeneous nucleating sites for evolving gases and thus each shot can be surrounded by pores.
- ii) The alloying elements in the solidifying melt may segregate so that the solid/infiltrant interface has the lowest solute content and therefore can be weaker than both the shot and the last solidifying melt.

c) Failure of shot: The starting shot can have internal porosity or subscale oxides, both of which can cause the shot to fail first. Also the initial carbon concentration is necessarily low to maximize the degree of diffusion; approximately 0.01 to 0.1 wt % carbon. As the diffusion process proceeds the carbon concentration of the shot is increased by at least ten fold, i.e. from 0.1 to 1.0 wt % carbon. The increased carbon content of the shot implies that the shot will be supersaturated with respect to oxygen; CO evolution is unlikely due to the difficulty of forming a pore within the shot. During the later stages of solidification when large tensile stresses are developed; the inclusions in the shot and the tendency for CO evolution may result in preferential porosity formation within the shot to accommodate the

solidification shrinkage.

Langford and Cunningham (1) have shown that the ductility of SD castings is strongly dependent on the total oxygen content of the casting. For economic reasons one would like to know if low quality high oxygen content shot can be utilized for SD castings, thus the need to establish the effect of shot quality on the mechanical properties of the resultant casting. On the other hand, if one utilizes high quality shot having a low oxygen content and no porosity; then the quality and resulting properties of the SD casting will solely be governed by the infiltrant melt in terms of the solidification shrinkage involved.

The central focus of this work has been to establish:

- i) The effect of shot quality on the ductility of the resulting casting.
- ii) The location and mechanism of accommodation of solidification shrinkage.

7.2 CAVITATION DUE TO SOLIDIFICATION SHRINKAGE - LITERATURE REVIEW:

Once the throat area formed by three touching shot particles (location of highest local planar packing) has been frozen shut, solidification of the remaining trapped liquid will cause large negative pressures to develop. These negative pressures (hydrostatic tensile stresses) can be accommodated by cavity formation in the solid or liquid. Assuming that homogeneous nucleation of a cavity is not possible an absence of impurities (nucleating sites) in the shot and liquid should lead to the plastic deformation of the casting as a whole. The infiltrated melt will, in the later stages of solidification, exist as isolated

liquid pools and as such heterogeneous nucleation sites at a number of locations will not be available. Homogeneous nucleation of cavities is unfavorable since the Fe-C melt has a high surface tension and a low vapor pressure.

The presence of dissolved oxygen in the melt is however inevitable and the question of CO bubble nucleation under large negative pressures must be considered. Though both homogeneous and heterogeneous gas bubble/cavity formation mechanisms have been proposed, there is no general agreement on the subject. If homogeneous nucleation of a gas bubble is not possible in the system, the use of deoxidizers in the melt is not recommended since the secondary deoxidizing products will serve as heterogeneous nucleating sites. On the other hand, if it is possible to nucleate gas bubbles or cavities homogeneously the use of deoxidizer can only serve to change the location and shape of porosity formed in the casting.

Hirschfield and Weinberg (2) solidified pure iron containing various amounts of dissolved oxygen, under supercooling of up to 216°C but found no decrease in the total porosity of the casting. In fact for the same oxygen levels they report an increase in the porosity of the casting with increased degree of supercooling. Unless one were to assume that some impurities were present in the melt which selectively act as nucleating sites for pores but not for solid iron; the results suggest that pores can be formed homogeneously.

The possibility of eliminating or suppressing porosity in a casting requires the comparison of two different pressure terms:

- i) The negative pressure within the liquid required to form a pore or cavity homogeneously.
- ii) The negative pressure within the isolated liquid pools which will exceed the yield strength of the surrounding solid shell and thus cause the casting as a whole to plastically deform accommodating the solidification shrinkage.

If the negative pressures required to render the casting in a plastic state are less than the pressures required to nucleate a pore homogeneously, formation of pores can be suppressed in a casting completely, at least theoretically.

The negative pressure required for the formation of a pore of critical size in a liquid has been calculated by Fisher (3). The tensile strength of a liquid or the negative pressure for formation of a stable pore accordingly is given by (3):

$$P_L = - \left[\frac{16\pi \gamma_{LV}^3}{3(EKT \ln(\frac{NkT}{h}) - \Delta f_0^*)} \right]^{1/2} \quad (1)$$

where: T = temperature, °K

γ_{LV} = surface tension

k = Boltzman's constant

N = Avogadro's number

h = Planck's constant

Δf_0^* = activation free energy for a molecule motion into or away from the pore surface.

Campbell (4) has evaluated the negative pressures that are required to render a spherical casting plastic due to the negative pressures in the entrapped melt. The negative pressure in the liquid, P_L , for a spherical casting of radius b when the radius of solid/liquid interface is equal to a , is given by:

$$P_L = P_{atm} + \frac{2\gamma_{SL}}{a} + \frac{2\gamma_{SV}}{b} - 2Y \ln\left(\frac{b}{a}\right) \quad (2)$$

where: P_L = Pressure in the liquid pool

P_{atm} = Atmospheric pressure

γ_{SL} = solid/liquid surface tension

γ_{SV} = solid/vapor surface tension

Y = Yield strength of the solid metal at the melting point

b = radius of solidifying sphere

a = radius of solid/liquid interface

For $b = 1$ cm, where b corresponds to the radius of solidifying sphere or the half distance between isolated liquid pools in a casting; the minimum pressure that can be attained in the entrapped liquid pool is approximately -1400 atmospheres (4). Using Fisher's formula (3) for fracture strength of liquids (Eq. 1), Campbell (4) estimated the tensile strength of liquid iron as -70,000 atmospheres. Hence, it would seem that homogeneous nucleation of cavities in entrapped regions of liquid iron in a casting is most unlikely.

One cannot however, disregard the presence of dissolved oxygen in the melt which will have an effect on the mechanism of pore formation. Levine (5) has considered the homogeneous evolution of CO in Fe-C-O

melts, and takes into account the surface active properties of oxygen. In obtaining the reversible work required to form a vapor nucleus, Levine's analysis takes into account the electrostatic work involved in forming oxygen ions (O^-) as a chemiabsorbed layer at the liquid/vapor interface; thus the Laplace equation for mechanical equilibrium for the pore is modified to (5):

$$P_L - P_g = \frac{2(\gamma_{LV} - \sigma_o)}{r^*} \quad (3)$$

where: P_L = pressure in the liquid melt

P_g = gas pressure inside the pore

r^* = critical radius for the pore

γ_{LV} = surface tension of the melt

σ_o = electrostatic energy density of the surface

region; depends on the oxygen content of the melt.

Taking into account the effect of dissolved oxygen on the fracture strength of liquids, Fisher's formula can be modified to:

$$P_L = - \left[\frac{16\pi(\gamma_{LV} - \sigma_o)^3}{3(kT \ln(\frac{NkT}{h}) - \Delta f_o^*)} \right]^{1/2} \quad (4)$$

σ_o , the electrostatic energy density of the surface region (at the pore) is a function of temperature and the dissolved oxygen content of the melt. When σ_o is approximately equal to γ_{LV} (at some critical concentration of dissolved oxygen), there is no barrier to homogeneous nucleation (5), and thus formation of porosity will occur spontaneously without the requirement of high tensile forces in the melt. For iron melt, at 1823°K, Levine estimates the critical dissolved oxygen content of the melt ($\sigma_o = \gamma_{LV}$) as 0.001 to 0.003 wt % (5).

Thus even if one were to start with liquid iron containing as low as 3 ppm of dissolved oxygen, cavities can form homogeneously when the fraction of solid exceeds 0.9. In view of the above it seems impossible to suppress the formation of cavities in SD castings. If deoxidizers are used in the melt to keep the dissolved oxygen concentrations low, the secondary inclusions can act as heterogeneous nucleation sites for cavities either in the liquid melt or in the solid near the solid/liquid interface.

7.3 EXPERIMENTAL PROCEDURE:

The assembly of the shot, particle valve, and melt charge is shown in Figure 1. The heating and casting procedures are essentially the same as in the experiments conducted for microsegregation studies using cones (see Chapter 6). As such in this section only the differences in process parameters (material, length of casting, infiltration pressure, holding time, etc.) are listed.

Shot: Two different kinds of shot were used: i) decarburized peening shot in the 20-25 mesh (0.071 to 0.085 cm) size range and ii) argon atomized shot in the 25-30 mesh (0.06 to 0.071 cm) size range. Quality differences of these shot particles are discussed in detail in the subsequent section.

Melt: Two different melts were used to which different alloying elements were added.

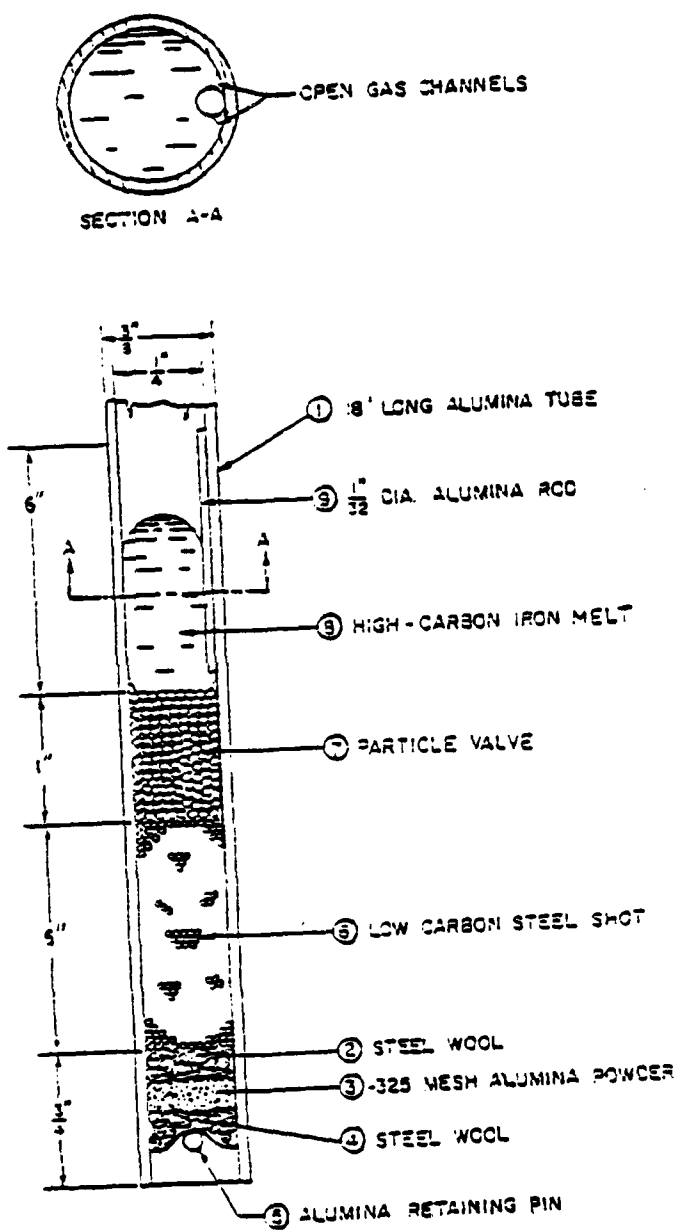


Figure 1. Mold arrangement for making 0.25" diameter by 5" long SD cast pins. Circled numbers indicate sequence of assembly. (Mold logic based on Ref. (1).)

Melt A: Fe-2.2 wt % C

Melt B: Fe-2.2 wt % C, 0.74 wt % Mn, 0.17 wt % Si
and 0.01 wt % Al.

Process Temperature: 1372°C

Length of Casting: 5 inches

Infiltration Pressure: 80 psi gauge for 20-25 mesh (0.071 to
0.085 cm) particles; 100 psi gauge for 25-30 mesh
(0.06 to 0.071 cm) particles.

Holding Time: 15 minutes (time at process temperature after
melt infiltration)

Heat Treatment: The cast product was sectioned for microstructural analysis and mechanical testing of heat-treated specimens. The as cast samples were heated to 1150°C (kept at temperature for 15 minutes), quenched in a salt bath maintained at 400°C for 15 minutes and then air cooled to room temperature. The samples were then austenitized at 800°C for 30 minutes, water quenched and then tempered at 600°C for 30 minutes. Tensile test specimens (gauge length = 1.0 inch, diameter = 0.16 inches), machined from the heat treated samples, were retempered at 600°C for an additional 30 minutes. Subsequently, the samples were tested in tension at a strain rate of 0.01 min^{-1} .

7.4 RESULTS AND DISCUSSION*:

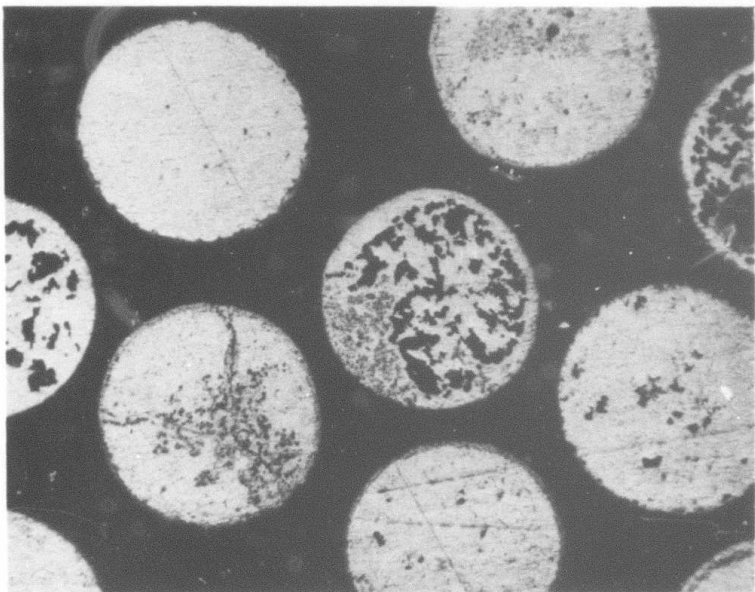
Effect of Shot Quality on Casting Ductility:

Peening Shot: The peening shots were produced by water atomization and were thus heavily oxidized. In addition, the peening shot contained high concentrations of carbon, silicon and manganese. The peening shot was decarburized using CO/CO₂ mixture at 1000°C. Figures 2a and 2b show the cross-section of the decarburized particles. The particles are free from porosity however the extent of decarburization varies from one particle to another. While large concentrations of carbon are evident in some particles (Fig. 2a) others are devoid of carbon and exhibit the formation of subscale inclusions (Fig. 2a and 2b). The oxide scale, in particles which have residual carbon, will be reduced by SSVCD (solid state vacuum carbon deoxidation) (1), as the shot is heated up to the process temperature under vacuum. In contrast, the oxide scale will not be reduced in particles which are devoid of carbon.

Figure 3 shows the microstructure of a casting made with heavily oxidized peening shot (carbon < 0.01 wt %, 0.8 - 0.86 wt %) in which some particles are completely delineated from the matrix. The resulting castings under tensile loads failed without showing any plastic deformation. In the fractograph (Fig. 4) one can see that the fracture surface followed the easy path provided by the porosity and oxides at the solid/

*In castings made with Fe-C, Fe-C-Al melts the shot and the later solidifying melt could not be clearly identified. As such, unless otherwise stated, the microstructures shown and the reported % elongations are for castings made with melt B.

(a)
Nital etch
Mag. 50X



(b)
Nital etch
Mag. 100X

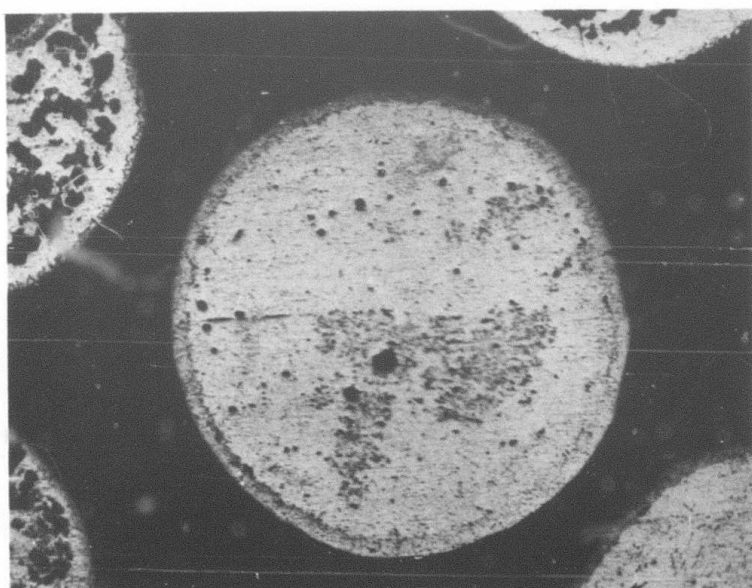


Figure 2. Micrograph of peening shot showing uneven decarburization and formation of subscale oxide inclusions.

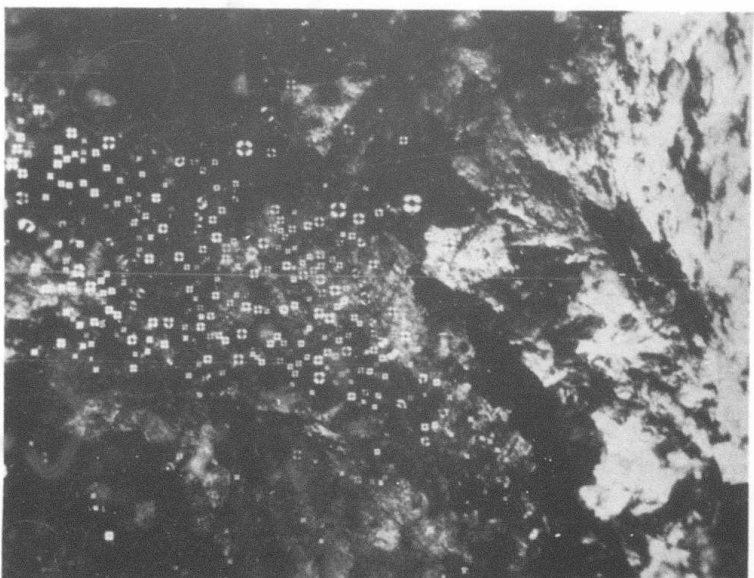
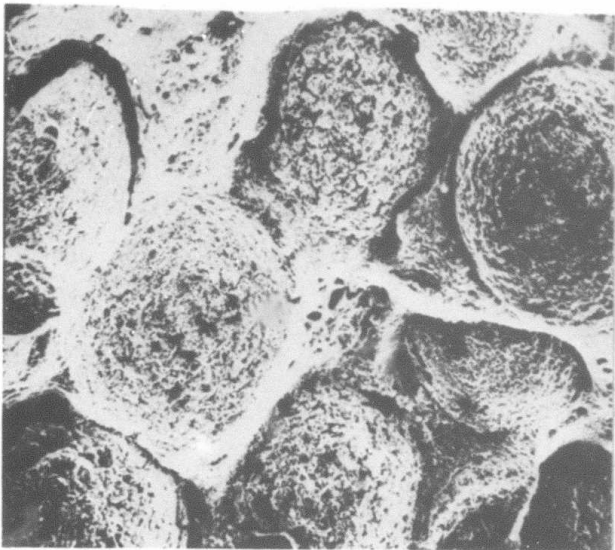


Figure 3. Microstructure of casting made with peening shot showing delineation of the shot at the shot/infiltrant interface.

(a)
Mag. 100X



(b)
Mag. 500X

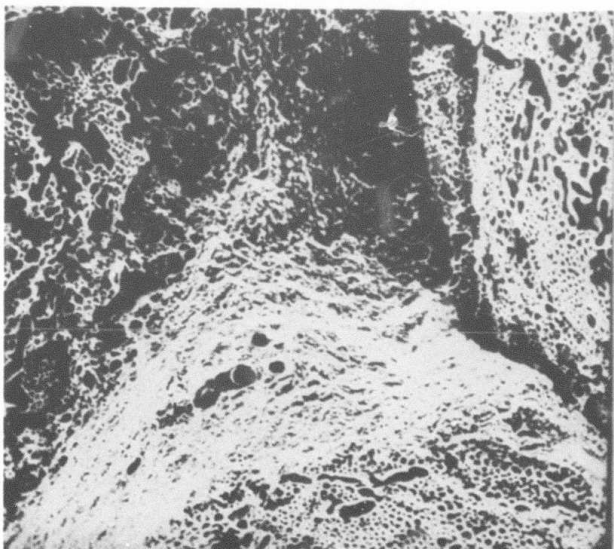
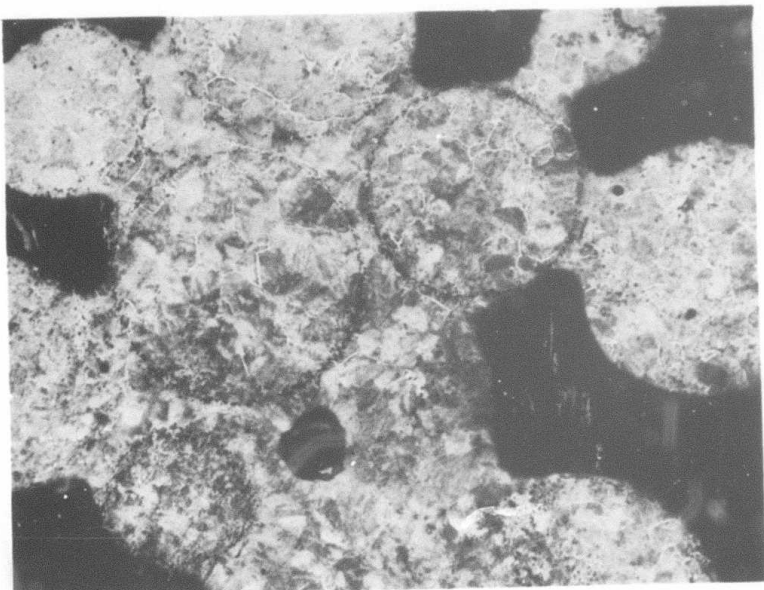


Figure 4. Fracture surface of heat-treated SD casting made with peening shot, showing failure starting at the shot/infiltrant interface.

infiltrant interface. Referring to Fig. 3a one can note that the particle in the upper left hand corner which is completely delineated from the matrix shows no porosity inside the particle, whereas other particles show considerable amount of porosity. This could have only been possible if the tensile stresses due to solidification shrinkage were essential for the formation of pores within the particle. Since the particles have high oxygen content these can form due to CO evolution also, but if CO evolution was possible within the particles without high negative pressure, the particles with obviously higher oxygen content (the delineated particles) should have also shown porosity within the particles.

To check if the negative pressures developed during the solidification process contributed to the formation of porosity in the shot, the experiments were repeated with the same quality peening shot (carbon < 0.01 wt %, oxygen = 0.8 to 0.86 wt %) but the melt was decanted before solidification was complete. Since the melt had been decanted before feeding channels were blocked off, the partially solidified casting will not show any porosity caused in accommodating solidification shrinkage. Figures 5a and 5b show the micrograph of the resultant partially solidified casting. The casting showed formation of small, unconnected pores caused by CO evolution at the solid/infiltrant interface. However, there were no particles in the casting which were completely delineated from the later solidified melt or showed large pores within the particles. It can be concluded, therefore, that the complete delineation of particles and void formation within the shot

(a)
Nital etch
Mag. 50X



(b)
Nital etch
Mag. 200X



Figure 5. Microstructure of partially solidified SD casting (the melt was decanted following infiltration) showing porosity formation at the shot/infiltrant interface.

occurred under the influence of negative pressures developed due to solidification shrinkage.

Castings made with peening shot of lower oxygen content (carbon < 0.01 wt %, oxygen ≈ 0.16 wt %) did not show delineation of the shot at the shot/infiltrant interface (Fig. 6), but the interior of the particles showed that large size pores had evolved during the solidification process (Figs. 6a and 6b). The resulting castings showed only limited ductility (total elongation ≈ 6.5%). The fractograph (Fig. 7) shows that the shot failed first but the fracture occurred through the shot as compared to the failure at the shot/infiltrant interface.

Argon Atomized Shot: The Ar atomized shots were much cleaner and lower in oxygen content (carbon < 0.01 wt %, oxygen < 0.015 wt %). The particles were free of large oxide inclusions or CO evolved porosity except that some had large centralized pores caused due to entrapment of the atomizing gas, Ar (Fig. 8). The microstructures of the casting, made from the atomized shot, are shown in Figs. 9 and 10. Some of the shots had large centralized pores, but these are not shown since they obviously pre-existed in the starting shot. No pores were observed at the solid/infiltrant interface or just below the shot surface. The only porosity caused in the shot and believed to have occurred during the SD process is the evenly distributed small size pores in the middle of the shot (Fig. 10). It cannot be conclusively proven that these did form during the SD process, but no centralized small pores were observed in the atomized shot, and hence the conclusion. The pores formed in the shot however are much smaller in comparison to the pores formed in the last melt to freeze, which can also be seen in Fig. 10.

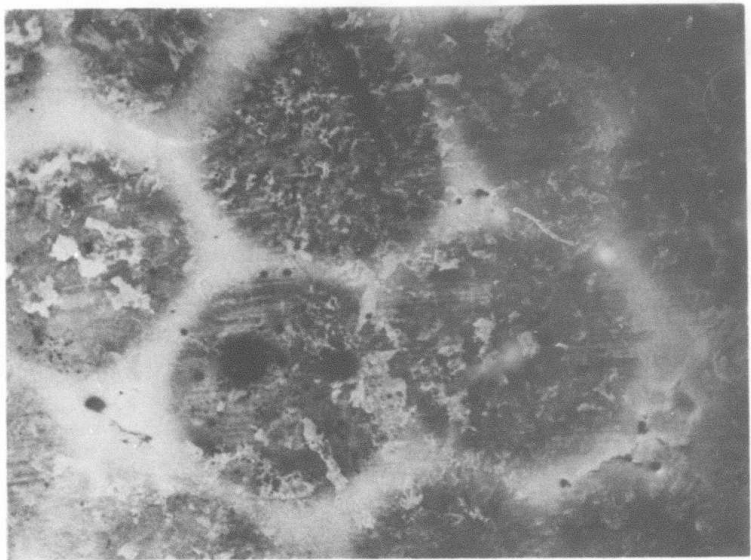
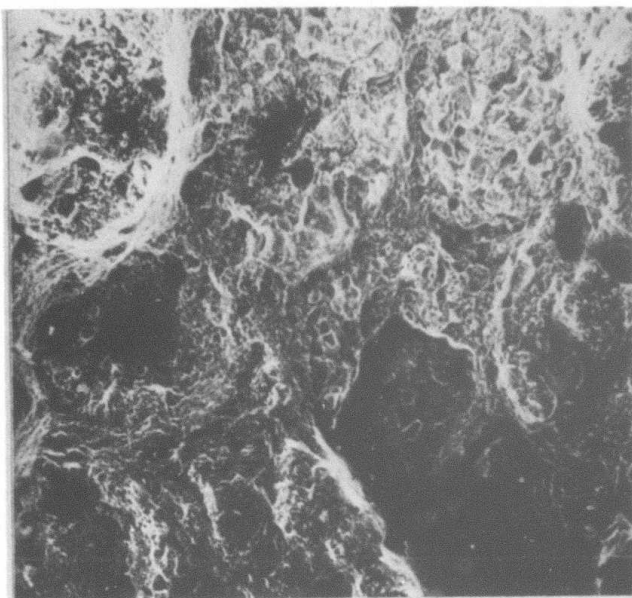


Figure 6. Microstructure of SD casting made with peening shot, showing porosity formation within the shot under the influence of the tensile stresses due to solidification shrinkage.
(Melt: melt A + 1.0 wt % Mo.)

(a)
Mag. 100X



(b)
Mag. 200X

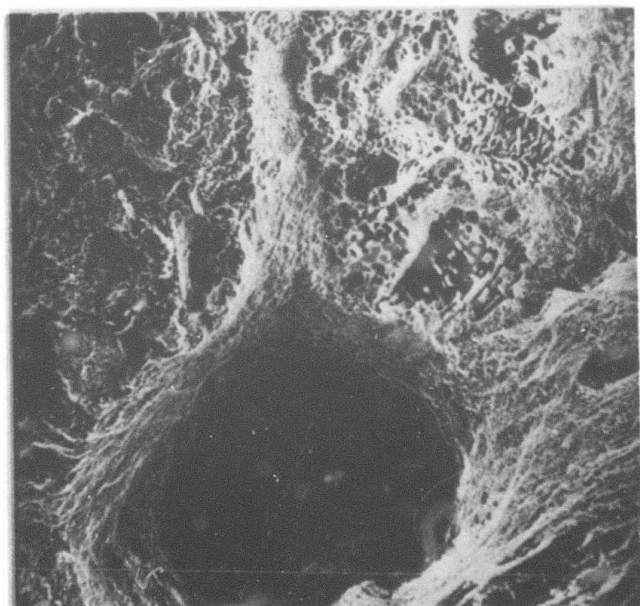


Figure 7. Fracture surface of heat treated casting, made with peening shot, showing failure of the shot and the solidified melt. The fracture started through the shot as compared to fracture starting at the shot/infiltrant interface, Fig. 4.

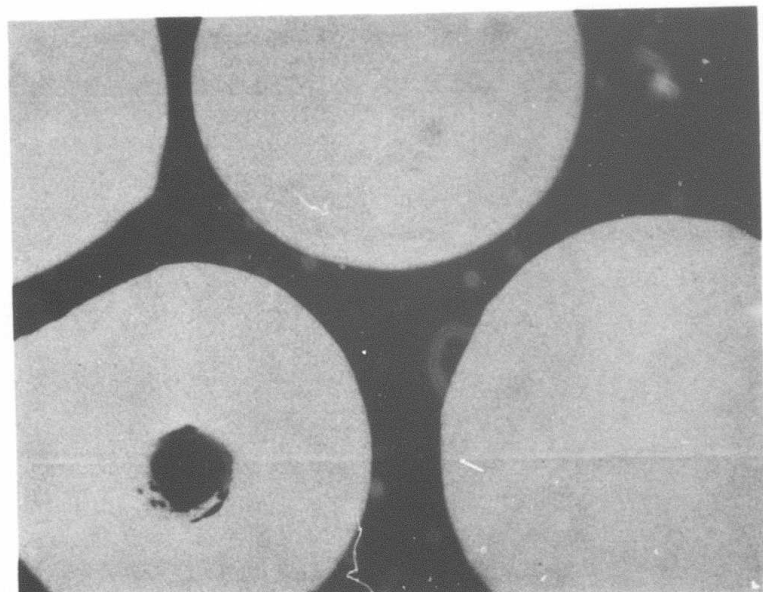


Figure 8. Argon gas atomized iron shot. Mag. 100X.

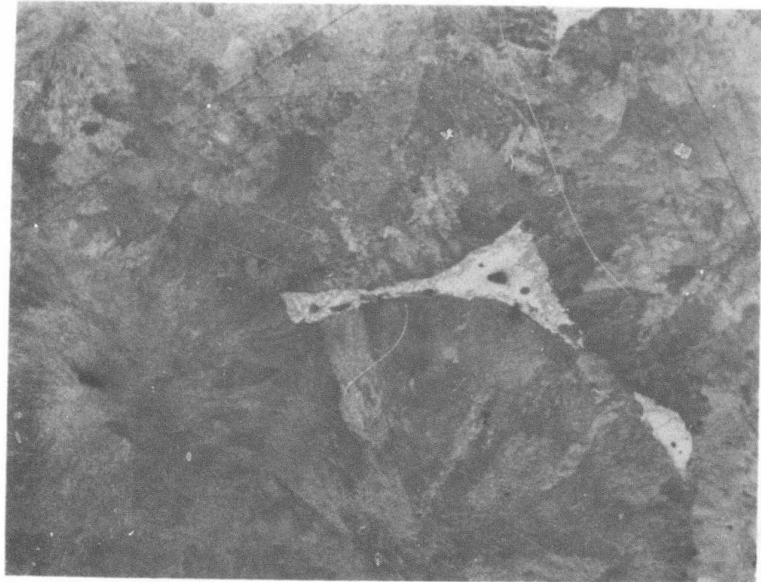


Figure 9. Microstructure of SD casting made with argon atomized iron shot. Formation of porosity in the last solidifying melt can be seen but the shot/infiltrant interface cannot be identified. (Melt: melt B + 1.0 wt % Mn). Nital etch; Mag. 100X.

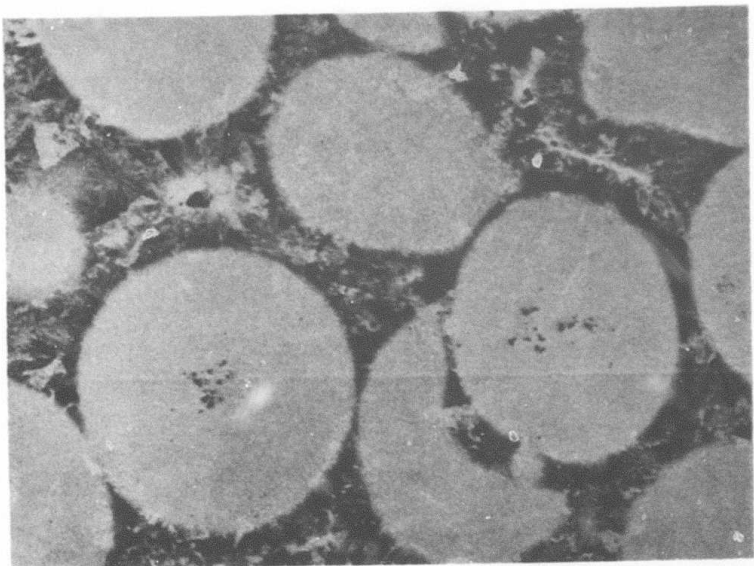


Figure 10. Microstructure of SD casting (made with argon atomized alloyed iron shot) showing shot, solidified melt and porosity in the solidified melt. Nital etch, Mag. 50X.

The castings made with argon atomized shot showed higher ductility (average elongation of 12%) than the castings made from the peening shot and the fracture surface was more uniform (Fig. 11).

Accommodation of Solidification Shrinkage:

In the castings made from the low quality peening shot, part of the solidification shrinkage is accommodated by formation of pores in the shot. Feasibility of making 100% dense castings would require use of porosity free high quality shot and the ability to suppress cavity formation in the melt. The results of the castings made with argon atomized shot indicate that suppression of cavity formation is not possible. When deoxidizers were used in the melt, large size irregular pores were always found located in the region of the last solidifying melt (Fig. 10). Figure 12 shows a region, from the same casting, where the mechanism of cavitation can be identified. The micrograph clearly shows that the solid adjacent to the solid/liquid interface fractured under the influence of the large negative pressures (due to the solidification shrinkage). In contrast, to the irregular pores formed in the last solidifying region (Fig. 12), a melt region which has solidified before large negative pressures develop does not contain any porosity (Fig. 13).

The following mechanism of pore formation, as sequentially occurring events is proposed:

- 1) Once the feeding of the melt has been choked off, further solidification causes negative pressures to develop within the melt. The negative pressures can be relieved by formation

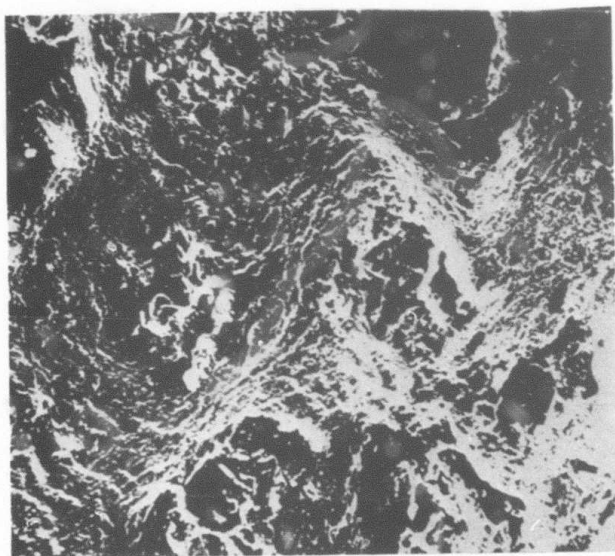


Figure 11. Fractograph of heat treated SD casting made with argon atomized iron shot. Mag. 100X.

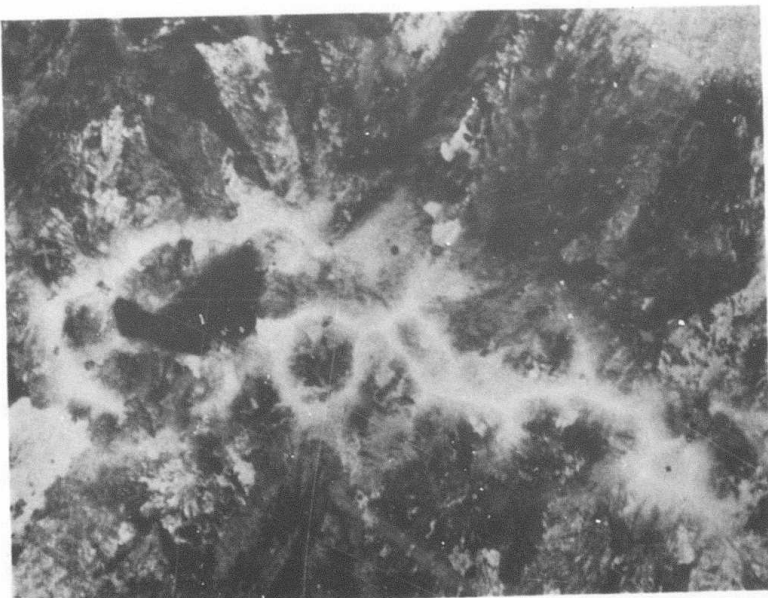
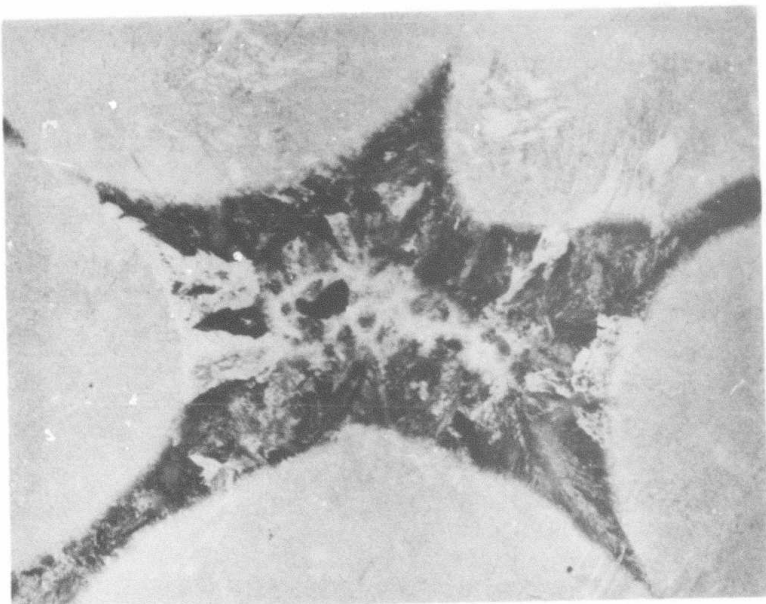


Figure 12. Formation of shrinkage caused porosity in the last solidifying melt. (Same casting as shown in Fig. 10.)



Figure 13. Microstructure of SD casting made with argon atomized shot showing region of solidified melt with no porosity. (Same casting as shown in Figs. 10 and 12). Nital etch, Mag. 200X.

of a pore in the melt. However, if no pores are formed in the melt, the solid at the solid/liquid interface fractures under the influence of these negative pressures.

- ii) The melt adjacent to the solid/liquid interface flows into the formed cavity thereby increasing the negative pressures and causing further tearing of the solid.
- iii) The negative pressures continue to increase until formation of a stable (critical size) pore takes place. Once a pore has been formed in the melt, it can grow spontaneously and relieve the negative pressures. The remaining melt thus flows out leaving behind the irregular type of pore seen in Fig. 12.

When a pore is formed in the melt during the early stages of solidification, no tearing of the already solidified melt will take place. The resulting pore will still be located in the last melt to freeze but will be spherical in shape (Fig. 14). The spherical pores were observed, when deoxidizers (Si, Mn, Al) were not used in the melt and also in castings made from peening shot (high oxygen content in shot). The spherical shape of the pore suggests that evolution of CO occurred during the early stages of solidification. The solidification shrinkage was then accommodated by expansion of the pore.

Probable causes for early formation of a CO bubble are:

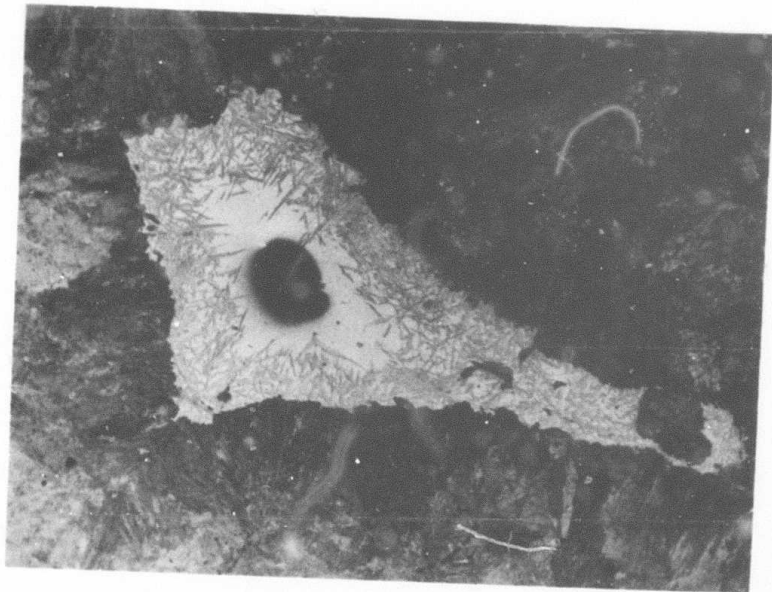


Figure 14. Spherical pore in the last solidifying melt of casting made with peening shot. (Melt: melt B + 1 wt % Mn). Nital etch, Mag. 100X.

- 1) When no deoxidizers are present the dissolved oxygen content of the melt increases rapidly as solidification proceeds. Since CO evolution can occur homogeneously (see theoretical section) at levels of dissolved oxygen as low as 0.001 wt % there was no barrier for cavity formation.
- 2) The peening shot has a high oxygen content. If the liquid is superheated, it will partially remelt the shot or attack the surface oxides on the shot. The sudden increase in the oxygen content of the melt will result in CO evolution.

Ternary Alloying Elements as Strengtheners:

In the previous chapter dealing with segregation of alloying elements it was pointed out that strongly segregating elements can be used to preferentially strengthen the volume around the pore, i.e. the last melt to freeze. However, addition of alloying elements to the melt will affect the mechanical properties of the resultant casting only when the fracture starts from the pores formed in the solidifying melt. In castings made from peening shot, fracture was shown to have started by failure of the shot or the shot/infiltrant interface. Addition of 1 wt % alloying elements (Mo, or extra Mn) to the melt in fact did not change the ductility (measured as total % elongation to fracture) of the resultant casting.

In contrast, the shot in castings made from the argon atomized shot was relatively defect free. Fracture therefore would initiate from the pores formed in the last melt to freeze. The ductility of

the casting, hence, can be improved by addition of alloying elements to the melt. Addition of extra 1 wt % Mn to the melt in castings made from argon atomized shot fractured at a 16% elongation (as compared to 12% elongation for castings made with the basic melt).

7.5 CONCLUSIONS:

- 1) It has not been possible to suppress cavitation in the solidifying melt. The porosity due to solidification shrinkage is isolated and occurs in the last melt to freeze.
- 2) When deoxidizers are used, CO evolution is suppressed, and the resulting porosity is irregular in shape and is found in the region of the last melt to solidify.
- 3) When CO evolution occurs during the early stages of freezing the resulting porosity (added effect of solidification shrinkage) is spherical in nature but is still found in the last melt to freeze.
- 4) Castings made with low quality peening shot show lower ductility, and fracture starts by failure of the shot/infiltrant interface or of the shot itself. The ductility of the resulting casting cannot therefore be improved by addition of alloying element to the melt.

- 5) In castings made from high quality low oxygen shot, failure starts from the pore in the last melt to freeze. The ductility of the casting can be improved by strengthening of the volume around the pore via ternary alloying element additions to the melt.

REFERENCES

1. G. Langford and R. E. Cunningham: Met. Trans. B., 1978, Vol. 9B, pp. 5-19.
2. D. A. Hirschfeld and F. Weinberg: Met. Trans., 1978, Vol. 9B, pp. 321-322.
3. J. C. Fisher: Journal of Applied Physics, 1948, Vol. 19, pp. 1062-1067.
4. J. Campbell: Trans. TMS-AIME, 1967, Vol. 239, pp. 138-142.
5. H. S. Levine: Met. Trans., 1973, Vol. 4, pp. 777-782.

CHAPTER 8

ECONOMIC MODEL FOR A RAPID CYCLE STEEL CASTING
PROCESS USING DIFFUSION SOLIDIFICATION

by

George Langford

SUMMARY

A new process such as steel casting by diffusion solidification (SD) is not easy to compare with older, competing processes such as investment casting, machined wrought steel, forged steel, etc. without the benefit of a long period of development via trial-and-error and detailed engineering design. In order to compensate for this handicap, the present work develops an economic model for process of making cylindrical 1 wt. pct. steel castings by SD which considers the process-sensitive costs of raw materials, process heat, machining, and capital. Optimization techniques are used to calculate the lowest total costs for 1000 annual metric tons of these SD casting as functions of process parameters, variable (i.e. uncertain) process constants, and the process variables. The results indicate that the process conditions assumed and/or used in the experimental phase of the ongoing research on the SD process are consistent with the optimal parameters and variables developed by use of the economic model. In all cases the cost of the raw material - mostly atomized low carbon steel shot - is the paramount process parameter to which the most attention needs to be paid to reduce total costs in any future research. There is substantial flexibility in the choice of casting sizes, (higher raw material costs dictate that we make smaller castings of optimal size); that is, there is a modest cost penalty compared to total process costs for making castings as much as three times smaller or larger than the optimum length. The process-related costs contribute least to the total costs of making SD castings from relatively expensive shot, indicating that the most economic advantage to be gained is in the field of premium quality or high alloy steel castings.

Table of Contents: Section 8. Economic Model for a Rapid Cycle
Steel Casting Process Using Diffusion Solidification

	<u>Page</u>
8.1 Introduction	468
8.2 Assumed Process Logic	468
8.3 Process Costs	470
8.4 Detailed Calculations	471
8.4.1 Raw Materials	471
a. Shot	471
b. High Carbon Iron	473
c. Mold Material and Particle Valve	474
d. Total Raw Material Costs	474
8.4.2 Capital and Operating Costs	474
a. Casting Furnace	474
b. Pressure Vessel	479
c. Machining Costs	480
8.4.3 Constraints	481
a. Infiltration Pressure	481
b. Particle Size and Particle Size Range	483
8.5 Computations	483
8.6 Discussion of the Results of the Computations	485
8.6.1 Costs	485
8.6.2 Variables, Parameters, and Variable Constraints	486
8.7 Conclusions	488

CHAPTER 8

Economic Model for a Rapid Cycle Steel CastingProcess Using Diffusion Solidification8.1 Introduction

In this chapter, an economic model is developed in order to make an estimate of the yearly cost of producing 1000 metric tons (10^6 kg) of steel castings by diffusion solidification^(1, 2). This exercise is mainly intended to identify the most important process parameters and variables by dimensional analysis. Although it is still too early to make a one-for-one comparison of these hypothetical costs to those of well-established alternative processes, optimization techniques are used here to substitute a rational design for invaluable and unassailable experience already gained with competitive processes. Every tangible cost is treated as explicitly as possible in this abstract treatment of a casting of unspecified size and simple shape in order that constructive criticism and informed further development of the diffusion solidification casting process are both expedited.

8.2 Assumed Process Logic

The hypothetical diffusion solidification (SD) process for "rapid cycle steel casting" is outlined below.

- A mold is formed from non-wetting bonded refractory particles by conventional investment molding techniques.
- The mold is filled with low carbon spheroidal steel shot having specified size and size distribution.
- A "particle valve"⁽³⁾ of coarse, non-wetting refractory particles of specified size and shape is placed on top of the steel shot.
- A melt charge of high carbon iron is placed on top of the particle valve (PV).
- The mold, steel shot, PV, and melt charge are heated together to the process temperature by a direct technique (such as high-frequency induction or forced gas infiltration- see Chapter 2 so that no time is lost waiting for heat to diffuse through the bulk of the mold and the metallic components of the casting.
- The entire heating apparatus and mold assembly are evacuated during the heating cycle. The inert gas is saved for later use by accumulation within an ancillary pressure vessel.
- Immediately the assembly reaches the process temperature, the vacuum chamber enclosing the heating apparatus and mold assembly is rapidly backfilled with the inert gas at sufficient pressure to force the liquid cast iron to infiltrate the low carbon steel shot.
- The newly-formed casting is held at the process temperature long enough to achieve the desired degree of carbon homogeneity.
- The completed homogenized casting is removed from the furnace while still hot, and a new assembly is inserted to begin a new casting cycle.

8.3 Process Costs

The yearly inputs for making 1000 metric tons (10^6 kg) of 1 wt.pct. carbon steel castings are listed qualitatively below. Labor, interest, quality control, process instrumentation, administration, shipping, materials handling and similar costs are not considered in the present analysis because they are too sensitive to the detailed nature of the final product and because they are likely to be quite similar to the corresponding costs of a competing process.

- Raw Materials

- 660 metric tons of spheroidal, 0.05 wt.pct. carbon steel shot
- 440 metric tons of 2.5 wt.pct. carbon iron
- 100 metric tons of refractory mold material and binder
- 10 metric tons of coarse refractory PV material

- Operations

- Sensible heat of raw materials at casting temperature
- Heat flow to surroundings during casting and homogenization
- Work dissipated by vacuum pump/compressor
- Work expended during removal of PV by machining

- Capital

- Casting furnace
- Power supply for casting furnace
- Pressure vessel to enclose casting furnace
- Vacuum pump/compressor for evacuation/infiltration
- Machinery for cutting off the PV and waste melt charge from each completed casting

8.4 Detailed Calculations

8.4.1 Raw Materials

a. Shot

The SD casting process is dependent on a supply of spheroidal low carbon steel shot of specified size distribution. It will be assumed here that the quantity of shot being used by the SD process is sufficient to warrant construction of suitable atomization equipment by a primary metals producer, thereby avoiding an extra remelting of the refined steel prior to atomization. Candidate atomization processes have recently been reviewed by Lawley⁽⁴⁾. There are three specific costs associated with steel shot for the SD process:

- Refining and maintaining a low level of oxides and other inclusions.
- Mean particle size of the shot, \bar{d} . More energy and capital are needed to produce finer shot.
- Particle size distribution, measured in terms of the ratio of the largest to the smallest usable shot size, R . The smaller is R , the greater the fraction of unusable shot which must be diverted or scrapped.

In SD casting of steel, the first factor above is critical to the manufacture of a ductile product⁽¹⁾; however, it will be neglected in the present analysis because the increased cost of special efforts to achieve a given low inclusion level would only be justifiable by an increased value of the product.

The second factor, the cost of making shot of a

particular mean particle size, is negligible for SD casting in steel because the surface energy (associated with a given mass of steel shot of the particle size under consideration) is extremely small, and even extremely inefficient atomization processes cannot make the input energy to atomization a significant quantity. There is no cost penalty for size of the least expensive of all spheroidal steel powder, shot-peening shot, in the range of shot diameters used for SD casting. Therefore, this factor also will be neglected.

The third factor, the cost of the narrowness of the shot size distribution has substantial significance because conventional atomization processes produce a wide range of particle size distributions⁽⁴⁾. This cost can be estimated conservatively by considering that the cost of the entire output of the atomization plant is applied only to the size fraction actually used for the SD process. In other words, off-size fractions are assumed to have no value, but their costs are included in the cost of raw material. Expensive processes (rotating electrode, rotating disc, ultrasonic) give narrow particle size distributions, and inexpensive processes (steam, Ar or air atomization) produce wide ones. The net effect is that the cost of a particular size fraction is nearly independent of the method of manufacture (this is not physically necessary, which leaves room for considerable cost savings). Low cost conventional atomization processes are thereby favored, because the off-size fractions can probably be absorbed by other markets. Therefore, the unit cost of particles of a particular size range will be somewhat arbitrarily defined as

$$C_{\delta} = C_p \left(\frac{\Delta}{\delta} \right) \quad (1)$$

where

$$\delta = \ln R$$

$$R = d_u / d_l \quad (2)$$

$$\Delta = \ln \left(\frac{d_{\max}}{d_{\min}} \right)$$

and C_p is the unit cost of the entire output of the chosen atomization process, d_u is the upper limit of usable particle sizes, d_l is the corresponding lower limit, and d_{\max} and d_{\min} define the entire range of shot sizes produced by the atomization process.

It is presumed in this analysis that the chosen atomization process is operated so that the mean particle diameter is within the desired size range.

b. High Carbon Iron

The iron used for the melt charge must have a composition (exclusive of the extra carbon) close to the aim composition of the steel castings. However, the results of Paliwal et al (5) indicate that the best melt charge composition will indeed be different from the shot composition so that the net microsegregation will be acceptable. Hence it will be necessary to purchase pre-alloyed melt charge in the form of 2.5 wt.pct. carbon coarse shot. The associated cost is assumed to be the same as the overall cost of the atomized steel shot, C_p . The effect of the lower atomization temperature on the cost of the high-carbon shot is assumed to be offset by the more specialized nature of this product than low-carbon steel shot.

c. Mold Material and Particle Valve

A general, non-specific molding method is considered here because the molding cost is sensitive to the complexity of the casting as in any competing process. The molding and PV material costs are assumed to be linearly related to the mass of molding material handled, which in turn is assumed to be linearly related to the mass of castings made, say 8 pct. of that quantity (giving a mold volume about one-half of the metallic volume of the casting):

$$\text{Mold and PV costs} = (10^6 \text{ kg/year})(0.08)(C_r) \quad (3)$$

where C_r is the unit cost of the refractory material.

This is a substantial cost, which could be reduced by recycling of used mold material, the more so if the bonding method caused little or easily reversible contamination of the refractories.

d. Total Raw Material Costs

The total yearly cost of raw materials for 10^6 kg of 1 wt.pct. carbon steel castings is (assuming 10 wt.pct. scrap loss in cropping the PV off the finished casting) obtained by combining Equations (1) and (3):

$$\text{Total Raw Material Cost, \$/year} = [660 C_p (\Delta/\delta) + 440 C_p + 80 C_r] 10^3 \quad (4)$$

8.4.2 Capital and Operating Costs

a. Casting Furnace

The working volume of the furnace used to heat the casting components (mold, shot, particle valve and melt charge) to the process temperature is given by the relationship:

$$V_f = \frac{\text{Superficial volume of castings per year}}{(\text{Seconds per year}/\text{cycle time in seconds})} \quad (5)$$

$$= \frac{(12)(10^6 \text{ kg/year})(1/\rho_c)(t_c)}{(2.592 \times 10^7 \text{ s/year})}$$

which assumes 300 twenty-four hour working days per year, where the factor of twelve accounts for the extra volume of the mold, PV, furniture, void space, and working room within the furnace volume, and ρ_c is the density of the finished casting. Equation (5) also assumes that more than one mold assembly can be treated at once in the furnace.

The cycle time, t_c , is given by the relationship

$$t_c = t_t + t_i + t_s + t_h + t_r \quad (6)$$

where

t_t = heating time (an optimizable variable)

$$t_i = \text{infiltration time} \approx \alpha t_s \quad (7)$$

(where α is an optimizable fraction between 0 and 1)

$$t_s = \text{solidification time} = 0.13 (d_u^2/D) \quad (8)$$

(where D is the diffusivity of carbon in austenitic iron at the process temperature)

$$t_h = \text{homogenization time} = 0.14 (d_u^2/D)(H) \quad (9)$$

(where H is an optimizable homogenization index

equal to the number of 9's; i.e.,

H = 2 for 99 pct. homogenization, which in turn represents ± 1 pct. variation in the local composition from the intended carbon content; ($1 < H < 3$)

t_r = idle and reloading time, assumed to be approximately equal to the sum of the other components of t_c

Equations (8) and (9) were derived by Sreshta⁽⁶⁾ for narrow size fractions and are herein used with the upper limit d_u of a broader size fraction as conservative estimates.

Equations (6) through (9) can be combined to yield an estimate of the cycle time for the casting furnace:

$$t_c = 2 [t_t + (d_u^2/D)(0.13 + 0.13\alpha + 0.14H)] \quad (10)$$

The casting furnace will cost C_f per m^3 but will last only one year due to changing product design and wear and tear, so its capital cost will be obtained from Equations (5) and (10):

$$\begin{aligned} \text{Capital Cost of} \\ \text{Casting Furnace} &= \frac{(12)(10^6)(1/\rho_c)}{(2.592 \times 10^7)} [2(t_t + (d_u^2/D)(0.13+0.13\alpha+0.14H))] C_f \\ &= 0.9259 (C_f/\rho_c) [t_t + (d_u^2/D)(0.13+0.13\alpha+0.14H)] \end{aligned} \quad (11)$$

The energy put into the casting furnace goes partly to raise the temperature of the casting components and associated furniture and partly into the surroundings as waste heat. The sensible heat q_s supplied per year to the casting components at the process temperature is given by the relationship:

$$q_s = (1.210 \times 10^6 \text{ kg/year})[1.5 c_p(T_f - T_a) + 0.4\Delta H_f] \quad (12)$$

Where c_p is the mean heat capacity of the casting components, T_f is the process temperature, T_a is ambient temperature, ΔH_f is the heat of fusion of iron at the process temperature, and the factor of 1.5 accounts for the insulated portion of the furnace which inevitably must be heated along with the casting components.

In order to estimate the heat losses during the casting

operation, it is convenient to assume a certain casting and furnace geometry as shown in Figure 1. Note that it is assumed that the "master" furnace is subdivided into one or more units, each designed to hold one casting. Each casting is heated and insulated separately. The heat loss, Q_1 , per casting during the heatup phase of the casting operation is given by

$$Q_1 = A_i \frac{k}{x_i} \int_0^{t_f} \dot{T}_t dt = 24.4 k l t_t^2 = 24.4 k (T_f - T_a) t_t^2 \quad (13)$$

Where A_i is the exposed area of furnace insulation ($\approx 4.89 l^2$), k is the thermal conductivity of the furnace insulation, l is the casting length (a characteristic dimension, also the infiltration depth), and the surface temperature of the insulation is conservatively assumed to remain at ambient because it is in direct contact with the water-cooled induction coil.

The sensible heat, Q_s , to be supplied to each casting by the power supply is given by that casting's contribution to the total mass of a year's production of castings; the assumed casting geometry is shown in Figure 2.

$$\begin{aligned} Q_s &= q_s (\text{mass of one casting}/10^6 \text{ kg}) \\ &= q_s [\rho_c l^3 (\pi/36 \times 10^6)] \end{aligned} \quad (14)$$

The furnace power supply must be sized so that it can economically raise the furnace temperature in a reasonable time, t_t , and it must supply the sensible heat, Q_s , plus the heat loss, Q_1 . If the temperature of the casting assembly is raised at a uniform rate, the power requirement per casting is therefore given by \dot{Q}_t :

$$\dot{Q}_t = \frac{A_i k l}{x_i} (T_f - T_a) + Q_s / t_t = 48.9 k l (\Delta T_f) + Q_s / t_t \quad (15)$$

where

ΔT_f is the temperature rise ($T_f - T_a$).

The furnace power supply will be given a useful lifetime of 10 years and will cost C_{FPS} per kilowatt, so its yearly cost will be:

$$\text{Cost of Casting Furnace Power Supply, \$/year} = (\dot{Q}_t)(C_{FPS})(n_c)/(n_{FPS}) \quad (16)$$

where n_{FPS} is the efficiency of the furnace power supply and n_c is the number of castings made per furnace cycle, $\frac{2}{3} (V_f/V_i)$, where V_i is the insulated volume associated with each casting, $(2\pi/9)l^3$, and the factor of $\frac{2}{3}$ accounts for packing inefficiency.

The heat loss, Q_2 , per casting during the constant temperature portion of the casting cycle is given by:

$$\begin{aligned} Q_2 &= (A_i)(k)(\Delta T_f)(t_i + t_s + t_h)/x_i \\ &= 48.9(k)(\Delta T_f)(l)(d_u^2/D)(0.13 + 0.13\alpha + 0.14H) \end{aligned} \quad (17)$$

If electrical power costs, C_e , per kilowatt hour, the operating cost of these heat inputs is obtained from the sum of Equations (13), (14), and (17):

$$\text{Operating Cost of Energy Input to Casting Furnace} = (C_e)(Q_s + Q_1 + Q_2)/n_{FPS} \quad (18)$$

The quantity of castings, n_y , made per year is given by the ratio of the total mass of castings made in one year to the mass of one casting:

$$n_y = (10^6 \text{ kg})/\rho_c l^3 \pi / 36 \quad (19)$$

Therefore, the total cost of the energy input to the casting furnace is given by the product of Equations (18) and (19):

Operating Cost of Energy

$$\text{Input to the Casting Furnace, \$/year} = \frac{(C_e/n_{FPS})(Q_s + Q_1 + Q_2)(10^6)}{(\rho_c l^3 \pi / 36)} \quad (20)$$

b. Pressure Vessel

For the relatively low pressures to be encountered in SD casting, the material cost of a pressure vessel will be negligibly small. However, there is some question about whether it is better to design for zero gauge pressure (in which atmospheric pressure is used to effect infiltration by backfilling the previously evacuated vessel) or for some substantially higher pressure in order to reduce the cycle time by enabling a smaller shot size to be used.

Therefore, we will assume a cost-pressure relationship to enable further study of this problem. A simple vacuum vessel need only be designed against elastic collapse and contains no stored energy of compressed gas. A high pressure vessel contains large amounts of stored energy proportional to its working pressure and volume; this increases its design cost as well as its absolute cost. A vacuum vessel with appropriate closures, vacuum pump, compressor, accumulators, and other hardware costs, C_o per m^3 , whereas, a pressure vessel would cost $C_o(P_i/P_a)$ per m^3 , where (P_i/P_a) is the ratio of infiltration (working) pressure to ambient (atmospheric) pressure.

Let the volume, V_o , of the pressure vessel be equal to twice the furnace volume, $2V_f$. Using the same cycle time as that given by Equation (10) and assuming a ten-year life:

Capital Cost of Pressure
Vessel, \$/year

$$\begin{aligned}
 &= \frac{(2)(12)(10^6)(C_o)(P_i/P_a)}{(10)(2.592 \times 10^7)(\rho_c)} [2(t_t + (d_u^2/D)(0.13+0.13\alpha+0.14H))] \\
 &= 0.1852 [t_t + (d_u^2/D)(0.13+0.13\alpha+0.14H)](C_o/\rho_c)(P_i/P_a)
 \end{aligned} \tag{21}$$

The capital and energy costs of evacuating and accumulating high pressure inert gas during the casting cycle are both negligible, because the $P_i V_o$ product is small in comparison to heating costs; the evacuation can take place during the heating phase (taking time, t_t , to be optimised with respect to heating costs only), and the pressure accumulation can be accomplished during all but the infiltration time ($t_s - t_i$) if two accumulators are used (one of variable volume to receive inert gas at atmospheric pressure from the vacuum pump and the other of constant volume and substantial construction to receive the output of the compressor).

c. Machining Costs

It is assumed that the particle valve containing some frozen cast iron will adhere to the end of the casting through which it was infiltrated, and that it will have to be removed by the use of either an abrasive cutoff wheel or an oxy-fuel cutting torch (followed by a finishing operation). Both these methods have an approximately constant cost per unit area of cut^(7, 8, 9) over a range of thicknesses from 10mm to 200mm, including labor and supplies; capital costs are negligible or included in the operating costs of the supplies. Therefore, the machining cost is given by the relationship:

Machining Cost,
\$/year

$$\begin{aligned}
 &= (\text{Number of pieces cut per year})(\text{area cut per piece})(C_m) \\
 &= \frac{(10^6 \text{ kg/year})(V_c/\ell)(C_m)}{(\rho_c)(V_c)} \quad (22)
 \end{aligned}$$

Where V_c is the metallic volume of one casting (note that it cancels out of the equation), ℓ is the infiltration distance, and C_m is the cost of machining, $\$/m^2$.

8.4.3 Constraints

a. Infiltration Pressure

The optimizable variables in the SD process are subject to the constraint that it takes at least a certain pressure, P_i , to effect infiltration according to the equation predicted by Langford and Cunningham⁽¹⁾:

$$P_i = 25 \times 10^6 \rho k_d^4 (1 - f)^2 \left(\frac{D}{\alpha_{LC}} \right)^2 \frac{\ell^3}{d^5} \quad (23)$$

Where ρ is the density of the infiltrating liquid (6770 kg/m^3), k_d is the distribution coefficient from the phase diagram (the ratio of solidus composition to liquidus composition (0.4 for Fe-C)), f is the space filling fraction for the shot (0.60 for spheroidal particles), D is the diffusivity of solute in the solid ($5.7 \times 10^{-16} \text{ m}^2/\text{s}$ for C in Fe at 1350°C in the present case), α_{LC} is the ratio of the infiltration time to the maximum possible infiltration time defined by the near-closure of the openings between shot particles, ℓ is the infiltration depth, and d is the particle (shot) diameter. Sreshta⁽⁶⁾

has measured the infiltration kinetics for the system, low carbon steel shot/high carbon iron melt at 1185°C, and has found that Equation (23) may underestimate the pressure required for successful infiltration by no more than a factor of two.

Sreshta⁽⁶⁾ has also defined a macrosegregation parameter (as in Equation (7) here) which is the ratio of the infiltration time to the solidification time; comparison of the two different definitions yields the relationship:

$$\alpha_{LC} = (48.) \alpha \quad (24)$$

According to Sreshta⁽⁶⁾, α must be less than 0.005 to achieve acceptable carbon homogeneity.

Equations (23) and (24) can be combined along with the above constraint on α as well as the experimental results of Sreshta; this yields a practical equation for P_i :

$$P_i = (2)(25 \times 10^6)(6770 \text{ kg/m}^3)(0.4)^4(1-0.60)^2 \frac{5.7 \times 10^{-10} \text{ m}^2/\text{s}}{(48.)(0.005)} \frac{\ell^3}{d_\ell^5}$$

$$= 7.821 \times 10^{-9} \ell^3 d_\ell^{-5} \quad (25)$$

Here the lower limit, d_ℓ , of the range of particle sizes $d_\ell < d < d_u$ has been used to estimate the required infiltration pressure on the grounds that the smallest interstitial passageways will freeze first. Because of the extremely strong dependence of P_i on d , this is a highly conservative assumption. Failure of this assumption will lead to higher than expected quality in terms of macrosegregation.

b. Particle Size and Particle Size Range

Preliminary calculations indicated that the particle sizes, d_x and d_u , and their range, R, returned for the optimum total cost by the computer, are both too large for practical atomization. Therefore, additional constraints setting upper limits on d_u and R were added as shown below:

$$d_u(\text{max}) \leq 3 \times 10^{-3} \text{ m} \quad (26)$$

$$R(\text{max}) \leq 10 \quad (27)$$

8.5 Computations

The unconstrained costs calculated from the preceding equations are shown in uncondensed form in Tables 1 through 6. Each table reduces the abstract equations into a sum of discrete terms, each expressed as a constant times the optimizable variables (some raised to various powers) and "variable constant(s)".

These terms are brought together into a single expression for the yearly cost of 1000 metric tons of SD castings in Table 7, where the constraint that α must be less than 0.005 (according to Sreshta⁽⁶⁾) has been introduced, assuming that it will be an active constraint at the optimum. Note that the subscripts of the old and new term constants are the same. Table 8 lists the "base case" estimate of the optimum values of the principal variables which was used to compute a first order estimate of the relative weights of the twenty terms in the cost equation for purposes of simplification of the computer analysis. Alternatively, these relative weights could be used to condense the utility function to few enough terms to enable use of the geometric programming (non-computer) techniques described by Wilde⁽¹⁰⁾. Dembo⁽¹¹⁾ has described

an approach to sensitivity analysis for geometric programming.

Table 9 lists the components of the optimization problem as prepared for solution by the Random Search and Direct Search non-linear programming algorithms described by Siddall⁽¹²⁾. All terms have been used because of the condensation made possible by setting $\alpha = 0.005$ as described above.

Table 10 lists the direct results of the computer calculations for the case of unconstrained casting size, ℓ , heating time, t_t , and particle size range, R (actually, with four independent variables but two active constraints - PHI(1) AND PHI(2) in Table 9 - there are actually only two truly independent variables in Table 10).

Table 11 shows the results of the computer calculations under the same conditions as for Table 10 but with the added constraint of arbitrarily chosen casting size, ℓ . Table 12 presents another set of results for an arbitrarily varied D_{max} the upper limit on the particle size range. In Table 12, there are again two independent variables.

Table 13 shows the origin of a series of equations used to evaluate the dependent process parameters: total cycle time, t_c , casting furnace volume, V_f , number of castings made per cycle, n_c , number of castings made per year, n_y , mass of one casting, m_c , and cost per kg of particles used for the solid charge, c_s .

Tables 14, 15 and 16 are complementary to Tables 10, 11 and 12 and show the variations of these selected dependent process parameters corresponding to the optimum independent variables and "variable constants" (C_p , P_{max} and D_{max}).

8.6 Discussion of the Results of the Computations

8.6.1 Costs

- . Materials costs dominate, especially for oversize castings and castings made from costly particles.
- . Energy costs represent about 17% of the total cost of castings made from particles costing \$2/kg, half as much for \$10/kg particles; the casting furnace power supply efficiency has a profound effect.*
- . Capital costs are extremely small for all conditions, mainly because the casting furnace power supply has a ten-year span of utility.
- . Total costs increase by about \$2/kg for casting lengths three times smaller or larger than the optimum length, regardless of the cost per kg of atomized particles or of the maximum allowable infiltration pressure P_{max} .
- . Total costs cannot be reduced arbitrarily by decreasing the particle cost, C_p , because the optimum occurs at a smaller particle size range, R , the lower the particle cost, thereby increasing C_s , the cost per kg of particles

*More calculations should be performed here with various values of n_{FPS} (see Tables 3 and 4); there was not sufficient time to do so; in the present study, a highly conservative value of 0.1 was used (see Ref. 13, Chapter 2 of this report).

actually used for the casting. Conversely, total costs increase slowly with increasing C_p leading us to pursue greater cost savings with castings of greater alloy content or higher quality (justifying greater atomization expense).

8.6.2 Variables, Parameters and Variable Constants

- . The independent variables, ℓ , d_ℓ , t_t and R , all fall within reasonable ranges; clearly, rather large, compact (low surface-to-volume ratio) castings are favored by this analysis. Specifically, t_t is larger than the heating times already proven feasible in Chapter 2 (Ref. 13).
- . The optimum value of the infiltration pressure, P_i , is reasonably low except for the most expensive shot, where the last seven-fold increase in the infiltration pressure to the optimum barely reduces the total cost at all. There is little cost penalty for using substantially less than the optimum infiltration pressure. This keeps us away from the imposing and dangerous pressure vessels so necessary in hot isostatic pressing, where 1000 atm. is a common consolidation pressure.
- . Increased infiltration pressure increases the utilization of particles or, alternatively, the size of casting that can be made economically.
- . The particle cost, C_p , has no effect at all on the operating parameters for making castings of arbitrary length. This

increases the versatility of optimally designed equipment. Only the interiors and induction coils of the casting furnace would have to be changed.

- . The heating time, t_h , is directly proportional to casting length. Therefore, direct heating by appropriate choice of the frequency of the alternating magnetic field is highly appropriate; see Chapter 2 (Ref. 13).
- . The cycle time, t_c , is approximately proportional to the square root of casting length; this clearly favors large SD castings whose conventional solidification time is controlled by Chvorinov's Rule (solidification time proportional to casting length squared). However, the absolute cycle times calculated here are longer than normal solidification times. Please keep in mind that the present process produces 90% homogenized SD castings, which cannot be done by conventional solidification plus homogenization in any reasonable time except by atomization followed by HIP.
- . To keep t_c below one 8-hour shift length, the upper limit of the particle size range must be kept below 3mm, the maximum commercially available particle size of atomized shot.
- . The cycle time, t_c , is longer for cheaper particles, but this does not compensate for the much greater number of optimum-sized castings which must be made from the more expensive particles. Therefore, labor costs will rise as

the particle cost and quality rise, although no direct calculations of labor cost were attempted here.

- . Note that the number of castings made per cycle, n_c , and the furnace volume, V_f , can both be subdivided into more than the one "master" casting furnace assumed in the model. This can be done without penalty (except for instrumentation and other minor details which were already neglected) because the furnace and pressure vessel(s) are both costed on a volume basis and because the heat losses are calculated for individually insulated casting assemblies. An alternative interpretation of V_f and n_c is that V_f represents the total volume of individual casting furnaces and n_c the total number of furnaces (each containing one casting assembly) which must be tended. The cycle time, t_c , would be unaffected by this new viewpoint.

8.7 Conclusions

An economic model has been developed for diffusion solidification casting of steel which predicts process conditions in the same ranges as those studied experimentally. The total process cost rises much more slowly than the cost of the atomized shot necessary for the solid charge of the casting, indicating that it would be more profitable to apply the SD process first to the more expensive steel alloys. The model predicts that the promised increase in casting yield over conventional casting can be achieved with modest infiltration pressures (especially in comparison to hot isostatic compaction) even under the conservative assumption that under-size shot has no economic value.

It was found that the energy and capital costs for the SD casting process are only 10 to 20% of the total cost; machining costs are only ca. 10%. The cost of raw materials, especially the atomized shot, was found to be dominant: 50 to 97% of the total. Therefore, further research to improve the efficiency of atomization of low carbon steel in terms of minimizing costs and off-size fractions would be highly justified.

There is substantial flexibility in the choice of casting size and various processing parameters without incurring large cost increases, mainly because of the corresponding freedom of choice of compensating variables. The optimum heating and cycle times are quite long (but note that the SD process produces essentially completely homogeneous castings within this simple cycle), but vary rather slowly with casting size.

The present calculations show that the already proven feasible casting parameters can be combined to produce castings at a modest premium over the cost of the raw material (atomized shot). The extra costs attributable to the SD process are about \$2/kg for \$0.1/kg shot, \$2.5/kg for \$1/kg shot, \$3/kg for \$2/kg shot, and \$6/kg for \$10/kg shot. Most of these extra costs are for scrapped off-size fractions.

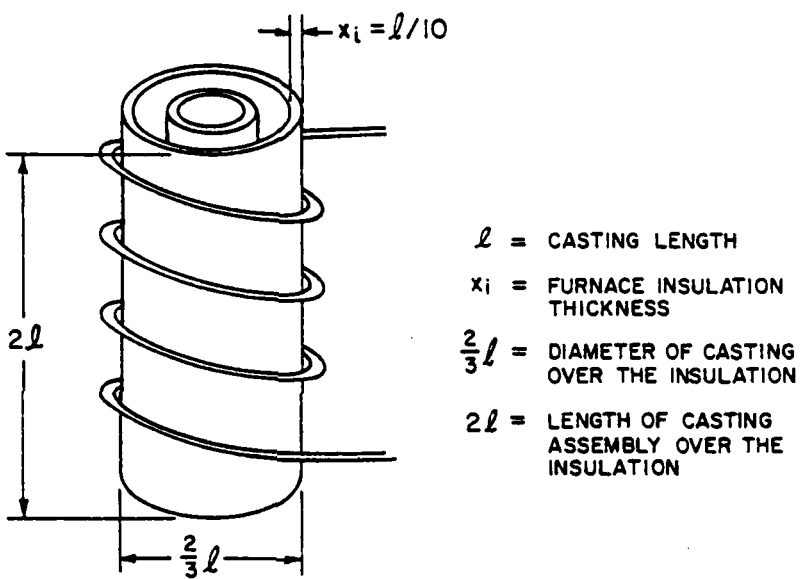


Figure 1. Casting and Furnace Geometry

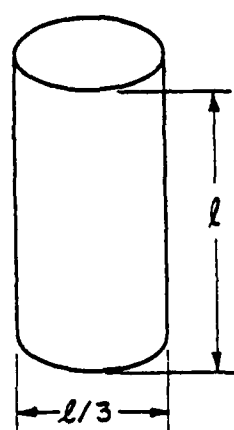


Figure 2. Casting Geometry

REFERENCES

1. G. Langford and R. E. Cunningham: Steel Casting by Diffusion Solidification, Met. Trans., 1978, vol. 9B, pp. 5 - 19.
2. G. Langford and D. Apelian: Diffusion Solidification, J. Metals, 1980, vol. 32 (No. 9), pp. 28 - 33.
3. M. Paliwal, D. Apelian, and G. Langford: Performance of a Porous Refractory Valve for Liquid Metals, Met. Trans., 1980, vol. 11B, pp. 39 - 50.
4. A. Lawley: Atomization of Specialty Alloy Powders, J. Metals, 1981, vol. 33 (No. 1), pp. 13 - 18.
5. M. Paliwal, D. Apelian, and G. Langford: Microsegregation of Ternary Alloying Elements in Steels Cast by Diffusion Solidification, to be submitted to Met. Trans., (Chapter 6 of this report).
6. H. A. Sreshtha, G. Langford, and D. Apelian: Kinetics of Interactive Liquid Metal Infiltration and Diffusion Solidification, to be submitted to Met. Trans. (Chapter 5 of this report).
7. L. S. Krueger: The Abrasive Cut-off Wheel, Steel Foundry Facts, Issue No. 204, 1960.
8. J. B. Hibbs and K. G. Rawson: Aspects of Cutting and Fettling Steel Castings, British Foundryman, 19 , vol. 67 (No. 9), pp. 231 - 239.
9. Anon: AIRCO Cutting Guide, AIRCO.
10. D. J. Wilde: Globally Optimal Design, Wiley - Interscience, New York, 1978.
11. R. S. Dembo: The Sensitivity of Optimal Engineering Designs Using Geometric Programming, Eng. Optimization, 1980, Vol. 5, pp. 27 - 40.
12. J. N. Siddall: Analytical Decision-Making in Engineering Design, Prentice Hall, Inc., Englewood Cliffs, New Jersey, 1972.
13. H. A. Sreshtha, G. Langford, and D. Apelian: Rapid Heating of Unbonded Steel Powder, to be submitted to the Journal of the Metal Powder Industries Federation (Chapter 2 of this report).

TABLE 1
Materials Cost

$$\text{Materials} = [660 C_p \left(\frac{\Delta}{\delta} \right) + 440 C_p + 80 C_r] 10^3$$

but,

$$\Delta \approx 2.3$$

$$\delta = \ln R$$

$$C_r \approx \$10/\text{kg}$$

so the Materials Cost, \$/year

$$= \left[\frac{660 C_p (2.3)}{\ln R} + 440 C_p + 80 (10) \right] 10^3$$

$$= [1518 C_p (\ln R)^{-1} + 440 C_p + 800] 10^3$$

$$\text{Materials Cost, } \$/\text{year} = C_1 C_p (\ln R)^{-1} + C_2 C_p + C_3$$

where $C_1 = 1.518 \times 10^6$

$$C_2 = 0.440 \times 10^6$$

$$C_3 = 0.800 \times 10^6$$

and C_p is a "variable constant" for the purposes
of the sensitivity analysis.

TABLE 2Casting Furnace - Capital Cost

$$\text{Casting Furnace Capital Cost} = \frac{12 \times 10^6}{2.592 \times 10^7} \left(\frac{c_f}{\rho_c} \right) [2(t_t + (d_u^2/D)(0.13+0.13\alpha+0.14H))]$$

where

$$c_f = \$5000/m^3 \text{ (estimated)} \quad 0 \leq \alpha \leq 1$$

$$\rho_c = 7850 \text{ kg/m}^3 \quad 1 < H < 2$$

$$d_u = R d_\lambda$$

$$D = 5.7 \times 10^{-10} \text{ m}^2/\text{s}$$

$$= 0.5898[t_t + 1.754 \times 10^9 R^2 d_\lambda^2 (0.27+0.13\alpha)] \text{ for } H = 1$$

Casting Furnace Capital Cost, \$/year

$$= c_4 t_t + c_5 R^2 d^2 + c_6 \alpha R^2 d^2$$

where $c_4 = 0.5898$

$$c_5 = 2.793 \times 10^8$$

$$c_6 = 1.345 \times 10^8$$

and $d_\lambda \equiv d$ for simplicity

$H = 1$ because this always will minimize the total cost.

TABLE 3

Casting Furnace Power Supply - Capital Cost

Casting Furnace Power Supply Capital Cost

$$= \frac{\dot{Q}_t C_{FPS} n_c}{10 n_{FPS}} \quad \text{where } \dot{Q}_t = 48.9 k\ell (\Delta T_f) + Q_s/t_t$$

$$n_c = (V_f/\lambda^3)(3/\pi)$$

$$V_f = (12 \times 10^6 / 2.592 \times 10^7) (t_c / \rho_c)$$

$$t_c = 2[t_t + (d_\lambda^2 R^2 / D)(0.13 + 0.13\alpha + 0.14 H)]$$

$$Q_s = (1.210 \times 10^6) [1.5 c_p \Delta T_f + 0.4 \Delta H_f] (\rho_c \lambda^3 \pi / 36 \times 10^6)$$

$$k = 0.173 \text{ J/(sm}^2(\text{°C/m}))$$

$$\Delta T_f = 1330^\circ\text{C}$$

$$c_p = 0.2 \text{ cal/(g°C)} = 0.2(4185.5) \text{ J/(kg°C)}$$

$$\Delta H_f = 63.7 \text{ cal/g for pure Fe}$$

$$= 58 \text{ cal/g for alloy} = 58(4185.5) \text{ J/kg}$$

$$C_{FPS} = \$1000/\text{kw} = \$1 \text{ w}^{-1} = \$/\text{sJ}^{-1}$$

$$\eta_{FPS} = 0.10$$

$$\rho_c = 7850 \text{ kg/m}^3$$

$$D = 5.7 \times 10^{-10} \text{ m}^2/\text{s}$$

H = 1 because this always will minimize the total cost.

$$d_\lambda = d \text{ for simplicity}$$

Casting Furnace Power Supply
Capital Cost, \$/year

$$= C_7 \lambda^{-2} t_t^{-2} + C_8 \lambda^{-2} R^2 d^2 + C_9 \lambda^{-2} \alpha R^2 d^2 + C_{10} + C_{11} R^2 d^2 t_t^{-1} + C_{12} \alpha R^2 d^2 t_t^{-1}$$

$$\text{where } C_7 = 1.265$$

$$C_{10} = 1.650 \times 10^5$$

$$C_8 = 1.990 \times 10^8$$

$$C_{11} = 7.815 \times 10^{13}$$

$$C_9 = 2.885 \times 10^8$$

$$C_{12} = 3.764 \times 10^{13}$$

TABLE 4
Total Heat Cost

$$\text{Total Heat Cost} = (C_e / \eta_{FPS})(Q_s + Q_1 + Q_2)(10^6) / (\rho_c l^3 \pi / 36)$$

$$\text{where } Q_s = (1.210 \times 10^6)(1.5 c_p \Delta T_f + 0.4 \Delta T_f)(\rho_c l^3 \pi / 36 \times 10^6)$$

$$Q_1 = 24.4 k l t_t \Delta T_f$$

$$Q_2 = (48.9 k \Delta T_f l R^2 d_l^2 / D)(0.13 + 0.13 \alpha + 0.14 H)$$

and the parameters are:

$$C_e = \$0.10/\text{kwh} = (0.1 / 3.6 \times 10^6) \$/\text{J}$$

$$\eta_{FPS} = 0.10$$

$$c_p = 0.2 (4185.5) \text{ J/kg}^\circ\text{C}$$

$$\Delta H_f = 58 (4185.5) \text{ J/kg}$$

$$k = 0.173 \text{ J/(sm}^2(\text{C/m}))$$

$$\Delta T_f = 1330^\circ\text{C}$$

$$D = 5.7 \times 10^{-10} \text{ m}^2/\text{s}$$

$$\rho_c = 7850 \text{ kg/m}^3$$

H = 1 because this always will minimize the total cost.

d_l = d for simplicity

Total Heat Cost, \$/year

$$= C_{13} + C_{14} l^{-2} t_t + C_{15} l^{-2} R^2 d^2 + C_{16} \alpha l^{-2} R^2 d^2$$

$$\text{where } C_{13} = 5.940 \times 10^5$$

$$C_{14} = 2.276$$

$$C_{15} = 2.161 \times 10^9$$

$$C_{16} = 1.040 \times 10^9$$

TABLE 5Pressure Vessel - Capital Cost

Pressure Vessel Capital Cost

$$= (2)[(12 \times 10^6 / 2.592 \times 10^7)(2C_o P_i)/(10\rho_c P_a)][t_t + (R^2 d_l^2 / D)(0.13 + 0.13\alpha + 0.14H)]$$

where

$$P_i = [6.932 \times 10^8 D^2 l^3 d_l^{-5} \alpha_{LC}^{-2}] (2)$$

$$\alpha_{LC} = (48.)\alpha$$

the parameters are:

$$C_o = \$5000/m^3$$

$$\rho_c = 7850 \text{ kg/m}^3$$

$$D = 5.7 \times 10^{-10} \text{ m}^2/\text{s}$$

$$P_a = 1 \text{ atm} = 10^5 P_a$$

H = 1 because this always will minimize the total cost

d_l = d for simplicityPressure Vessel Capital
Cost, \$/year

$$= C_{17} l^3 d^{-5} \alpha^{-2} t_t + C_{18} l^3 d^{-3} \alpha^{-2} R^2 + C_{19} l^3 d^{-3} \alpha^{-1} R^2$$

where

$$C_{17} = 2.306 \times 10^{-19}$$

$$C_{18} = 1.092 \times 10^{-10}$$

$$C_{19} = 5.260 \times 10^{-11}$$

TABLE 6
Machining Cost

$$\text{Machining Cost} = 10^6 C_m / \rho_c l$$

The parameters are

$$C_m = \$0.10/\text{in}^2 = 0.10/(25.4 \times 10^{-3})^2 \text{ \$/m}^2 \\ = \$155 \text{ m}^{-2}$$

$$\rho_c = 7850 \text{ kg/m}^3$$

$$\text{Machining Cost, \$/year} = C_{20} l^{-1}$$

$$\text{where } C_{20} = 1.975 \times 10^4$$

TABLE 7

499

Total Yearly Cost of 1000 Metric Tons of SD Steel Castings (for $\alpha = 0.005$)

Term Number	Type	Term	T_n	Base Case \$/Year	Relative Weight	Included in Computer Analysis?
1	Materials cost	$C_1 C_p (\ln R)^{-1}$	1.518×10^6	1.886×10^6	0.2268	Yes
3	(Table 1)	C_3	0.800×10^6	0.800×10^6	0.0962	Yes
4	Casting	$C_4 t$	0.5898	1769	0.0002	Yes
5	Furnace Capital	$C_5 R^2 d^2$	2.793×10^8	2514 }	0.0003	Yes
6	Cost (Table 2)	$C_6 R^2 d^2$	6.725×10^5	6 }		(5+6)
7	Casting	$C_7 \ell^{-2} t$	1.265	3.795×10^5	0.0456	Yes(7+14)
8	Furnace Power	$C_8 \ell^{-2} R^2 d^2$	5.990×10^8	5.391×10^5	0.0650	Yes (8, 9, 15+16)
9	Supply Capital	$C_9 \ell^{-2} R^2 d^2$	1.442×10^6	1298 }		
10	Cost	C_{10}	1.650×10^5	1.650×10^5	0.0198	Yes
11	(Table 3)	$C_{11} R^2 d^2 t^{-1}$	7.815×10^{13}	2.345×10^5	0.0283	
12		$C_{12} R^2 d^2 t^{-1}$	1.882×10^{11}	565 }		Yes (11+12)
13	Total Heat Cost	C_{13}	5.940×10^5	5.940×10^5	0.0714	Yes
14	(Table 4)	$C_{14} \ell^{-2} t$	2.276	6.828×10^5	0.0821	Yes (7+14)
15		$C_{15} \ell^{-2} R^2 d^2$	2.161×10^9	1.945×10^6	0.2345	Yes (8, 9, 15+16)
16		$C_{16} \ell^{-2} R^2 d^2$	5.200×10^6	4680 }		
17	Pressure Vessel	$C_{17} t \ell^3 d^{-5}$	9.224×10^{-15}	356	0.0000	Yes
18	Capital Cost	$C_{18} \ell^3 d^{-3} R^2$	4.368×10^{-6}	506 }	0.0001	Yes (18+19)
19	(Table 5)	$C_{19} \ell^3 d^{-3} R^2$	1.052×10^{-8}	1 }		
20	Machining Cost (Table 6)	$C_{20} \ell^{-1}$	1.975×10^4	1.975×10^5	0.0238	Yes
Totals		20 $\sum_{n=1}^N T_n$		8.315×10^6	1.000	All terms

Notes:

The following groups of terms can be combined: 5+6, 7+14, 8+9+15+16, 11+12, 18+19.

In Table 9, the terms are numbered by the first term in each of these groups, and the constant of that term is the sum of the constants for the group.

TABLE 8

500

Estimated Values of the Variables at the Base Case

<u>Variable x_i</u>	<u>Description of x_i</u>	<u>Reasonable Range of x_i</u>	<u>Estimated Value of x_i for the Base Case</u>
z	infiltration depth (a characteristic dimension of the casting)	0.01 - 3 m	0.1 m
d	lower limit of shot diameter	0.1 - 2 mm	0.6 mm
$R \cdot d$	upper limit of shot diameter	0.1 - 5 mm	3 mm
R	ratio of upper to lower limit shot diameters	1 - 20	5
t_t	time to bring casting components to the process temperature of 1350°C	$10^3 - 10^5$ s	3000 s
c_p	cost of unsized shot (a "variable constant")*	0.10 - 10 \$/kg	\$2/kg
p_i	allowable infiltration pressure*	$10^5 - 10^7$ Pa	10^6 Pa

*Notes

c_p and p_i are not optimizable variables; instead, they are varied in the computer analysis to investigate the sensitivity of the optimal variables to these market - or management - sensitive parameters.

TABLE 9

Nomenclature, Terms, Constants, Utility Function
and Constraints Used in Computer Analysis

501

<u>Variables</u>		<u>Ranges</u>
EL	= x(1) = λ	0 < x(1) < 1 m
DL	= x(2) = d_λ	0 < x(2) < 0.003 m
TT	= x(3) = t_t	0 < x(3) < 10^5 s
AR	= x(4) = R	1 < x(4) < 10
PMAX	= P_i) changed by operator for CP = C_p) each computer run	10^5 to 10^7 Pa
		0.10 to \$10/kg

<u>Terms</u>		<u>Constants, C_n</u>
T1	= $C1 \cdot CP / ALOG(AR)$	1.518 E 06
T2	= $C2 \cdot CP$	0.440 E 06
T3	= $C3$	0.800 E 06
T4	= $C4 \cdot TT$	0.5898
T5	= $C5 \cdot AR^{**2} \cdot DL^{**2}$	2.800 E 08
T7	= $C7 \cdot TT / EL^{**2}$	3.541
T8	= $C8 \cdot AR^{**2} \cdot DL^{**2} / EL^{**2}$	2.767 E 09
T10	= $C10$	1.650 E 05
T11	= $C11 \cdot AR^{**2} \cdot DL^{**2} / TT$	7.834 E 13
T13	= $C13$	5.940 E 05
T17	= $C17 \cdot TT \cdot EL^{**3} / DL^{**5}$	9.224 E -15
T18	= $C18 \cdot EL^{**3} \cdot AR^{**2} / DL^{**3}$	4.379 E -06
T20	= $C20 / EL$	1.975 E 04

Utility Function

$$U = \sum_{n=1}^{20} T_n = T1 + T2 + T3 + T4 + T5 + T7 + T8 + T10 + T11 + T13 + T17 + T18 + T20 \text{ (as listed above)}$$

Constraint

$$\begin{aligned} \text{PHI}(1) &= PMAX - 7.821 * EL^{**3} / DL^{**5} / 10.0^{**9} \\ \text{PHI}(2) &= (3.0 \text{ E-03}) - AR * DL \\ \text{PHI}(3) &= 10.0 - AR \end{aligned}$$

(Computer program will not allow PHI(1) to become negative.) PHI(1) and PHI(2) are active at the optimum; PHI(3) is not.

TABLE 10

Results of Computer Optimization Runs Using the Random Search and Direct Search Non-Linear Programming Algorithms
(only t_t and R are completely independent)

502

Case	Variables at the Optimum						Total Cost of 10 kg of castings Made Yearly (10 ⁶ dollars)
	C_p (\$/kg)	P_{max}^* (atm)	l (mm)	d_l (mm)	t_t (s)	R (mm/mm)	
1	0.1	1	570	1.71	7500	1.76	2.168
			602	1.76	8000	1.70	2.165
2	0.1	10	786	1.31	6300	2.30	2.018
			901	1.42	9000	2.12	1.999
3#	0.1	36.76	881	1.08	7200	2.29	1.979
		35.79	894	1.09	7300	2.30	1.979
4	1.0	1	293	1.15	4100	2.62	4.279
			295	1.15	4200	2.61	4.279
			293	1.15	4100	2.62	4.279
5	1.0	10	403	0.875	5600	3.43	3.698
			398	0.868	5600	3.46	3.702
			403	0.875	5600	3.43	3.698
6	1.0	100	506	0.633	5200	4.74	3.435
			487	0.618	5100	4.85	3.436
7#	1.0	135.2	466	0.567	4200	4.80	3.438
		135.2	466	0.567	4200	4.80	3.438
8	2.0	1	235	1.00	3300	2.99	6.175
			229	0.987	3200	3.04	6.174
			229	0.987	3200	3.04	6.174
9	2.0	10	307	0.743	4400	4.04	5.284
			324	0.767	4900	3.91	5.289
			304	0.739	4200	4.06	5.283
10	2.0	100	392	0.543	5400	5.53	4.802
			380	0.533	4400	5.63	4.796
			385	0.537	4700	5.59	4.796
11#	2.0	221.5	367	0.445	3400	6.22	4.765
		221.2	367	0.445	3400	6.21	4.765
		221.3	366	0.444	3300	6.21	4.765
12	10	1	124	0.685	1800	4.38	18.81
			122	0.677	1700	4.43	18.81
			125	0.685	1800	4.38	18.81
13		10	156	0.495	2200	6.06	16.19
			157	0.496	2500	6.05	16.19
			158	0.499	2600	6.01	16.19
14		100	204	0.367	2400	8.18	14.46
			189	0.351	2400	8.56	14.44
			190	0.352	2500	8.53	14.44
15#		729.2	264	0.288	3000	8.28	14.23

NOTES TO TABLE 10

* P_{max} is the maximum allowable value of the infiltration pressure
 P_i ; 1 atm = 10^5 Pa = 14.7 psi.

+ d_u was constrained in all cases to be less than 3 mm.

In cases 3, 7, 11, and 15 there was no constraint on P_{max} . These runs were optimized by a direct search method; note that the total cost in these cases failed to dip significantly below the cases with constrained infiltration pressure. Cases 3, 7, 11, and 15 have three independent variables (λ , t_t , and R).

TABLE 11

Results of Further Computer Optimization Runs Using
the Random Search Technique to Examine the Sensitivity
of Total Cost to Casting Length as a Parameter

504

Case	Variables at the Optimum					R (mm/mm)	Total Cost of kg of Casting Made Yearly (10 ⁶ dollars)
	C _p (\$/kg)	P _{max} * (atm)	l (mm)	d _{l+t} (mm)	t _t (s)		
16	2	1	100	0.601	1400	4.99	8.018
				0.601	1400	4.99	8.018
				0.601	1400	4.99	8.018
17			200	0.910	2800	3.29	6.211
				0.910	2700	3.29	6.212
				0.910	2800	3.29	6.211
8#			231#	0.991#	3200#	3.02#	6.174#
18			300	1.16	4200	2.58	6.319
				1.16	4200	2.58	6.319
				1.16	4200	2.58	6.319
19			400	1.38	5600	2.17	6.811
				1.38	5600	2.17	6.811
				1.38	5600	2.17	6.811
20			500	1.58	6900	1.90	7.510
				1.58	6900	1.90	7.510
				1.58	6900	1.90	7.510
21			600	1.76	8200	1.70	8.410
				1.76	8200	1.70	8.410
22			800	2.09	11000	1.43	11.06
				2.09	11000	1.43	11.06
				2.09	11000	1.43	11.06
23			1000	2.39	13000	1.25	15.99
				2.39	13000	1.25	15.99
				2.39	13000	1.25	15.99
24	2	10	200	0.574	2800	5.22	5.509
				0.574	2800	5.22	5.509
				0.574	2800	5.22	5.509
9#			312#	0.750#	4500#	4.00#	5.285#
25			400	0.871	5400	3.45	5.365
				0.871	5400	3.45	5.365
				0.871	5400	3.45	5.365
26			600	1.11	7800	2.70	5.785
				1.11	7800	2.70	5.785
				1.11	7800	2.70	5.785
27			800	1.32	9800	2.27	6.351
				1.32	9800	2.27	6.351
				1.32	111Q0	2.27	6.352
28			1000	1.51	11500	1.99	7.031
				1.51	11500	1.99	7.031
				1.51	11500	1.99	7.031

TABLE 11 (continued)

Case	Variables at the Optimum					Total Cost of 10^6 kg of Castings Made Yearly (10^6 dollars)	
	C_p (\$/kg)	P_{max}^* (atm)	l (mm)	d	$d_l \dagger$ (mm)	t_t (s)	
13#	10	10	157#	0.498#	2400#	6.04#	16.19#
29			200	0.574	2800	5.22	16.38
				0.574	2800	5.22	16.38
				0.574	2800	5.22	16.38
30			400	0.871	5500	3.45	18.70
				0.871	5500	3.45	18.70
				0.871	5500	3.45	18.70
31			600	1.11	7800	2.70	21.53
				1.11	7800	2.70	21.53
				1.11	7800	2.70	21.53
32			800	1.32	9800	2.27	24.66
				1.32	9900	2.27	24.66
				1.32	9900	2.27	24.66
33			1000	1.51	12000	1.99	28.22
				1.51	11300	1.99	28.22
				1.51	11600	1.99	28.22

Notes:

* P_{max} is the maximum allowable value of the infiltration pressure

$$P_1; 1 \text{ atm} = 10^5 \text{ Pa} = 14.7 \text{ psi.}$$

† d_u was constrained in all cases to be less than 3 mm.

Cases 8, 9, and 13 from Table 10 are included to indicate the optimum for unconstrained casting length.

TABLE 12

506

Results of Further Computer Optimization Runs Using
the Random Search Technique to Examine the Sensitivity
of Total Costs to the Maximum Particle Size Dmax as a Parameter

Case	Parameters			Variables at the Optimum				Total Cost of 10 kg of Castings Made Yearly (10 ⁶ dollars)
	C _p (\$/kg)	P _{max*} (atm)	D _{max} (mm)	l (mm)	d _{eff} (mm)	t _t (s)	R (mm/mm)	
34	2	1	1	72.7	0.496	1700	2.02	8.722
35			2	151	0.771	3000	2.60	6.799
				167	0.816	3800	2.45	6.918
36			3	229	0.987	3200	3.04	6.174
37			4	350	1.27	9700	3.14	5.932
				335	1.24	7800	3.22	5.904
38			5	437	1.46	11500	3.43	5.706
				449	1.48	12700	3.38	5.713
39			6	541	1.65	15700	3.63	5.565
40			8	755	2.02	24900	3.96	5.377
41			10	957	2.33	43100	4.29	5.258
				995	2.38	42700	4.20	5.256
42	2	10	1	115	0.413	2800	2.42	7.032
43			2	196	0.567	2300	3.53	5.595
				201	0.576	2100	3.47	5.591
44			3	290	0.719	6500	4.17	5.326
45			4	430	0.910	7800	4.40	5.111
				429	0.908	7800	4.41	5.111
46			5	554	1.06	12100	4.72	5.000
47			6	686	1.20	16900	4.99	4.923
48			8	1035	1.54	48400	5.20	4.869
49			10	1211	1.69	42300	5.91	4.799
50	10	10	1	63.2	0.288	2100	3.47	21.040
51			2	109	0.400	2500	5.00	17.364
				98.9	0.377	1000	5.31	17.059
52			3	199	0.573	2800	5.23	16.371
53			4	199	0.573	3900	6.98	15.677
				245	0.649	4500	6.17	15.688
54			5	312	0.751	15800	6.66	15.482
				304	0.739	12200	6.77	15.379
55			6	348	0.801	9500	7.49	14.998
56			8	481	0.973	16600	8.23	14.608
57			10	627	1.14	27400	8.77	14.351
				632	1.15	27200	8.73	14.351
58			15	1033	1.54	59600	9.75	14.015
59			20	1644	2.03	85700	9.84	13.986

NOTES TO TABLE 12

* P_{max} is the maximum allowable value of the infiltration pressure
 P_i ; 1 atm = 10^5 Pa = 14.7 psi.

† D_{max} is the maximum allowable value of the upper limit d_u of the range of particle sizes used to make the casting.

TABLE 13

Calculations of Process Parameters Dependent
on the Optimizable Variables

A. Cycle Time, seconds

$$\begin{aligned}
 t_c &= 2[t_t + (d_u^2/D)(0.13 + 0.13 \alpha + 0.14 H)] \\
 &= 2[t_t + (R^2 d_\ell^2/D)(0.13 + 0.13 \alpha + 0.14 H)] \\
 &= 2 t_t + (9.496 \times 10^8) R^2 d_\ell^2 \quad \text{for } \left\{ \begin{array}{l} \alpha = 0.005, H = 1, \text{ and} \\ D = 5.7 \times 10^{-10} \text{ m}^2/\text{s} \end{array} \right.
 \end{aligned}$$

B. Casting Furnace Volume, m^3

$$\begin{aligned}
 V_f &= \frac{12 \times 10^6}{2.592 \times 10^7} \left(\frac{t_c}{\rho_c} \right) = (5.898 \times 10^{-5}) t_c \\
 &= (1.180 \times 10^{-4}) t_t + (5.601 \times 10^{-4}) R^2 d_\ell^2
 \end{aligned}$$

C. Number of Castings Made per Cycle

$$\begin{aligned}
 n_c &= (2/3)(V_f/V_i) ; \quad V_i = (2\pi/9)d_\ell^3 \\
 &= (1.126 \times 10^{-4}) t_t d_\ell^{-3} + (5.348 \times 10^{-4}) R^2 d_\ell^2 d_\ell^{-3}
 \end{aligned}$$

D. Number of Castings Made per Year

$$\begin{aligned}
 n_y &= (10^6) / (\rho_c d_\ell^3 \pi / 36) \\
 &= (1460.) d_\ell^{-3}
 \end{aligned}$$

E. Mass of One Casting, kg

$$\begin{aligned}
 m_c &= V_c \rho_c = (7850\pi/36) d_\ell^3 \\
 &= (685.04) d_\ell^3
 \end{aligned}$$

F. Cost per kg of the Particles Used for the Solid Charge

$$\begin{aligned}
 \text{Unit cost of particles} &= C_\delta = C_p \left(\frac{\ln \Delta}{\ln R} \right) \\
 \text{actually used} &= 2.303 C_p (\ln R)^{-1}
 \end{aligned}$$

TABLE 14

Effects of Particle Cost C_p and Maximum Infiltration Pressure P_{max} on Selected Dependent Process

Parameters at Optimum Conditions (λ , R , and t_t unconstrained)

Dependent Parameters (See Table 13 for equations)

Case	C_p (\$/kg)	P_{max} (atm)	D_{max} (mm)	t_c (s)	Casting Mass m_c (kg)	Cycle Time t_c (s)	Furnace Vol. ^{**} V_f , (m ³)	No. of Castings Made Per Cycle n_c	Cost Contributions to the Total			Capital % %
									Total Cost (10 ⁶ dollars)	Cost Materials %	Cost Heat %	
									No. of Casting Made Per Cycle	%	%	
1	0.1	1	3	127	24000	1.39	7	2.17	51	33	14	2
2		10		332	21000	1.25	2 or 3	2.17	52	32	14.	2
3		36.76*		489	21000	1.36	1 or 2	1.98	51	32	16	1
4	1.0	1	3	17.3	17000	0.99	37	4.28	66	22	11	2
5		10		44.9	20000	1.17	17	3.70	67	21	10	1
6	100			79.1	19000	1.11	9	3.44	64	21	14	1
7	135.2*			69.2	15000	0.91	5 or 6	3.44	64	21	14	1
8	2.0	1	3	8.20	15000	0.88	71	6.17	71	18	9	1
9		10		19.3	17000	1.00	34	5.28	73	17	9	1
10	100			39.1	18000	1.06	18	4.80	72	17	10	1
11	221.3*			33.6	14000	0.82	9	4.77	70	16	12	1
12	10.	1	3	1.25	12000	0.71	369	18.8	82	11	6	1
13		10		2.63	14000	0.80	199	16.2	84	10	5	1
14	100			4.64	13000	0.79	111	14.4	85	9	5	1
15	729*			12.6	11000	0.67	20	14.2	87	6	6	1

Note: * Cases 3, 7, 11, and 15 had no constraint on P_{max} .

** 8 Hours Cycle Time = 28800 s.

TABLE 15

Effects of Casting Length λ , Particle Cost C_p , and Maximum Infiltration Pressure P_{max}
on Selected Dependent Process Parameters at Optimum Conditions (R and t_t unconstrained)

Dependent Parameters (See Table 13 for equations)

Case	C_p (\$/kg)	P_{max} (atm)	D_{max} (mm)	λ (mm)	Casting				Cost Contributions to the Total			
					Mass m_c (kg)	Cycle Time t_t (s)	Casting Furnace Vol. V_f , (m ³)	Per Cycle n_c	Total Cost (10 ⁶ Dollars)	Materials %	Heat %	Capital %
									No. of Castings Made			
16	2	1	3	100	0.69	11000	0.67	640	8.02	45	36	17
17				200	5.48	14000	0.84	100	6.21	68	20	10
8#				231#	8.20	15000	0.88	71	6.17#	71	18	9
18				300	18.5	17000	1.00	35	6.32	77	15	7
19				400	43.8	20000	1.16	17	6.81	82	12	6
20				500	85.6	22000	1.32	10	7.51	85	10	4
21				600	148	25000	1.47	6 or 7	8.41	88	8	4
22				800	351	30000	1.76	3	11.1	91	6	2
23				1000	685	34000	2.02	2	16.0	94	4	2
24	2	10	3	200	5.48	14000	0.83	100	5.51	64	23	12
9#				312#	19.3	17000	1.00	36	5.28#	73	17	9
25				400	43.8	19000	1.14	17	5.37	77	15	7
26				600	148	24000	1.42	6	5.79	82	12	6
27				800	351	28000	1.66	3	6.35	85	10	5
28				1000	685	32000	1.85	2	7.03	87	9	4
									0.1		0.3	

Note: # Cases 8 and 9 had no constraint on λ .

** 8 Hours Cycle Time = 28800 s.

TABLE 15 (Continued)

Effects of Casting Length λ , Particle Cost C_p , and Maximum Infiltration Pressure P_{max}
on Selected Dependent Process Parameters at Optimum Conditions (R and t_t unconstrained)

Case	Dependent Parameters (See Table 13 for equations)												
	Parameter			Casting **			No. of Castings Made Per Cycle						
	C_p (\$/kg)	P_{max} (atm)	D_{max} (mm)	λ (mm)	m_c (kg)	Time t_t (s)	Furnace Vol. V_f , (m ³)	Total Cost (10 ⁶ Dollars)	Cost Materials	Heat	Capital %		
13#	10	10	3	157#	2.63	14000	0.80	199	16.2#	84	10	5	1
29		200	5.48			14000	0.83	100	16.4	88	8	4	1
30		400	43.8			19000	1.15	17	18.7	93	4	2	0.3
31		600	148			24000	1.43	6	21.5	95	3	1	0.2
32		800	351			28000	1.65	3	24.7	96	3	1	0.1
33		1000	685			32000	1.87	2	28.2	97	2	1	0.1

Note: # Case 13 had no constraint on λ .

** 8 Hours Cycle Time = 28800 s.

TABLE 16
Effects of Maximum Particle Size D_{max}, Particle Cost C_p, and Maximum Infiltration Pressure P_{max} on Selected Dependent Process Parameters at Optimum Conditions (ϱ , R, and t_t unconstrained)

Case	Dependent Parameters (See Table 13 for equations)										
	Parameter			Casting **			No. of Castings Made Per Cycle n _c			Cost Contributions to the Total	
	C _p (\$/kg)	P _{max} (atm)	D _{max} (mm)	Mass m _c (kg)	Cycle Time t _c (s)	Vol. V _f (m ³)	Total Cost (10 ⁶ Dollars)	Materials	Heat	Machining	Capital %
34	2	1	1	0.26	4300	0.25	625	8.72	69	20	8
35		2	2.38	9700	0.57	157	6.80		72	19	8
36		3	8.20	15000	0.88	71	6.17		71	18	9
37		4	29.4	35000	2.04	45	5.93		73	18	8
38		5	57.3	47000	2.76	31	5.71		73	18	9
39		6	108	66000	3.87	23	5.57		73	18	9
40		8	295	111000	6.52	14	5.38		72	17	10
41		10	600	181000	10.7	12	5.26		72	18	10
											0.4
42	2	10	1	1.05	6600	0.39	241	7.03	73	18	7
43		2	5.15	8500	0.50	64	5.60		73	17	8
44		3	16.8	21000	1.27	49	5.33		71	19	9
45		4	54.6	46000	1.81	22	5.11		73	17	9
46		5	117	48000	2.83	16	5.00		73	17	9
47		6	221	68000	4.01	12	4.92		73	17	10
48		8	758	158000	9.30	8	4.87		72	17	10
49		10	1215	179000	10.6	6	4.80		71	17	12
											0.3

Note: ** 8 Hours Cycle Time = 28800 s.

TABLE 16 (Continued)

Effects of Maximum Particle Size D_{max} , Particle Cost C_p , and Maximum Infiltration Pressure P_{max} on Selected Dependent Process Parameters at Optimum Conditions (λ , R , and t_t unconstrained)

Case	C_p (\$/kg)	P_{max} (atm)	D_{max} (mm)	Dependent Parameters (See Table 13 for equations)							
				Casting		Furnace Vol. V_f , (m^3)	Per Cycle n_c	Cost Contributions to the Total			
				Mass m_c	Time $t(s)$			Total Cost (10^6 Dollars)	Cost Materials	Heat	Machining
50	10	10	1	0.17	5100	0.30	1140	21.0	83	11	5
51		2	0.89	8800	0.52	378	17.4	84	10	4	1
52		3	2.63	14000	0.80	199	16.2	84	10	5	1
53		4	5.40	23000	1.36	164	15.7	83	11	6	1
54		5	20.9	55000	3.26	102	15.5	85	10	4	0.4
55	10	10	6	28.9	53000	3.14	71	15.0	85	9	5
56		8	76.2	94000	5.54	48	14.6	85	9	6	0.3
57		10	169	150000	8.84	34	14.4	85	9	6	0.2
58		15	755	333000	19.6	17	14.0	85	8	7	0.1
59		20	3045	551000	32.5	7	14.0	85	7	8	0.1

Note: ** 8 Hours Cycle Time = 28800 s.

9. CONCLUSIONS

G. Langford

D. Apelian

9. CONCLUSIONS

The diffusion solidification (SD) process has been studied to develop a rapid cycle casting process for steel. The SD process makes use of the principle of solidification by mass transfer rather than by heat transfer, so that a new scaling law applies: time for SD freezing is proportional to $L^{6/5}$ rather than L^2 (as in conventional thermal freezing), where L is a characteristic dimension of each of a series of geometrically similar castings. An economic model for the SD process has been developed and used to examine the sensitivity of the total process costs (exclusive of labor, instrumentation, administrative, and space requirements) to various input parameters.

The advantages of SD casting include:

- No heat need be rejected to the surroundings to effect freezing; the process of freezing by SD is nearly isothermal.
- The solidification time for large, bulky SD castings is shorter than for conventionally solidified ones.
- No riser is necessary because there is only 40% as much solidification shrinkage to be accommodated, and because the remaining porosity is uniformly distributed.
- Homogeneous casting compositions can be achieved, especially in alloys which ordinarily exhibit microsegregation during conventional solidification.
- Casting and process design are greatly simplified because there is no need to plan for directional solidification. The theoretical models of the process statics and kinetics have been proven experimentally.

The SD casting process has been proven feasible in the present or previous work for the following systems by direct experimentation:

- carbon steels (zero to 2 wt. pct. C).
- malleable high carbon steels (i.e. Si-containing steels which readily graphitize).
- composite, "lean" stainless steels (i.e., based on infiltration of 60 wt. pct. of low carbon steel shot with 40 wt. pct. of Fe-Cr-Ni stainless steel liquid).
- ultra high carbon high speed steel.
- tin bronzes (the entire list of copper-rich alloys to which SD could be applied has been reviewed and a casting design nomogram has been established).
- iron-silicon.
• iron-phosphorous. } (for magnetic applications)
- ternary iron-carbon-X alloys, where X is Co, Mo, V, Mn, Si or Cr (only Cr microsegregation is uncontrollable).

The design techniques for SD casting has been established theoretically and corroborated by quantitative experiments. A design nomogram relating casting size, shot size, infiltration kinetics, homogenization kinetics, and macrosegregation has been developed for the iron-carbon system. The infiltration, solidification, homogenization and macrosegregation kinetics have been theoretically modelled and proven experimentally. The particle valve (PV) used to control the infiltration step during SD casting has been modelled theoretically and the model has been proven to be quantitatively correct and its range of applicability and failure mechanisms studied. Low

carbon iron shot to be used in the SD process were manufactured using two different routes: by gas atomization in a bottom pour furnace and by decarburization of commercially available peening shot using CO/CO₂ mixture. The two methods represent the extremes in terms of shot quality and cost; inert gas atomization representing the high cost technology for manufacturing high quality shot. Large batches of peening shot could not be decarburized evenly in this study due to unavoidable gradients in the composition of CO/CO₂ mixture as it flows across the packed bed of the peening shot. Even decarburization of particles can, however, be achieved by using a rotary type furnace which would insure that all particles experience the same average gas composition. Both permanent and throw-away molding methods have been shown to be feasible. Two direct (having size independent heating rates) and one indirect heating methods for the shot have been evaluated in terms of attainable heating rates and heating efficiencies. A new kind of microsegregation law has been discovered and its form established empirically; this new law, which requires the composition of a ternary alloying element to vary continuously across the solid/liquid interface, enables normal mircosegregation to be defeated in many ternary iron-carbon-X systems (Co, V, Mn, Mo, Mn and Si, but not Cr). Therefore, essentially homogeneous ternary alloys can be produced in many Fe-C-X systems in spite of the slow diffusion of the (substitutional) element X in the solid relative to the liquid. Casting machines based on heating by magnetically induced eddy currents, forced gas infiltration (direct routes) and thermal radiation (an indirect method) have been designed qualitatively in terms of process logic.

Casting quality has been evaluated in terms of the following interactions:

- Infiltration pressure/shot size/infiltration depth vs. micro- and macro- segregation of carbon.
- Inert gas pressure in mold vs. casting density and pore distribution; the shot region of the mold assembly need not be evacuated if the infiltration pressure exceeds 707KPa (7 atm.).
- Shot purity and deoxidation practice vs. shrinkage cavitation, gas evolution, and the location and shape of the resulting pores, as well as casting ductility.

10. PUBLICATIONS, PRESENTATIONS AND PERSONNEL

PUBLICATIONS

Publications and technical reports, related to the SD process, published, are listed below:

1. D. Apelian, G. Langford, "Rapid Cycle Casting of Steel", Annual Report to ARO for period July 1, 1977-June 30, 1978, Contract No. DAAG 29-77-C-0028
2. ibid, biannual progress reports.
3. M. Paliwal, D. Apelian, G. Langford, "Performance of a Porous Refractory Valve for Liquid Metals", Metallurgical Transactions, Vol. 11B, March 1980, pp. 39-50.
4. D. Apelian, "Solidification Processing Research: An Overview", Research Directions, Vol. 3, No. 1, 1980.
5. G. Langford, D. Apelian, "Diffusion Solidification", Journal of Metals, Vol. 32, September 1980, pp. 28-33.
6. M. Paliwal, D. Apelian, G. Langford, "Microsegregation of Ternary Alloying Elements During Diffusion Solidification of Iron-Carbon Based Alloys", submitted to Metallurgical Transactions, July 1981.
7. D. Apelian, "Cast Structures" in Encyclopedia of Materials Science and Engineering, Subject Editor: G. E. Dieter.
8. D. Apelian, "Solidification Mechanics and Mechanisms" in Encyclopedia of Materials Science and Engineering, Subject Editor: G. E. Dieter.
9. D. Apelian, "New Developments in Aluminum Processing", in Proceedings of Second International Symposium of Aluminum Transformation Technology and its Applications, August 1981, Buenos Aires, Argentina, published by Aluar and ASM.
10. D. Apelian, "Novel Solidification Processes", in Proceedings of Solidification Processing, Genootschap Metaalkunde van het TI-K.VIV, Leuven, Belgium, in press.
11. G. Langford, "Casting of Cu Alloys by Diffusion Solidification", presented at the AFS annual meeting, March 1981, Cincinnati, Ohio.

PAPERS IN PROGRESS

12. M. Paliwal, D. Apelian, G. Langford, "Porosity Formation in Diffusionally Solidified Steel Castings", to be submitted to Metallurgical Transactions.
13. H. Sreshta, G. Langford, D. Apelian, "Rapid Heating of Unbonded Packed Bed of Spheroidal Steel Particles", to be submitted to Metallurgical Transactions.
14. H. Sreshta, G. Langford, D. Apelian, "Kinetics of Melt Infiltration During Steel Casting by Diffusion Solidification", to be submitted to Metallurgical Transactions.

TECHNICAL PRESENTATIONS

1. D. Apelian, "Rapid Cycle Casting Techniques for Ferrous Alloys", A discussion seminar presented at the 1977 Engineering Foundation Conference at Rindge, N. H., August 1977.
2. G. Langford, D. Apelian, et al; "Rapid Cycle Steel Casting via Diffusion Solidification", AIME Fall Meeting, St. Louis, MO, October 1978.
3. H. Sreshta, G. Langford, D. Apelian, "Rapid Heating of Unbonded Steel Powder and Porous Compacts", AIME Fall Meeting, St. Louis, MO., October 1978.
4. M. Paliwal, D. Apelian, G. Langford, "Performance of a Porous Refractory Valve for Liquid Metals", AIME Fall Meeting, St. Louis, MO, October 1978.
5. D. Apelian, "Diffusion Solidification", seminar presented at the Army Materials and Mechanics Research Center, Watertown, Massachusetts, December 1979.
6. H. Sreshta, G. Langford, D. Apelian, "Casting Manufacture by Diffusion Solidification", 109th AIME Annual Meeting, Las Vegas, Nevada, February, 1980.
7. M. Paliwal, D. Apelian, G. Langford, "Structure and Properties of Diffusion-Solidified Steel Castings", 109th AIME Annual Meeting, Las Vegas, Nevada, February 1980.
8. C. Lall, D. Apelian, G. Langford, "Aluminum-Lithium Castings Made by Diffusion Solidification", 109th AIME Annual Meeting, Las Vegas, Nevada, February 1980.
9. D. Apelian, "Mathematical Modeling of Solidification Processes", invited lecture at Sandia Laboratories, Albuquerque, New Mexico, November 1980.
10. D. Apelian, "Melt purification and Diffusion Solidification", invited lecture at Carpenter Technology, Reading, PA, January 1981.
11. D. Apelian, "Novel Solidification Processes", Solidification Processing International Symposium, Katholieke University, Leuven, Belgium, April 8-9, 1981.
12. D. Apelian, "Innovative Processes", at NASA-Lewis, Cleveland, Ohio, May 1, 1981.
13. D. Apelian, "Novel Solidification Processes", at Case-Western Reserve University, Cleveland, Ohio, May 1, 1981.

PERSONNEL

The following graduate students completed Ph.D. Theses on different aspects of rapid cycle casting of steel:

- M. Paliwal, "The Diffusion Solidification Process: Particle Valve; Microsegregation; Structure and Properties", June 1981.
- H. Sreshta, "SD Kinetics and Casting Machine Design", June 1981.

Dr. Chaman Lall obtained postgraduate (post-Doctoral) experience in Solidification Processing. Dr. Lall had obtained his Ph.D. from the University of Birmingham.